AD-A136 193 1982 NAVAL RESEARCH LABORATORY REVIEW(U) NAVAL RESEARCH 1/3
LAB WASHINGTON DC A E ROBSON ET AL. 1983

UNCLASSIFIED F/G 14/2 NL

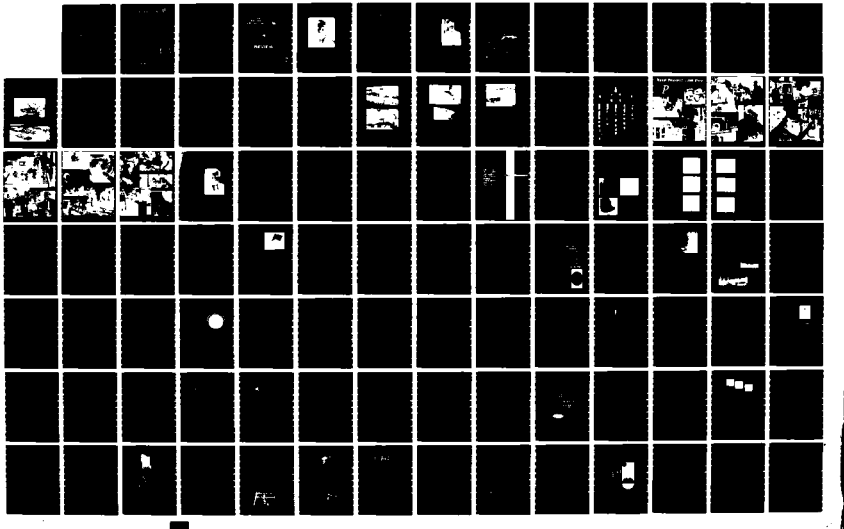

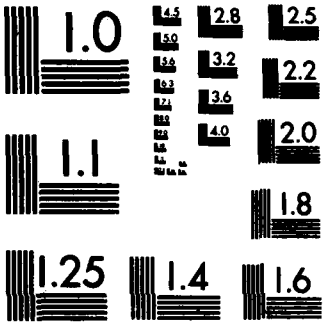

922—First radio broadcast of a presidential address. 1922—First detection of a moving ship by radio waves (birth of navy radar). 1922—
rst transmission of printed messages and photographs by radio. 1924—First flight of a radio-controlled ft. 1924—
evelopment of the first high-frequency, high-powered, crystal-controlled radio transmitters. 1924—First airborn io. 1925—
evelopment of the Navy's first high-frequency radio receiver. 1926—Publication of theory of the radio "skip dist foundation
f modern wave-propagation theory). 1927—First transmission of radio signals twice around the world. 1927-34 d develop
ent of gamma-ray radiography as a technique for determining the soundness of metal structures, castings, a 1928—Firs
ross-country radio transmissions from an airplane. 1928—First detection of an airplane in flight by radio waves. se of X-ray
iffraction to study battery-active materials. 1931-33—First use of lithium hydroxide in the purification of CO_2 1931-33—
levelopment of the first hydrogen detection system for submarines. 1932—Development of the Navy's first Ver / (VHF) air
raft communication system. 1933—First application of radio beacons to land aircraft. 1934—First detection of aircraft by pulse radar
934-38—Development of shipboard foundry sand technology. 1935—Sonar echo-ranging system developed using NRL Rochelle salt trans
lucer. 1936—Radar duplexer enabling radar transmission and reception on the same antenna developed. 1936—Research on and the produc
ion of potassium superoxide as an oxygen source for rebreathers critical to damage-control operations aboard ships initiated. 1937—
evelopment of the U S 's first Identification Friend or Foe (IFF) radio system. 1939—XAF radar (first Navy operational radar) installed on the
attleship USS NEW YORK. 1939—Development of the radar plan-position indicator (PPI). 1939—Development of the liquid thermal-diffusion
ethod for separating uranium isotopes. 1939—Development of the Navy's first radio pulse altimeter. 1939-43—Acoustically transparen
ntifouling paint which greatly extended the service life of sonar domes invented. 1939—First application of sea markers for personnel adrift
t sea. 1940—Submarine radar developed. 1940—Introduction of the Ponomat ASW noisemaker on ships during World War II. 1940—
evelopment of organic linings for fuel storage and distribution tanks. 1940—Introduction of temperature-indicating paints for the remote
onitoring of component temperatures. 1940-41—Hydrogen eliminator for submarines developed. 1940-41—Development of a method fo
anufacturing uranium bexafluoride. 1941—Development of antijam techniques for Navy radar systems. 1941-45—Pilot plant for the impreg
ation of all the activated carbon (500 tons) used by the Navy in World War II placed in operation. 1941-45—Development of activated car
on impregnated CW protective clothing. 1943—Development of the first electronic countermeasure systems for ships and submarines
943—Development of practical equipment for the mitigation of precipitation static interference on aircraft. 1943—Initial development of pro
ein foam for the extinguishment of fuel fires. 1943—Chemically deposited coatings for reducing (or increasing) the reflection of transparen
urfaces, such as lens systems, and fighter-plane canopies developed. 1944—Electrically conducting wicks developed for use as static
ischargers on military and commercial aircraft. 1944—Development of the first radio-controlled bomb. 1944-45—Development of rubbe
utter values for pulse jet engines. 1945—First use of laboratory-equipped planes to study radio and radio propagation in the troposphere
945—Development of nonflammable hydraulic fluids. 1945—Development of vapor-phase corrosion inhibitors for the protection of ferrou
etals against corrosion. 1945-57—Introduction of cellulose-caprate optical cement for optical systems subjected to extreme variations in
ltitude and temperature. 1946—Development of the first UHF antenna multicoupler system. 1946—Development of a shipboard radio hom
ng system for carrier-based aircraft. 1946—First application of cryptography in radar identification. 1946—First far-ultraviolet spectrum o
he sun obtained from a V-2 rocket (birth of the Navy space program). 1946—Discovery of tropospheric scatter beyond the horizon. 1946—
evelopment of helicopter gear for antisubmarine warfare. 1946-50—Radar absorbent materials for camouflage and deception developed
947—Development of blimp sonar for antisubmarine warfare. 1948—Discovery of high temperature anti-oxidant additives, which lead to th
evelopment of high-temperature synthetic lubricants. 1948-55—Development of highly sensitive electrochemical recorder paper. 1949—
igh-frequency cross-correlation storage and narrow-band radar spectrum. 1949—Development of high-resolution radar, which lead to air
ort taxi radar. 1949—First measurement of the effects of extreme ultraviolet and X-ray solar radiation on the ionosphere. 1949—
evelopment of the real-time ballistic missile impact predictor (for test range safety). 1949—Detection of fission products in fallout from th
irst Russian atomic bomb. 1949-50—Development of the Explosion Bulge Test (EBT), a reliable method for determining the performanc
haracteristics of hull weldments for submarines and ships. 1950—Development of the graphic range-ra / o
ttack using sonar systems. 1950—Development of the solid-state personnel radiation dosimeter. 1950 ha
ne mi ts, which resulted in the weight of submarines being reduced as much as four to oot
ully s rave antenna placed in operation. 1950—Development of optically-aware fluores inc
950- of dry lubrication for guns and ammunition. 1950-1958—Basic knowledge of soli an
uid f metal developed. 1951—Advantages of low-frequency sonar for greatly increa ec
951- e signals reflected off the moon (world's largest parabolic antenna used). 1951— va
ve a t for armaments. 1951-53—Invention of the Crack-Starter Method (CSM) for st 2-
evel ectron memory tube having indefinitely long memory combined with instantaneous t Development o
he fo ise on aircraft crash fires. 1952—Development of high-efficiency CW BW aerosol filters, the first all-glass filters pro
ucec hines. 1952—Useful life of high-visibility fluorescent paints improved. 1952—ND-Mark V Protective Mask developed
952 il-Ductility-Transition Temperature introduced. 1952—First computer analysis made of aircraft target interception an
nterc (Triangle System). 1952—Development of the first television submarine periscope buoy. 1953—Development of the fer
oma ifter and isolater in a rectangular waveguide. 1953—First detection and measurement of interstellar ionized hydroge
loud idio sources. 1953—Development of the magnetic-aspect indicator for high-altitude rockets. 1953—Mass spectromete
evel flights in the upper atmosphere. 1953—First measurement of the water vapor in the upper atmosphere using ultraviole
etec evelopment of Over-the-Horizon Radar. 1954—Photography from Aerobee 150 launched at White Sands, New Mexico
rov ew from space of a major storm cloud formation. 1954—NRL NAREC digital computer placed in operation (prior to th
eve nmercial digital computers). 1954—Development of a high-resolution sonar for mine detection. 1954—Traveling wav
scil eveloped for recording events in the ionosphere announced. 1954—Development of the first successful aircraft chaf
isp ntegrated atmospheric analyzer for nuclear submarines developed. 1954-55—Guidelines established for SSN submarin
on 57—Problem of fogging and icing of submarine periscope windows solved. 1954—First radio communications using th
noo relay station. 1955—Development of the sonar echo trap for aiding the identification and classification of sonar tar
ets. 1955—First U S electron microprobe designed and constructed. 1955—Project VANGUARD established at NRL. 1955—New system
riginated for the cathodic protection of ships' hulls. 1955—Hydrogen embrittlement identified as one of the major causes of failures

1982 REVIEW

Naval Research Laboratory

Washington, D.C.

Sixty Years of Science and Technology for the Navy and the Nation 1923-1983

ser radar beams to optical images visible in high ambient light. 1971—Giant magnetostriction constants observed in rare-earth iron intermet
llic compounds. 1971—Development of the Laser-Oscillation Range Technique (LORT). 1971—First observation of de Hass Van Alphe
ffects in titanium. 1971—Development of the flame laser (first purely chemical CO laser). 1971—First measurement of crystal growth b
olographic interferometry. 1972—First observation of de Hass Van Alphen effects in titanium-iron alloys. 1972—Development of the Ratio
nalysis Diagram (RAD) procedure for fracture-safe design of metals. 1972—First manned space observatory placed on the moon (Apollo
6). 1973—Development of the oscillation-range technique. 1973—NRL-developed X-ray structure-analysis techniques used to improve publ
ealth. 1973—New technique devised to detect and inspect ultra-thin barrier films. 1973—NRL-produced cesium used to detect heart prob
ms. 1973—Development of an improved hydrophone calibrator. 1973—All-weather technique devised to measure sea surface oil spills
973—NRL experiment flown aboard NASA's Skylab. 1973—Technique developed for suppressing closed space fires with nitrogen. 1973
lot program initiated for the use of neutron radiotherapy for the treatment of cancer. 1973—First use of OTH radar to detect distant storm
sea. 1973—First application of Synthetic Aperture Radar (SAR) to map ocean current boundaries. 1974—Development of the Light BE
ameria (LIBEC) system for deep ocean search and inspection. 1974—First cure of structural adhesives with radiation. 1974—Development o
n expendable submarine hydrophone. 1974—Development of a towed-buoy communications system for submarines. 1974—Technique dev
ed to give color judgement to color blind persons. 1974—Optically pumped continuous-wave laser developed. 1974—Protectant agains
arine borer infestation developed. 1974—Development of a chemical sea-surface marker to aid persons lost at sea. 1974—Activation of the
orld's first orbiting rubidium-vapor atomic oscillator (TIMATION III Satellite). 1974—World fluorocarbon (ozone) problem discovered by NRL
nvironmental studies. 1974—Voice digitizer developed for Navy high-frequency communications. 1974—Discovery of the green-flame
henomenon. 1974—First application of laser photolysis for materials analysis. 1974—Development of an X-ray fluorescence technique to
etect metallic water pollutants. 1974—Discovery that polymeric material fires transport toxic gases. 1974—Development of a fiber-optic
diation dosimeter. 1974—Effective chemical technique devised to separate water from fuel oils. 1975—First use of a laser receiver system
perform ocean and oil spill measurements. 1975—Development of a video system for deep-ocean search and inspection missions.
975—Highest known critical-current-density superconducting wire developed. 1975—Development of an air-collision avoidance system
975—X-ray detector developed for Apollo-Soyuz mission. 1975—Ultraviolet chemical laser action discovered. 1975—Holographic data
orage technique developed. 1975—Coupling device for fiber-optic communications systems developed. 1975—First use of skywave radar
monitor sea conditions (SEA ECHO). 1975—System developed to predict lightning threats to space launches. 1975—Improve refractory
eramic material developed for high-temperature gas turbines. 1975—Lost-cost X-ray diffraction technique developed for measuring submi
ogram asbestos pollution particles. 1975—NRL XUV telescope flown aboard the OSO-8 Satellite. 1975—Special filter devise to reduce oi
scharge from Navy ships. 1975—Inertial-inductive storage system developed. 1975—Technique developed for the production of isotopes
nitrogen and hydrogen for medical and nuclear power purposes. 1975—Discovery of the first X-ray pulsar beyond the Milky Way. 1975—
evelopment of improved low-frequency hydrophones for submarine detection. 1975—NRL experiment flown aboard Apollo spacecraft during
pollo-Soyuz mission. 1976—Passive microwave imaging system developed for the all-weather remote sensing of the ground and sea sur
ce. 1976—Development of a nondestructive method for determining essential metallic components in rocket and missile assemblies.
976—Development of the vertical-tube combustion reactor for studying combustion processes. 1976—Environmentally safe mosquito
ntrol technique (monocular films) developed and successfully tested. 1976—Development of a new technique to improve the strength o
rbon fiber materials used in laboratory and commercial materials. 1976—Improved air filtration system devised for nuclear reactors.
976—New fluoropolymer materials developed having wide applications in defense systems and in the civilian domain. 1976—Low-cos
ethod devised to detect and track sea ice using OTH radar. 1976—Small personal air sampler developed to monitor contaminants in areas
ntaining hazardous fumes. 1976—Very-Long-Baseline Interometry (VLBI) technique used to form world's largest radiotelescope. 1976—
evelopment of the TRAKX (Tracking Radar at Ka- and X-band) radar (the first precision low-angle tracking radar). 1976—Invention of a new
rbon dioxide (CO_2) fire extinguisher delivery horn (eliminated static electricity hazard). 1976—Development of the world's most powerful
bmillimeter radiation generator. 1976—Coherent laser radiation generated at a wavelength of 53.22 nanometers (the shortest wavelength
er recorded at that time). 1976—Radar technique devised to differentiate "sea spikes" from floating debris. 1976—Development of new
ramics for gas turbine ship-propulsion systems. 1976—Stereo-acoustic technique developed for displaying defects in materials. 1976—
vention of a fusion reactor system in which a tritium plasma is confined within a field-reversing deuterium ion layer. 1976—SOLCHFM (sola
ergy) concept introduced. 1976—Technique developed for improving wire ropes through controlled overstressing. 1976—High-current ion
am accelerator developed. 1976—First ion beams generated at a power level above 200,000 megawatts. 1976—Automated Scanning
w-Energy Electron Probe (ASLEEP) method for diagnosing failures in electronic systems developed. 1976—Development of a radar
tectable seamarker. 1976—Development of a highly directional (reduced intercept) millimeter-wave antenna. 1976—Development of
gh-performance low-temperature lubricant for rapid-fire machine guns. 1976—Development of a procedure for the shore-based testing o
drophones. 1976—Technique developed to enhance the detection of radar targets in a multipath environment. 1976—Development of
mputerized acoustic-calibration system for underwater sound projectors and hydrophones. 1976—Development of a nondestructive test to
udy the composition and structure of intractable organic polymers. 1976—Development of the Coherent Anti-Stokes Ramon Spectroscopy
ARS) technique for studying flames, electrical discharges and photochemical systems. 1977—First demonstration of the separation o
drogen isotopes by a plasma chemistry technique. 1977—Fiber optics coupler for microoptical circuits developed. 1977—ELF underse
mmunications antenna (SQUID) developed. 1977—Technique devised for demulsifying oily waste in ships' bilges and storage tanks.
ssing and separating nuclear wastes. 1977—Concept developed to improve efficiency of a
d to grow high-purity crystals for semiconductors. 1977—Development of a high-power
f the TRApped Plasma Avalanche Triggered Transit (TRAPATT) Device as power source and
que developed to improve and modify materials. 1977—World's largest X-ray detector (Experi
O spacecraft. 1977—NRL's long-term tropical research used to set metal corrosion guidelines.
easurement antenna developed. 1977—NRL superconducting wire, first developed in 1973
ed to heat plasmas to fusion temperatures using neutralized ion beams. 1977—Plasma
sotope demonstrated. 1977—Einstein's theory of relativity confirmed by the atomic clock
. 197?—Development of the atmospheric random monitor. 1977—Development of a high
1977—Use of high-powered lasers for high-strength high-speed welding demonstrated.

REVIEWED AND APPROVED
25 August 1983

John A. McMorris II

JOHN A. McMORRIS II, Captain, USN
Commanding Officer

NRL-2668-0036-10/83-3000

NAVAL RESEARCH LABORATORY

1982

REVIEW

WASHINGTON D.C. 20375

THE 1982 NAVAL RESEARCH LABORATORY REVIEW

is dedicated to the memory of

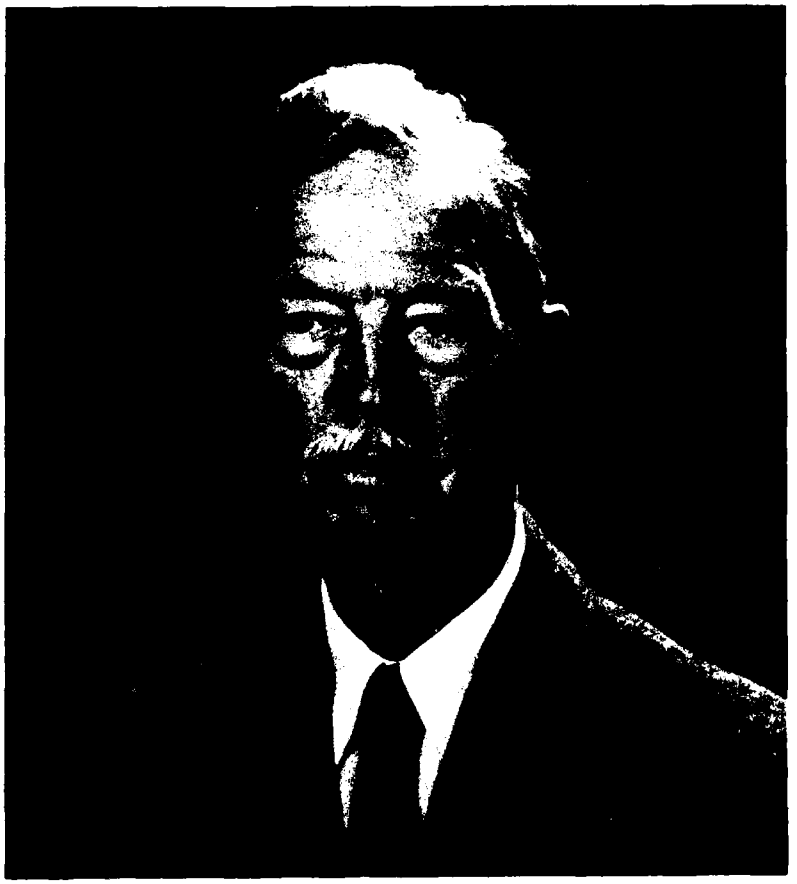

Dr. Edward Olson Hulburt

1891 - 1982

Dr. Hulburt was the first civilian director of research at the Naval Research Laboratory, and a pioneer of a wide range of physical research including spectroscopy, atmospheric optics, astronomy, and geophysics. The celebrated scientist joined the staff of NRL in 1924, just one year after the Laboratory opened. His early research in space technology developed into a continuing program at NRL which is being conducted today by Dr. Hulburt's namesake—the E. O. Hulburt Center for Space Research. Dr. Hulburt served as director of research from 1949 until his retirement in 1955. In 1945 he was a recipient of the Navy's Distinguished Civilian Service Award. We are proud to dedicate the 1982 NRL Review to his memory.

Mission . . .

To conduct a broadly based multidisciplinary program of scientific research and advanced technological development directed toward new and improved materials, equipment, techniques, systems, and related operational procedures for the Navy. In fulfillment of this mission, the Naval Research Laboratory:

Initiates and conducts scientific research of a basic and long-range nature in scientific areas of special interest to the Navy.

Conducts exploratory and advanced technological development deriving from or appropriate to the scientific program areas.

Within areas of technological expertise, develops prototype systems applicable to specific projects.

Performs scientific research and development for other Naval commands and, where specially qualified, for other agencies of the Department of Defense and, in defense-related efforts, for other Government agencies.

Upon request from appropriate Naval commands, assumes responsibility as the Navy's principal R&D center in areas of unique professional competence.

Serves as the principal activity for the Navy and its contractors in providing accurate calibration, test, and evaluation services on acoustic transducers and materials; in providing a service whereby an inventory of calibrated standard acoustic transducers are maintained for issue; and in performing research and development to advance the state of the art of acoustic measurements and standard transducers.

Performs research and development on sonar transducers and related acoustic materials.

Furnishes scientific consultative services for the Navy and, where specially qualified, for other agencies of the Department of Defense and, in defense-related efforts, for other Government agencies.

Provides to the Navy determinations of performance characteristics of developmental and prototype devices through limited engineering test and evaluation services.

PREFACE

The NRL *Review* reports the major unclassified work performed at the Naval Research Laboratory (NRL). It is the only NRL publication that also contains background information about the Laboratory, a listing of patents, papers, and awards, and significant events that occurred during the past year.

The publication date of this edition—1983—is a significant one for the Laboratory, for it marks our 60th anniversary. In 1923, the Laboratory consisted of five small buildings on the bank of the Potomac River and a dozen or so scientists. Today, we have grown to more than 150 buildings which house approximately 3200 dedicated men and women and their scientific equipment.

Over the years the Laboratory has continually grown—and changed—in response to changing Navy and national needs and priorities as well as changes in perceived scientific opportunities. Our primary sponsors include the Chief of Naval Research, the Chief of Naval Material, the Systems Commands, and other Navy laboratories; however, the diversity of our capabilities also allows us, when appropriate, to serve other customers—the U.S. Army and Air Force, NASA, industry, and academia.

NRL's research and past accomplishments embrace nearly all of the physical sciences. Such a large, multidisciplinary laboratory is an essential part of a successful military research and development program. The broad spectrum of talent and technological know-how at NRL permits us to solve problems that could not be handled by small, specialized laboratories.

NRL's position is unique in that we operate directly under the Chief of Naval Research, who reports to the Assistant Secretary of the Navy for Research, Engineering and Systems. This direct link fosters a highly diversified research program.

Publication of the *Review* gives us an opportunity to assess and report our contribution to the Navy and to the Department of defense as well as the broader scientific communities we serve. As

CAPT John A. McMorris II, USN
Commanding Officer
Naval Research Laboratory

NRL is a part of the Office of Naval Research, the development and orderly flow of research results is a principal concern of NRL management. The *Review* also serves as a resource document to our customers and to the whole scientific community.

As you read this *Review* marking NRL's 60th year of operation, we hope you will agree that the Laboratory functions in the tradition under which it was founded—people—programs—progress—innovation; and that this combination will continue to foster discovery, inventiveness, and scientific advances for the nation and the fleet.

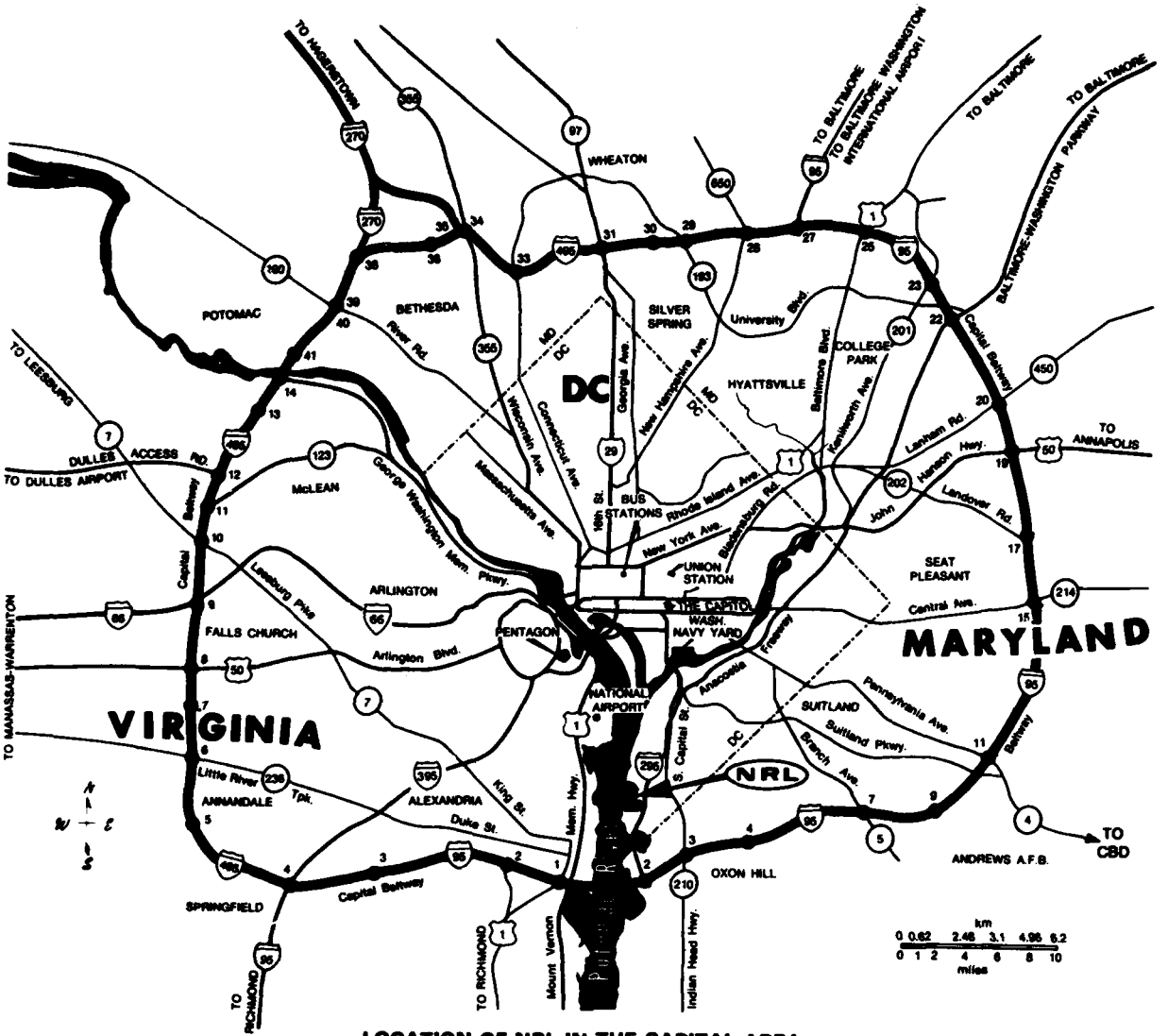

LOCATION OF NRL IN THE CAPITAL AREA

12/82

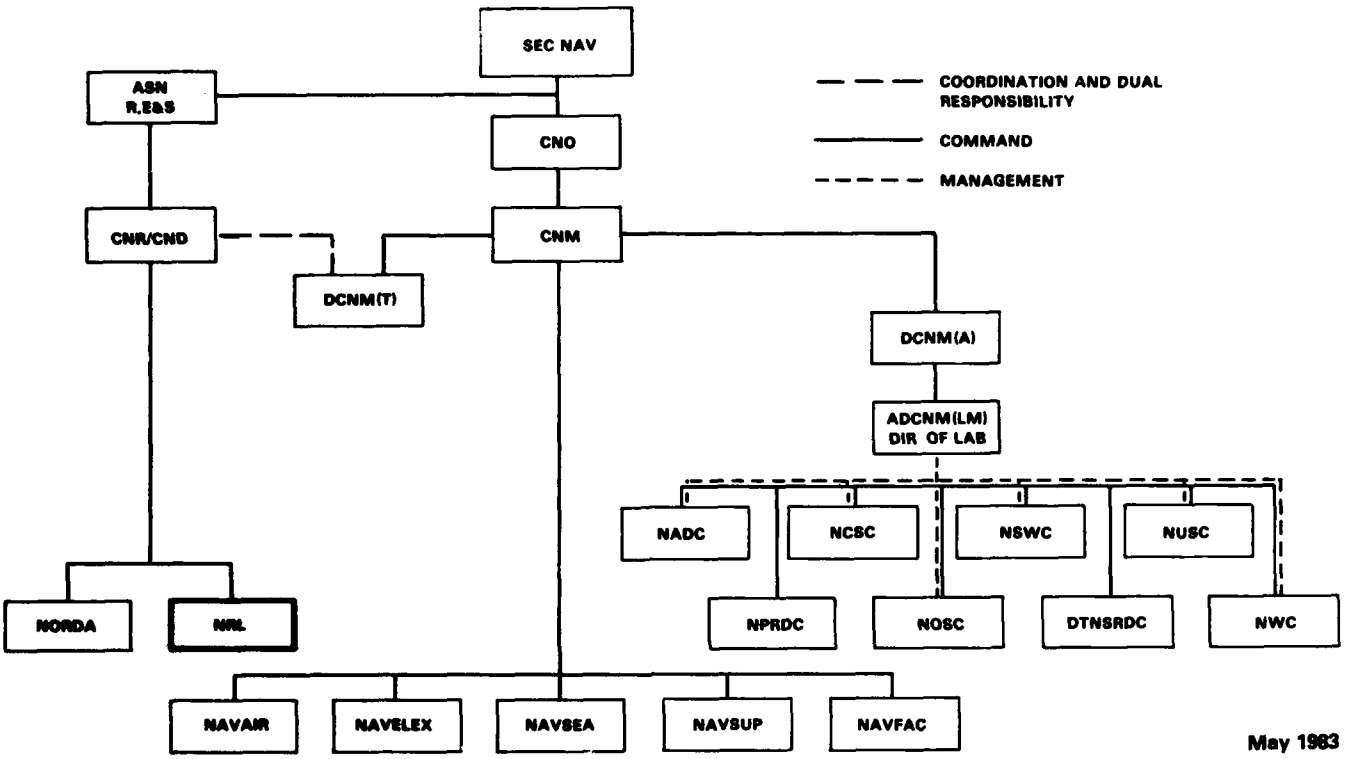

May 1983

ASN R,E&S – ASSISTANT SECRETARY OF THE NAVY RESEARCH,ENGINEERING & SYSTEMS

CNR/CND – CHIEF OF NAVAL RESEARCH/CHIEF OF NAVAL DEVELOPMENT
DCNM(T) – DEPUTY CHIEF OF NAVAL MATERIAL (TECHNOLOGY)
NORDA – NAVY OCEAN RESEARCH & DEVELOPMENT ACTIVITY
DCNM(A) – DEPUTY CHIEF OF NAVAL MATERIAL (ACQUISITION)
ADCNM (LM) DIR. OF LAB. – ASSISTANT DEPUTY CHIEF OF NAVAL MATERIAL (LOGISTICS MANAGEMENT) DIRECTOR OF LABORATORY
NADC – NAVAL AIR DEVELOPMENT CENTER
NCSC – NAVY COMMAND SUPPORT CENTER
NSWC – NAVAL SURFACE WEAPONS CENTER
NUSC – NAVAL UNDERWATER SYSTEMS CENTER
NPRDC – NAVY PERSONNEL RESEARCH & DEVELOPMENT CENTER
NOSC – NAVAL OCEAN SYSTEMS CENTER
DTNSRDC – DAVID TAYLOR NAVAL SHIP RESEARCH & DEVELOPMENT CENTER
NWC – NAVAL WEAPONS CENTER

May 1983

CONTENTS

CONTENTS

THE LABORATORY
THEN AND NOW

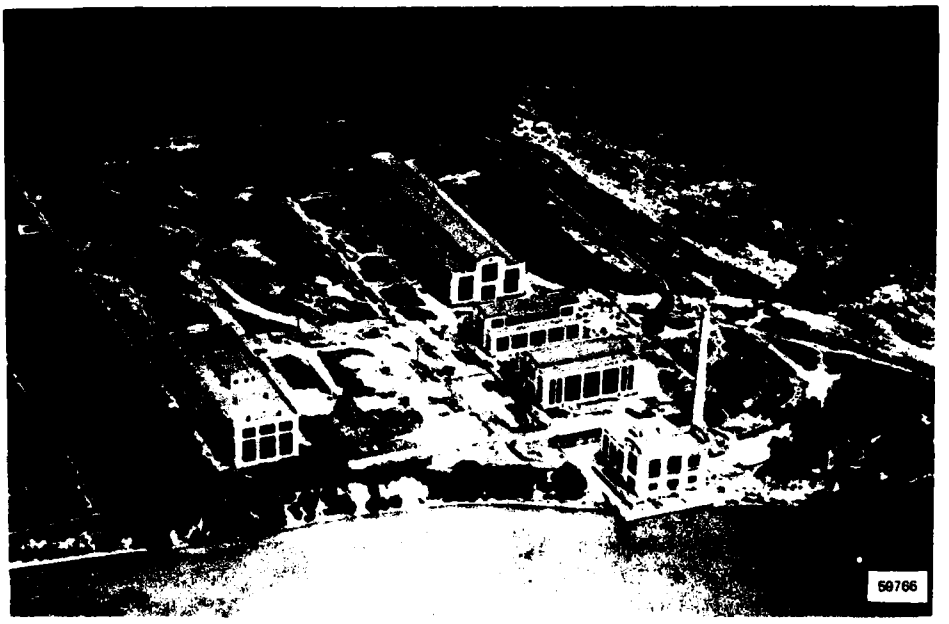

1923

1982

Historical Background

At a time when government and science seem inextricably linked, when virt ·lly no one questions the dependence of national defense on the excellence of national technical capabilities, it is instructive to recall that in-house defense research is rather recent. The Naval Research Laboratory (NRL), the first modern research institution created within the United States Navy, began operations in 1923.

The first step came in May 1915, a time when Americans were deeply worried over the great European war. Thomas Edison, asked by a *New York Times* correspondent to comment on the conflict, argued that the nation should look to science. "The Government," he proposed in a published interview, "should maintain a great research laboratory.... In this could be developed. . .all the technique of military and naval progression without any vast expense." Secretary of the Navy Josephus Daniels seized the opportunity of Edison's public comments to enlist his support. Edison agreed to serve as the head of a new body of civilian experts, named the Naval Consulting Board, to advise the Navy on science and technology. The Board's most ambitious plan was the creation of a modern research facility for the Navy. Congress allocated $1.5 million for the institution in 1916, but wartime delays and disagreements within the Naval Consulting Board postponed construction until 1920.

Its two original divisions, Radio and Sound, pioneered the fields of high-frequency radio and underwater sound propagation. They produced communications equipment, direction-finding devices, sonar sets, and, perhaps most significant of all, the first practical radar equipment built in this country. They also performed basic research, participating, for example, in the discovery and early exploration of the ionosphere. In addition, the Laboratory was able to work gradually toward its goal of becoming a truly general research facility. By World War II, five new divisions had been added: Physical Optics, Chemistry, Metallurgy, Mechanics and Electricity, and Internal Communications.

Total employment jumped from 396 in 1941 to 4400 in 1946, expenditures from $1.7 million to $13.7 million, the number of buildings from 23 to 67, and the number of projects from 200 to about 900. During the conflict, scientific activities necessarily were concentrated almost entirely on applied research. New electronics equipment—radio, radar, sonar—was developed. Countermeasures were devised. New lubricants were produced, as were antifouling paints, luminous identification tapes, and a sea marker to help save survivors of disasters at sea. A thermal diffusion process was conceived and used to supply some of the ^{235}U isotope needed for one of the first atomic bombs. NRL also type-tested a host of new devices that poured from booming wartime industry before they were certified as reliable for the Fleet.

After the war, scientific research was widely recognized as a vital national resource, and the Laboratory had a major and continuing role to play in providing it. When the Office of Naval Research was created in 1946, NRL was transferred to it; NRL thus became the *corporate laboratory* of the Navy, as it was later to be called.

The demands of this new position necessitated substantial reorganization. Rapid expansion had met wartime demands, but had left NRL improperly structured to address long-term Navy requirements. One major task—neither easily nor rapidly accomplished—was that of reshaping research management, that is, transforming a group of largely autonomous scientific divisions into a unified institution with a clear mission and a fully coordinated research program. The first attempt at reorganization vested power in a committee composed of all the division superintendents. This committee was impracticably large, so in 1949 a civilian director of research was named and given full authority over the program. Associate directors were added in 1954.

During the 37 years since the war, the areas of study at the Laboratory have included basic research concerning the Navy's environment of sea, sky, and space. Investigations have ranged widely, from monitoring the sun's behavior, to analyzing marine atmospheric conditions, to measuring parameters of the deep oceans. Detection and communications capabilities have benefited by research that has exploited new portions of the electromagnetic spectrum, extended ranges to outer space, and provided means of transferring information reliably and securely even through massive jamming. Sound in the sea, submarine habitability, lubricants, shipbuilding materials, fire fighting, and other subjects have also been steadfast concerns.

The Laboratory has pioneered naval research into space, from atmospheric probes with captured V-2 rockets, through direction of the Vanguard project—America's first satellite program—up to involvement in such projects as the Navy Global Positioning System. Today, NRL is the

Navy's lead laboratory in space research. Also it has evaluated serious new threats, such as the effects of intense radiation or of forms of shock and vibration on aircraft, ships, and satellites.

Guiding NRL's diverse activities through the years has been a single aim: to conduct pioneering scientific research and development that will provide improved materials, equipment, techniques, systems, and operations.

Organization and Administration

The position of NRL within the Navy, as illustrated on the organization chart that appears on page viii of this *Review*, is that of a field command under the Chief of Naval Research.

Heading the Laboratory with joint responsibilities are the naval commanding officer and the civilian director of research. Directly under them are staff functions that provide central services such as security and personnel management. Line authority passes from the commanding officer and the director of research to five associate directors of research in the following areas:

- Technical services
- General science and technology
- Systems research and technology
- Material science and component technology
- Space and communications technology

The first of these provides centralized technical support, the other four are the research directorates responsible for executing NRL's research and development program. Further details of the organization of the Laboratory are given on the organization chart that appears on page 10 of this *Review*.

The current NRL Commanding Officer, Captain John A. McMorris, II, assumed official duties at NRL in September 1981, becoming the twenty-fifth Naval officer to hold the position since 1923. At the time, he joined then Director of Research Dr. Alan Berman in exercising these joint responsibilities. Dr. Berman resigned from the research directorship, after 15 years in the position, in June 1982. Dr. A. I. Schindler, Associate Director for Research, Materials Science and Components Technology Directorate, served as acting Director of Research while a select committee conducted a nationwide search for Dr. Berman's replacement. The committee selected Dr. Timothy Coffey, formerly NRL Associate Director for Research, General Science and Technology Directorate, for the directorship in November 1982. Dr. Coffey became the fifth person to hold the position since its establishment in 1948.

Administering the organization and operation of NRL to ensure that it runs effectively and efficiently is a dynamic process and one which requires top leadership to effect a balance between stability and change. In previous years, this concern for sound administration has been indicated by the number of reorganizations made annually in an on-going effort to keep the Laboratory's structure fully attuned to its evolving functions. In 1982, this concern was indicated by stability, rather than change in organizational relationships. A year of transition at the top management level, NRL experienced personnel transitions in the research directorship, in two of the associate directorships, in five of the research division superintendencies, and in three of the technical support divisions headed by Naval officers. Under the leadership of acting personnel in many key management positions, NRL's top management made no major reorganizations during the year, but rather maintained continuity in the existing structure.

Financially, NRL operates under the Naval industrial fund system, which requires that all costs, including overhead costs, be charged to production units, viz., research job orders. Funding for scientific projects in 1981 came from the Chief of Naval Research, the Naval Systems Commands, the Naval Material Command, and other government agencies, such as the Defense Advanced Research Projects Agency, the Department of Energy, and the National Aeronautics and Space Administration. NRL's relationship to its sponsoring agencies, both inside and outside the Department of Defense, is defined by a comprehensive policy on interagency support agreements.

Besides funding for scientific work, NRL received some Navy monies for general construction, maintenance, and operations. In fiscal year 1981, the Laboratory's budget was $292.5 million.

Personnel

The distribution of regular full-time NRL employees as of December 31, 1982, was:

Military	
Officers	32
Enlisted	90
Total	122

Civilian	
Senior Executive Service	28
Scientific and engineering professionals	1265
Scientific and engineering subprofessionals	299
Support professionals	98
Support subprofessionals	206
Clerical, administrative, and other General Schedule	718
Wage Board	522
Total	3136

The highest university degrees held by permanent employees as of December 31, 1982, were as follows:

Bachelors	511
Masters	327
Doctors	675
Total	1513

Further information concerning opportunities of NRL employees for higher education may be found in the section "Continuing Education and Training" at the back of this *Review*.

Main Laboratory Facilities

NRL's main laboratory complex in Washington, D.C., houses the major portion of its extensive facilities and support services. These include a wide variety of sophisticated facilities for advanced research. The following description gives an illustrative glimpse of some of these tools of modern science and technology.

NRL uses over 200 computer systems to provide high-speed data processing and numerical computation. The largest and most powerful of them, a Texas Instruments Advanced Scientific Computer located in the Research Computation Division, has a central processor, a high-speed bipolar central memory with a million-word capacity, and a disk storage capacity of over 450 million words.

The TI computer system is particularly well-suited to scientific usage, including vector calculations.

In addition, researchers may use an optimizing Fortran compiler and other software packages to facilitate their programming tasks. The Research Computation Division also has a DEC System-10 computer that furnishes data management support to the whole Laboratory on a time-share basis, a PDP-11 media-to-media transfer facility, and off-line graphics capability via the Technical Information Division's DICOMED.

NRL has been a major center for space research and technology since the late 1940s, and for 35 years, it has provided technical expertise and guidance for the nation's civilian and military space programs. NRL's facilities supporting the Laboratory's efforts in space science include the E.O. Hulburt Center for Space Research, the 26.0 M (85 ft.), high-precision radio telescope (at Maryland Point), and antennas for radio astronomy. In its role as the Navy's lead center for space research, NRL also builds and assists in launching Navy satellites. NRL facilities which support this role include anechoic chambers, clean rooms, various devices for studying effects of shock and vibration, noise, solar radiation, and other factors and equipment for telemetry, tracking, and data reduction. To process data from the SEASAT space vehicle, the Laboratory has developed, jointly with Bendix Corporation, a Synthetic Radar Data Preprocessing System that relies on a 42-track, high-density, digital tape recorder.

For studies in plasma physics, NRL has high-power pulsed sources to generate intense electron and ion beams, powerful discharges, and various types of radiation which span the spectrum from x rays to microwaves. The largest of these pulsers is Gamble II for the study of production of megampere ion beams and their use for producing very hot, high-density plasmas. It is also used in development of inductive switching to allow its input to increase from 2 TW to substantially higher levels needed for new generation weapon effects simulators. Smaller electron-beam pulsers are used in the study of propagation of the electron beams through the atmosphere, and in investigations of beam interaction with magnetic fields or structures to generate microwave pulses sufficiently powerful to break down air at atmospheric pressure. Related research involves lasers. NRL's PHAROS III neodymium glass laser can generate powerful beams for examining laser-matter interactions; applications presently include: inertial fusion research and high-altitude nuclear explosion effects. Lasers are equally important in other parts of the research program. They are used to guide long discharges in the atmosphere that are being studied as part of finding better propagation modes for electron beams, as *instantaneous* antennas that radiate RF signals, and for possible other military applications. Finally, facil-

ities are being designed and constructed (combining the established technology with new concepts) to study methods of accelerating electrons to high energy at very high current levels. Such facilities will provide the technology needed in the development of very compact (and economical) accelerators for advanced military systems.

To support studies in condensed matter and radiation technology, NRL has a 60-MeV linear electron accelerator, a 75-MeV sector-focusing cyclotron, a 5-MV positive-ion Van de Graaff accelerator, a 2-MV electron Van de Graaff accelerator, a high-current 200-kV ion implantation system, a cobalt-60 radiation source, and a helium-3 dilution refrigerator. Taken together, these versatile facilities are unique in the Department of Defense. They are used for a variety of experiments, including the modification of materials by means of ion implantation and experiments on the radiation vulnerability and hardening of earth satellite components.

The field of electronic warfare has been a growing concern at NRL since the 1940s. A major area of expansion is simulation studies, which not only eliminate many costly field measurements but also permit rigorous and repeatable analysis in a controlled environment. As research tools, NRL has a mobile infrared signature measurement and simulation facility and a Hybrid RF/FR missile seeker simulation facility. A complex, computer-supported central target simulator is now operating with good results, and its capabilities are being expanded to accommodate a broader range of electronic warfare problems. A radar cross-section measurement facility and other advanced research facilities have made NRL the Navy's lead laboratory for in-house exploratory development in electronic warfare.

Numerous installations support NRL's contributions to the continuing evolution of electronic science and technology. One is the new microelectonics processing facility, a humidity-controlled, dust-free environment, in which photolithography or chemical etching techniques produce custom microelectronic devices and circuits on semiconductor chips. Other important facilities, include several scanning electron microscopes, and electron beam lithogaphy systems, a crystal-growing facility including molecular beam epitaxy, and a high-field-magnet facility with superconducting magnets to produce over 200 kOe. The magnetic facility provides opportunities for the study of electrical, optical, and other properties of material under magnetic stress.

The characteristics of materials also can be examined with a number of other instruments. NRL has capabilities for x-ray analysis and electron and Auger spectroscopy. It has a high-performance secondary ion mass spectrometer that represents a standard for surface analysis and significantly extends the diagnostic capability of the technique. A high-resolution, high-performance, reverse-geometry mass spectrometer is used for probing reactions between ions and molecules. NRL has a variety of machines with capacity up to 272,000 kg for testing fatigue and fracture of new materials.

For acoustical investigations, NRL has three large research tanks, instrumented for studying echo characteristics and for device development. Experimental studies in fluid mechanics can be made in a multipurpose wind-wave channel. Measuring 30 m long by 1.2 m wide by 1.8 m deep, the channel is equipped with a mechanical bulkhead to generate regular waves and a special fan to make wind waves. An associated water tunnel has a large blow-down channel with a 15-m test section for acoustic and flow-induced vibration studies of towed line arrays and flexible cables. For acoustic surveillance array processing, researchers have access to the multichannel programmable digital data processing system, a system of DEC computers, high-speed array processors, and peripherals for up to 256 channels.

NRL is a major center for research in optical sciences. NRL scientists have played a significant role in the Fiber Optic Sensor System (FOSS) Program, a joint Navy/DARPA research effort for exploiting the effects of various energy fields on the optical signal in a fiber waveguide to develop a new class of multipurpose generic sensor systems. NRL optical scientists have been involved in the area of optical information processing. Recent research efforts have been undertaken with optical techniques to perform signal processing operations at very high speeds. Among the NRL facilites available to NRL optical scientists, as they undertake these and other investigations, are the infrared mobile optical radiation laboratory, facilities for the synthesis and characterization of optical glass compositions and for the fabrication of optical fibers, a hybrid optical/digital image processing facility, and facilities for fabrication and testing integrated optical devices.

NRL has world-wide renown as the "birthplace of radar"; and the Laboratory has maintained its reputation as a leading center for

radar-related research and development for a half-century. An impressive array of facilities managed by NRL's Radar Division continue to contribute to this reputation. These include an antenna measurement laboratory, a radar area measurement system, a radar research and development activity (at CBD), an IFF ground station, and six separate facilities relating to specific types of radar systems.

NRL has been a major center for chemical research in support of Navy operational requirements since the late 1920s, and has made major contributions in the areas of submarine atmosphere monitoring and control systems, fire suppression, and paints and coatings. The NRL Chemistry Division continues this tradition of excellence with a diversity of facilities for chemical and surface diagnostics and for tribology, paints and coatings, polymers, battery test and evaluation, fuels, combustion research, and high- and low-temperature chemistry.

NRL has supported research in environmental (ocean and atmosphere) science and technology since the 1940s and became a major center for ocean science and marine technology in the late 1960s. Currently, NRL's Environmental Sciences Division undertakes a broad range of studies, primarily ocean-related, using facilities such as the balloon launch and tracking facility, the gas chromatography, electrophysiological and neurophysiological laboratories, the previously noted wind/wave tank which is also used for simulating ocean dynamics, an instrumented facility at the Waldorf Annex for continuous instrumented recording of environmental phenomena, and a towed thermistor chain, an array of sensors which are used in oceanographic research. These efforts are complemented by those of the Marine Technology Division, which conducts studies to improve Navy platforms using computer-aided stress analysis, a shock and vibration laboratory, and facilities for studying wave generation and effects, stresses on towed line arrays and flexible cables, and geophysical flows and wakes.

In recent years, NRL has become heavily involved in information science and technology. Much of this effort supports Navy requirements in space systems and in communications and navigations. Major information technology facilities include a microwave space research facility, a satellite communications antenna facility, the Navy Center for Applied Research in Artificial Intelligence, a computer architecture and evaluation facility, and facilities for HF and SIGINT analysis.

With these and other research facilities, NRL scientists are able to undertake advanced research in 15 broad fields. These include:

- Communications
- Countermeasures
- Devices technology
- Directed energy devices
- Energy conversion
- Environmental effects
- Hydrodynamics and aerodynamics
- Materials
- Navigation
- Radiation technology
- Sensor systems
- Sonar standards
- Surveillance systems
- Undersea technology
- Weapons guidance

The high-quality instrumentation required to support such a diversity of research represents a capital investment of over $100 million.

Field Stations

NRL has acquired or made arrangements over the years to use a variety of field sites or auxiliary facilities, for research that cannot be conducted in Washington, D.C. They are located in Maryland, Virginia, California, Florida, and Puerto Rico. The two largest facilities are the Chesapeake Bay Detachment (CBD) and the Underwater Sound Reference Detachment (USRD).

CBD, which occupies 68.1 hectares near Chesapeake Beach, Maryland, provides facilities and services for research in radar, fire-control equipment, optical devices, materials, communications, and other subjects.

USRD, located at Orlando, Florida, functions in many ways like a standards bureau of underwater sound. Its semitropical climate and two clear, quiet lakes are distinct assets to its research and development on underwater reference standards and its improvement of techniques

Chesapeake Bay Detachment, located in southern Maryland

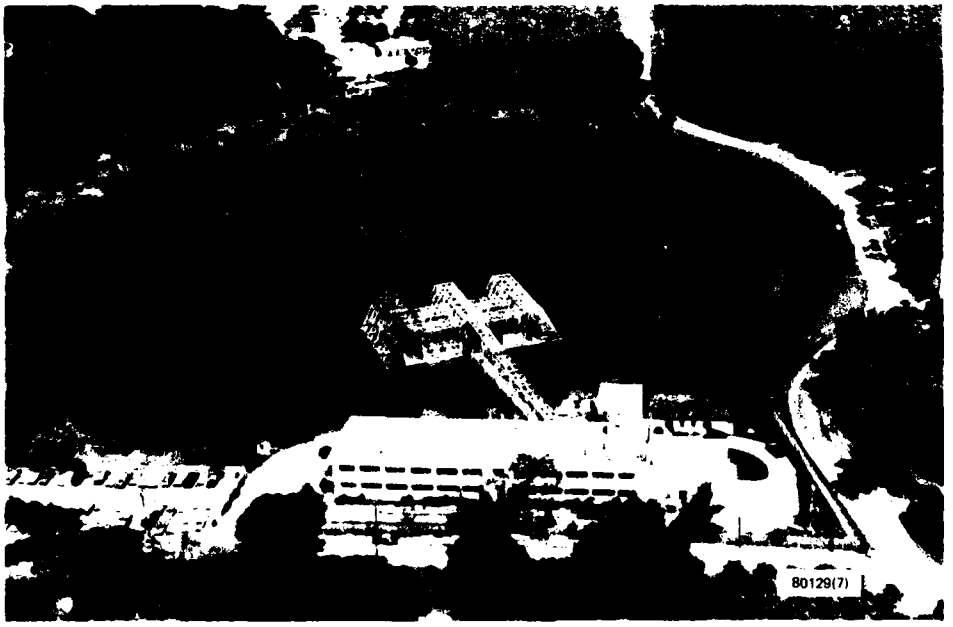

Underwater Sound Reference Detachment test site for underwater acoustic devices near Orlando, Florida

to calibrate, test, and evaluate underwater acoustic devices. USRD has an anechoic tank for simulating ocean depths to 700 m and smaller pressure tanks for simulating depths to 7000 m. The Detachment has provided acoustic equipment and calibration services not only to hundreds of Navy activities and their contractors but also to allied governments.

Some field sites have been chosen primarily because they provide favorable conditions for the operation of specific antennas and electronic subsystems. Maryland Point, Maryland, has two radio telescopes with antennas measuring 25.6 m and 26 m in diameter, respectively, for radio astronomy research; NRL's Waldorf facility has an 18.3-m X-band antenna and an S-band

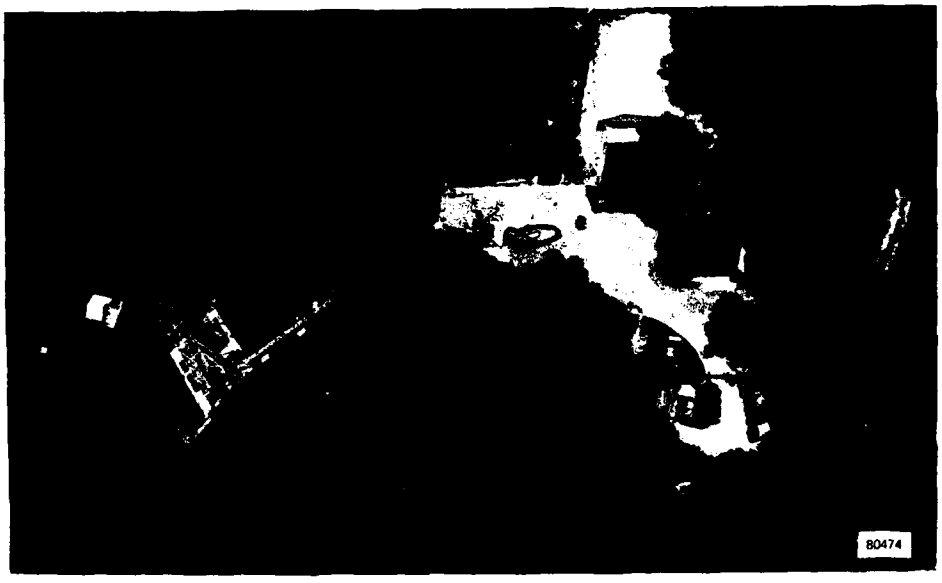

USRD's Leesburg facility

NRL's Tilghman Island test site

antenna of the same size for space and communications research. Pomonkey, a third field site in Maryland, has a free-space antenna range for the development and testing of a variety of antennas. Another facility used in improving communications is the antenna model measurement range in Brandywine, Maryland. Here, scaled model ships can be set up and rotated in the center of a range 305 m in diameter to provide data that aid in theoretical and experimental antenna design. The Laboratory has installations for satellite tracking in Blossom Point, Maryland, and at Vandenberg Air Force Base, California.

Research Platforms

NRL's principal research vessel, USNS *Hayes*, is a 75-m, 3475-metric-ton ocean-going catamaran packed with scientific instruments. Operated by the Military Sealift Command and named for Harvey C. Hayes, the initial head of NRL's Sound Division and a pioneer in underwater acoustics, the USNS *Hayes* has served as the Laboratory's research ship for 10 years. During that time she has sailed on many major cruises, pursuing investigations in acoustic bathymetry, geophysics, environmental chemistry, and bioluminescence.

For airborne research, NRL has three four-engine turboprop P-3A *Orions* and one four-engine turboprop P-3B *Orion*. These airplanes annually log about 1300 hours of flying time on projects ranging from magnetic bathymetry to electronic countermeasure research to studies of radar signal reflections.

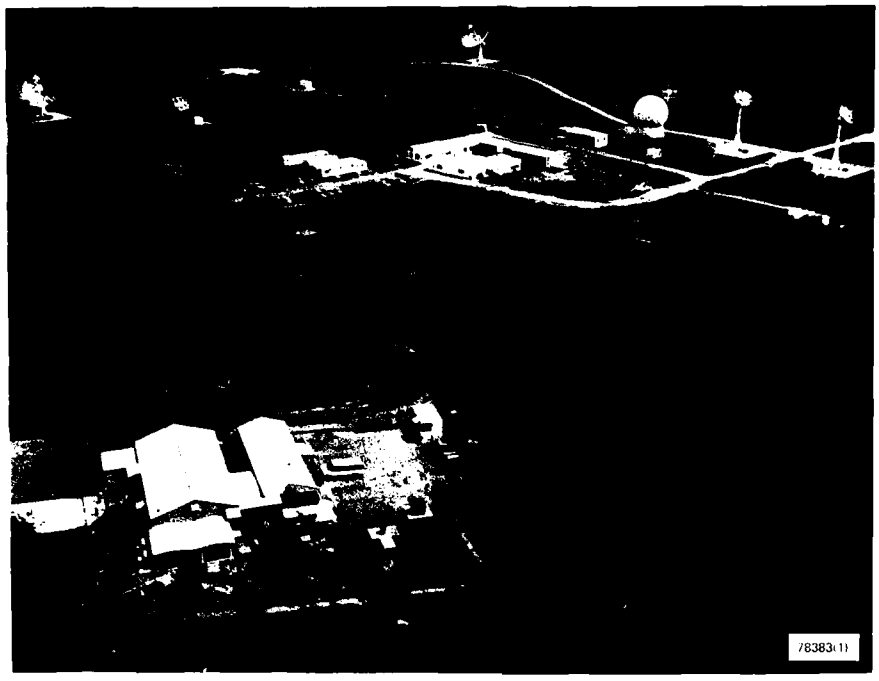

Satellite tracking station, Blossom Point, Maryland

Maintenance and Construction

Shifting priorities in research programs require renovations and modifications to existing facilities. Guiding this development is a master plan that defines potential new construction sites. A three-phase corporate facilities investment plan is being developed. Phase I will assess current and future facility requirements for the research community. Phase II will study the existing NRL physical plant and estimate life cycle repair costs. Phase III will meld Phase I and II and determine the optimal use of NRL's budget to rehabilitate existing facilities. Current projects to modify facilities to conform to new research requirements have been undertaken or will shortly be undertaken in buildings 3, 16, 60, 71, and 256. Additionally, a new building will be constructed for code 6500.

Increased energy efficiency has been a major NRL goal for the last several years. Major projects under construction at this time are the replacement of the steam distribution system, reduction of window sizes in various buildings, conversion from steam to hot water heating systems, installation of exterior insulation and roof insulation to various buildings, and conversion of constant air volume to variable air volume systems in the annex buildings.

The boilers at the heating plant are scheduled for replacement beginning in late FY-83. This replacement is required for NRL to meet the air pollution discharge limits as set by the District of Columbia. Currently, natural gas service is being installed. The new boilers will be able to burn natural gas, sludge gas purchased from Blue Plains or fuel oil.

New construction is planned for NRL. A 36,000 SF-laboratory building is scheduled to begin construction in FY85 for the Optical Sciences Division. Future military construction projects are planned for the Tactical Electronic Division, Plasma Physics Division and Underwater Sound Reference Detachment in Orlando, Florida.

Further Information

The NRL *Fact Book* gives more details about the Laboratory and its operations. It lists major equipment, current fields of research, field sites, and outlying facilities, and it also presents information about the responsibilities, organization, key personnel, and funding of the divisions, detachments, and other major organization units. Copies are available by request from

Commanding Officer
Attention Code 2630.1
Naval Research Laboratory
Washington, DC 20375

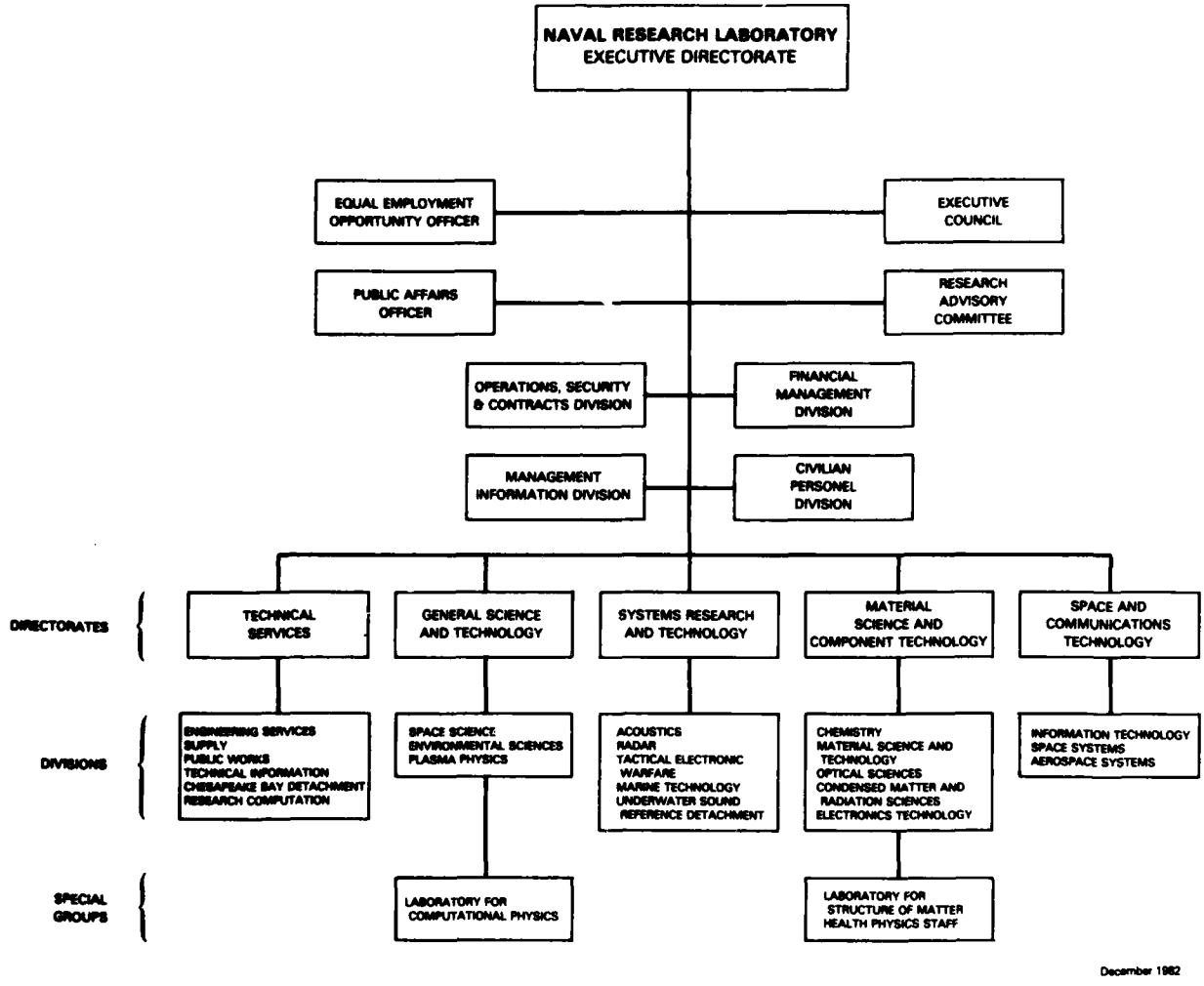

Organization of the Directorates, December 1982

ORGANIZATIONAL CHART
DECEMBER 1982

COMMANDING OFFICER
Code 1000
CAPT J A McMorris II, USN
x73403

DIRECTOR OF RESEARCH
Code 1001
Dr T Coffey x73301

DEPUTY EQUAL EMPLOYMENT OPPORTUNITY OFFICER
Code 1003
S Eason x72486

OPERATIONS, SECURITY & CONTRACTS DIVISION
Code 1200
CAPT J B Morris, USN x73621
- Operational Services
- Security
- Contracting
- Research Requirements & Applications
- NRL Flight Support Detachment

MANAGEMENT INFORMATION DIVISION
Code 1400
Dr A H Aitken x73666
- Research Program Admin
- Facilities & Equip Control
- Management Info Systems
- Program & Resource Analysis

PUBLIC AFFAIRS OFFICER
Code 2010
J W Gately, Jr x72541

FINANCIAL MANAGEMENT DIVISION
Code 1300
R W Steinbach x73406
- Budget
- Accounting
- Disbursing

CIVILIAN PERSONNEL DIVISION
Code 1800
D J Blome x73421
- Personnel Operations
- Employee Development
- Employee Relations

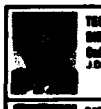

TECHNICAL SERVICES DIRECTORATE
Code 2000
JD Brown x72879

GENERAL SCIENCE AND TECHNOLOGY DIRECTORATE
Code 4000
Dr T Coffey* x73324

SYSTEMS RESEARCH AND TECHNOLOGY DIRECTORATE
Code 5000
R R Rojas x73294

MATERIAL SCIENCE AND COMPONENT TECHNOLOGY DIRECTORATE
Code 6000
Dr A I Schindler x73566

SPACE AND COMMUNICATIONS TECHNOLOGY DIRECTORATE
Code 7000
Dr B Wald x72964

PATENT COUNSEL
Code 0004
Dr W T Bho x73427

LABORATORY FOR COMPUTATIONAL PHYSICS
Code 4040
Dr J P Boris x73065

OCEANOGRAPHIC COMPUTER APPLICATIONS GROUP
Code 5003
D Seager x72384

LABORATORY FOR STRUCTURE OF MATTER
Code 6030
Dr J Karle x72665

INFORMATION TECHNOLOGY DIVISION
Code 7500
Dr J R Davis x72903
- Naval Center for Applied Research in Artificial Intelligence
- Comm Systems Engineering
- Transmission Technology
- Integrated Warfare Technology
- *Computer Science & Systems*

SAFETY OFFICER
Code 2070
H.C Kennedy, Jr x72240

SPACE SCIENCE DIVISION
Code 4100
Dr H Gursky x73363
- X-Ray Astronomy
- Radio & IR Astronomy
- UV Measurements
- Gamma & Cosmic Ray Astrophysics
- Solar Physics
- Solar Terrestrial Relationships
- Ionospheric Effects

SMP FACILITY GROUP
Code 5004
L G Goh x73266

HEALTH PHYSICS STAFF
Code 6070
J N Stone x72232

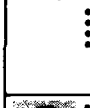

SPACE SYSTEMS DIVISION
Code 7700
P G Wilhelm x76547
- Elec Syt & S/C Integ
- Terrestrial Systems
- Mechanical Systems
- Sys Eng & Analysis
- Digital Systems

ADMINISTRATIVE SERVICES OFFICE
Code 2020
L V Dabney x73060

ACOUSTICS DIVISION
Code 5100
Dr J C Munson x73482
- Acoustics Media Characterization
- Applied Ocean Acoustics
- Physical Acoustics
- Sys Engr & Advanced Concepts
- Software Systems Dev
- Large Aperture Acoustics

CHEMISTRY DIVISION
Code 6100
Dr W H Carhart* x73026
- Chemical Diagnostics
- Polymeric Materials
- Inorganic & Electrochem
- Surface Chemistry
- Combustion & Fuels

AEROSPACE SYSTEMS DIVISION
Code 7900
Dr R A LaFenda x73468
- Space Sensing Applic
- Advanced Systems
- Systems Research
- Aerospace Systems
- Space Applications

ENGINEERING SERVICES DIVISION
Code 2300
J.D. Brown* x72300
- Mechanical Engineering & Drafting
- Electronic & Engineering Fabrication

ENVIRONMENTAL SCIENCES DIVISION
Code 4300
Dr C.H. Chiuk* x72974
- Ocean Dynamics
- Atmospheric Physics
- Environmental Chemistry
- Environmental Biology

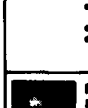

RADAR DIVISION
Code 5300
Dr M I Skolnik x72936
- Radar Analysis
- Radar Techniques
- Search Radar
- Target Characteristics
- Identification Systems
- Airborne Radar
- Electromagnetics

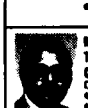

MATERIAL SCIENCE & TECHNOLOGY DIVISION
Code 6300
Dr B B Rath* x72926
- Environmental Effects
- Physical Metallurgy
- Ceramics
- Composite Materials
- Mechanics of Materials
- Thermostructural Materials

SPACE SYSTEMS DIVISION
Code 7700
P G Wilhelm x76547
- Elec Syt & S/C Integ
- Terrestrial Systems
- Mechanical Systems
- Sys Eng & Analysis
- Digital Systems

SUPPLY DIVISION
Code 2400
CDR J.R. McGraw, USN x73446
- Purchasing/Procurement Control
- Receipt Control
- Material
- Auto Inventory Mgt
- Technical

PLASMA PHYSICS DIVISION
Code 4700
Dr B L Ossakow x72723
- Plasma Radiation
- Laser Plasma
- High-Power Electromag Radiation
- Expan Plasma Physics
- Plasma Technology
- Geophysical & Plasma Dynamics
- Plasma Theory

TACTICAL ELECTRONIC WARFARE DIVISION
Code 5700
L A Cosby x72191
- Offboard Countermeasures
- EW Support Measures
- Airborne EW Systems
- Ships EW Systems
- Advanced Techniques

OPTICAL SCIENCES DIVISION
Code 6500
Dr T G Giallorenzi x73171
- Optical Probes
- Applied Optics
- Laser Physics
- Electrophysical Technology
- Optical Techniques

PUBLIC WORKS DIVISION
Code 2600
CDR J MacLaughlin, USN x73371
- Engineering
- Maint, Util & Transp
- Maintenance Control
- Administrative

MARINE TECHNOLOGY DIVISION
Code 5800
Dr R T Swem x73314
- Marine Systems
- Structural Integrity
- Fluid Dynamics

CONDENSED MATTER & RADIATION SCIENCES DIVISION
Code 6600
Dr J T Schriempf x72931
- Radiation Surv & Detect
- Metal Physics
- Radiation-Matter Interact
- Matls Modification & Analy
- Condensed Matter Physics

TECHNICAL INFORMATION DIVISION
Code 2600
E.E. Kerbrides x73360
- Information Services
- Technical Library
- Publications
- Photographic

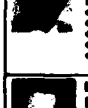

UNDERWATER SOUND REFERENCE DETACHMENT
Code 5900
Dr J.E. Blue
306-659-5120
- Technical Services
- Acoustical Systems
- Transducer
- Measurements

ELECTRONICS TECHNOLOGY DIVISION
Code 6800
Vacancy x73626
- Solid State Devices
- Electronic Material Tech
- Surface Physics
- Microwave & mm Wave Tube Tech
- Microwave Technology
- Semiconductors
- Magnetism

CHESAPEAKE BAY DETACHMENT
Code 2700
Vacancy 301-257-2111
- Security
- Operations
- Maintenance & Support

RESEARCH COMPUTING DIVISION
Code 2800
A.G. Ellis x72751
- Operations & Engineering
- Software Sys. & Support
- Transitioning Computer

Direct-in-Dialing
(202) 76-ext.

AUTOVON
28-ext.

*ACTING
†INDICATES ADDITIONAL DUTY AS ASSOCIATE SUPERINTENDENT
— — — ADDITIONAL DUTY

Naval Research Laboratory

People Programs Progress

P-1973

Interactive Graphics and Automatic Test equipment are used to aid R. Cantone in troubleshooting complex electronic equipment at NRL's Navy Center for Applied Research Artificial Intelligence.

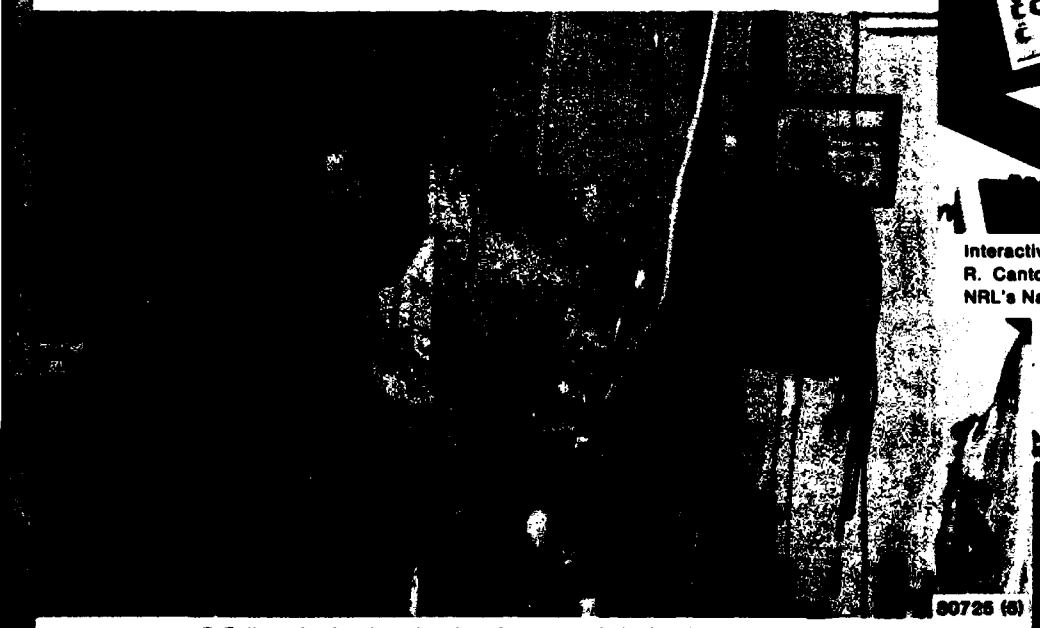

80725 (6)

E. Balizer checks piezoelectric polymer sample in the photoacoustic cell.
See article on page 137.

79465 (2)

G. Prinz makes adjustments on the Molecular Beam Epitaxy facility at NRL's main site prior to film growth.

P-1918 (2)

S. Collins adjusts helium liquifier. Similar liquifiers will be used with superconductive motors and generators for Navy ship propulsion systems of the future.

76109

J. Krebs investigates the effects of stress on the electronic paramagnetic resonance spectra of deep level centers in GaAs.

80725 (24)

R.G. Hughes mounts test specimen to size surface cracks. See article on page 130.

80725 (34)

G. Fritz (l) and M. Kowalski set up to calibrate the imaging x-ray detector. See article on page 94.

80516

K. Stern adjusts the electrode used in the electrodisposition of refractory carbide coatings.

79514

J. Reed uses a scanning electron microscope which has been adapted for evaluation of both irradiated and unirradiated materials.

S K. Numrich (l) and N. Dale prepare submerged target for acoustic measurements. See article on page 62

80725 (10

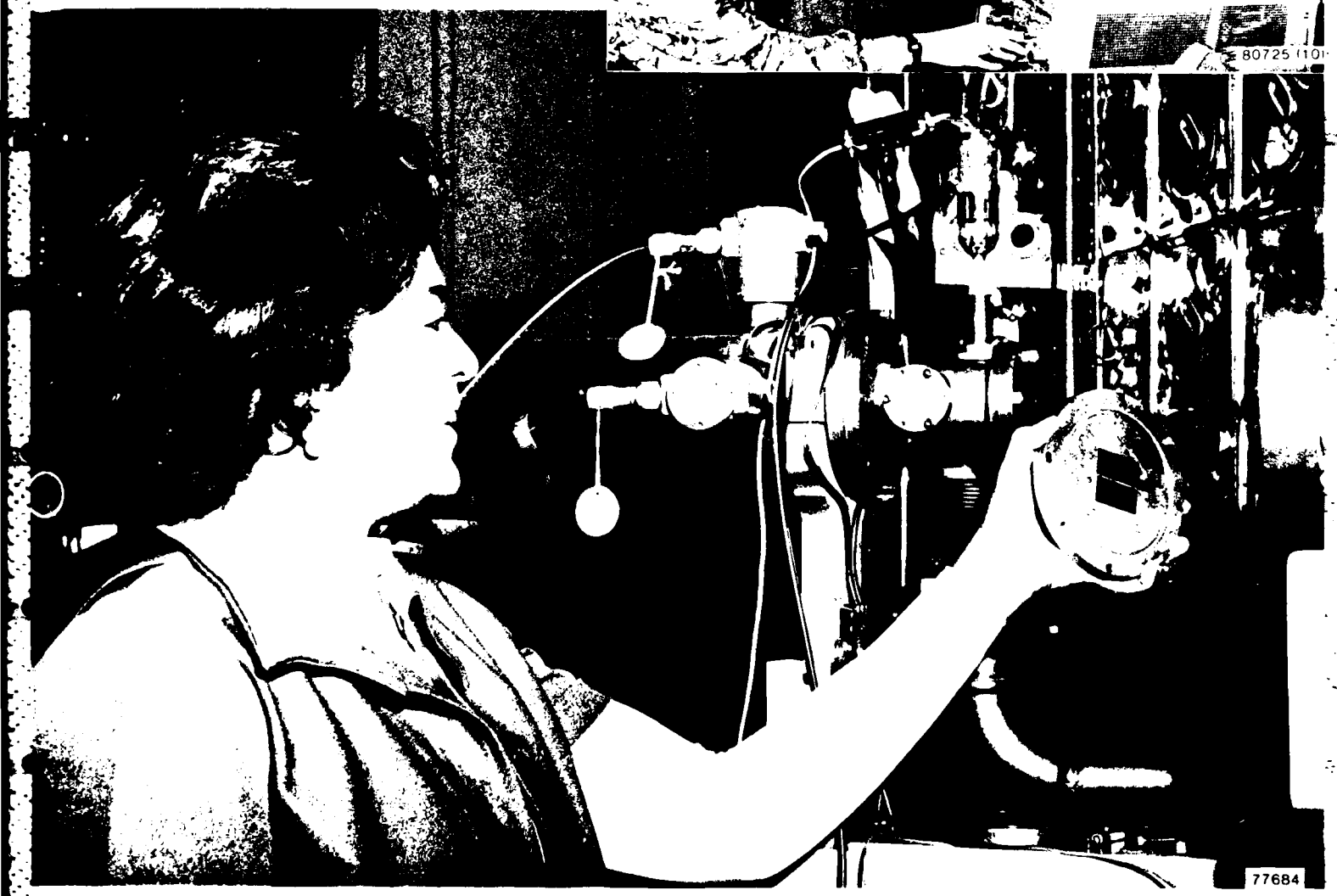

77684

D. Walker, research physicst, uses the proton beam of the 5 MeV Van de Graaff to study radiation damage in solar cells designed for satellite power systems.

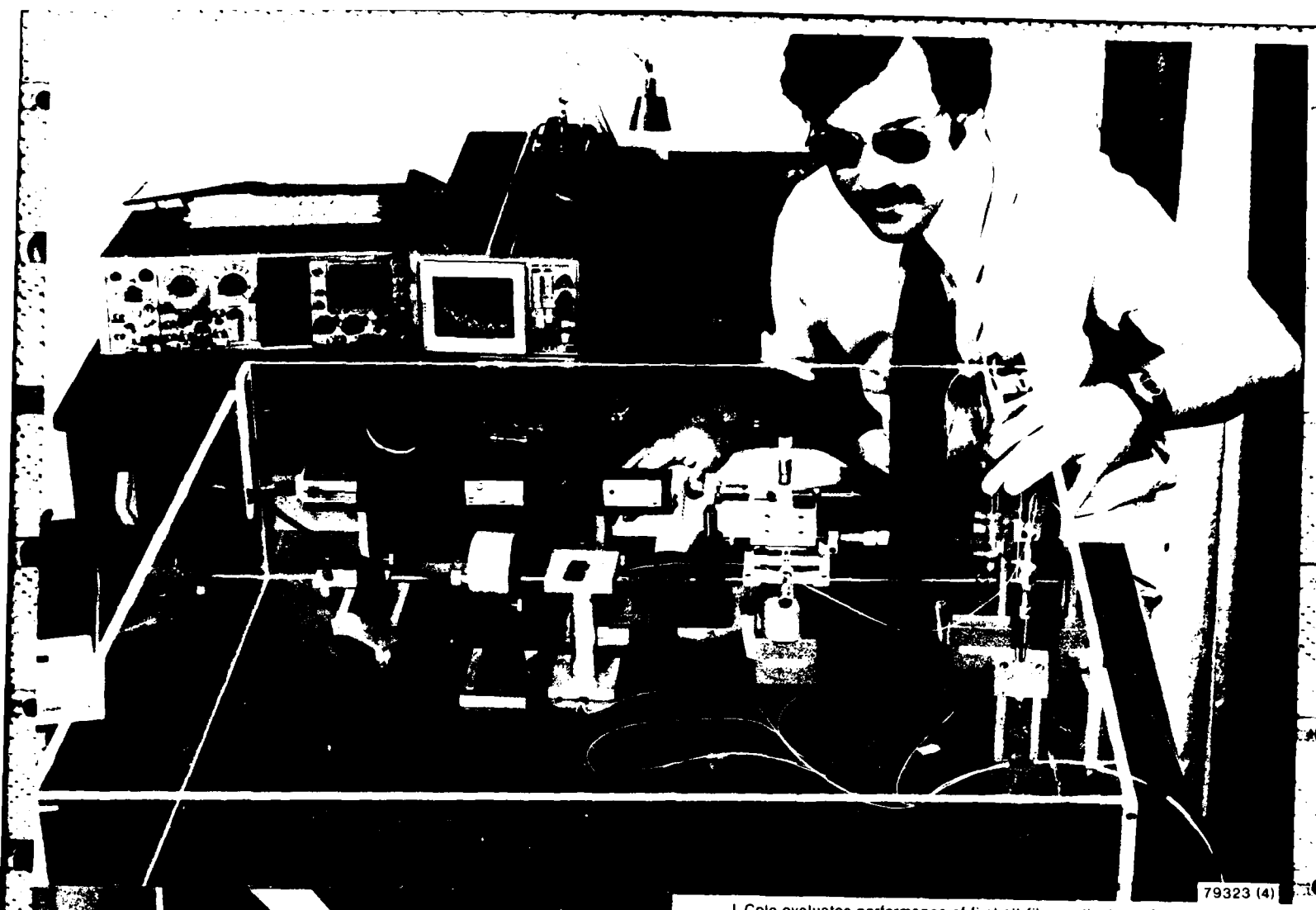

79323 (4)

J. Cole evaluates performance of first all-fiber optical interferometric acoustic sensor which uses optical couplers developed at NRL.

79755 (1)

R. Panayappan and D. L. Venezky peeling away rust using a process that they developed.

80725 (30)

H. Gerber prepares salt-particle coated mirror for emplacement in the saturation hygrometer. See article on page 82.

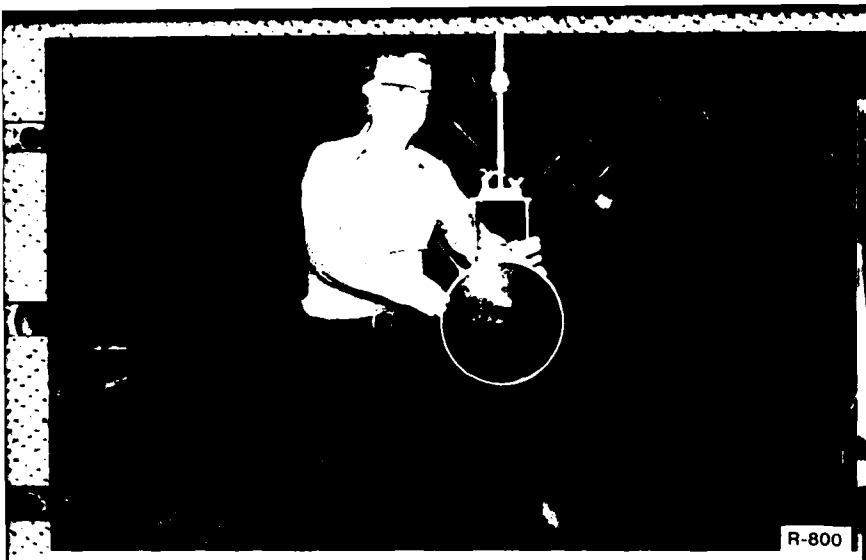

R-800

F. Schimmel rigs a hydrophone in the interior of USRD's anechoic chamber.

R 799

Searching for icebergs near the Arctic Circle. J. Deaver operates radar search control used to plot courses to iceberg targets beneath the clouds.

77155 (3)

P.G. Burkhalter inserts a sample holder into a portable x-ray spectrometer which is used for chemical analysis of air and water pollution samples.

79688 (1)

R. Surratt and C. Schoppet align the large switching network which simulates radar targets and electronic countermeasure signals in the anechoic chamber at NRL's main site.

R 798

NRL scientists undergoing water survival training. The training is required of all scientists flying missions aboard military aircraft.

R 797

). Gubser inspects a dilution refrigerator, which is used to ring materials to .01 degree above absolute zero (-459.69°F).

R 798

W. Morris, R. Naber, and B. Okawa repair underwater cable system aboard USNS Hayes under trying conditions (time: 3AM).

79093

P. Klein carrying out low temperature photoluminescence measurements in GaAs.

P-1920 (15)

T. Francanella (l) and K. Kihlstrom prepare ultra high vacuum (UHV) sputter system for deposition.

R 795

J. Guiliani adjusts apparatus for detecting toxic gases

THE NRL PROGRAM

This document reviews the unclassified research and development program of the Naval Research Laboratory for the 1982 calendar year. As such, it sets in perspective the accomplishments of over 3000 people and an expenditure in excess of $300 million. A detailed report of a program of this magnitude cannot be accomplished within the pages available to this publication. Rather, the document will attempt, through a discussion of a number of selected topics, to illustrate the nature of the NRL undertaking for 1982, the impact of this undertaking on the national and international scene, and the competence with which the undertaking was accomplished. Unlike the private sector, NRL cannot measure its success in a given year through its profit statement. NRL, however, is a contract research Laboratory, which is operated under the industrial fund principle. This means that the NRL product is marketed within the Navy and other government funding agencies. The sponsors have the choice of funding or not funding the NRL program. A measure of success, therefore, is seen by the growth in the overall Laboratory program. If the NRL program were viewed as being successful, one would expect the sponsoring community to continue its sponsorship. On the other hand, if the NRL product were found to be inferior, one would expect to see a decline in the overall Laboratory program. A review of the past several years, including 1982, indicates that the Laboratory has continued to grow at a healthy rate. To be sure, there are problem areas, as one would expect in any enterprise the size of NRL. Nevertheless, the overall enterprise appears to be in rather good shape, as is borne out by continuing sponsor interest in the Laboratory program.

The Laboratory is in the interesting situation of having near-term sponsor requirements to satisfy while at the same time maintaining its role as the Navy's corporate Laboratory with responsibility for conducting long-term research in areas of potential significance to Naval warfare. At any time, these two requirements are likely to be at odds with one another. Over the years, NRL has managed to deal successfully with these competing requirements. I believe as you read this *Review* you will conclude that again in 1982, the Laboratory has managed its resources to continue its long-standing tradition of scientific excellence, while successfully responding to high-priority, near-term Naval requirements.

As in previous years, the *Review* has been subdivided into a number of different categories. There is of course some arbitrariness in the selection of categories. The report taken as a whole should remove any difficulties created by forcing specific scientific topics into general categories.

Dr. Timothy Coffey
Director of Research
Naval Research Laboratory

Information processing and signal analysis is a subject which has been major business at NRL for many years. Under this topic, we include our developing programs in artificial intelligence. Examples of our work here include programs to automate the process of recognition of man-made objects under the sea. These programs take advantage of recent progress in the development of microcomputers and pattern recognition techniques. Another example of our research in this area involves studies of "superresolution" of sources. This program attempts to show that new technology can, in a practical fashion, resolve two sources whose angular separation is less than the beam width of the receiving aperture. Success in this area has practical applications such as the tracking of targets in the presence of nearby jamming, especially when the jammer source is within the beam width of the target. Other work in this area includes studies of the performance of various decision rules for a radar using frequency agility in the presence of broadband sidelobe jamming; the application of acoustooptic technology to the classification of complex signals received from many directions at once; the use of novel array control concepts and microprocessor or technology to the production of scanning phased array antennas with low side lobes; and finally, the application of artificial intelligence techniques into battle management systems.

The successful operation of the Fleet is dependent upon the development of electromagnetic systems for sensing the Naval environment. This is true for both peacetime and wartime operations. A number of important NRL contributions were made in this area during 1982. A remote sensing experiment was conducted in July off Nantucket Island. The objective of this experiment was to delineate the hydrodynamic processes responsible for surface expressions of bathymetry in shallow water and coastal areas. This was a multisensor experiment, including coordinated *in situ* and remote sensing measurements. The ability to rapidly assess shallow-water environments is currently of great interest to the Navy. Another series of measurements of radar scatter from the sea has resulted in the observation of a new scattering mechanism which leads to very strong scattering of horizontally polarized radiation from small amplitude shoaling swell waves. Understanding these new observations could lead to improved target detection in the presence of sea clutter, improved capabilities in radar remote sensing of the sea surface, and in synthetic aperture radar imaging of ocean waves. Another experiment demonstrated the feasibility of measuring surface wave parameters from a moving ship under real ocean conditions.

In the field of marine geosciences, a study has been undertaken examining the potential of Freon-11 as a tracer of oceanographic mixing. Freon-11 is a man-made gas which has accumulated in the atmosphere during the past three decades. Thus, Freon-11 can potentially provide temporal information on ocean mixing processes. The study determined the distribution of Freon-11 in the Western Atlantic Ocean from the area of Iceland to the Scocia Sea, which is southeast of the southern tip of South America. The study found an absence of Freon-11 at depths greater than 1500 m in tropical and subtropical zones indicating that deep ocean water in these areas has not been at the surface during the past thirty years. Another study which began in this area is aimed at determining and understanding the fine-scale structure within the ocean. Understanding the fine-scale structure has important oceanographic and Naval applications. Important work also has been done on baroclinic instabilities in Gulf Stream rings. This work was a theoretical interpretation of extensive experimental data collected on a Gulf Stream ring in the vicinity of Bermuda. Finally, studies were undertaken which demonstrated the viability of gravity measurement from fixed wing aircraft. Accurate knowledge of spatial variations in the earth's gravity are required for inertial guidance systems, improvements in gravitational and geoidal models of the earth, and estimation of topographic structure in oceanic areas with sparse bathymetric data. The ability to collect such data from aircraft will significantly increase the rate at which gravimetry surveys can be conducted.

In the area of acoustic systems and technology, a study was undertaken of the geometric dispersion in an ocean channel. This study led to estimates of the maximum dispersion-induced bandwidth and limitations on the useful integration time arising from dispersion. The results of this research have applications to undersea surveillance, underwater communications, and ASW. Another study examined the possibility of acoustic identification of underwater targets. This study attempted to exploit the fact that all submerged targets exhibit elastic behavior when interrogated by sound waves. It is hoped that this fact can be used to identify, not simply the presence of an underwater target, but the nature of

the underwater target. A related effort is reported which examines new techniques, and will hopefully lead to far less costly numerical predictions for scattered or radiated signals from complex submerged structures. Finally, a study is reported on the sound radiation caused by extensional waves for a flat plate submerged in a fluid. This work is a new contribution to the theory of elasticity and demonstrates that sound radiation by extensional waves is not negligible, but makes a significant contribution to the acoustic field, generated by a plate vibrating in water.

NRL conducts a broad program in the area of optical research and optical systems technology. One report demonstrates a technique for achieving a high degree of spatial uniformity from a laser beam. This accomplishment is especially important to areas such as high-gain laser fusion, which requires a high degree of uniformity in the laser irradiance to produce a uniform ablation pressure on the inertial confinement fusion pellet. Another report explains the observed focal shift in laser beams passing through lenses. This work has important applications in the design of optical systems. An area which is of growing importance is that of optical probing of fast chemical reactions. This work addresses the use of ultrafast optical techniques to study the formation and kinetics of energetic fragments, and promises to provide the Navy with important information on the efficiency and sensitivity of existing fuels, propellents and explosives, and may lead the way to the synthesis of improved energetic materials.

Atmospheric and ionospheric research is of continuing interest and importance to the Laboratory as well as the Fleet. The nature of the work has, of course, changed dramatically over the years, as problems have been identified and solved, and as the demands of military systems have become more sophisticated. This year, work is reported on HF communication channel response to a wide-band probing signal. This work resulted from interest in spread spectrum techniques for communication in the HF band, which has led to a requirement for a better definition of HF channels. Work is also reported on the phenomenology of ionospheric irregularities. This is an area where NRL has made major contributions in both the experimental understanding of ionospheric irregularities and in their theoretical interpretation. Finally, work is reported on the phase transition in the atmosphere between water vapor and liquid water for the purpose of understanding the formation of hazes and fogs because of their adverse effects on Naval operations. Important new effects relative to fog formation also are reported.

NRL has been a major player in the field of space science and technology since the beginning of the space program. This year, work is reported on submicrosecond time synchronization using the GPS satellites. It is expected that accuracy of better than 50 ns can be achieved by the method reported. Work is also reported on analytic orbit prediction. Most satellite tracking systems use numerical integration programs, which are calculation intensive and require the capabilities of large computer systems. The orbit program which is reported can easily be run on current personal size computers, and appears to be highly accurate. In the area of space science, work is reported whose ultimate goal is to predict the large scale features of the sun's magnetic field. It is well known that the sun displays a variety of phenomena involving the activity of magnetic fields. Some of these phenomena can dramatically affect the earth's environment. The results reported indicate that the ultimate goal of this program may be achievable. This would be a major scientific and technological accomplishment. Related work is reported on dynamic modelling of the solar atmosphere. It is hoped that this work will lead to the solution of one of the major unsolved problems in solar physics, namely, the nature of the physical processes that produce and maintain the high temperature regions in the upper solar atmosphere. On the experimental side of space science, the development of an efficient imaging x-ray detector is reported. This work has important applications to the field of x-ray astromony. Work is also reported on hard x-ray emission from the Crab Pulsar. The observations were made from a balloon-borne hard x-ray observatory. The results of the measurements are difficult to explain within the context of current pulsar models.

An area which has become of increasing importance at the Laboratory over the past 10 years is that of high-power radiation sources and pulse-power technology. This work has fascinating and potentially very important applications to Naval and military systems. One accomplishment reported in this document is the development of a plasma antenna. It is demonstrated that a laser-guided electrical discharge in the atmosphere can establish an ionization channel

which can be used as an antenna for the transmission of electromagnetic radiation. The plasma antenna was nearly as good in the transmitting or receiving mode as an equivalent copper antenna. Recent theoretical studies by NRL of particle-beam propagation in the atmosphere are summarized. Work is also reported on model development for the description of the radiation dynamics of laser heated plasmas. This work has important applications in such fields as inertial confinement fusion and nuclear weapons effects simulation. Work is reported which is aimed at understanding the phenomena associated with the absorption of high-power electromagnetic waves by surfaces. This work focuses on the atmospheric breakdown which occurs when a high-power microwave beam is focussed onto a surface.

A significant fraction of the Laboratory's effort is dedicated to understanding the properties of materials and how to modify and analyze them. This includes work on the radiation-thermal aging of polymers, which explains the reactions which can occur when materials are exposed simultaneously to radiation and heat. Work is reported on the NMR spectroscopy of synthetic metals. Synthetic metals are materials which combine the electrical conductivity of metals with the favorable properties of polymers, such as flexibility, high strength-to-weight ratio, ease of fabrication and low cost. Another report details the piezoelectric properties of oxygen-modified antimony sulfur iodide. This compound is a potentially important material for Navy underwater sound transducers.

Protective coatings are of considerable importance to the Navy. In this regard work is reported on the oxidation of yttrium-bearing high-temperature alloys and electrodeposition of refractory carbide coatings. Another approach to surface modification is that of ion implantation. Work is reported on the improved scuffing resistance of gear steel, using ion implantation. It is well known that the growth of fatigue cracks can lead to premature or even catastrophic failure in structural components that are subjected to repeated loads. In this area, work is reported on the control of fatigue in steels. This work sheds considerable light on understanding the fundamental nature of fatigue. Another report shows that the presence of sulphur is detrimental to stress-corrosion-cracking resistance of steel welds. Materials for use at high temperatures in a high-neutron flux environment (for example, fusion reactors) are of considerable current interest. An NRL study on the radiation resistance of ferritic stainless steels is reported. Two promising steel alloys have been studied. A report is given on acoustoelastic stress measurements. This work relates to an emerging new technology in the field of nondestructive evaluation. A new method is described, which uses ultrasonic Rayleigh waves to determine the crack height of surface-breaking cracks. This method should lead to the reliable sizing of surface-breaking cracks and be less sensitive than existing methods to operational variables. It is likely that electroactive and piezoelectric polymers will be increasingly important to the Navy. They have applications to lightweight batteries, conductive coatings, and acoustic devices, etc. A method is described for predicting the properties of chain polymers. This method provides a description from first principles of semiconducting, metallic and piezoelectric chain polymers with a degree of sophistication that previously was achieved only from molecules. An application of ion mass spectrometry to organic adsorbates is reported. This has applications to study of organic compounds which are produced as products of hydrocarbon fuel combustion. Many of these compounds are carcinogenic, mutagenic, or have other biologically adverse effects. Work is reported on certain unique properties of europium molysulfide. This material has interesting and unusual superconducting properties and demonstrates that although the material is anomalous in many ways, an understanding of it can be achieved through the proper set of complementary measurements. Work is also reported on the spectroscopy of piezoelectric polymers, which have important applications as acoustical transducers and coatings of optical fibers to enhance their performance as sensors. Work is reported on the effects of porosity and grain size on wear in ceramics. Because of their properties, ceramics are used in the shaft seals in Trident submarines. The lifetime and reliability of shaft seals depends upon a number of material properties over which the Navy currently has little control. The NRL studies have begun to throw light on the mechanisms of wear in these materials. Further studies should permit the specification of microstructural properties. Work is also reported on new quality control testing techniques for rubber composites. The Navy relies heavily on quality control testing to ensure that materials or articles procured will perform satisfactorily. In the case of rubber composites,

the standard tests were found to be inadequate for certain Navy needs. A new technique was developed to resolve this problem.

The areas of structure and fluid mechanics have become of increasing importance at NRL in the past several years. Part of the motivation in the area of structural mechanics is the space shuttle, which will be able to deploy satellites of unprecedented size. These satellites are likely to be very flexible and will give rise to a new generation of control problems. NRL has undertaken a research effort into the dynamics and control of large flexible structures in space. The Laboratory has also been examining wave forces on cylinders. This program was motivated by the observation that the prediction of wave forces on marine structures is still largely an empirical process. This work has resulted in improved techniques for predicting wave forces on structures and has provided new insight into the mechanics of the wave-structure interaction. To assist the Navy with the design of submerged cable systems, the Laboratory is studying the vibrations of marine cables. This study was undertaken in the context of validating, through field observations, a recently developed computer code. The validation of this code gives us a significant new tool for the design and analysis of underwater structures involving cables. In the area of computation of fluid mechanics, work is reported on the pseudospectral solution of the inviscid equations of motion. These techniques have traditionally been used for the calculation of complex incompressible flows. The work reported extends the technique to the solution of compressible flows, and examines the question of how accurately and efficiently it can treat discontinuities, such as shock waves.

The Laboratory conducts considerable work in the area of component technology and the development of specialized devices. Work is reported on an InP:Fe laser, which has important potential applications to the field of ultralow-loss optical fibers. The laser operates at 3.53 μm. Work is also reported on high transition temperature, niobium nitride thin films. There are important Naval applications related to the fabrication of Josephson junctions with superconducting electrodes made of this material. Another article reports that NRL scientists have been able to grow single crystal iron films, using the technique of molecular beam epitaxy. The report lists some of the remarkable magnetic properties of these films. These properties are particularly important for the application of these films to devices. Electronic and electrooptic applications of III-V semiconductors have expanded rapidly with the availability of bulk single crystals of the binary alloys gallium arsenide and indium phosphide. There are, however, a number of applications for which ternary or quaternary alloys would be better than the binary compounds. Investigations of new techniques for growing single crytals of III-V ternary and quarternary alloys are reported, as well as of acoustooptical signal processing. Such processors can have important practical applications to various computer intensive problems, especially where size, weight, and power consumption are limited. Work is reported on thermophotovoltaic power sources for hardened spacecraft. Solar cells which are the standard source of power for spacecraft are degraded by natural radiation and are vulnerable to the radiation produced by nuclear detonations. NRL has undertaken a program to develop spacecraft power systems which will convert solar energy to electrical energy with neither the radiation vulnerabiltiy of solar cells nor the costs and dangers of radioisotope systems.

The preceding is a brief overview of this *Review*. As previously mentioned, this document is not intended as a comprehensive review of the NRL program, but rather as a sampling of the type of research which is ongoing at the Laboratory. The *Review* does not address the classified work which is underway, nor does it address the substantial amount of consultation and assistance provided by the Laboratory to the Navy and other defense organizations. Nevertheless, it is hoped that you will acquire a reasonable understanding of the Laboratory's program and a feeling for its impact on the nation's research and development enterprise.

ARTIFICIAL INTELLIGENCE, INFORMATION PROCESSING, SIGNAL TRANSMISSION and ANALYSIS

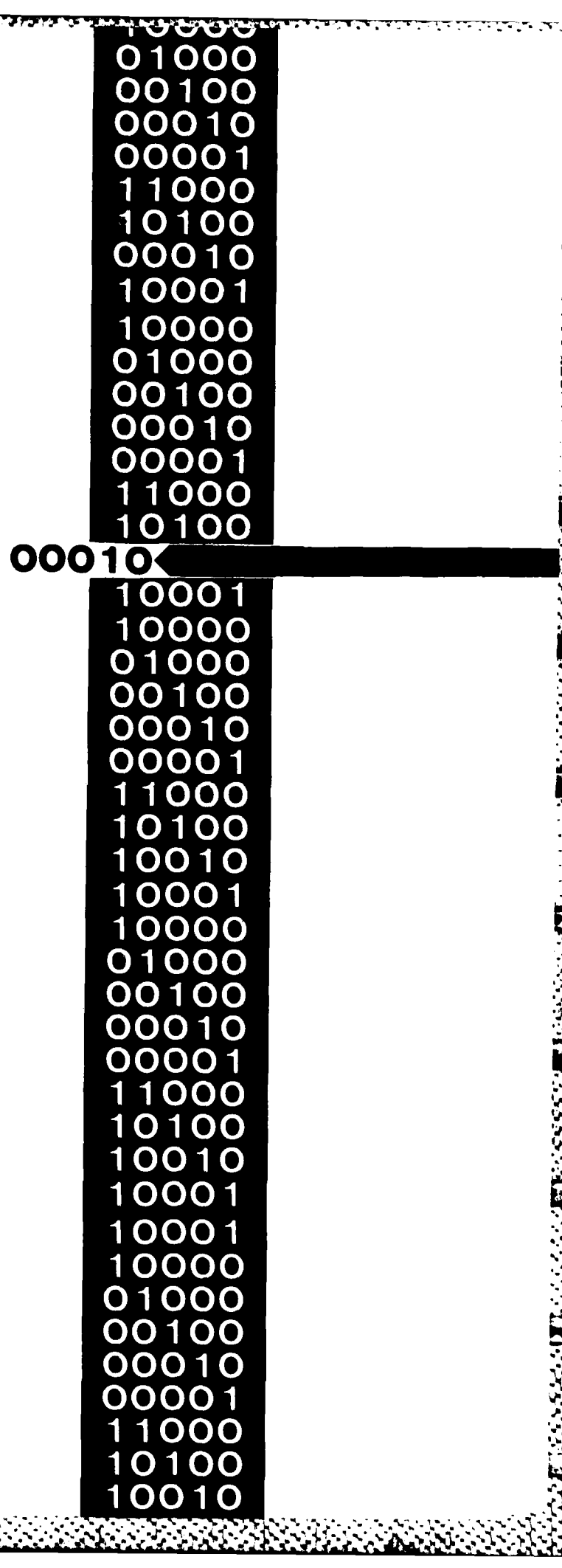

ARTIFICIAL INTELLIGENCE, INFORMATION PROCESSING, SIGNAL TRANSMISSION AND ANALYSIS

The rate at which sensors can collect data is now so great that automatic data processing is essential to make full use of the information received. Some of NRL's efforts in the development of hardware and software for this purpose are described in this section.

Recognition of Man-Made Objects Under the Sea, by L.M. Buckler and H.A. Johnson, *Marine Technology Division*

NRL has participated in a number of important undersea search operations including the search for the *Thresher* and *Scorpion* submarines and the hydrogen bomb that was lost off the coast of Spain. Data from such operations, using sensors such as side-scan sonar, magnetometers, TV, and photographs, are often hard to interpret and subject to human error because, at the state-of-the-art, these data must be interpreted visually by the operator. As an example, the photograph that displayed the *Thresher* draft markings was initially set aside as having no value; on later reflection the operator retrieved it and discovered the draft markings.

To take advantage of recent progress in the development of microcomputers and pattern recognition techniques, NRL and the University of Illinois have collaborated in a study of automatic or semiautomatic undersea search techniques, using information from various sensors. At long range, shape and texture features were examined using the highlight and shadow areas of side-scan sonar records; at short range, optical features were observed.

A number of undersea photographs were digitized and processed with different algorithms in an attempt to identify man-made objects on the ocean floor. Figure 1 depicts three images, namely: (a) a ship (*LeBaron Russell Briggs*) taken at a range of 9 m, (b) the same ship taken at a range of 14 m, and (c) a picture of the ocean

(a)

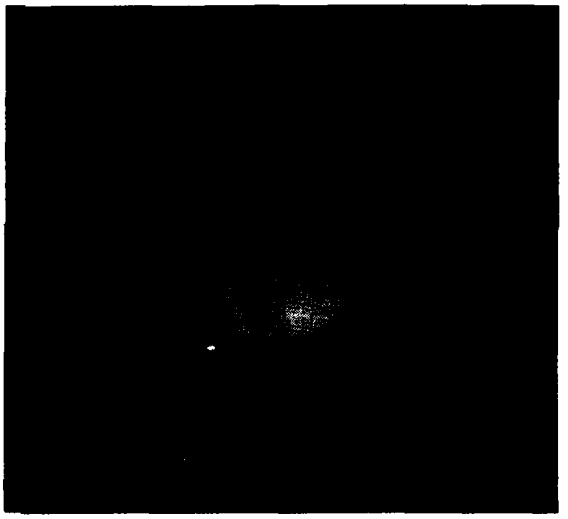

(b)

(c)

Fig. 1 — Original underwater photographs (a) LeBaron Russell Briggs at 9-m range, (b) Same ship, 14-m range, (c) Ocean floor, no man-made objects

floor. Algorithms were developed to detect the presence of major edges in each image. The image was then characterized by several shape descriptors obtained from information about these edges. Finally, based on one or more of the shape descriptors, a decision was made as to whether or not a given object was man-made. The basis of these methods is the observation that man-made objects tend to have longer and smoother edges than natural objects and that the orientation of their edges tends to be concentrated in a few directions.

The results of applying the edge detection algorithms to each image in Fig. 1 are shown in Fig. 2. Each edge consists of one or more connected linear segments. Three image shape descriptors are calculated from the characteristics of the edges. The first descriptor ($\bar{L}$) is the average edge length for the image, equal to the total length of all edges divided by the number of edges. The second descriptor (S) characterizes the smoothness of the image. The *variation* of an edge is defined as the sum of the absolute values of the changes in direction taken when traversing the edge from one end to the other. S is calculated by dividing the sum of the edge variations by the sum of the edge lengths. The third descriptor is an edge orientation histogram, $h(\theta)$ vs θ where $h(\theta)$ is the sum of the squares of the lengths of all linear segments that make an angle θ (between 0 and 360°) with the horizontal axis.

Values of $\bar{L}$ and S for the images in Fig. 1 are given in Table 1. Note that the edges of man-made objects are longer (larger $\bar{L}$) and smoother (smaller S).

Table 1

Image	Fig. 1a	Fig. 1b	Fig. 1c
$\bar{L}$ (inches)	1.15	0.96	0.80
S (radians/inch)	1.55	1.75	2.35

Finally, the histograms of $h(\theta)$ vs θ for the three images are shown in Fig. 3 with edge pictures superimposed on them. Note that the histograms for images containing man-made objects have more pronounced peaks at their preferred orientations.

The features that have been identified using optical sensors may be combined with clues from other sensors to locate man-made objects, thus improving undersea search and classification operations.

[Sponsored by NAVSEA]

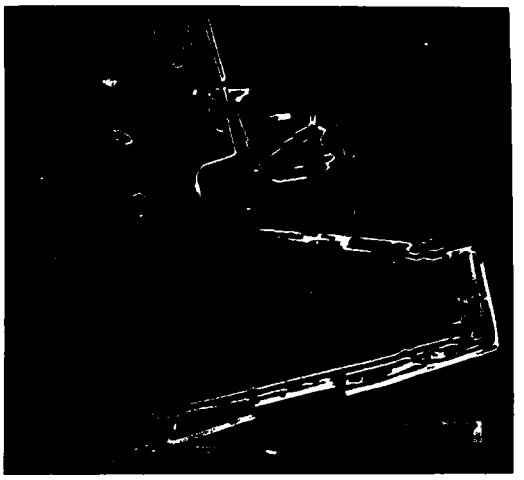

(a)

(b)

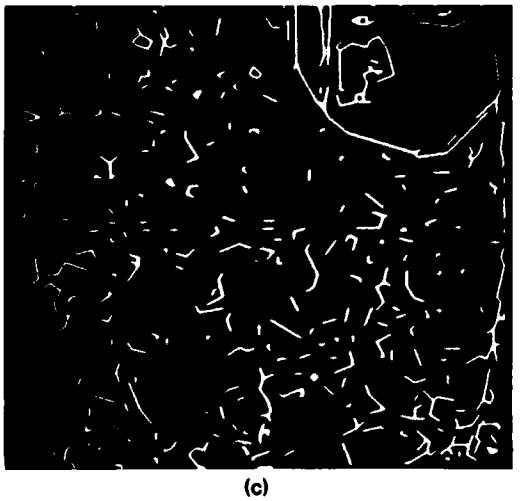

(c)

Fig. 2 — Results of edge-detection algorithms applied to the photographs in Fig. 1

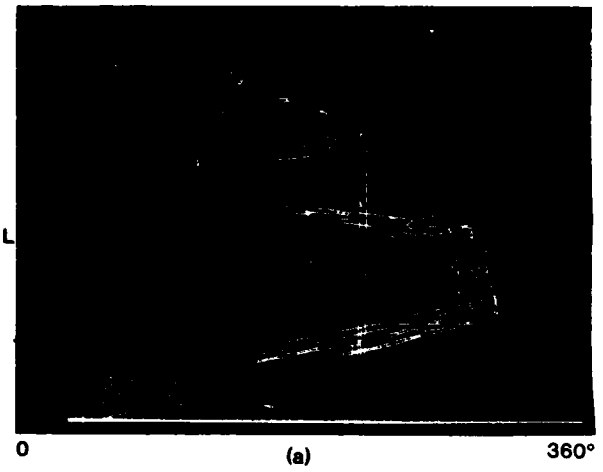

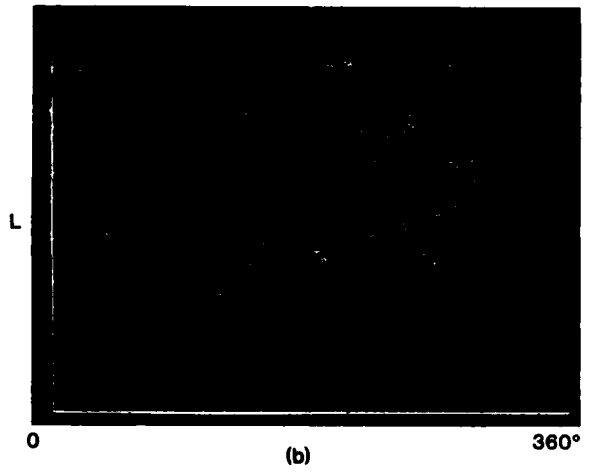

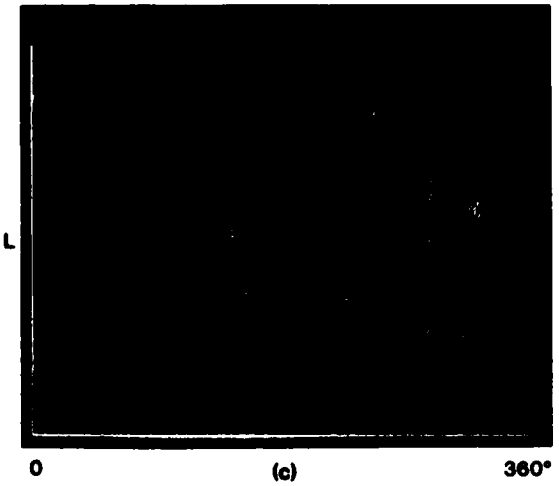

Fig. 3 — Histograms of line length vs angle #

REFERENCES

1. T.S. Huang, R.Y. Tsai, J.K. Cheng, L.M. Buckler, and H.A. Johnson, "Toward Automatic Undersea Search Using Pattern Recognition Techniques," *Proc. 6th International Conference on Pattern Recognition,* Munich, Germany, October 19-22, 1982.

2. L.M. Buckler, T.S. Huang, H.A.Johnson, and A.L. Steinbach, "A Feasibility Analysis of Computer-Aided Underwater Search Techniques," NRL Memorandum Report 4721, January 28, 1982.

A "Superresolution" Target-Tracking Concept, by William F. Gabriel, *Radar Division*

"Superresolution" of sources has intrigued physical scientists ever since Lord Rayleigh demonstrated his optical aperture resolution criterion over a century ago, namely, that two sources cannot be resolved if their angular separation is less than the beamwidth of the receiving aperture. Many ingenious *superdirectivity* schemes have been proposed over the years, but the price of any significant improvement over Rayleigh's limit has always turned out to be truly formidable. This situation is being changed by a new technology which derives largely from modern spectral estimation techniques [1], and adaptive array antenna processing systems [2].

NRL has been involved in this new technology for several years (see the *1980 NRL Review,* pp. 23-26) and has contributed significantly in bringing several research programs to the threshold of practical systems development. Such systems are called *data adaptive* because they adapt to the total signal environment experienced by an array of sensors, using all available degrees-of-freedom of the system. This is in contrast to a conventional array antenna where the degrees-of-freedom (in this case the element weights) are fixed and do not adapt to a changing input signal environment. Another way of looking at this fundamental difference is that a conventional antenna does not use all of the information that is available in the RF signal wavefront arriving at its aperture.

One of the practical applications of interest to the Navy is the tracking of targets in the presence of nearby jamming and, in particular, when the jammer source is within a beamwidth of the

target. This situation usually renders effective tracking impossible. We are currently investigating an adaptive system approach simplified to the block diagram shown in Fig. 4. After the analog-to-digital (A/D) converters at the antenna elements, the processing system is entirely digital. The system continuously computes and updates a sample covariance matrix upon which off-line processing is conducted at periodic intervals to estimate the locations and relative power levels of interfering sources, using the best available estimation algorithms [1,2]. This information is then used to assign optimized weights to the elements of a digital spatial filter which attenuates the signal from all sources that have been determined by the logic to be interference. The filtered signal is then processed by search/track beamformer algorithms to find and track the targets of interest in the conventional radar manner.

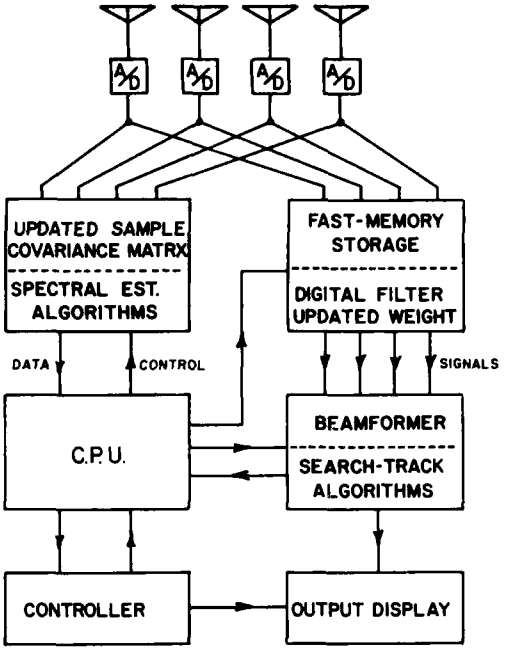

Fig. 4 — Concept of adaptive array tracking system

To demonstrate the concept, Fig. 5 illustrates a simple simulation example in which we have a single 3 dB signal-to-noise ratio (S/N) target located at -4° azimuth and appearing in a single range bin per pulse repetition frequency (PRF) period. There are also six jammer sources of different strengths and locations which appear in N adjacent range bins per PRF period. The receiving aperture is an 8-element linear array with elements spaced at half-wave-length intervals. Upon forming sample covariance matrices averaged over 256-range-bin samples, and processing with an Eigenanalysis algorithm [1], we get digital estimates of relative source power vs azimuth angle. These estimates are then used to compute weights for the elements of the digital filter leading to an effective filter insertion loss vs azimuth angle shown in Fig. 6. Note that only enough adaptive insertion loss is applied to each element to drop an interference source into the noise.

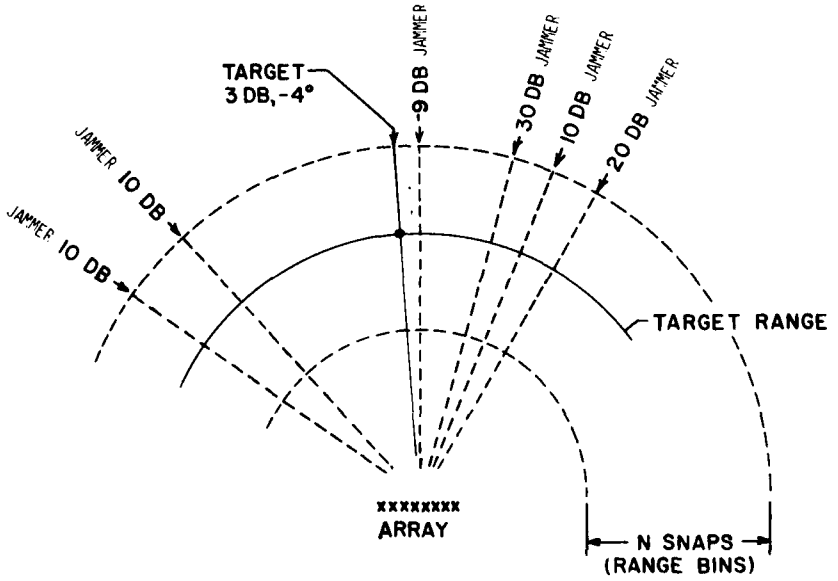

Fig. 5 — Range/Azimuth geometry used in simulation

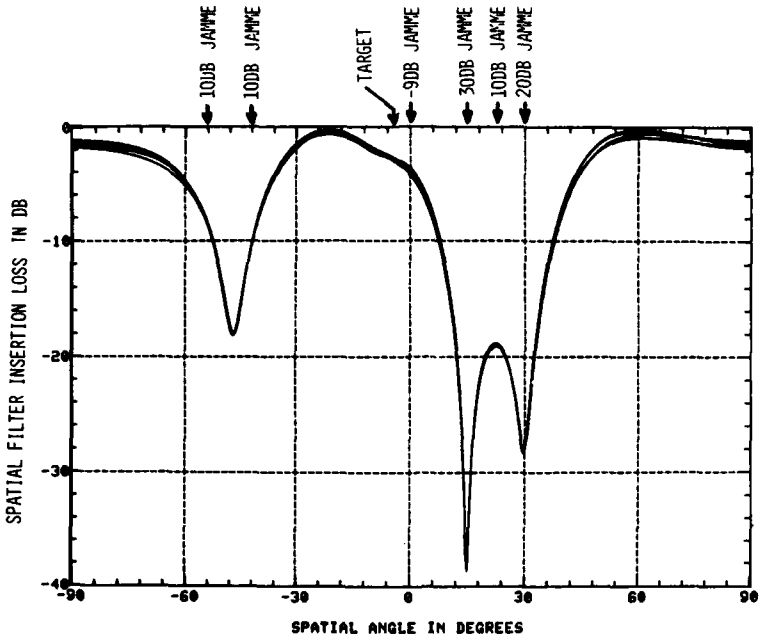

Fig. 6 — Insertion loss of adaptive spatial filter

There are three regions of relatively low insertion loss where target signals could easily get through the filter (-90° to -60°; -35° to 0°; and +42° to +90°). Tracking could be accomplished anywhere within these clear regions. As the target gets closer to a strong jamming source, the insertion loss increases rapidly; however, if the target S/N is sufficient to overcome the insertion loss, we should still be able to track, thus achieving superresolution tracking within a beamwidth. The filtered signal in our example permitted easy monopulse tracking of the 3-dB S/N target at -4°.

Future research efforts at NRL will include the evaluation of critical performance characteristics such as false alarm tolerance, filtering imperfections, wavefront distortions, tracking accuracy vs separation, and response to multiple jammers in the mainbeam. Prospects for practical application of these superresolution techniques look bright since modern A/D converters have reached satisfactory performance levels, sophisticated algorithms required for processing the sensor data are continually being improved, and the modern digital computers essential for implementing the algorithms and handling the large amounts of data are continually improving in processing speed and cost effectiveness.

[Sponsored by NAVAIR and ONR]

REFERENCES

1. D.H. Johnson, "The Application of Spectral Estimation Methods to Bearing Estimation Problems," Special Issue on Spectral Estimation, *Proc. of the IEEE,* **70,** 1018, 1982.

2. W.F. Gabriel, "Spectral Analysis and Adaptive Array Superresolution Techniques," *Proc. of the IEEE,* **68,** 654, 1980.

A Nonsuppressing CFAR Detector, by Jon D. Wilson, *Radar Division*

The current trend in radar is to replace operator intervention in the detection process with automatic detection. An automatic detector declares a detection when the radar signal exceeds a threshold which is set at a level that gives a desired probability of false alarm (P_{fa}). A fixed threshold is adequate to limit the number of false alarms when the target is to be detected against a background of known statistics such as a Rayleigh distribution of noise with known power. When the background level is unknown, as in the case of clutter, a variable threshold is necessary. For this purpose, a technique known as a constant false alarm rate (CFAR) detector is used; this

dynamically sets the threshold on the basis of the background level.

Specifically, for a pulsed radar (in which pulse length determines range resolution), a digital CFAR detector samples the returned signal at a rate corresponding to its pulse length. These samples then cycle through a shift register (SR) with a capacity of 20 to 30 samples. The sample in the center of the SR is known as the *test cell.* The first two or three samples on either side of the test cell are called *guard cells.* The other samples in the SR, termed *reference cells,* are summed to estimate the background level that is used to set the threshold. As the returned signal passes through the SR, each sample in turn becomes the test cell and is tested against this dynamic threshold. If several pulses are returned from a target (as in the case of a scanning surveillance radar) the returned signals are summed range cell by range cell and then passed through the SR. This type of CFAR detector maintains a reasonably constant false alarm rate if the background is either locally homogenous clutter or jamming with a cell-to-cell variation of values somewhere near a Rayleigh distribution.

With closely spaced targets, however, one target can be in the reference cells when the other is in the test cell. The return from the target in the reference cells will distort the estimate of the background level and raise the threshold. This will suppress detection of the target in the test cell unless some way can be found to reduce the effect of the extraneous target.

This NRL study shows that a conventional CFAR as previously described can be modified to be nonsuppressing by adding multiple taps to the SR. These taps permit subdivision of the surrounding region of reference cells into N subregions, each of which can be used to set its own threshold. The test cell can be compared with these N thresholds and a detection declared when the test cell exceeds some number M of these. Extraneous targets in one or more subregions can then cause unusually high thresholds but still not suppress detection until the number of subregions involved exceeds N-M.

A parametric study has been performed to determine appropriate values for N, M, and the number of samples in each subregion. There are many tradeoffs involved in the selection of these parameters, but when operating on a single linearly detected return from a nonfluctuating target in a background of Rayleigh distributed noise with a P_{fa} of 10^{-3}, good detection performance can be obtained with $N = 6$, $M = 4$, and with 4 samples. This means that a detection occurs when the test cell exceeds 4 out of 6 thresholds with each threshold based on 4 samples.

Figure 7 shows the performance of 3 types of detector at a P_{fa} of 10^{-3} when there is no interfering target. The detector with the best performance, defined as the least signal-to-noise-ratio (S/R) required for a given probability of detection (P_d), is the detector with a fixed threshold set for the actual background level. The conventional CFAR detector using a threshold based on a 24-sample estimate of the background level pays a penalty of approximately 1 dB in S/N for equivalent P_d compared with the fixed threshold detector, while the nonsuppressing CFAR detector pays only a fraction of a dB additional penalty. The performance of the same detectors in the presence of interfering targets is shown in Fig. 8, which demonstrates that the nonsuppressing CFAR detector should have a considerable advantage over the conventional CFAR. In Fig. 8, the S/N has been fixed at a level derived from Fig. 7 which gives a P_d of 0.90 for a conventional CFAR. The values on the abscissa are the simple

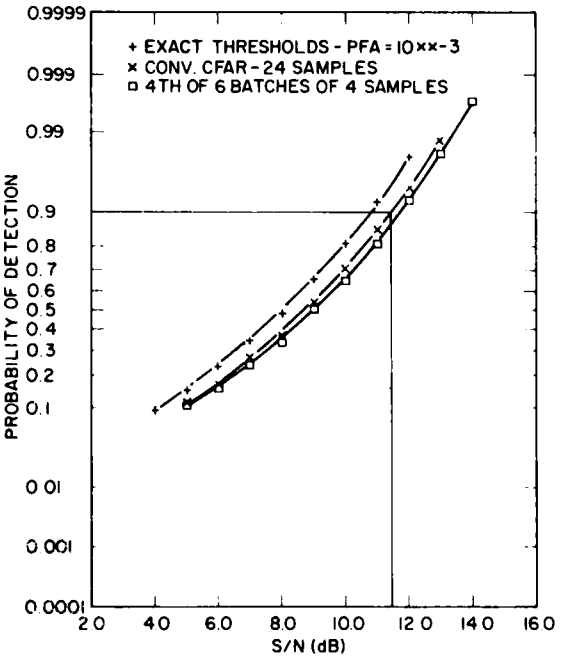

Fig. 7 — Detection performance of various detectors with no interference present

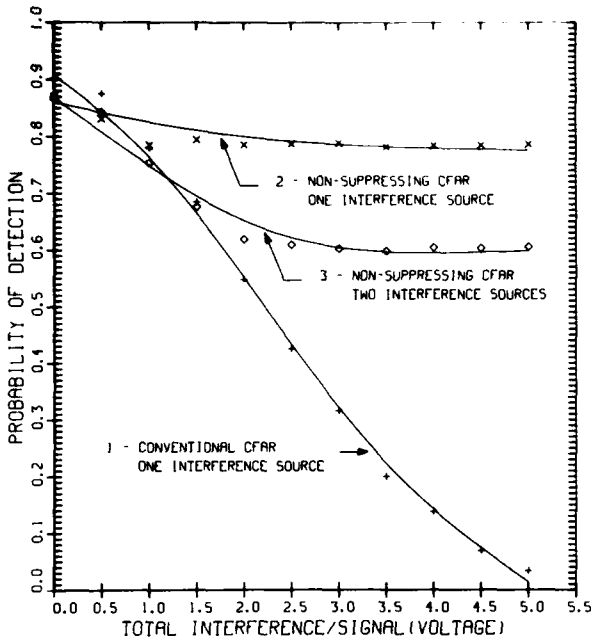

Fig. 8 — Effect of interference on probability of detection. The S/N ratio is chosen so that the conventional CFAR would have a P_d of 0.9 in the absence of interference.

ratio of the interference voltage to the signal voltage. The curve for the conventional CFAR demonstrates the effect on P_d of a single interference source in the reference cells. An interference source equal in voltage to that of the signal drops the P_d to 0.75, and an interference of 4 times the signal drops the P_d to 0.15. The other two curves show the performance of an $M = 4$, $N = 6$ nonsuppressing CFAR with interference affecting either one or two of the thresholds. With one interference source, the P_d is still nearly 0.8, and even with two interference sources, the P_d is near 0.6. With more interfering sources present, other values of M and N would be chosen.

This nonsuppressing concept has been evaluated with simulated and recorded radar data and shows potential for improving radar detection in a raid environment and for providing better estimates of the number of raiding aircraft. The hardware modifications required to implement the nonsuppressing CFAR are modest, and a simplified version of this technique is being implemented in a demonstration system which is being built at the Chesapeake Bay Detachment.

[Sponsored by NAVSEA]

A Comparison of Automatic Detectors for Frequency-Agile Radars, by Paul K. Hughes II and Gerard V. Trunk, *Radar Division*

When a surveillance radar transmits at a constant frequency, a jammer needs only to jam a narrow bandwidth to reduce the radar detection range by a significant amount. To force the jammer to spread its energy over a wider bandwidth, and consequently to reduce its effectiveness, many modern radars change their frequency from pulse-to-pulse, a technique known as *frequency agility.* When frequency agility is used, the jamming power received in a sidelobe can vary by as much as 20 dB between pulses even though the transmitted jamming power is constant over the radar bandwidth. This is because the received sidelobe jamming power depends upon the antenna gain in the direction of the jammer, usually a direction away from the radar's mainbeam, and this gain can vary by as much as 20 dB with a change of transmitted frequency.

We have investigated and compared the detection performance of various decision rules for a radar using frequency agility in the presence of broadband sidelobe jamming. Under these circumstances the noise power at the output of an envelope detector varies from pulse to pulse and since the noise power is unknown, no optimal test exists which will maximize the probability of detection (P_d) for a given false-alarm probability (P_{fa}). Suboptimal tests must be used. It has been shown that good detection performance can be obtained using the ratio detector developed earlier by NRL, [1]. The ratio detector sums signal-to-noise power ratios for N pulses and compares the sum to a threshold. The threshold is determined by standard techniques, assuming that jamming is white Gaussian noise. The signal-to-noise power ratios are determined using the maximum likelihood estimate of the unknown noise power.

The ratio detector has good detection performance in the presence of thermal noise or jamming since it will detect targets even though only a few returned pulses have a high signal-to-noise ratio. However, short-pulse interference (random interference received intermittently from other radar sources) will cause the ratio detector to declare false alarms. To reduce the number of false alarms when short-pulse interference is present, the individual power ratios can be limited to a small enough value so that interference will only cause a few false alarms. The detection performance of the ratio detector, with and

without such limiting, was compared with the more commonly used decision rules, such as the cell averaging constant false alarm rate (CFAR) detector, the log integrator, and the binary integrator, [1].

To compare the performance of the various detectors, P_d vs S/N curves were generated using computer simulation. All results presented here are for the case of six pulses integrated, and a P_{fa} of 10^{-6} arising from thermal noise. For nonfluctuating targets (returning the same signal at each pulse) in thermal noise only, the cell-averaging CFAR is the best detector; however, the ratio detectors and log integrator are within a few tenths of a decibel of the cell-averaging CFAR. The binary integrator is 1 to 1.5 dB worse than the cell-averaging CFAR. For fluctuating targets (Fig. 9), the variation in performance is between 0 and 3 dB. The cell-averaging CFAR is still the best detector. The ratio detector is better than the log integrator, which is better than the binary integrator.

The results for fluctuating targets in jamming with a maximum jamming-to-noise ratio of 20 dB are shown in Fig. 10. The ratio detector without limiting is now the best detector, and the ratio detector with limiting is the next-best detector. If there is no problem arising from short-pulse interference, one would use the ratio detector without limiting; and if there are short-pulse interference problems, one would normally use the ratio detector with limiting.

Since the ratio detector without limiting can be several dB better than the ratio detector with limiting, an alternative possibility is to use the ratio detector without limiting and then test to decide whether the received signal is from a target or is interference. Such a second test was used to detect the presence of short-pulse interference after a detection had been declared by the ratio detector without limiting. Figure 11 shows the P_d curve when a second detector is added and the corresponding curves for the ratio detector alone, with and without limiting, in the presence of 20 dB jamming and a Rayleigh-fluctuating target. In this case, the second detector recovers about half of the lost detection performance of the ratio detector with limiting. However, as the probability of occurrence of an interference spike increases and P_{fa} is maintained at constant low value, the detection performance of the second detector decreases faster than the performance of the ratio detector with limiting. This is largely due to the increased probability that two of the six pulses will contain an interference spike. If the probability of an interference

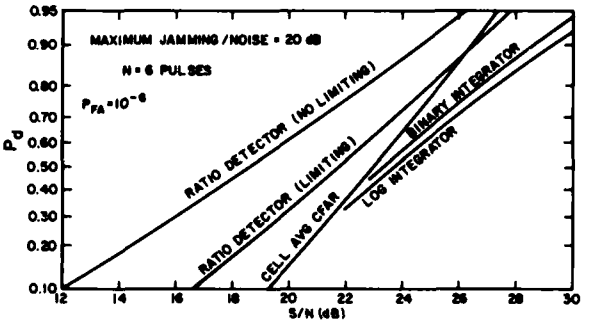

Fig. 10 — Curves of P_d vs S/N for the cell-averaging CFAR, ratio detectors, log integrator, and binary integrator and for a target fluctuating with a Rayleigh distribution with $P_{fa} = 10^{-6}$, and maximum jamming-to-noise ratio = 20 dB

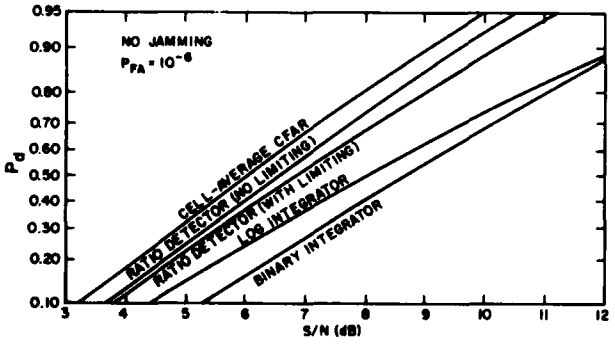

Fig. 9 — Curves of P_d vs S/N ratio for the cell-averaging CFAR, ratio detectors, log integrator, and binary integrator and for a target fluctuating with a Rayleigh distribution and $P_{fa} = 10^{-6}$

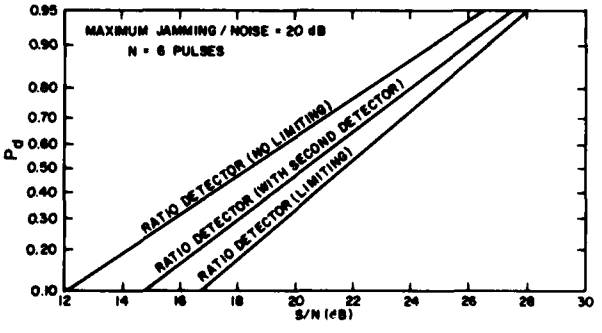

Fig. 11 — Curves of P_d vs S/N for ratio detectors and ratio detector with a second detector and for a target fluctuating with a Rayleigh distribution, and maximum jamming-to-noise ratio = 20 dB

spike exceeds 10^{-3}, little difference is seen between the ratio detector with limiting and the second detector.

Our results have provided a comparison of automatic target detection rules for frequency-agile radars in the presence of jamming. It is planned to perform field tests to verify these techniques in the near future. Successful results would lead to enhanced automatic detection performance of radars in the presence of jamming.

[Sponsored by ONR]

REFERENCES

1. G.V. Trunk, "Automatic Detectors for Frequency-Agile Radars," NRL Report 8571, April 1982.

Signal Analysis with Integrated Optics and Microelectronics Processing, by A.E. Spezio, *Tactical Electronic Warfare Division,* G.W. Anderson, *Electronic Technology Division,* and W. Burns, *Optical Sciences Division*

The increasing density and sophistication of radar signals in the electromagnetic environment requires the development of equipment capable of rapidly classifying complex signals received from many directions at once. Acousto-Optic (A-O) technology contributes to this capability by providing instantaneous signal decomposition into channels corresponding to arrival direction and frequency, and by reducing implementation cost through the use of hybrid (and eventually monolithic) integrated optics (I-O). A broad interdisciplinary NRL team, with strong technical cooperation from the Air Force Wright Aeronautical Laboratory is currently applying optics and microelectronics to the development of future electronic warfare systems.

The developmental signal processing module shown in Fig. 12 is an initial result of this multidisciplinary effort. In this module, a wide segment of the RF spectrum is continuously monitored and signal descriptions are generated as digital words describing the frequency and amplitude of each signal. The module includes an integrated optical assembly performing frequency channelization, and a microelectronic integrated circuit which digitally encodes the channelized signals.

The A-O signal processing occurs in a planar integrated optical substrate. The functions performed are illustrated in Fig. 13. Light from a semiconductor laser is collimated in a geodesic

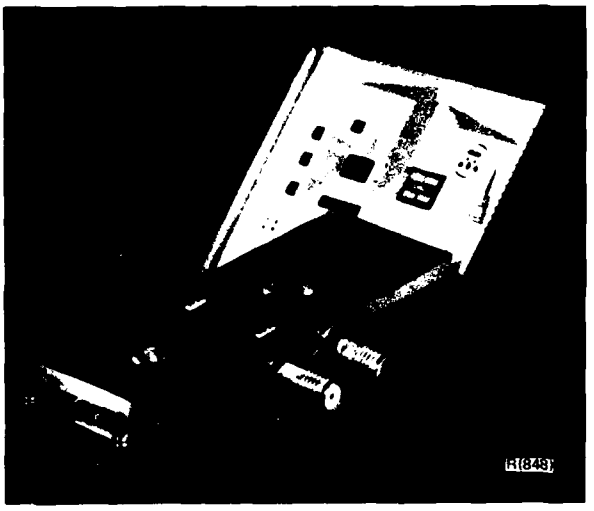

Fig. 12 — Developmental signal processing module

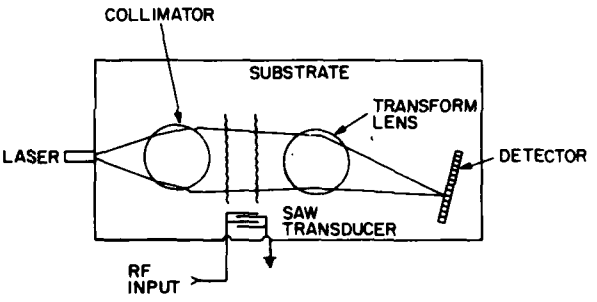

Fig. 13 — Integrated optical signal processing functions

microoptic lens which has been formed by milling an aspherical depression in the substrate surface. Light is confined to the surface contour by an optical waveguide. Signals intercepted from the environment are converted by a transducer into surface acoustic waves which alternately compress and expand the substrate surface, forming a weak diffraction grating. Bragg interaction of the collimated light with the distorted surface produces a deflected light beam whose angle of deflection corresponds to the applied frequency. This arrangement results in frequency channelization and signal sorting. Deflected outputs are focused onto a detector array for detection and subsequent signal processing. Acoustic-optic linearity allows complex signals to be processed simultaneously.

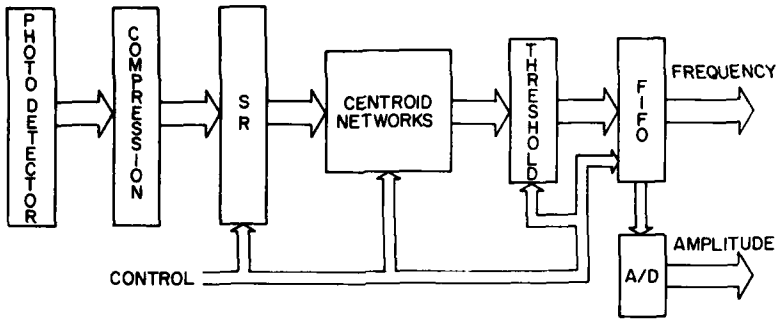

Fig. 14 — Microelectronic signal processing functions

Microelectronic signal processing converts the signals from the integrated optical circuit into descriptive digital reports. Functions executed by the microelectronic circuits are indicated in Fig. 14. Optical input signals are transformed to analog electronic signals at the detector. These signals are compressed and passed to an analog shift register. A transversal filter in the centroiding network rejects extraneous responses and stores the significant signals in a first-in first-out memory. These signals, together with a corresponding frequency word, are sent to the output through an analog-to-digital converter. Thus, received RF signals are reported as digital words which can be processed further by conventional techniques such as bearing computation and arrival-time measurement and analysis.

The developments described here are expected to lead to a new class of signal processing elements which will supercede current receiver practice and significantly augment digital signal processing capabilities. This technology will ensure continued viability of the Navy's electronic warfare systems in an increasingly complex electromagnetic environment.

[Sponsored by NAVELEX]

Distributed Microprocessors for Phased-Array Applications, by E.E. Maine and J.M. Willey, *Radar Division*

Innovations in array control concepts, coupled with microprocessor technology, can be applied to scanning phased-array antennas in order to produce low sidelobes. The Fixed Array Surveillance Radar, a phased-array radar system currently being developed at NRL, uses distributed microprocessors to steer the beam and to monitor the state of the active components in the array. The use of microprocessors simplifies the information flow necessary for steering the beam and provides a versatile array monitoring system.

The data paths involved in the beam steering process are depicted in Fig. 15. The primary computer acts as the radar scheduler, developing the sequence of beam-pointing directions and transmission frequencies according to a programmed operating doctrine. The beam-pointing directions and frequency are transmitted over a data link to the master controller. The pointing directions are expressed in terms of phase gradients to be applied in the horizontal and vertical planes of the array. The master controller synchronizes the communication and operation of the antenna, signal processor, receivers, exciter and transmitter subsystems. We are concerned here with the antenna subsystem. The frequency and phase gradients are passed from the master controller to the array controller via a serial-optical data link, a pair of optical fibers forming the only control cabling between equipment located above and below decks. From the array controller, information flows on a parallel bus in a tree-like configuration to the individual phase-shifters on the backplane of the array. There are four possible addressing modes between the array controller and the phase-shifters: individual unit, single row, single column, and all units.

Upon receiving the frequency and phase gradients from the master controller, the array controller calculates phase values for each row and column. Using the row and column addressing modes, the array controller transmits these values sequentially to the phase-shifters. The frequency is transmitted to all units simultaneously. With these phase values in hand, the final setting of the phase-shifter for a particular unit is calculated by a microprocessor embedded in that unit. The

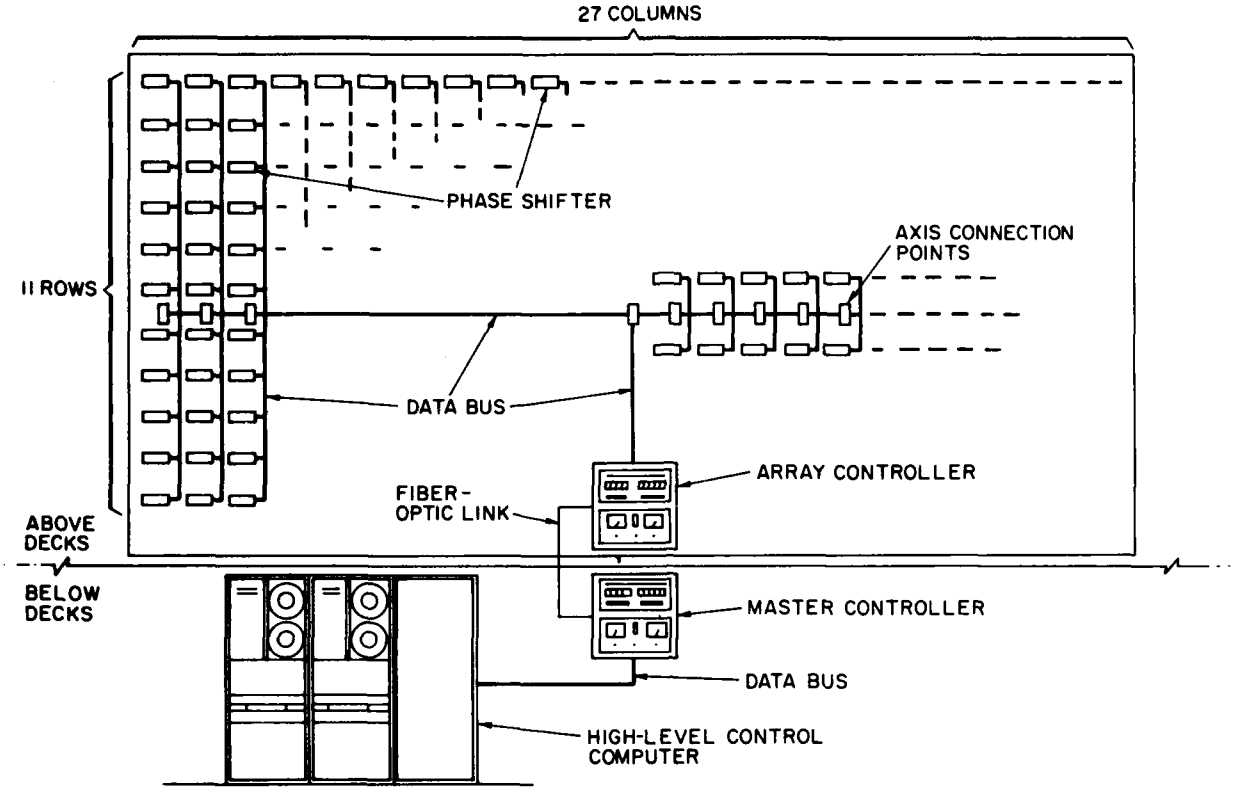

Fig. 15 — Arrangement of beam steering system

microprocessor also contains antenna calibration information which was transmitted at system start-up in the individual addressing mode; the final phase setting computation includes these effects as a function of frequency. When all phase-shifter settings have been computed, they are latched into the corresponding phase-shifter drivers with a single simultaneous command and the beam is steered to the new pointing direction.

Since the antenna was specifically designed to produce low sidelobes, the sidelobe performance will be degraded if even a small number of phase shifters fail. There is, therefore, a requirement to actively monitor the performance of the individual phase-shifters and alert the system operator if failures occur. Hardware has been included in the antenna to measure quantities from which the transfer characteristics of a particular R.F. transmission line in the antenna may be calculated. These measured values are transmitted to the array controller where the computations take place; each calculated value is compared to a reference for error determination. The measurements are made simultaneously on all transmission paths and the calculations are performed in nonreal time. A measurement can be made on each pulse with up to 20 sequential antenna states stored for nonreal-time computation.

The approach taken here allows the computational load for the beam steering function to be distributed efficiently over the entire array. It also allows dynamic inclusion of the antenna calibration, and can be extended to include the computational load of the antenna monitoring process. The system could in principle be expanded to include "soft healing" by closing the loop on phase-shifter failures by calculating around the units that the monitor has determined to be defective.

[Sponsored by NAVSEA]

An Expert System for Fire Direction, by J.R. Slagle, *Information Technology Division*

The techniques of artificial intelligence have reached the stage where they can be incorporated into tactical battle management systems. NRL has undertaken the development of an expert system for fire direction called BATTLE [1], which

is being designed as an upgrade to the Marine Integrated Fire and Air Support System (MIFASS). The Marine Corps has been developing MIFASS to plan, integrate, and coordinate the fire support task. In 1982, BATTLE was brought to the stage where it can find nearly optimal solutions to problems that are large enough to be of practical interest. For example, within a few seconds after being given the relevant data, it found 5 nearly optimal allocations of 8 batteries against 17 targets.

The method by which MIFASS automatically allocates weapons to targets has several shortcomings. The desirability of massing several weapons must be determined separately and specified to the system in advance; the effectiveness of a weapon is determined by a small number of static factors not reflecting the dynamic complexity of a battlefield; and the allocation technique can lead to poor resource allocation. For example, MIFASS allocates weapons to targets sequentially by matching the most effective weapon against the most valuable target, the most effective remaining weapon against the next most valuable target, and so on. Suppose that target 1 is slightly more valuable than target 2, that weapon A is slightly more effective than any other weapon against target 1, and that weapon A is the only effective weapon against target 2. The present version of MIFASS would direct weapon A against target 1 and direct nothing against target 2.

BATTLE improves on MIFASS by providing optimal and nearly optimal recommendations for the allocation of a set of weapons to a set of targets. The allocation is computed in two phases, both using artificial intelligence techniques. In the first phase, the effectiveness of each individual weapon against each target is analyzed. This analysis is based on the full complement of relevant and dynamic battlefield factors as determined by a Marine Corps artillery expert. Effectiveness is computed using a *database* and a *computation network*. The second phase uses the results of phase one to generate allocation plans specifying which target, if any, each weapon is to attack. BATTLE automatically recommends massing if it is warranted.

In determining the effectiveness for each weapon-target pair, MIFASS currently takes into account restrictions directly related to the weapon and target, notably fire time, fire zones, and the availability of ammunition. However, it ignores many dynamic factors which can be decisive in a military engagement, such as the combat readiness of personnel, resupply possibilities for various resources, and the weather. BATTLE takes these additional factors into consideration using the computation network, a structure imposed on the database consisting of a set of *nodes*, and a set of directed *links*, between nodes. The links connect nodes in *antecedent* and *consequent* relationships. Figure 16 illustrates these relationships and identifies the nodes. The value of *EFFECTIVENESS* is the consequent of the antecedents *WITHIN MAXIMUM RANGE, GOOD MATCH* for the weapon, and *OUTSIDE MINIMUM RANGE*. The system can compute the values of nodes that are unavailable by exploiting these relationships. If values in the database change, BATTLE updates the nodes linked to the new data. In this way information is propagated through the database.

The BATTLE system provides two ways of entering data into the database: the *volunteer* mode, in which a user enters data directly, and the *questioning* mode, in which BATTLE conducts an information-gathering dialogue with the user. We have devised a merit system [2], which chooses the most profitable line of questioning (as determined by the likely effect on the top node) for BATTLE to pursue. The user is asked only those questions most relevant to weapon-target effectiveness, rather than all possible questions. This saves time while still providing nearly optimal solutions to the problem.

The second phase selects an allocation plan which maximizes the total amount of destruction, taking into account the value of the targets. A weapon allocation tree is constructed as a framework for exploring possible allocation plans. Each allocation plan corresponds to a path from the root of the allocation tree to a unique leaf, including all plans that involve massing. The number of leaves of an allocation tree ($(t + 1)^w$ for w weapons and t targets) is too large to traverse for realistic fire support situations, so we *prune* the tree during its traversal. Artifacts that can speed the second phase selection are available to the operator. If these artifacts are not used, BATTLE is guaranteed to find the best solutions; if the artifacts are used, the solutions found will still be nearly optimal.

BATTLE has demonstrated the applicability of expert system technology to a particular Marine Corps resource allocation problem. The

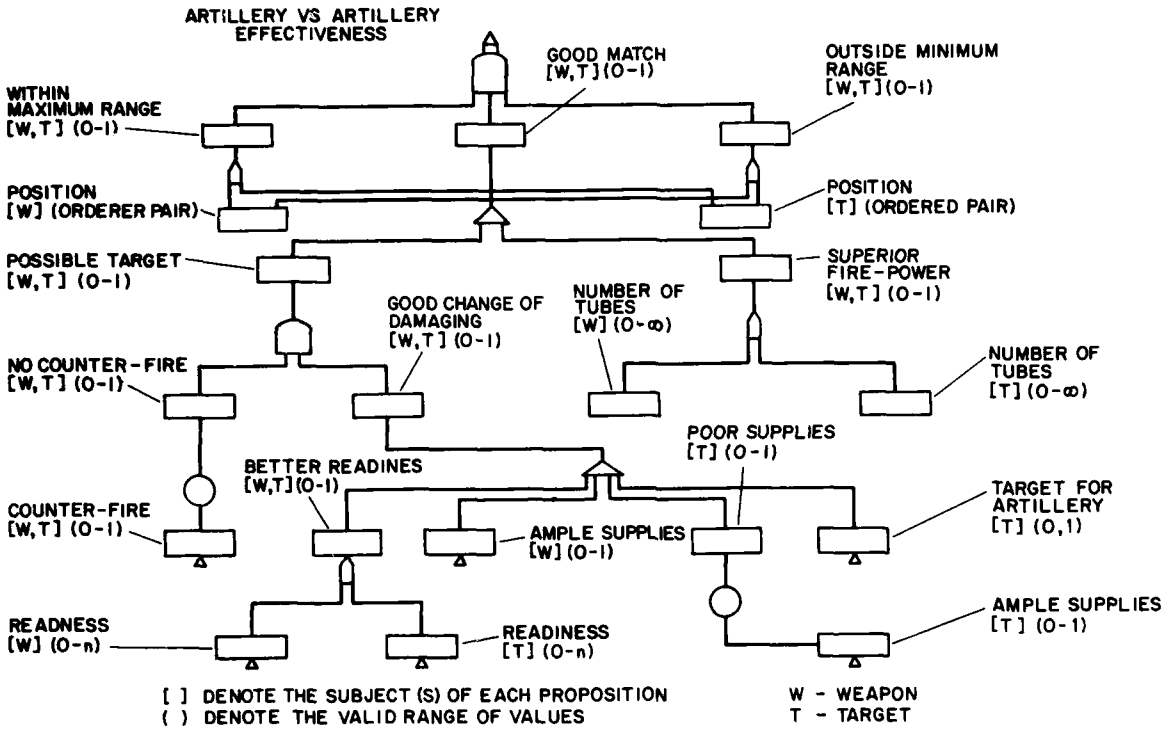

Fig. 16 — Part of a BATTLE computation network. Nodes such as *GOOD-MATCH* have values, in this case a strength of belief that the target should be fired on by the weapon. They also have links to other nodes that determine the computational relationships of antecedents and consequents. The tombstone shape, for instance, is a probabilistic *and* link that takes the product of the antecedents as the value of the consequent.

inclusion of artillery expertise in the system will soon allow the target values, on which allocation depends, to be determined automatically. Work is also proceeding on providing automatic recommendations which include the munitions and number of volleys a unit should fire. We are investigating the use of more efficient representation schemes that will make the system faster, require less storage and be more easily programmable for small field computers.

[Sponsored by ONR and ONT]

REFERENCES

1. J.R. Slagle, E.J. Halpern, H. Hamburger, and R.R. Cantone, "BATTLE, An Expert Decision Aid for Fire Support Command and Control," NRL Memorandum Report 4847, July 1982.
2. J.R. Slagle and E.J. Halpern, "An Intelligent Control Strategy for Expert Consultant Systems," NRL Memorandum Report 4789, April 1982.

ELECTROMAGNETIC SENSING IN THE NAVAL ENVIRONMENT

ELECTROMAGNETIC SENSING IN THE NAVAL ENVIRONMENT

The reflection of radar waves from the surface of the sea not only provides remote measurement of the sea state but also, surprisingly, can reveal details of the ocean bottom. This section describes some NRL work in this area.

Remote Sensing in the Nantucket Shoals, by G.R. Valenzuela, J.A.C. Kaiser and W.D. Garrett, *Environmental Sciences Division* and D.T. Chen, *Aerospace Systems Division*

Images of the ocean obtained from SEASAT synthetic aperture radar (SAR) contain a wealth of ocean features ranging from mesoscale eddies to internal and surface waves. In particular SAR and side-looking airborne radar (SLAR) images of shallow water such as the Nantucket Shoals and the English Channel show features that can be correlated with the topography of the bottom (Fig. 1). These features cannot be the result of direct probing of the sea bottom by the electromagnetic radiation, since microwaves penetrate only a few centimeters into sea water and the water depth is generally meters or tens of meters. The observed patterns must therefore be the result of hydrodynamic processes which are coupled to the bottom topography and modulate the amplitude of those ocean surface waves whose length is comparable to the radar wavelength, and which are the main contributors to the radar reflection.

Fig. 1 — SEASAT SAR image of Nantucket Shoals taken on August 27, 1978 at 13:34:14 GMT. Covers an area of about 100 km × 100 km.

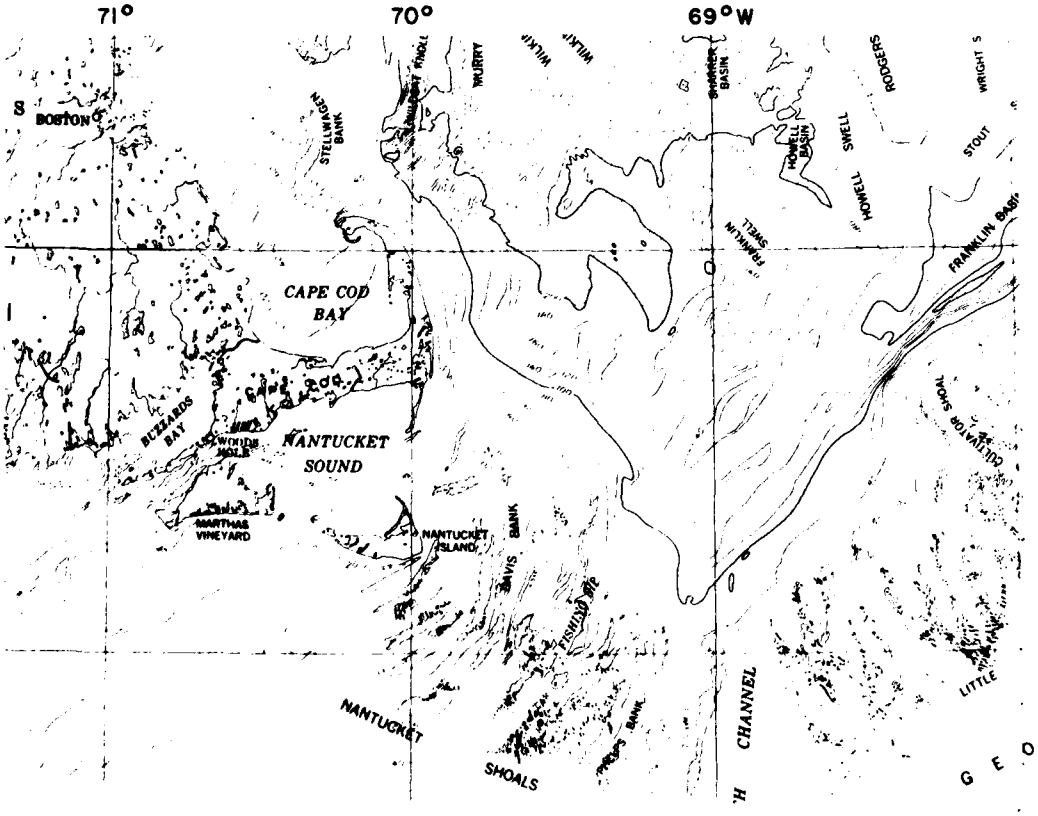

Fig. 2 — Complex bathymetry of Nantucket Shoals. The region shown includes the image of Fig. 1.

In 1980 NRL scientists proposed a comprehensive remote sensing experiment called Surface Expression of Bathymetry Experiment (SEBEX) [1] in the Nantucket Shoals involving coordinated remote and local measurements to identify the processes responsible for the correlation of surface features with the bottom topography. The SEBEX program eventually evolved into the present NRL Remote Sensing Program on current-wave interactions, which includes the previous objectives of SEBEX. The aim of the program is to develop and validate appropriate hydrodynamic and electromagnetic scattering models by means of theoretical work, controlled wavetank studies and experiments in the ocean.

The first of the NRL Remote Sensing Experiments (RSE) was conducted during July 1982 in the vicinity of Phelps Bank in Nantucket Shoals, Massachusetts (Fig. 2) to investigate the interactions of current fronts and tides with ocean surface waves and their effect on radar images. Air-sea temperature difference (atmospheric stability) and wind vector were also of major concern in this experiment. Two auxiliary experiments on the chemistry and physics of ship wakes and Langmuir circulation were also performed.

The RSE involved the *USNS Hayes* research vessel, which performed standard oceanographic and meteorological measurements plus a hydrographic survey of the Phelps Bank area. Coordinated and nearly simultaneous remote measurements were made from NRL's P-3 Orion research aircraft with an X-band remote ocean wave spectrometer (ROWS), laser profilometer, strip camera and infrared thermal scanner, and from two US Marine Corps RF-4 aircraft with X-band APD-10 SAR systems. In addition, an L-band ROWS dual-frequency radar was on board *USNS Hayes* and bathymetric contour plots of the Phelps Bank area were available from a shipboard precision depth recorder. The NRL RSE involved a dozen NRL scientists as well as scientists from NORDA, David Taylor NSRDC, the Environmental Research Institute of Michigan, and the Institute of Oceanographic Sciences, England.

The NRL RSE was the first experiment fully dedicated to solving the mystery of the surface expressions of bathymetry. A preliminary assessment of the experiment indicates that the data collected were of good to excellent quality. The surface features were persistent and in some cases so evident that they could be seen with the naked eye (Fig. 3). Strong opposing tidal currents produced current gradients on the order of $10^{-3}s^{-1}$

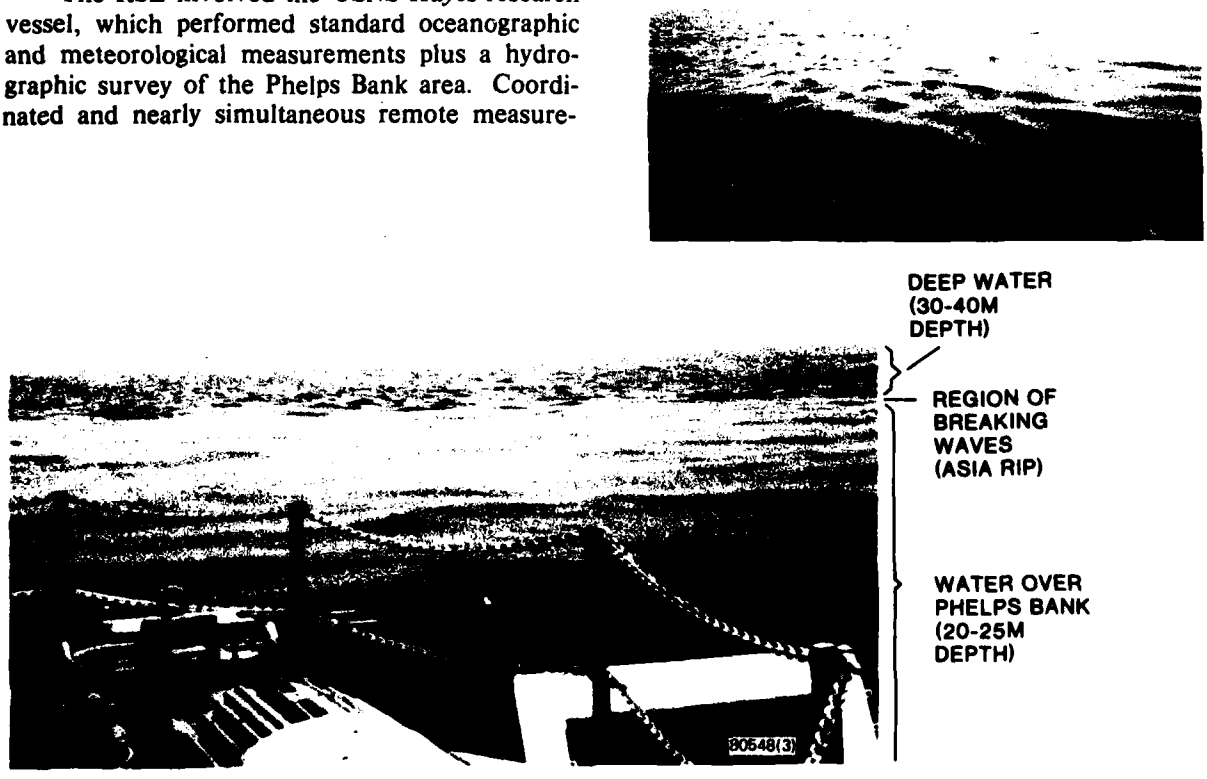

Fig. 3 — Visual evidence of surface expression of bathymetry, July 14, 1982 at 1450 GMT, Asia Rip in Phelps Bank. Insert: Side view of Asia Rip Boundary.

and prevented the less energetic ocean waves from propagating from the upper part of the figure, where the depth was 37 m, to the lower part of the figure, where the depth was 20-25 m. The optical illusion of calm water in the lower part of the figure is probably caused by the absence of intermediate length waves (5 m to decimeter wavelengths) which cannot propagate against the strong opposing tidal current of 1 m/s and therefore break at the current rip.

The short Bragg waves causing the scattering of electromagnetic radiation at L- and X-band are rapidly regenerated by the wind and appear in the lower part of Fig. 3. Preliminary investigation of the remote sensing data shows large unexplained fluctuations in the backscattered power (30 dB at X-band and 15 dB at L-band) which correlate with the bottom topography; these and other data from the first RSE are still being analyzed. A more definitive experiment is planned for 1984 exploiting the opportunities for remote sensing afforded by the SIR-B shuttle flight, and a concluding experiment will be performed in 1986. We hope by then to have a definitive explanation of this phenomenon.

[Sponsored by ONR]

REFERENCE

1. G.R. Valenzuela and D.T. Chen, "Plan for a Remote Sensing Experiment in the Nantucket Shoals (SEBEX) (December 1, 1980) "NRL Report 8659, February 1983.

Dual Polarized Radar Scatter from Shoaling Waves, by D.B. Trizna, *Radar Division*

Recent NRL measurements of radar scatter from the sea have resulted in the observation of a new scattering mechanism never before reported: very strong scattering of horizontally polarized radiation from small-amplitude shoaling swell waves. *Shoaling* is the term used to describe the process in which long swell waves, which are sinusoidal in deep water, change their shape as they enter shallow water approaching a beach. They develop an ever steeper trochoidal profile as they move into shallower water and finally break because of the dynamically unstable height-to-wavelengh ratio. The physics of this development is well understood, and shoaling waves provide very convenient targets for radar studies. In addition, breaking waves at the shore and post-break water flowing up the beach were studied in greater detail than ever before.

Previous experiments using high-resolution radars have observed returns from discrete features on the sea surface such as wind-blown ripples or capillary waves, wedge-like features at the top of wave crests, and specular facets of waves. Our new observation is the first to show strong horizontally-polarized and weak vertically-polarized scatter from low amplitude swell waves of sinusoidal shape. Our experiment used a high-resolution radar (5-meter side scattering cell) capable of transmitting vertically and horizontally polarized pulses alternately at a 6 kHz rate. This technique allows us to study nearly simultaneous returns at each polarization from shoaling waves as they approached the shoreline from beyond 600 m offshore on a sloping beach.

The U.S. Army Coastal Engineering Research Center's instrumented pier at Duck, N.C., provides an excellent facility for investigation of shoaling waves, and was selected for this radar experiment. This facility regularly provides information on bottom profiles, wind direction, wind speed, and wave height along several points along the pier and farther out to sea. With the above information available, we collected data late in the spring of 1982 during periods of low to moderate wave conditions. Swell was always present to some degree, typically with 6-10 s periods, and nearly normal to the shoreline. Several features of radar scatter were observed which have never been previously reported. First, we detected strong horizontally-polarized discrete radar returns from the crests of small amplitude swell waves. These returns were continuous in character as the wave shoaled, and are not explained by the traditional model of scatter from capillary waves or breaking wave features. Second, we observed that the fluctuation rates in the radar returns from breaking waves at the shoreline were quite different for the two polarizations. Third, we found surprisingly large returns from the leading edge of the post-break water running up the beach. This last item is the first observation of scatter from a discrete corner-shaped edge feature.

The significance of these new observations is that the transverse coherence of the scattering surface must be taken into account when considering discrete scattering features of the ocean surface. This is in contrast to Wright's two-scale model of sea scatter, which treats the capillary

waves responsible for radar scatter as uniformly distributed with random phases across an ocean wave. Each of the three observations presented here requires consideration of the wave structure transverse to the direction of wave propagation, that is, along the crest of the wave. Understanding these new observations could lead to improved target detection in the presence of sea clutter, improved capabilities in radar remote sensing of the sea surface, and in synthetic aperture radar imaging of ocean waves.

[Sponsored by ONR]

Measurement of Directional Ocean-Wave Spectra From a Moving Ship, by Dale L. Schuler, Allen B. Reeves, and Wah P. Eng, *Aerospace Systems Division*

Directional waves surrounding a ship are the primary cause of ship motions that degrade the effectiveness of a Naval vessel by lowering the performance of crew and equipment. Most wave measurements are now obtained from instruments such as buoys which measure sea-surface properties at only one point. Means are needed to acquire time histories of wave-height spectra over wide areas of the sea in order to provide data for better ship design. Ships are excellent platforms for this purpose. Aircraft are less-desirable platforms because their limited time on station restricts their ability to acquire long-time histories, and their availability is also restricted by factors such as weather and cost. Ships, on the other hand, can be held stationary for temporal wave development studies, or can make measurements while underway to simulate conditions during tactical operations. In the future, ships may be equipped with wave-measurement systems to provide real-time information for active stabilization systems.

In July 1982 a shipboard ocean-wave spectrometer, developed at NRL, was tested aboard the research vessel *USNS Hayes.* The spectrometer uses an extension of radar techniques tested successfully from cliffs [1], towers [2], and aircraft (*1981 NRL Review,* pp. 47-48). The extension of this technique to shipboard use represents a significant achievement because the backscattered signals from waves contain a considerable contribution from the motion of the ship and a new system had to be developed to separate this effect from the wave data.

The effect of relative motion between sensor and sea surface was eliminated by using a new dual-channel Doppler cancellation circuit shown in Fig. 4. An existing coherent *L*-band radar was modified so that long (1 μs) and short (35 ns) pulses were sent out alternately. The backscattered returns from the long pulses did not resolve the ocean waves and constituted a reference channel which provided a signal representing the ship's motion along the line of sight. The short pulse returns constituted the data on actual wave

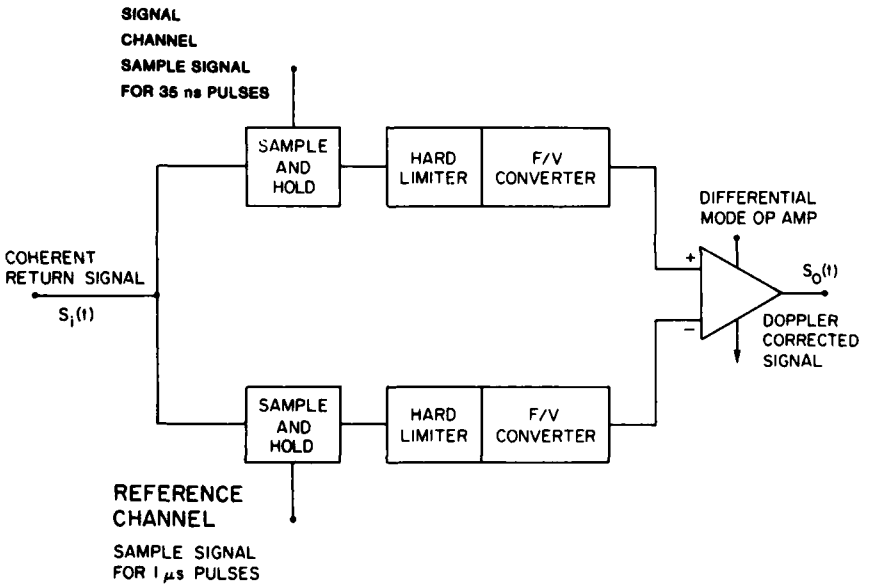

Fig. 4 — Doppler-cancellation circuit to correct for line-of-sight ship motions

orbital motions plus ship motion. These two backscattered microwave signals were mixed down to audio frequencies, coherently detected, and then subtracted. Ship motions orthogonal to the line of sight contributed only minor amplitude fluctuations in the signal (from polarization modulations) and were eliminated by a hard-limiting amplifier.

The system was one of many instruments aboard the *Hayes* on its 18-day cruise through the Gulf Stream and into the Nantucket Shoals for the 1982 NRL Remote Sensing Experiment. The radar system was supplemented by a computer for onboard data recording and processing, and a conventional accelerometer was bore-sighted with the system antenna to monitor the actual line-of-sight antenna motions. Figure 5a shows the location of the special 1.2-m antenna aboard the *Hayes* and the backscatter measurement geometry. The radial extent of the scattering cell could be made as short as 5.1 m so that information on ocean waves whose wavelength was longer than 10.2 m could be obtained. The main portion of the radar system, data recording, and processing equipment (including a DEC MINC 11 computer) were housed aft in the ship's main electronics laboratory. Figure 5b shows a typical seven-sided measurement pattern (heptagon)

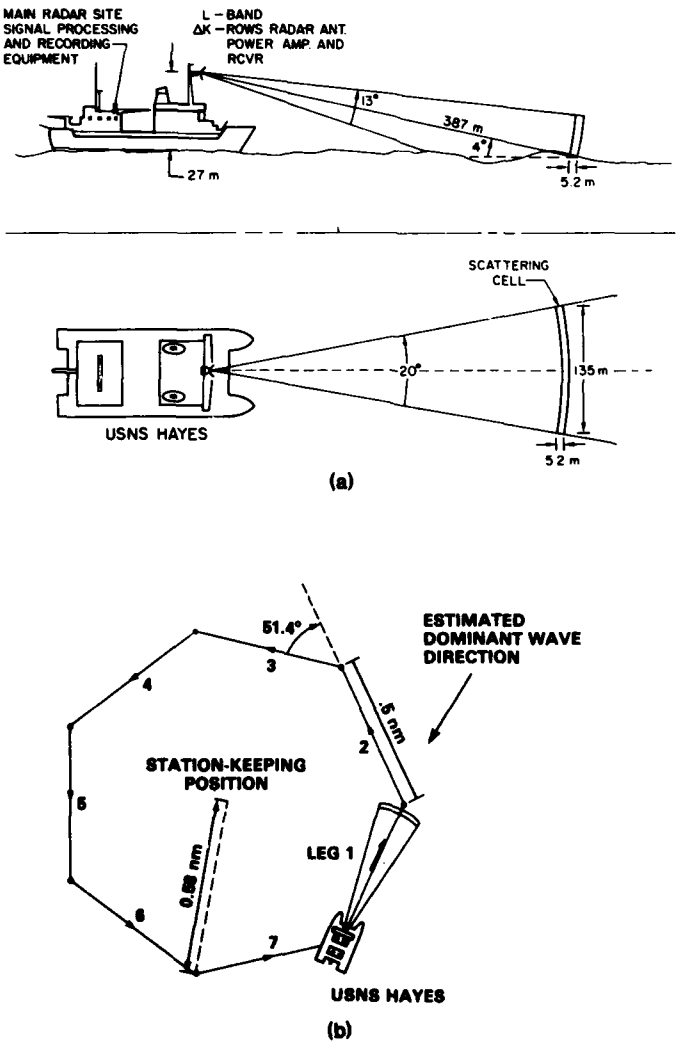

Fig. 5 — Measurement of directional wave height spectra from the USNS Hayes: (a) system installation and scattering geometry, (b) typical ship track during data acquisition periods

which was traced by the ship in order to measure the directional spectrum. This method of measurement was chosen, in spite of the fact that the antenna had a rotor, because the ship's heading could only be maintained constant when the ship was underway. Future systems will use electronically-switched horn antennas to obviate the need for such elaborate ship maneuvers.

Extensive data on wave-height spectra were taken during the *Hayes* cruise. Radar data-collection times were scheduled so that they just followed or preceded the deployment of wave buoys: a Cloverleaf buoy operated by the Institute for Oceanographic Sciences, and an ENDECO 956 buoy operated by the David Taylor Naval Ship Research and Development Center. Figure 6 shows an example of a fully processed directional wave-height spectrum measured by the radar and a comparative spectrum produced (almost simultaneously) by the IOS Cloverleaf buoy.

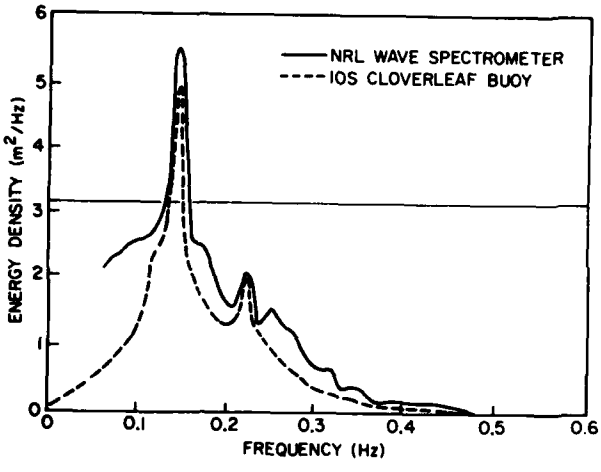

Fig. 6 — Estimated Average Wave Height Directional Spectrum. Radar data were taken while the USNS Hayes was moving at 3 kt on one leg of a heptagonal measurement pattern. Measurements taken 30 minutes later using a Cloverleaf buoy are shown for comparison.

This experiment demonstrates the feasibility of measuring surface-wave parameters from a moving ship under real ocean conditions. The new shipboard ocean-wave spectrometer can acquire large amounts of wave data at specific locations or along ocean tracks, can operate in rough weather better than conventional buoys, and can provide tactical support of fleet exercises to optimize sea-keeping and aircraft operations. The prototype system will be improved by the addition of a multiple-beam antenna which can be switched electronically to change the direction of observation. Future plans include taking an improved ocean spectrometer system to sea in 1984 as a principal research tool for the 1984 NRL Remote Sensing Experiment in the Nantucket Shoals.

[Sponsored by ONR]

REFERENCES

1. W.J. Plant and D.L. Schuler, "Remote Sensing of the Sea Surface Using One and Two Frequency Microwave Techniques," *Radio Science* **15**, 605 (1980).
2. D.L. Schuler, W.J. Plant, W.P. Eng, W. Alpers, and F. Schlude, "Dual-Frequency Microwave Backscatter from the Ocean at Low Grazing Angles: Comparison with Theory," *International Journal of Remote Sensing*, **3**, 363 (1982).

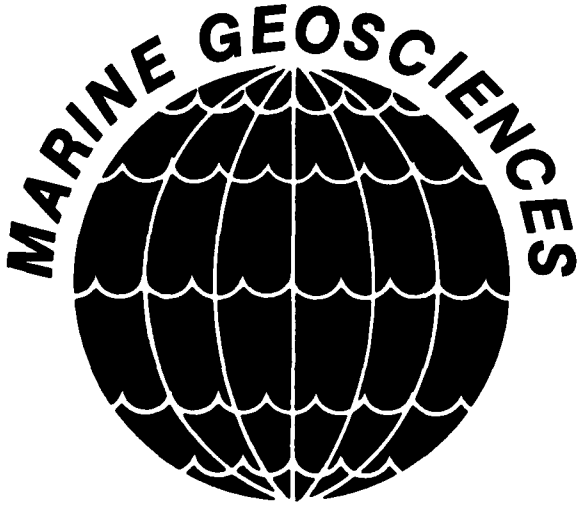
MARINE GEOSCIENCES

MARINE GEOSCIENCES

The Navy's main environment is the ocean. A better understanding of fundamental oceanic processes will lead to more effective Naval operations. Some highlights of NRL's research in this area are described in this section.

Freon-11 as a Tracer of Oceanic Mixing, by W.D. Smith and C.H. Cheek, *Environmental Sciences Division*

The man-made gas Freon-11 (CCl_3F) has accumulated in the atmosphere during the past three decades as a result of its extensive industrial applications and its use as a propellant for aerosol spray cans. (Fig. 1). The gas enters the ocean surface from the atmosphere and is transported to deeper waters by oceanic mixing. Since it is relatively inert chemically and can be detected at extremely low concentrations, Freon-11 can serve as a very useful tracer of large-scale ocean mixing and circulation. Detection of the tracer at any depth shows the presence of water that was at the surface at some time during the past 30 years. Thus, Freon-11 (as well as other man-made transient tracers such as Freon-12, ^3H, and ^{85}Kr) can provide *temporal* information on oceanic mixing processes which until now was not readily obtainable.

We have determined the distribution of Freon-11 in the western Atlantic Ocean from 63°N (Iceland area) to 59°S (Scotia Sea, southeast of the southern tip of South America). The range of latitude, exceeding one-third of the circumference of the earth, was covered by cruises of the *USNS Hayes* in 1976, 1980, 1981, and 1982. The cruise tracks are shown in Fig. 2. Samples of seawater were collected at various geographic locations and depths; the Freon-11 was stripped from solution by a carrier gas, separated by gas chromatography, and measured by an electron-capture detector. The concentrations are expressed in picoliters of Freon-11/l of seawater (equivalent to parts per trillion by volume).

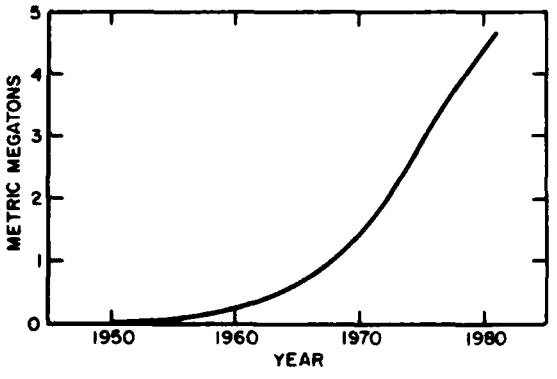

Fig. 1 — Cumulative release of Freon-11 to the atmosphere [1]

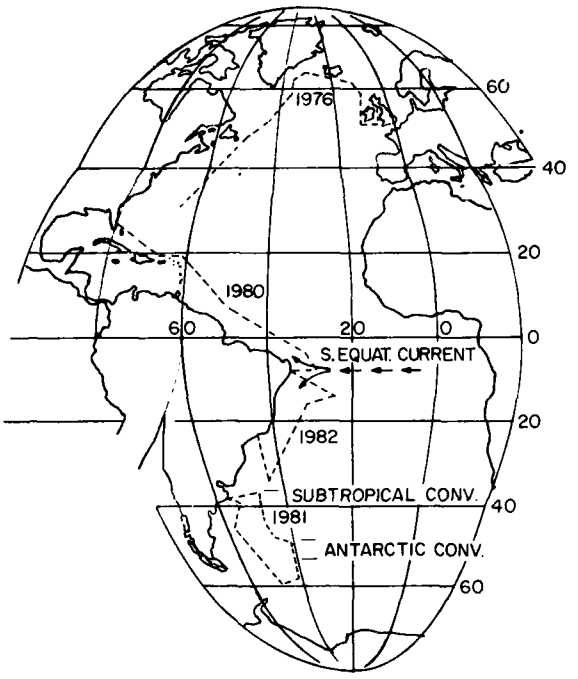

Fig. 2 — USNS Hayes Cruise Tracks, 1976—Glasgow, Scotland to Bermuda, July-August; 1980—Recife, Brazil to Coral Gables, Florida, Feb-March; 1981—Mar del Plata, Argentina to Mar del Plata, Argentina, Jan-Feb; 1982—Rio de Janeiro, Brazil to Recife, Brazil, Feb-Mar.

Figure 3 displays the distribution of the dissolved gas by lines of equal concentration (*isopleths*) on a graph of depth vs latitude. The dashed line below the isopleths shows the approximate depth at which the concentration falls below the detection limit (BDL). This representation involves three compromises. First, the vertical scale is exaggerated by a factor of about 2200 to show variation of concentration with depth over the 130° (14,446 km) of latitude covered by the graph. Second, the longitudes of the oceanographic stations are ignored, so the concentration lines are essentially projections of the isopleths on the plane of a single meridian. Third, the 5.5-year period over which the measurements were made is not considered. However, none of these compromises seriously influences the essential features of the distribution as displayed.

Within these limitations, Fig. 3 provides a picture of the extent to which surface waters have mixed into the depths of the western Atlantic Ocean during the past 30 years. The most prominent feature is the substantial variation of the depth of penetration with latitude. Only at high

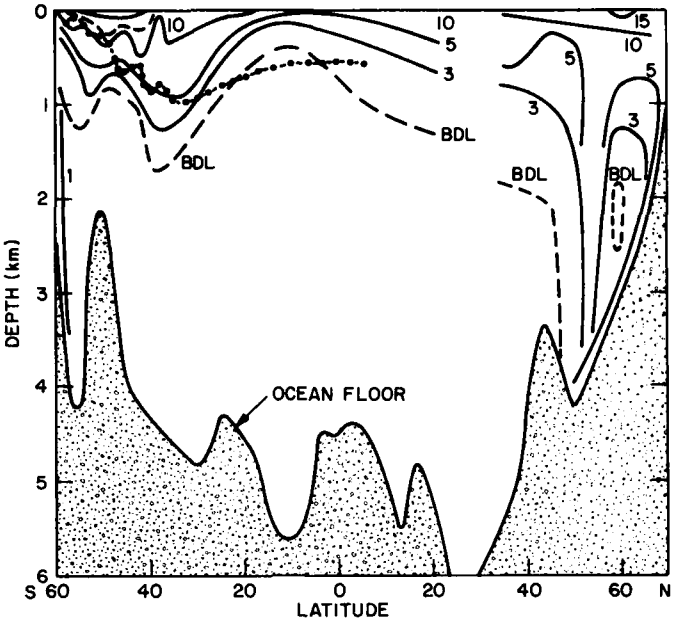

Fig. 3 — Freon-11 Distribution in Western Atlantic Ocean
—— 5, concentration isopleth, 5 picoliters per liter
----- , depths of Freon-11 concentration maxima
——BDL, depths where concentration is below detection limit
-·-·- , isopycnal for potential density 1.0272 grams/ml.

latitudes (>45°N and >55°S), where cold waters sink relatively rapidly, has the penetration extended into ocean depths greater than 2000 m. At lower latitudes the penetration is confined to the upper 1500 m, and the variations in the depth of the isopleths are explainable as consequences of known circulation patterns. It is known that seawater sinks in areas where surface currents converge, and rises where surface currents diverge; thus, the isopleths are deepest in areas of convergence and least deep in areas of divergence. The depth maxima at 50°-54°S and at 38°-40°S are attributed to the Antarctic Convergence and the Subtropical Convergence, respectively. The shallowest penetration is only about 400 m and occurs at 7°S, where the westward-moving South Equatorial Current diverges into northern and southern branches.

Depth profiles of Freon-11 at 40°-57°S have definite subsurface maxima. These maxima, whose depths are shown by the dashed line near the surface, are not accountable by vertical mixing and are attributed to lateral intrusion by water from the south containing higher concentrations of the tracer. This is supported by the fact that the isopleths are approximately parallel to the lines of constant density (*isopycnals*), shown as dots, along which lateral migration is known to occur. These observations strongly suggest that mixing at intermediate depths occurs principally by lateral migration along isopycnals on a time scale of decades.

The absence of Freon-11 at depths greater than 1500 m in tropical and subtropical zones shows that the deep ocean water in these areas has not been at the surface during the past 30 years. If the intrusion of Freon-11 into the deep ocean at low latitudes is monitored for several more decades, it will be possible to determine the mixing time on the scale of a century.

[Sponsored by ONR]

REFERENCE

1. Chemical Manufacturers Association Fluorocarbon Program Panel, World Production and Release of Chlorofluorocarbons 11 and 12 through 1981, September 15, 1982.

Ocean Temperature Fluctuations, by J.P. Dugan and B.S. Okawa, *Enviromental Sciences Division*

The ocean interior contains motions with spatial scales from millimeters to thousands of kilometers and time scales from fractions of a second to many years. Changes on the largest scale—that of the ocean basins—can take many years. On the other hand, there are major large-scale changes in the temperature structure in the upper ocean that occur seasonally. These large-scale fluctuations are collectively called the ocean *climate* while those with the smallest characteristic length are termed the *microstructure.* Between these extremes are a large range of length and time scales which have motions governed by vastly different physics. The largest (eddies, fronts, and boundary currents, or the oceanic mesoscale) are influenced by the wind stress, bottom topography, and the latitudinal variation of the Coriolis force. The intermediate scales (internal and inertial waves) depend upon the local density stratification and the Coriolis force, while the smallest lengths are dominated by molecular diffusivity. A large fraction of oceanographic work to date has been applied to the isolation and study of these many different processes.

It is important to know how much potential and kinetic energy is associated with each process in both frequency and wavenumber domains. This knowledge gives the physicist insight into the scales over which particular processes are dominant and provides a basis from which to synthesize models of ocean fluctuations which affect undersea systems. Because information on the distribution of energy over horizontal scales is particularly lacking, we have focussed our efforts upon acquiring the appropriate data and processing them to estimate the horizontal distribution of the energy in wavenumber space.

To enable us to construct an energy spectrum which spans a large range of wavelengths, initial work has been restricted to potential energy since this is easily estimated from measurements of temperature fluctuations. This has entailed assembling data from a variety of Navy R&D programs. Data were acquired in several different oceans at different depths and seasons using

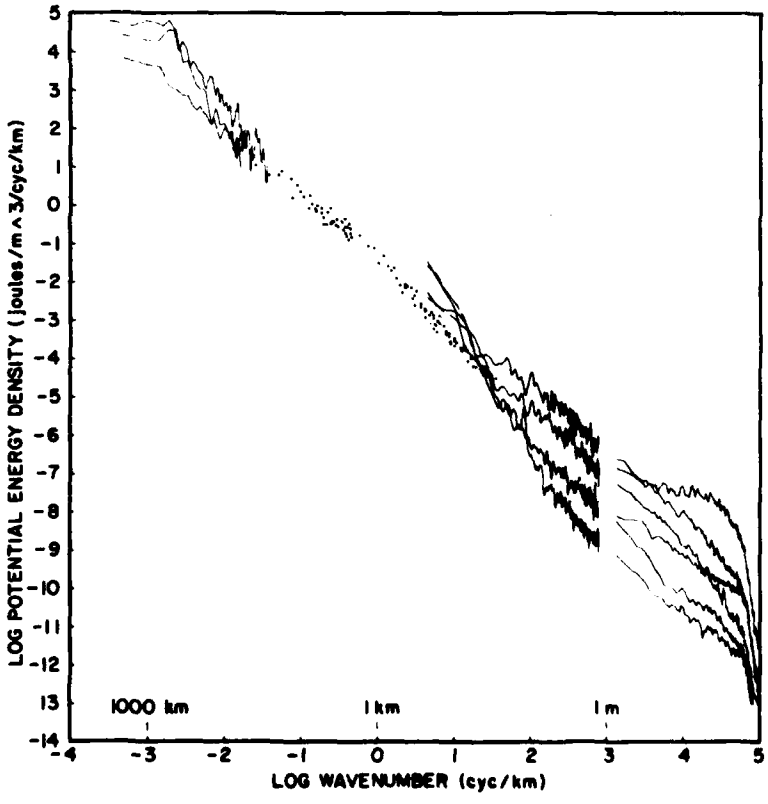

Fig. 4 — Potential energy spectrum. Lines represent NRL data, taken in different parts of the ocean, and dots represent data collected by E. Katz of the Woods Hole Oceanographic Institution.

different types of sensors. Expendable profiling instruments were used for scales from 2000 to 25 km; towed thermistors were used for scales from 10 km to 1 m; and a towed conductivity sensor was used for scales from several meters to 1 cm. Vertical water displacements can be estimated from the temperature fluctuations, and these are normalized to the local buoyancy of the water column to estimate the potential energy.

Figure 4 shows the essential results. The composite spectrum spans the scales from 1 cm to 2000 km, a wavenumber range of over 8 decades. The overall trend across these scales indicates that the spectral energy density is inversely proportional to the square of the horizontal wavenumber. The different traces were taken in different parts of the ocean, and it may be seen that considerable variability in energy level occurs near each end of the spectrum. The differences in energy level in the band of 100-1000 km are due to the presence or absence of large mesoscale features. Similarly, the large differences in level on scales less than about 10 m are due to the presence of absence of microstructure patches which involve dissipation. The exception is the band from 100 m to 50 km, which has little variability. The data in this band (designated by dots) were acquired by the Woods Hole Oceanographic Institution, and we ascribe the lack of variability either to the universality of the internal wave spectrum in the deep sea or to the limited amount of data available.

These unique results for potential energy provide estimates of temperature and sound speed fluctuation levels for various Navy applications. The challenge for the near future is to understand the sources of this variability and to obtain estimates of levels of kinetic energy.

[Sponsored by ONR]

Nonlinear Baroclinic Instability in Gulf Stream Rings, by R.P. Mied and G.J. Lindemann, *Environmental Sciences Division* and J.M. Bergin, *Acoustics Division*

Gulf Stream rings are vortices of current that are pinched off when the Gulf Stream undergoes a large loop-like meander toward the continental shelf or into the Sargasso Sea. During the period 8-19 June 1979, researchers aboard the *USNS Lynch* and *R/V Endeavor* conducted an extensive survey of one of these current features northwest of Bermuda using expendable bathythermographs (XBTs). The ships steamed three times in a star pattern over the ring while dropping XBTs at approximately 8 km intervals. The temperature information thus obtained was used to map the extent of the ring. Figure 5 shows depth contours of the 15°C isothermal surface, from which two features are apparent. The first is that the ring is not round, but oval. The second is that this oval appears to rotate counterclockwise, or in the direction of the flow. The most energetic fluid particles have orbited the ring more than three times in these ten days, therefore the shape perturbation cannot be directly associated with the circulation within the ring; it is more properly described by a wave propagating counterclockwise around the ring. In this work, we have sought to understand the mechanism that energizes this wave.

By using data on salinity and temperature as a function of depth taken aboard the *Endeavor*, we are able to map the surfaces of constant density. Assuming that the pressure gradient is largely balanced by the Coriolis force (the so-called *quasigeostrophic* assumption), we can calculate the velocities within the eddy [1]. Because of the roughly circular shape of the eddy, it is appropriate to employ cylindrical coordinates (r,θ,z) and time t to describe the motion. By this means the pressure $\phi(r,\theta,z,t)$ may be decomposed into a steady, circularly-symmetric basic state $\Psi(r,z)$ and a time-varying, azimuthally asymmetric component $\psi(r,\theta,z,t)$ which is the wave. Thus, the eddy is described by $\phi(r,\theta,z,t) = \Psi(r,z) + \psi(r,\theta,z,t)$. Strictly speaking, the basic state $\Psi(r,z)$ cannot be independent of time if the wave field $\psi(r,\theta,z,t)$ is allowed to grow or decay while exchanging energy with the basic state; nevertheless, this linearized approach has proved successful in identifying the energy source of the wave.

The basic state pressure can be subtracted from the total pressure ϕ to reveal the wave part ψ. Figures 6a and 6b display contour maps of ψ in the θ-z plane at radius $r = 40$ km corresponding to the eddy maps in Figs. 5a and 5b. Note that ψ has four cells (two positive and two negative) in each picture. This indicates that the travelling azimuthal wave is of the form $e^{2i\theta}$, which is consistent with the oval shape in Fig. 5. Moreover, the direction of tilt of the ψ pressure lines changes from leaning with the flow in Fig. 6a to leaning very slightly against the flow in Fig. 6b. The latter figure has the signature of a flow which is baroclinically unstable, that is to say, the potential energy stored in fluid particles that are

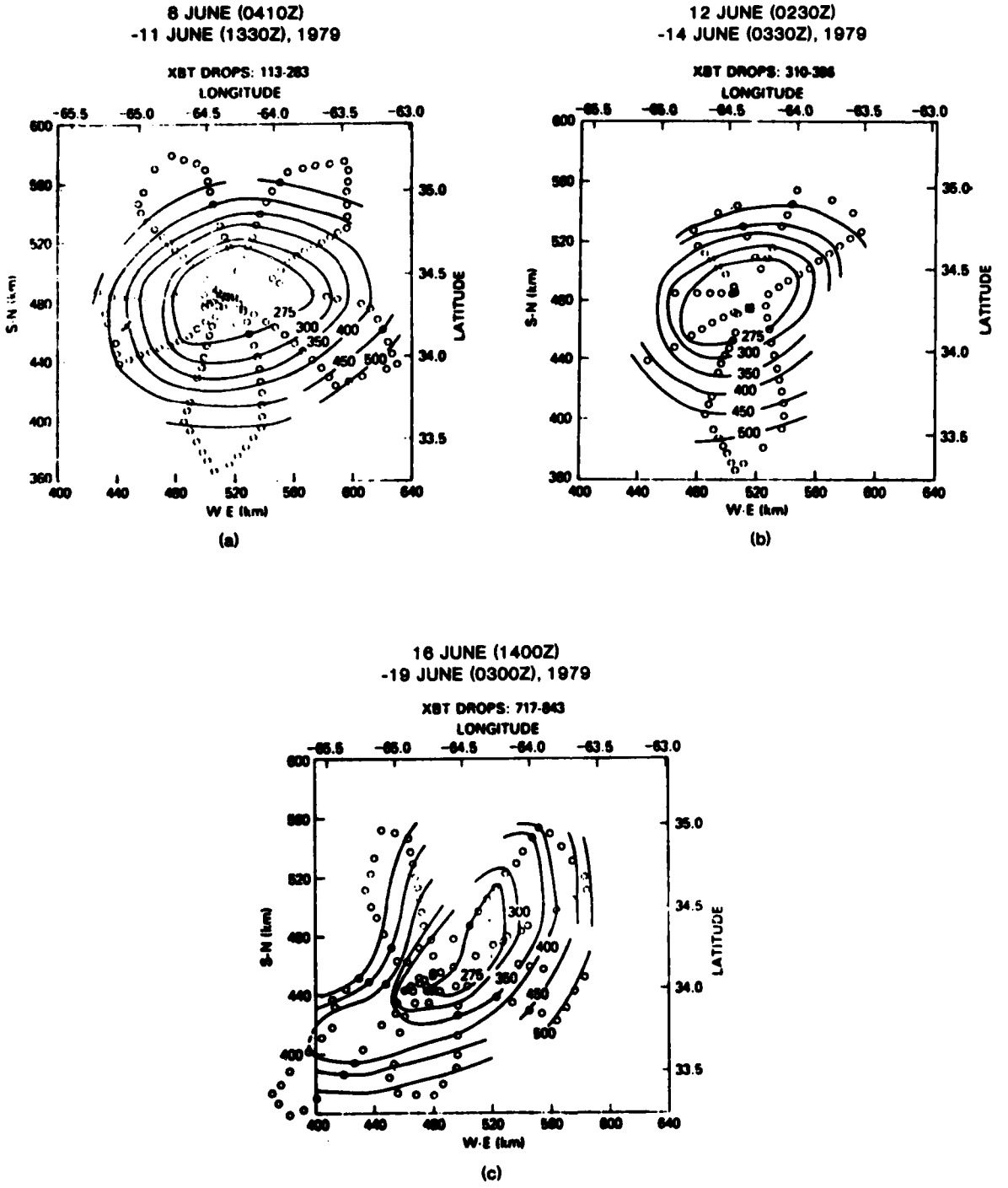

Fig. 5a,b,c — Depth contours of the 15°C isothermal surface in meters. Figures 5a, b are from the USNS Lynch; Figure 5c was obtained from the R/V Endeavor. The open circles represent the position of XBT casts, and the blackened square indicates the position of a NAVOCEANO STD cast.

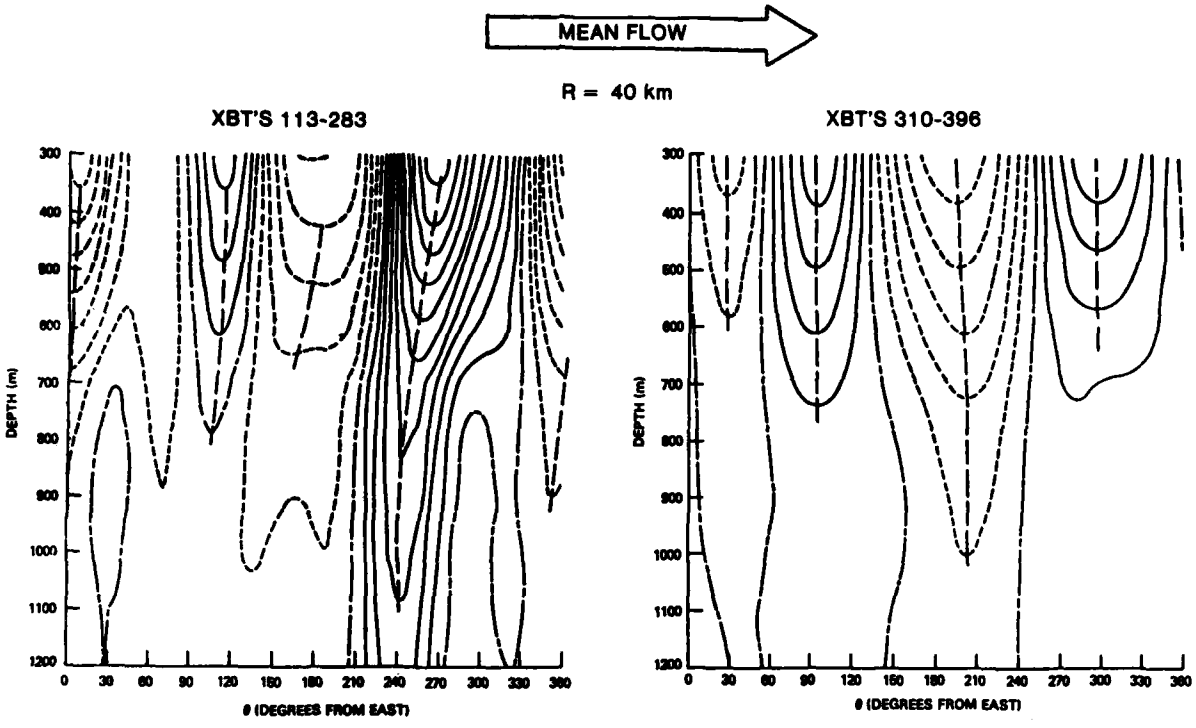

Fig. 6 — Vertical cuts of $\psi(r,\theta,z,t)$ for constant radius r = 40 km in the first and second eddy photograph (Fig. 5a and 5b); θ is increasing in the direction of the current (counterclockwise). Vertical lines have been drawn to connect the troughs of the contour lines to emphasize their direction of tilt with respect to the flow.

Contour code: ----- ($\psi < 0$); — · — ($\psi = 0$); —— ($\psi > 0$).
Contour level = $4.12 \cdot 10^2$ dynes cm^{-2} for Fig. 6a, and $8.24 \cdot 10^2$ dynes cm^{-2} for Fig. 6b.

moved above or below their equilibrium positions is being converted into wave energy. In Fig. 6a, the waves are decaying and thus yielding their energy to elevate the surfaces of constant density in the basic state Ψ. In Fig. 6b, on the other hand, the wave field ψ is growing and thus extracting energy from Ψ by lowering the surfaces of constant density.

The energy associated with a current feature in the ocean is the sum of its kinetic energy (in fluid velocity) and its potential energy (defined above). By forming the equation governing the energy contained in the disturbance ψ, we may identify and calculate the source terms by which energy is interchanged with the basic state. Having done this, we find that ~90% of the energy in the disturbance can be accounted for by the baroclinic instability mechanism [2].

We can also calculate time scales for the energy interchange. For the wave decay phase (Fig. 6a), this is ~4.5 days, while for the growth phase (Fig. 6b), this is ~16 days. The oval shape of the eddy is explained by the presence of an unstable wave which apparently undergoes periods of slow growth interspersed with periods of rapid decay. This mechanism causes the shape of the oval to change in a periodic fashion.

[Sponsored by ONR]

REFERENCES

1. Mied, R.P. and G.J. Lindemann, "The Propagation and Evolution of Cyclonic Gulf Stream Rings," *J. Phys. Oceanogr.* **9**, 1183 (1979).
2. Mied, R.P., G.J. Lindemann, and J.M. Bergin, "Azimuthal Structure of a Cyclonic Gulf Stream Ring," *J. Geophys. Res.*, **88**, 2530 (1983).

Airborne Gravimetry, by John M. Brozena, *Acoustics Division*

Accurate knowledge of the spatial variations in the earth's gravity field is required for several reasons. Among these are compensation of inertial guidance systems, improvements in gravitational and geoidal models of the earth used in orbital calculations, crustal density determination in regions of known topography, and estimation of topographic structure in oceanic areas with sparse bathymetric data. Measurement of gravity variations in oceanic areas is conventionally performed from surface ships or submarines, but the greater speed and range and lower cost per track mile of fixed wing aircraft make them attractive alternative platforms. The major difficulty in performing airborne gravity measurements is separating the variations in gravity from the effects of vertical acceleration of the aircraft.

Vertical acceleration of an aircraft can arise from variations in altitude or from the centripetal and Coriolis accelerations caused by motion over the curved surface of the earth. The first type of vertical acceleration can be determined by altimetry and the second by navigation. Previous airborne gravimetry experiments have been performed at high altitudes (between 4000 and 9000 m) and used relatively long data averaging periods to minimize the effects of vertical acceleration. This has hindered the detection of shorter wavelength gravity anomalies which are of considerable interest. Recent advances in technology, especially in navigation and altimetry, have made it possible to improve the accuracy of an airborne marine-gravimetry system. More accurate measurement of altitude allows operation at lower altitude. Greater accuracy in three-dimensional position and velocity determination permits averaging of the data over shorter times. The response of the system to short wavelength gravity anomalies is thus enhanced.

NRL has been conducting experiments since 1981 to test an airborne gravimetry system aboard a P3-A Orion research aircraft. The system was designed and assembled using state-of-the-art components. A Lacoste-Romberg air-sea gravity meter mounted on a three-axis stabilized platform is used to measure the local vertical component of gravity plus accelerations of the meter due to aircraft motion. Lacoste-Romberg gravity meters have demonstrated accuracies on the order of 1 mgal (10^{-3} cm s^{-2}) in a shipboard environment and have been used in several previous airborne experiments [1], [2]. Gravimeter data are filtered through three stages of analog filtering with time constants of 20 s each. Thus, the meter is not influenced by short period oscillations in acceleration due to aircraft motion. Vertical positioning of the aircraft is performed by high resolution radar and pressure altimeters. Vertical acceleration corrections to the gravity data were computed from the radar altimeter heights for the preliminary analysis presented here. The horizontal spatial sampling resolution was approximately 5 m and was sufficient to resolve fluctuations in height arising from sea waves.

Four navigation systems have been used for comparison purposes: a prototype Texas Instruments High Dynamic Global Positioning System (GPS), a Litton LTN-72 inertial navigation unit, a Digital Marine Electronics Corporation North Star 6000 Loran-C receiver, and airborne VLF/OMEGA. For our preliminary analysis, the GPS with a positional accuracy of about 10 m was used as the primary source of navigation. Velocities needed to determine the Eotvos corrections (centripetal acceleration and the vertical component of Coriolis accelerations) were calculated from derivatives of the GPS positions. Three

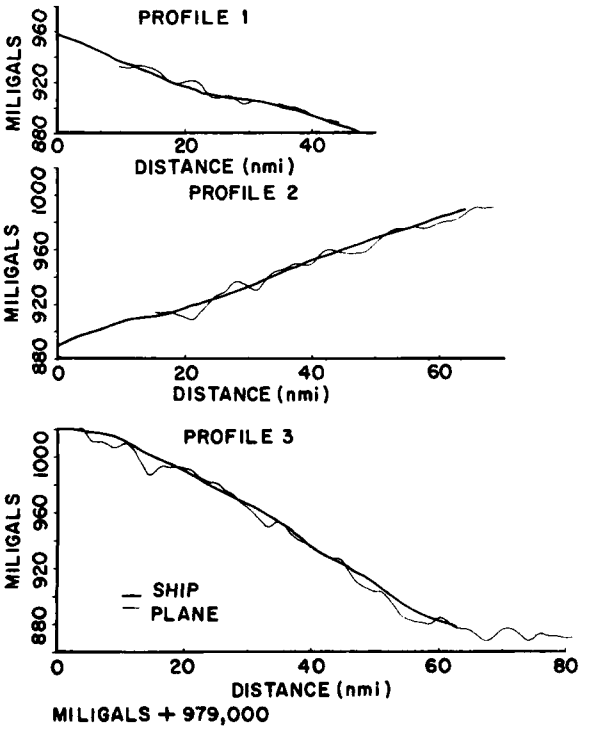

Fig. 7 — Comparison of gravimetry profiles

Hewlett Packard 1000 minicomputer systems with disc and tape storage performed the data acquisition and processing.

Results from one experiment are presented here as an example. Data-gathering flights were made over the Cape Charles-Wallops Island gravity equipment test and evaluation range. Figure 7 illustrates the observed gravity profiles compared with the known (reference) profiles along the tracks. The errors indicated in the figure could have been reduced by further filtering the data, but it was our intention to filter as little as possible to preserve the short wavelength response.

Our results demonstrate the feasibility of gravity measurement, from fixed-wing aircraft when state-of-the-art navigation and altimetry are used. Further increases in accuracy should be achievable through more sophisticated signal processing techniques and improvements in the various sensor systems. In addition, the use of satellite interferometric navigation should permit operation of the system over both land and ice-covered regions.

[Sponsored by ONR]

REFERENCES

1. R. L. Coons et al., "Evaluation Study of Airborne Gravimeter Operational Test," University of Wisconsin Geophysical and Polar Research Center, 1962,

2. E.J. Frey and R.B. Harlan, "Airborne Gravimetry Program," Massachusetts Institute of Technology Dept. of Aeronautics and Astronautics, 1969.

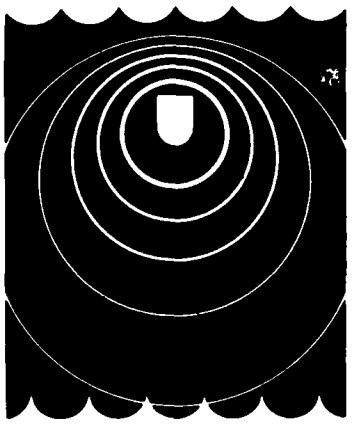

ACOUSTIC SYSTEMS and TECHNOLOGY

ACOUSTIC SYSTEMS AND TECHNOLOGY

Sonar has long been the principal means of locating underwater targets. This section includes some NRL research which indicates that analysis of the echoes could provide information about the nature of the target.

Geometric Dispersion in an Ocean Channel, by K.D. Flowers, *Acoustics Division*

Acoustic signals propagated in the deep ocean to distant surveillance receivers are often quite weak and must be coherently processed to increase their detectability. The time periods associated with the coherent processing are limited by the effects of the ocean duct on the transmitted signals.

When continuous-wave acoustic signals are propagated to distant receivers in the ocean, the phase of the received signal is not a linear function of either the signal frequency or the distance between the source and receiver. This nonlinearity in the phase is a result of the interaction of the acoustic wave with the ocean boundaries and variations in the speed of sound. That is, the nonlinear phase is caused by geometric (modal) dispersion. When either the source or receiver is in motion the nonlinearity is detected by the receiver as a variation of phase occurring randomly in time. These phase fluctuations limit coherent processing in two ways: they increase the signal bandwidth and they limit the useful integration time for correlating spatially or spectrally separated signals. We have made estimates of the maximum dispersion-induced bandwidth and limitations on the useful integration time arising from these effects.

An analytical model was developed at NRL from which dispersion effects on the bandwidth and useful integration times could be determined.

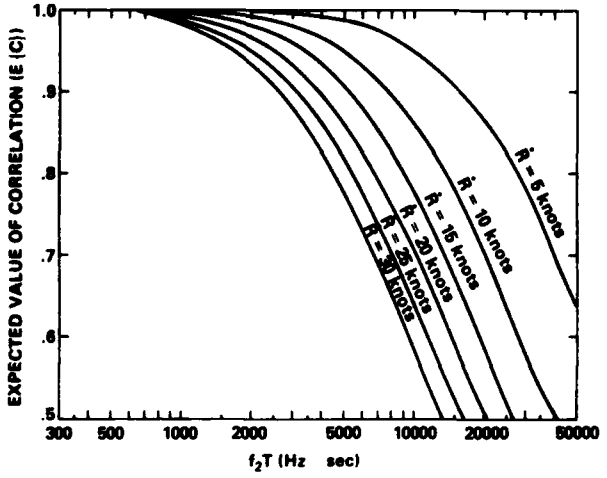

Fig. 1 — Expected value of the correlation (E[C]) vs f_2T with relative velocity $\dot{R}$ (knots) as a parameter. The frequency f_2 is the higher of the received pair and T is the integration time in seconds.

The model was used to calculate the phase of the acoustic field in a model ocean channel for several frequencies of interest. The rate of change of phase due to source and receiver motion is proportional to the instantaneous frequency, and the deviation of the instantaneous frequency from the average received frequency defines the dispersion-induced bandwidth. Signals received at spatially separated receivers (or signals of different frequencies at the same receiver) will have different instantaneous frequency deviations. The distribution of the differences of these deviations limits the useful integration times when cross-correlating the signals. It was determined that, when properly normalized, this distribution was independent of frequency and range. Analysis of a specifically designed ocean acoustic experiment in which phase variations and frequency deviation distributions were measured gave results which were statistically the same as given by the model.

The model calculations showed the maximum bandwidth due to dispersion to be $\Delta f \approx 2f\dot{R}\times10^{-5}$ where f is the frequency and $\dot{R}$ is the relative velocity between the source and receiver in m/s. For long-range surveillance using maximum values for f and $\dot{R}$, the bandwidth is of the order of 0.03 Hz. To estimate the effects of dispersion on coherent integration time, a function $E(C)$ representing the expected correlation of information carried by two spectrally separated signals of frequencies f_1 and f_2 was defined and, using the derived frequency deviation distribution, was calculated as a function of integration time T with f and $\dot{R}$ as parameters. The results are presented in Fig. 1, where the abscissa is the dimensionless parameter f_2T, f_2 is the frequency of the higher frequency signal and T the integration time. The curves are for different values of $\dot{R}$ in knots. (These results are independent of the frequency of the lower spectral line.) With $f_2 = 100$ Hz and $T = 100$ s ($f_2T = 10{,}000$) the expected value of the correlation ranges from .95 for $\dot{R} = 5$ knots to 0.55 for $\dot{R} = 30$ knots, clearly illustrating the degradation that results from dispersion. The operator of a system that must operate in the presence of noise and dispersion must weigh the consequences of increasing the integration time. In the presence of noise alone the operator may increase detection performance by increasing the integration time, but in the presence of dispersion this can actually reduce performance. There is therefore a maximum useful integration time beyond

which signal decorrelation outweighs the gain obtained by increasing the integration time.

The results of this research have applications to undersea surveillance, underwater communications, ASW, and associated systems that utilize the ocean as an acoustic transmission medium for signal intelligence purposes. We plan to extend the analysis and experiments to signals received at spatially separated receivers and to bottom-limited or shallow water situations.

[Sponsored by NAVELEX]

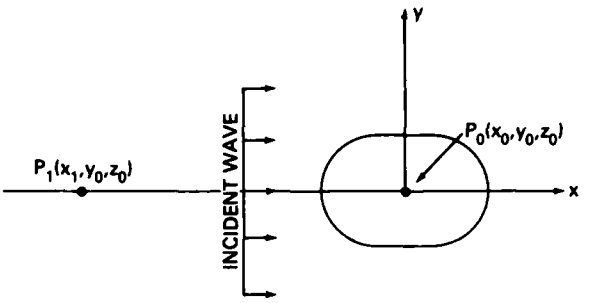

Fig. 2 — Geometry of the experiment. The source/receiver is placed at P_1 and the target is rotated about the y-axis which passes through the center of the body, P_0.

Acoustic Identification of Underwater Targets, by S.K. Numrich, N.H. Dale, and L.R. Dragonette *Acoustics Division,*

All submerged targets exhibit elastic behavior when interrogated by sound waves. Significant advances have been made recently in understanding the mechanisms involved in the elastic response of solid bodies and shells [1,2]. We are working to exploit this elastic response so that we may determine not only the presence of a submerged body, but its size and shape as well. Theoretical analysis of the targets of interest is either nonexistent or intractable over a broad range of frequencies and so much of the research is based on empirical observations.

Among the targets studied in NRL's small-scale modeling facility is a cylindrical brass shell with hemispherical end-caps. The shell is submerged and rotated as shown in Fig. 2. The sound source also functions as a receiver, measuring the sound backscattered by the shell. The received echoes are examined in the time and frequency domains. Figure 3 is a composite of typical time series and frequency analyses obtained in these experiments. In this case the echo was obtained with the shell rotated 67° away from the end-on position. The sound incident on the target was a short, relatively broadband pulse with measurable levels from 0.6 to 1.2 MHz. Most analyses performed in the frequency domain are expressed in terms of the nondimensional wavenumber, ka, where a is the significant dimension of the target body and k is 2π divided by the wavelength of the incident sound. Each of Figs. 3a, b, and c reveals pertinent information about the particular elastic waves generated on the target body which, when combined, begin to define the nature of the target itself.

In any given frequency region, the sound incident on the shell can generate both flexural and compressional waves in the shell's wall. The vibrational mode generated in each case depends on the material of which the shell is made, the thickness of the shell and the frequency of the incident sound. These vibrations can be visualized as a bending of the shell's surface in the case of flexural waves, or a squeezing and release of the surface for compressional waves. Once generated, these waves propagate around the shell, radiating sound into the water as they trace a path around its circumference. Each mode of vibration of the shell is associated with its own characteristic propagation speed. If the modes that have been excited can be identified, then the echo can be examined for time separations between returns that provide clues for determining the size and shape of the target body.

The time history of the echo contains the sound reflected by the surface of the body followed by the elastic returns. The record in Fig. 3a shows evidence of a significant elastic return in the shaded area. This individual return is isolated and examined in the frequency domain. Figure 3b shows a comparison of the frequency spectrum of the elastic return with that of the incident sound pulse. The narrower range of frequencies is typical for these modes, which are generated over limited frequencies for a shell of a given thickness. The entire time record is also examined in the frequency domain. Figure 3c shows this result after it has been normalized with respect to the incident sound spectrum. The peaks and valleys which occur at regular intervals are indicative of the presence of two returns interfering constructively or destructively. When the separation between the two returns is an integral number of

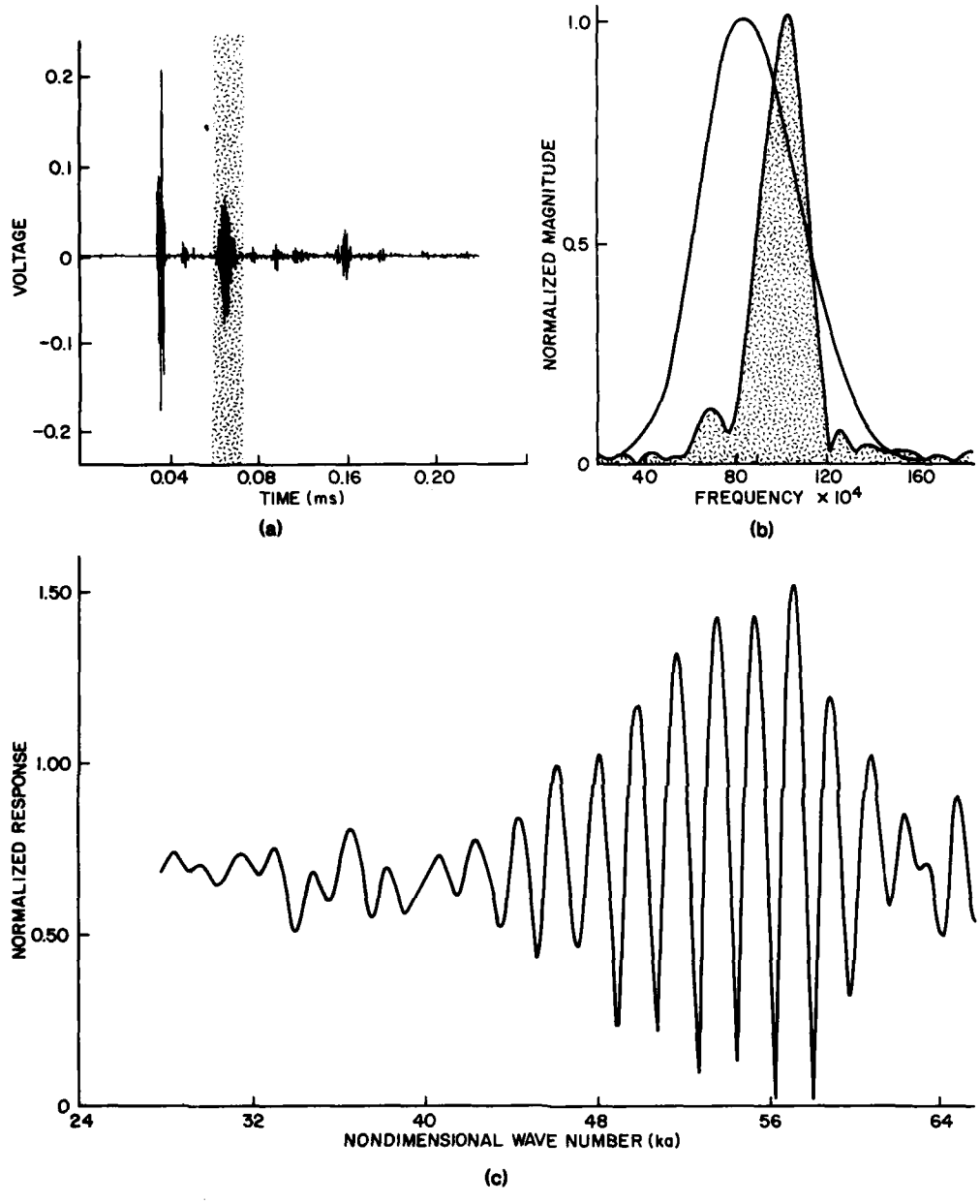

Fig. 3 — Composite of the records used in the analysis. (a) The time record showing the elastic return in the shaded area; (b) the frequency content of the elastic return (shaded) superimposed on the spectrum of the input signal; (c) the normalized spectrum of the entire time record plotted against *ka*.

path lengths, they add in phase (constructively) forming peaks; when they are exactly out of phase they tend to cancel. The separation between successive peaks determines the speed of the elastic waves through use of the relation

$$\Delta ka = c_e/c,$$

where c_e is the phase velocity of the elastic wave and c is the speed of sound in water. Now that the speed has been found, the separation in time between the first echo from the shell's surface and the elastic return can be used to find the distance that the sound has travelled. Since the path of the sound is known to trace the circumference

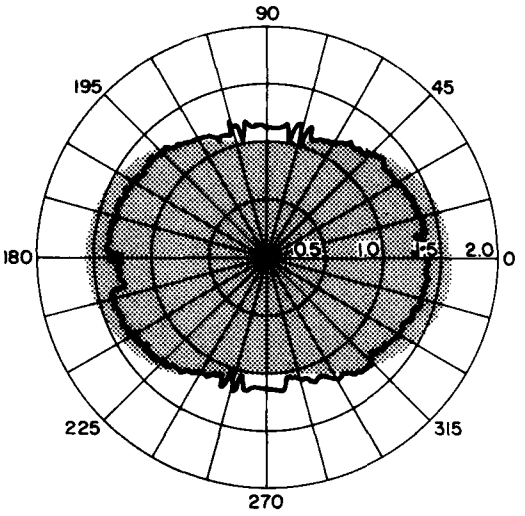

Fig. 4 — Comparison of the actual target shape (shaded) and the shape determined by analyzing the elastic waves.

of the shell, the size of the shell can be computed.

One of the questions addressed was whether these elastic waves are generated at sufficient strengths to be used at all angles to determine the shape of the target. In Fig. 4, the shape of the cylinder is shown as a shaded area. The bold line is the reconstruction of the target obtained from the method outlined above. The worst results occur at the ends where the error is about 6%. A systematic correction in normalization should readily improve this figure.

Since there is no complete theoretical model for this research, additional work is needed to generalize these results to targets of various dimensions, with discontinuities and internal structure. Preliminary efforts to detect buried targets and objects located in the proximity of other reflectors have been successful.

[Sponsored by ONR]

REFERENCES

1. S.K. Numrich, L. R. Dragonette, and L. Flax, "Classification of Submerged Targets by Acoustic Means," *Elastic Wave Scattering and Propagation*, V.K. Varadan, and V.V. Varadan, ed., Ann Arbor Science, 1982, Ch. 9 pp. 149-175.
2. L. R. Dragonette, "Schlieren Visualization of Radiation Caused by Illumination of Plates with Short Acoustical Pulses," J. Acoust. Soc. Am. 51, 920-935 (1972).

Submarine Acoustic Scattering and Radiation, by H. Huang, *Marine Technology Division*

The analytical prediction of acoustic signals from a submerged elastic structure responding to either an externally impinging acoustic wave or internally generated noise is a complex problem. It requires the simultaneous solution of the submarine dynamic structural response and the acoustic scattering and radiation problems in order to account properly for the interactions of the structure, the fluid medium, and the incident pulse or internal noise-generating mechanism. The exact formulation of this problem for a boundary of arbitrary shape often uses either the Helmholtz integral or the simple source integral representation of the solution to the wave equation for the surrounding fluid medium [1]. For numerical computation, either of the above integral equations together with the equation of motion of the elastic structure are transformed into a discrete system of matrix algebraic equations. The pressure and acceleration distributions on the interface between structure and fluid then have to be obtained prior to the calculation of the far-field quantities. The far-field calculation is comparatively straightforward; the bulk of the computation is to obtain the surface distributions. The matrices occuring in the acoustic equation must be recomputed for each desired frequency, leading to high computational costs whenever these matrices are large and the response at a number of frequencies is required. Moreover, depending on the computation strategy used, numerical instability can arise as a result of the so-called internal resonance of the integral representation.

We have developed an alternative analysis scheme which avoids these shortcomings. Our scheme determines the pressure and acceleration distributions on the fluid-structure interface using an adaptation of available theories to approximate the fluid-structure interaction, and then calculates the far-field acoustic signatures by integrating the Helmholtz integral exactly. This approach could save up to 75% of the computation cost for frequencies after the first one, particularly in cases where the acoustic, rather than the structural configuration dominates the size of the problem. In addition, the likelihood of incurring numerical instability is avoided.

The accuracy of this new approach is demonstrated here by comparing computed solutions with exact solutions for the classical case of

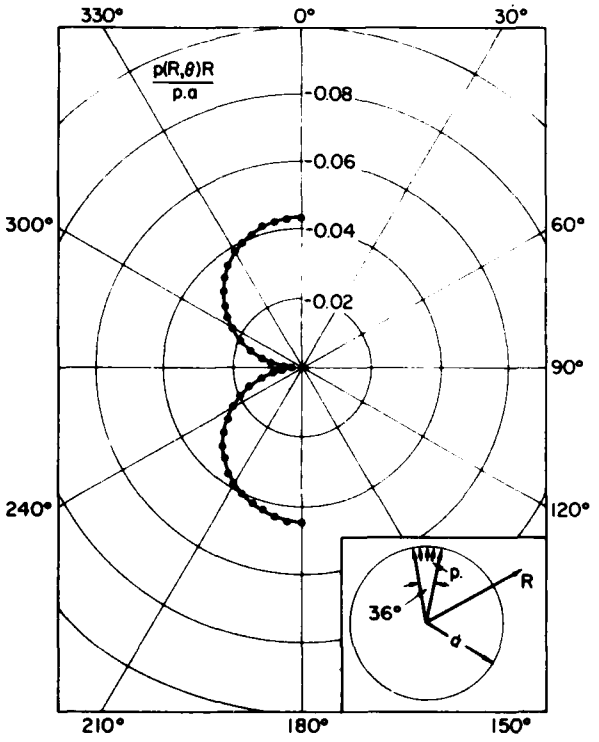

Fig. 5 — Low-frequency pattern of the far-field radiated pressure amplitude from a submerged steel shell with a thickness equal to 3% of the radius. The internal distributed excitation pressure subtends a polar angle of 36°. The wavelength of the sound is twice the circumference of the sphere——Exact solution. ●●● Computed solution. Far-field pressure is calculated from the surface pressure and the acceleration is obtained by the added mass approximation.

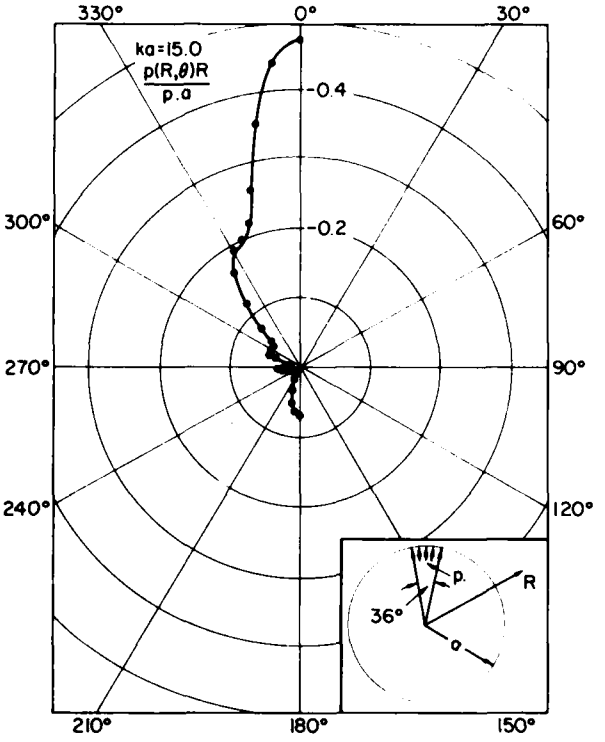

Fig. 6 — High-frequency pattern of the far-field radiated pressure amplitude from the same submerged shell as in Fig. 5——Exact solution. ●●● Computed solution. Far-field pressure is calculated from the surface pressure and the acceleration is obtained by the radiation damping approximation.

scattering and radiation from a submerged spherical elastic shell. Figure 5 shows the angular pattern of far-field radiation pressure from a submerged steel shell excited by internally applied distributed pressure at low frequency. Figure 6 shows similar results at high frequency. The figures confirm that the fluid-structure interaction can be approximated by added fluid mass at low frequency and radiation damping at high frequency, and that these simple approximations yield the correct far-field pressure. In the intermediate frequency range, we have adapted a theory known as the second order doubly asymptotic approximation (DAA2) [2]. Figure 7 demonstrates that DAA2 correctly predicts the echo signal over a range of frequencies from a submerged aluminum spherical shell impinged upon by a plane sound pulse.

The results of this research could lead to a stable and far less costly numerical method for predicting scattered or radiated signals from complex submerged structures.

[Sponsored by ONR and DTNSRDC]

REFERENCES

1. L.H. Chen, "Acoustic Emission from Submerged Structures," Chapter 9 from *Development In Boundary Element Methods—2*, P.K. Banerjee and R.P. Shaw eds., Applied Science Publishers Ltd., Essex, England, 1982, Ch. 9.
2. T.L. Geers, "Doubly Asymptotic Approximations for Transient Motions of Submerged Structures," *J. Acoustical Society of America*, **64**, 1626 (1978).

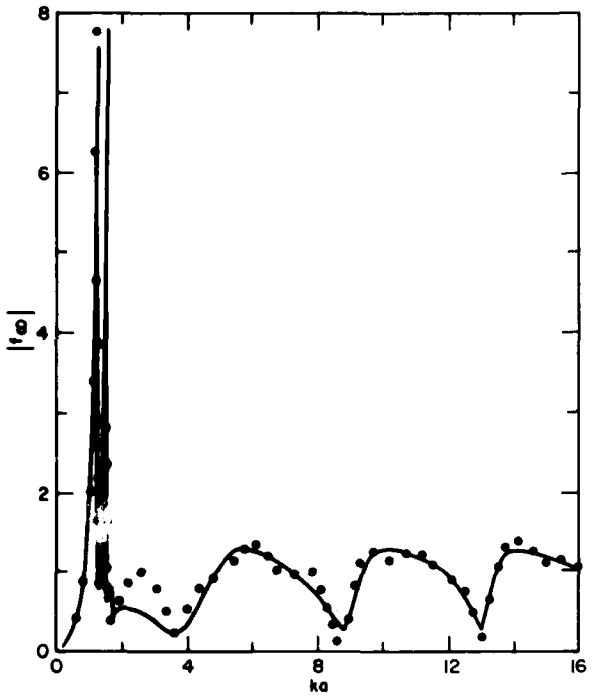

Fig. 7 — Echo signal returned by a submerged spherical aluminum shell with a thickness to radius ratio of 25:98.75. ——Exact solution. ●●● Computed solution. The echo is calculated from surface pressure and acceleration obtained by the second order doubly asymptotic approximation.

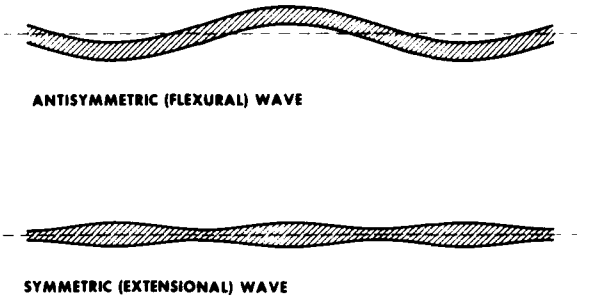

Fig. 8 — Antisymmetric and symmetric Lamb waves of zero order on an infinite elastic plate with free surfaces

Sound Radiation Caused by Extensional Waves, by A.J. Rudgers and P.S. Dubbelday, *Underwater Sound Reference Detachment*

When a time-varying force causes an elastic plate with free surfaces to vibrate, the many elastic waves propagating in the plate may be classified by linear elastic theory into two families of freely propagating modes called antisymmetric and symmetric Lamb waves. Figure 8 illustrates the simplest member, the zeroth-order wave, in each of the two families, with the wave amplitudes shown much exaggerated. While elasticity theory allows an infinity of orders of waves of each type to exist in a vibrating plate, in many practical problems only the zeroth-order and first-order waves are important.

When the plate is submerged in a fluid so that its surfaces are no longer free, a fluid-surface interaction takes place. If linear elasticity theory is applied to practical problems dealing with acoustic reflection or radiation by an elastic structure in a fluid, one is usually required to solve a three-dimensional elasticity problem which is generally a difficult task. Approximate structural theories have been developed to make the analysis mathematically tractable. These reduce three-dimensional problems to equivalent two-dimensional problems.

The Timoshenko-Mindlin (T-M) theory is an effective and widely used approximate structural model for analyzing flexural vibrations of thick elastic plates. These vibrations can be described in terms of the zeroth-order and first-order antisymmetric Lamb waves predicted by the exact linear theory of elasticity. In particular, the T-M theory has been used to predict the sound fields reflected or radiated by a plate when it is immersed in a fluid, and excited into vibration either by an impinging acoustic wave or by an applied force. The vibrations described by Lamb waves of the *symmetric* type have usually been ignored by structural theories, since these waves were thought to have only a negligible effect on the sound field either radiated or reflected by a vibrating plate.

We have recently developed a new approximate theory describing extensional vibrations of a thick plate. These are vibrations that are described in terms of the zeroth-order and first-order *symmetric* Lamb waves. This theory of extensional waves is the counterpart of the T-M theory of flexural waves and deals with symmetric Lamb waves to the same degree of approximation as the T-M theory treats the antisymmetric Lamb waves. The new theory and the T-M theory have been used together to calculate the sound radiated by metal plates of infinite extent with water on one side when they are excited by a harmonically-varying point force. The calculations of the sound field in the water thus include the effects of both flexural and extensional waves in the plate. One result of the calculations is to

show that sound radiation by extensional waves is *not* a negligible effect, but makes a significant contribution to the acoustic field generated by a plate vibrating in water.

This is demonstrated by analyzing the forced vibration problem illustrated in Fig. 9. A harmonic force is applied at a single point on the lower surface of a metal plate of infinite extent. There is water above the plate and vacuum below it. The point force causes elastic waves to propagate in the plate away from the origin, and these waves radiate sound into the water. We then calculate the radiated sound pressure that would be observed at various angular positions in the far field, that is, at a great many acoustic wavelengths from the driving point.

Figure 10 shows the calculated sound field radiated by a 5-cm-thick aluminum plate when the frequency of the exciting force is 24 kHz. The field is calculated using two different methods. First, the conventional T-M theory, which describes radiation caused only by flexural waves, is used and the dashed curve shows the result. The maximum in this curve near the observation angle of 38° is the lowest flexural coincidence maximum. This occurs at the angle for which the speed of the flexural waves propagating in the plate coincides with the trace speed along the plate of an acoustic wave in the water which radiates in that particular direction. For flexural waves there is a minimum, or critical, frequency below which this coincidence cannot occur. In this example the critical frequency is about 5240 Hz.

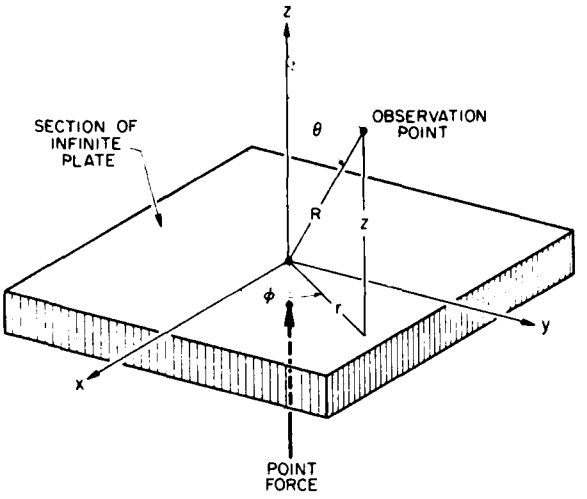

Fig. 9 — Geometry used when calculating the sound field radiated by an infinite fluid-loaded elastic plate excited by a harmonically varying point force.

The solid curve in Fig. 10 is calculated using the newly developed theory and accounts for extensional-wave effects as well as for the effects of flexural waves. A pronounced beam of acoustic radiation arising from an extensional-wave coincidence occurs at an observation angle of

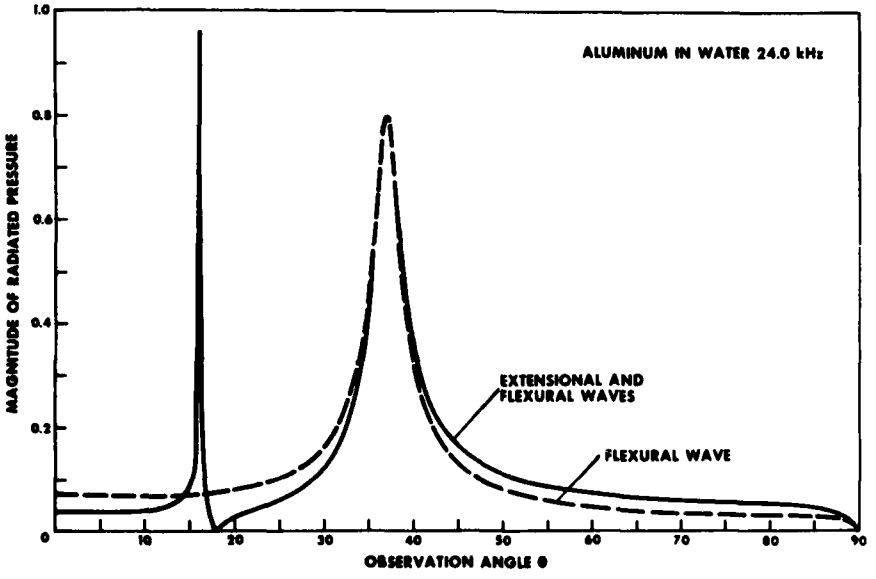

Fig. 10 — Normalized pressure field observed far from a 5-cm-thick, point-driven, aluminum plate radiating into water. The exciting frequency is 24 kHz.

about 16°. This beam, which is not predicted by the conventional theory, is more sharply defined than the beam of radiation caused by flexural waves.

The sharp sound beam caused by the extensional-wave coincidence is present even if the frequency of excitation is much lower than the flexural-wave critical frequency. This is illustrated in Fig. 11, which shows the sound radiated by a 5-cm-thick steel plate at 2 kHz. The new theory predicts a sharply defined radiated beam near 15°, caused by extensional-wave coincidence. This effect is absent if the calculation is made using conventional theory, which considers only flexural waves.

[Sponsored by ONR]

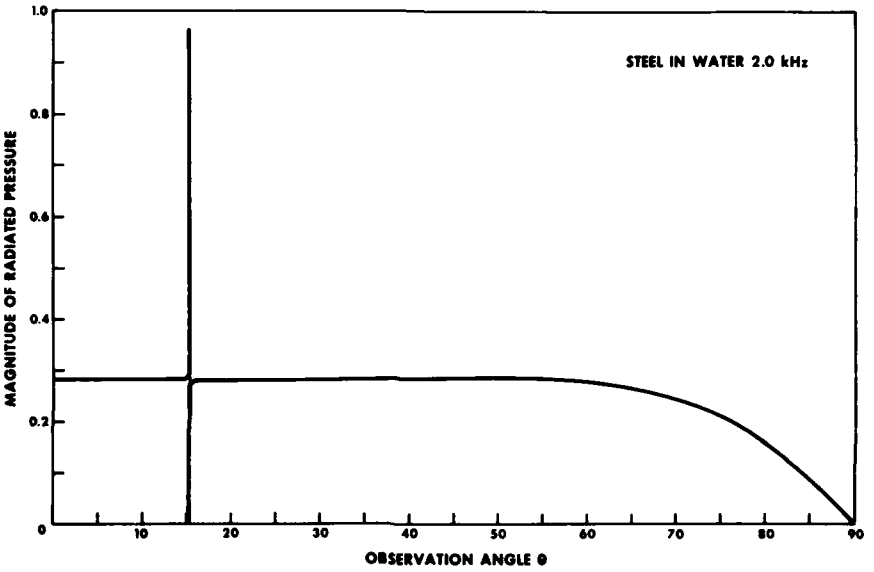

Fig. 11 — Normalized pressure field observed far from a 5-cm-thick, point-driven, steel plate radiating into water. The exciting frequency is 2.0 kHz.

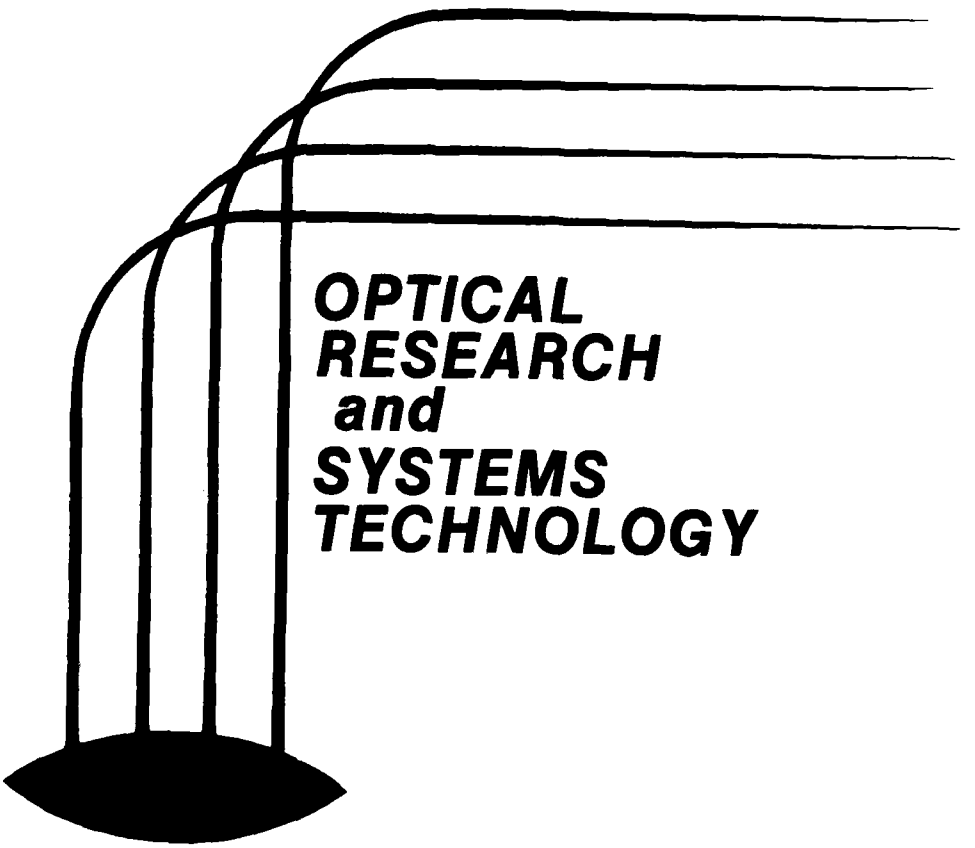

OPTICAL RESEARCH and SYSTEMS TECHNOLOGY

OPTICAL RESEARCH AND SYSTEMS TECHNOLOGY

Lasers have found widespread use in many branches of science and technology. The following articles illustrate how NRL is involved in a variety of laser applications.

Uniform Illumination by Induced Spatial Incoherence, by R.H. Lehmberg and S.P. Obenschain, *Plasma Physics Division*

Experiments on the interaction of laser beams with solid targets may be complicated by the nonuniformity of the intensity within the laser's focal spot. A specific application, high-gain laser fusion, requires a high degree of uniformity in the laser irradiance in order to produce a uniform ablation pressure at the pellet surface. Even allowing for lateral smoothing in the ablating plasma, illumination uniform to within ±10% is likely to be required, and with short wavelength lasers, where lateral smoothing is minimal, uniformity to within ±1% may be necessary.

Previous efforts to achieve uniform illumination have been frustrated by the imperfections in high-power laser systems. The cumulative effect of the small phase aberrations (both linear and nonlinear) introduced by each optical element of a multistage laser is to produce large random nonuniformities in the intensity of the output. These nonuniformities can only be partially controlled, at great expense, by using ultra-high quality optics and extensive beam relaying. To obtain the desired intensity and focal diameter with a lens of reasonable focal length, it is usual to place the target in the near field of the lens, rather than at the best focus, in which case nonuniformities in the laser output tend to be mapped onto the target. Although random nonuniformities may in principle be statistically smoothed by overlapping many independent beams at the target, in practice this may require a prohibitively large number of beam lines.

We have developed a simple technique which enables a high degree of illumination uniformity to be obtained with modest quality laser beams [1]. This technique induces a controlled amount of transverse spatial incoherence in the output beam of a broadband laser (bandwidth $\Delta\nu$) whose coherence time $t_c = 1/\Delta\nu$ is short compared with the pulsewidth t_p. The spatial incoherence is achieved by introducing different optical delays in different transverse sections of the beam, and choosing the increments between delays to be larger than t_c (Fig. 1). A wide aperture beam is thus broken up into a large number of independent beamlets. At the focus of a lens, these overlap to produce a complicated interference pattern modulated by a smooth envelope which characterizes the diffraction of an individual beamlet. For times long compared with t_c, the interference pattern averages out leaving only the smooth and reproducible diffraction profile. The target surface will effectively ignore the rapidly shifting interference pattern if its hydrodynamic response time t_h is very much greater than t_c. For example, for 1 μm light with 0.2% bandwidth $t_c \simeq 1.5$ ps, whereas t_h is usually at least 100 ps. The diffraction profile is not very sensitive to nonuniformities in the amplitude and phase of the incident beam; in fact, the beam need only be approximately uniform over the small width of each beamlet. We estimate that laser bandwidths as small as 0.2% would be adequate to implement this scheme for laser fusion.

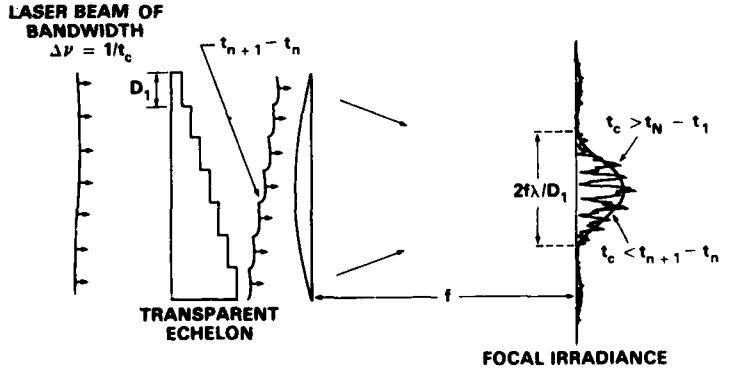

EXAMPLE: $\lambda = 1\mu m$, $D_1 = 5$ mm, $f = 5$ m $\Rightarrow$ 2 mm FOCAL SPOT

Fig. 1 — Use of spatial incoherence induced by a transparent echelon to smooth the focal spot irradiance of a broadband laser

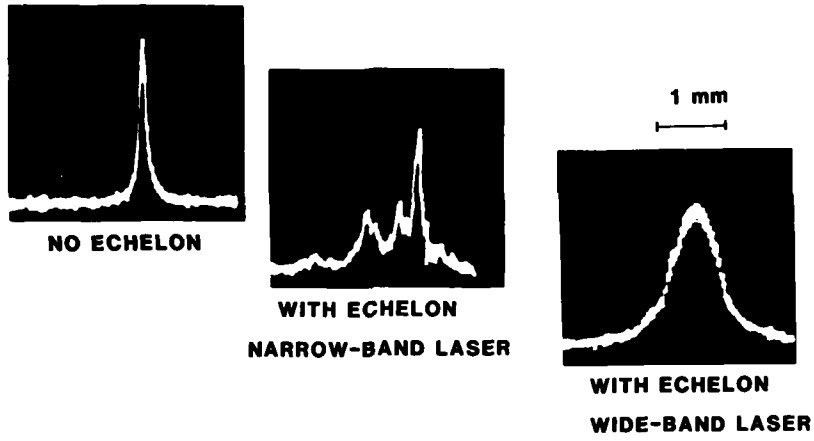

Fig. 2 — Vidicon laser profiles showing the broadened, smooth profile with the finite-bandwidth-laser/echelon combination

The concept illustrated in Fig. 1 can be extended to two transverse dimensions, for example by using using two perpendicular echelons, or by using a structure in which the steps consist of squares, closely packed hexagons, or concentric circles. If two perpendicular echelons are used, the incremental time delay introduced by each step on the second echelon should be as large as the total incremental delay across the first.

For laser fusion, one needs uniform illumination of a spherical surface. Earlier studies have shown that if the incident laser profiles are smooth, this can be achieved by overlapping a relatively small number (≥ 20) of beams. Before the new technique was available it was hard to achieve the necessary smooth and reproducible focal profile in each beam.

The principle of beam smoothing by induced incoherence has been demonstrated using an adjustable bandwidth glass oscillator and a transparent echelon-lens combination similar to the one shown in Fig. 1. The echelon, which consists of overlapped 1 mm thick glass slides cemented together to minimize losses, breaks the beam into $\sim$1 mm wide beamlets. The delay between adjacent beamlets is 1.7 ps. The beamlets then pass through a slit perpendicular to the echelon steps to achieve a one-dimensional geometry, and are focused onto a Vidicon camera by a 1 m focal length lens. The Vidicon measures the focal profile averaged over the laser pulsewidth. Figure 2 shows far-field profiles of the laser beam with and without the echelon. With sufficient bandwidth (0.2% in this case) the interference patterns produced by the echelon are smoothed out, and the residual profile was indeed found to be insensitive to aberrations in the incident beam.

In future work, we plan to implement the incoherence smoothing technique in the NRL Pharos laser system, and use it in target ablation studies. It should also be applicable to other processes, such as shock wave generation, which also require illumination by a concentrated laser beam.

[Sponsored by ONR and DOE]

REFERENCE

1. R.H. Lehmberg and S.P. Obenschain, "Use of Induced Spatial Incoherence for Uniform Illumination of Laser Fusion Targets," NRL Memo Report 5029, April 1983.

Focal Shift in Laser Beams, by W.H. Carter, *Space Systems Division*

It has been known for some time that focusing of laser beams passing through lenses cannot always be described using the well-known lensmaker's formula:

$$\frac{1}{d_1} + \frac{1}{d_2} = \frac{1}{f}, \qquad (1)$$

where d_1 is the distance from a planar object to an image-forming lens, d_2 is the distance from the lens to the image plane, and f the focal length of the lens, as illustrated in Fig. 3a. If we use this formula to predict the distance d_2' from a

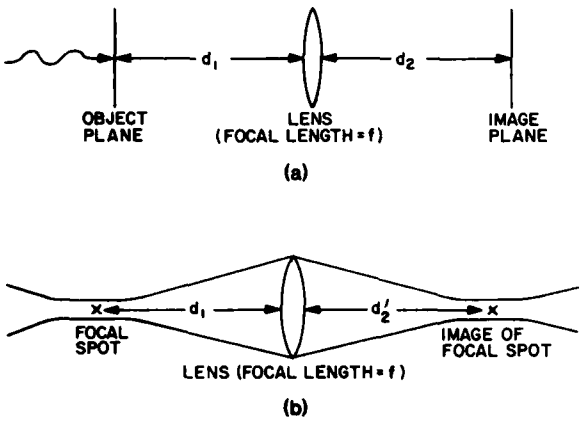

Fig. 3 — (a) Elementary imaging system, (b) focused laser beam

lens to the image of the focal spot for a simple Gaussian laser beam, we find that in general d_2' can be much smaller than d_2 as given by Eq. (1) (Fig. 3b). The difference $\delta = d_2 - d_2'$ is known as the *focal shift* and obviously has important consequences for the design of optical systems.

Any coherent, spherical, monochromatic wavefront emerging from a lens aperture and converging to focus can be characterized by the *Fresnel number* $N = a^2/\lambda R$, *where* a *is the* radius of the lens aperture, R is the radius of curvature over the wavefront at the aperture, and λ is the wavelength of the light. Wolf has recently found [1] that if $N >> 1$ then $d_2' = d_2$ so that Eq. (1) correctly gives the position of the image of the focal spot. However, if N is the order of 1 or smaller, then $d_2 > d_2'$ so that the image will always occur much closer to the lens.

In 1982, work at NRL has proved that, at least for a Gaussian beam, Wolf's condition on the Fresnel number is equivalent to a far-field condition [2]. To obtain this result it was necessary to define an effective Fresnel number N' over a plane perpendicular to the axis of an unapertured Gaussian beam by replacing the aperture radius a by the 1/e radius of the beam. Then using paraxial theory, it was shown that N' is equal to $(2\pi)^{-1}$ times the number of near-field lengths in the distance between the plane in which the effective Fresnel number is calculated and the focal plane. Thus, if is $N' < (2\pi)^{-1}$, the plane is in the near field of the focus and if $N' >> (2\pi)^{-1}$, the plane is in the far field of the focus. In the first case there will be a focal shift and in the second case there will not.

This work throws light on the underlying cause of the focal shift. It is well-known from paraxial theory that the spherical wavefronts within a beam have a common center of curvature at the focal point only in the far field of the focal point. In the near field the spherical wavefronts are centered on points further away, because as one approaches the focus the wavefronts flatten out to become plane in the focal plane. Geometric optics is an asymptotic approximation to wave optics in that it only describes light propagation in the far field of the focal caustic and always assumes spherical wavefronts with a common center of curvature at the focus. Thus, if $N' < (2\pi)^{-1}$, our results show that the plane is in the near field, and from paraxial wave theory we see that the wavefront curvature will be centered on a point beyond the focal point: an apparent shift from the geometric focal point.

In addition to this basic discovery, we have devised methods to assist with the design of optical systems that use focused laser beams, such as laser communication or laser weapons systems. In particular, the concept of a geometrical Fresnel number was introduced in which the radius of curvature of the wavefront is replaced by the true distance to focus. Simple expressions were found which show how the focal shift, wave front radius of curvature at the lens, beam radius at the lens, and focal region depend on the effective Fresnel number.

Finally we considered as an example the design of a laser communication system with given wavelength, receiver range, and beam radius at the transmitter. It was found that in general two solutions are usually possible. One solution places the lens in the far field of the receiver, while the other places it in the near field. Some characteristics of these two solutions were described and compared. The formulas we have derived are applicable rather generally to laser systems design where focusing a Gaussian beam in a specified plane is required.

[Sponsored by ONR]

REFERENCES

1. E. Wolf and Y. Li, "Conditions for the Validity of the Debye Integral Representation of Focussed Fields," *Opt. Commun.* **39**, 205 (1981).

2. W.H. Carter, "Focal Shift and Concept of Effective Fresnel Number for a Gaussian Laser Beam," *Appl. Opt.* **21**, 1989 (1982).

Optical Probing of Fast Chemical Reactions, by B.B. Craig, W.L. Faust, L.S. Goldberg and P.E. Schoen, *Optical Sciences Division*

Fast chemical reactions are often characterized by a very small energy of activation and a large energy release. They are usually initiated when the material is subjected to a sudden change of temperature, a mechanical shock, or short pulses of light or electrons. The molecules absorb energy from this stimulus and produce electronically and vibrationally excited species, free radicals and ions. These products are highly reactive and rapidly dissipate their energy through intramolecular and intermolecular mechanisms.

We have been using ultrafast optical techniques to study the formation and kinetics of the energetic fragments formed when energetic materials are hit by a very short ultraviolet laser pulse. Our first studies have involved simple compounds which may be used as generic models for processes of importance in fuels, explosives, and propellants. Our goal is to understand the reaction mechanisms that are responsible for energy release at the molecular level. This is a departure from the more traditional macroscopic approach to energetic materials research. Ultimately, we hope to be able to provide the Navy with important information on the efficiency and sensitivity of existing fuels, propellants, and explosives and provide a scientific basis for the design and synthesis of improved energetic materials.

Our unique capabilities allow us to deposit energy almost instantaneously into a selected molecular system using picosecond laser pulses, and to examine the initial fragmentation products with ultrafast time-resolved spectroscopy. Our excitation sources are neodymium-doped yttrium aluminium garnet (YAG) and phosphate glass modelocked lasers giving pulses of 1064 nm, 30 ps and 1054 nm, 5 ps respectively. By frequency doubling and redoubling we produce ultraviolet photolyzing pulses of 10 mJ energy. The high intensity of these short-pulse lasers allows excitation of the parent molecules by single photon and multiphoton processes. Those reaction products that emit light are identified spectrally and their history followed with either a crossed-field photomultiplier coupled to a digital oscilloscope with a net risetime of 0.6 ns, or a streak camera with a time resolution of a few picoseconds. Fragments in the ground state or otherwise nonemissive are studied by means of their absorption or fluorescence spectra, using a pulsed laser probe beam. By varying the time interval between the photolyzing pulse and the probe pulse, we are able to follow the evolution and decay of the transient species. During the past year, we have obtained important information on a variety of ground-state and emissive fragments (CN, C_2, NH, CH, NO_2) which were generated from several parent molecules in the gas phase. Such fragments are expected to be intermediates in the decomposition of common secondary explosives such as RDX and HMX.

Nonlinear excitation of acetylene (C_2H_2) by 266 nm pulses gives the C_2 diradical as the dominant emissive fragment [1]. Our results have shown conclusively that the lowest order process yielding emissive C_2 is unimolecular and occurs in less than 1 ns. Figure 4 illustrates that the C_2 Swan emission appears in about 200 ps. The unimolecular nature of the process has been confirmed by an isotopic labelling technique. Mixtures of $^{12}C_2H_2$ and $^{13}C_2H_2$ were irradiated, but no emission from the collisionally produced fragment ($^{12}C^{13}C$) was observed at times less than 1 ns. After several nanoseconds intermolecular $^{12}C^{13}C$ was detected, probably formed by collisions between excited CH fragments.

In contrast to acetylene, acetonitrile (CH_3CN) yields no prompt components of diatomic emission under similar multiphoton excitation conditions [2]. In this case all emissive populations (CN, C_2, NH and CH) are delayed,

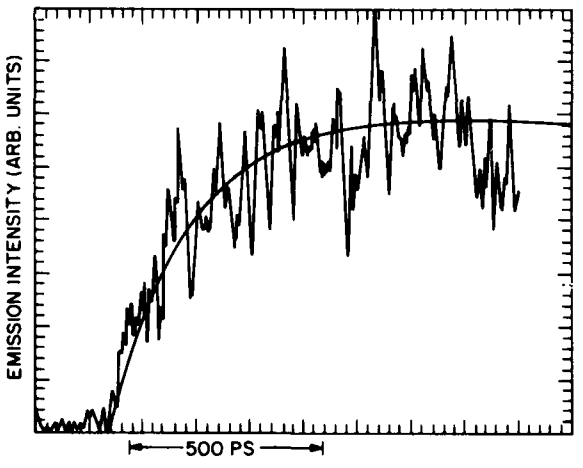

Fig. 4 — Streak camera record of the rise of C_2 Swan emission from acetylene (C_2H_2) at 5 Torr pressure following excitation at 266 nm. The model curve with a time constant of 215 ps represents the best fit to the data.

probably on account of the formation of quasi-stable intermediates of high electronic energy which may be *superexcited* species, whose total energy exceeds the ionization limits. Using isotopically labelled acetonitrile, we have identified two unimolecular processes yielding the dominant emissive species (CN $B^2\Sigma^+$), one in which the CN bond is preserved, consistent with C-C cleavage, and another in which the methyl carbon is associated with the nitrogen atom, suggesting that rearrangement (isomerization) has taken place.

In a new experiment, low intensity pulses of 264 nm light have been used to dissociate nitromethane (CH_3NO_2) by a one-photon process [3]. A second 5 ps laser pulse (527 nm) was used to study the transient species by laser-induced fluorescence. The observation that NO_2 is produced almost instantaneously (within our time resolution of 5 ps) suggests that 264 nm light dissociates nitromethane directly into CH_3 and NO_2 radicals (Fig. 5).

We have made considerable progress in elucidating the identity and kinetics of fragments produced in laser-initiated gas-phase reactions. We shall go on to identify the physical and chemical parameters that control the course of such reactions. Future work will extend our techniques to study similar processes in condensed phases, and to include more complex energetic materials. The data obtained should help identify the role of intermediates and free radical products in the initiation processes of energetic materials, and ultimately lead to improvements in these materials.

[Sponsored by ONR]

REFERENCES

1. B.B. Craig, W.L. Faust, L.S. Goldberg, and R.G. Weiss, "UV Short-Pulse Fragmentation of Isotopically-labeled Acetylene: Studies of Emission in Sub-nanosecond Resolution," *J. Chem. Phys.* **76**, 5014 (1982).
2. B.B. Craig, W.L. Faust, and R.G. Weiss, "Delayed Fragmentation of Acetonitrile upon Short-pulse UV Irradiation: Evidence for Long-lived Superexicted Intermediates," *J. Chem. Phys.* in press.
3. P.E. Schoen, M.J. Marrone, J.M. Schnur, and L.S. Goldberg, "Picosecond UV Photolysis and Laser-induced Fluorescence Probing of Gas-Phase Nitromethane," *Chem. Phys. Lett.* **90**, 272 (1982).

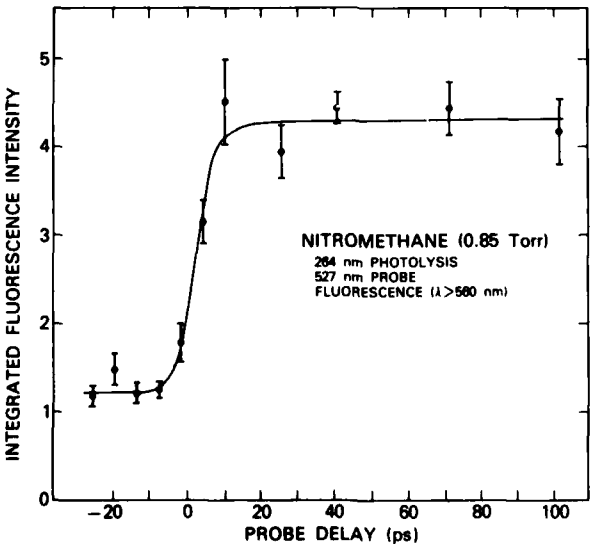

Fig. 5 — The laser-induced fluorescence signal from nitromethane (CH_3NO_2) as a function of delay time between the UV and probe laser pulses. The signal is attributed to NO_2.

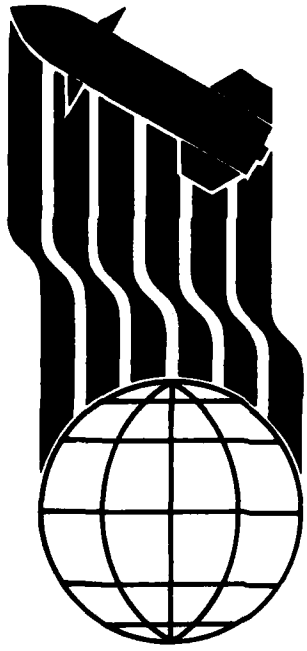

ATMOSPHERIC AND IONOSPHERIC RESEARCH AND APPLICATIONS TO MILITARY SYSTEMS

ATMOSPHERIC AND IONOSPHERIC RESEARCH AND APPLICATIONS TO MILITARY SYSTEMS

Atmospheric conditions at sea level affect Naval operations, while the state of the ionosphere affects communications. The articles in this section illustrate the range of NRL research in this very large region of the environment.

HF Communication Channel Response to a Wideband Probing Signal by L.S. Wagner and J.A. Goldstein, *Information Technology Division*

Interest in spread-spectrum techniques for communication in the HF band (2-30 MHz) has generated a need for better definition of HF channels for signals with instantaneous bandwidths as great as 1 MHz. The NRL Wideband HF Channel Prober program was established to meet this need. In 1982, measurements were made on a 126-km path over the ocean using the Sea-Echo HF radar facility on San Clemente Island as the transmitter and a receiver located at the Pacific Missile Test Center, Point Mugu, California.

Coded pseudonoise sequences are used to provide a wideband pulse sounding signal. Two modes are used: a narrowband (125 kHz) mode and a wideband (1 MHz) mode with effective pulse widths of 8 μs and 1μs respectively. The primary purpose of the narrow-band (*sounder*) mode is to define the condition of the ionosphere in a more or less conventional manner and to establish selected time windows for viewing the wide-band data. These windows are usually centered on particular skywave modes of interest. The windows are necessary to limit the data throughput in the wide-band (*prober*) mode to a rate which the system can handle in real time. The current set of windows allows a cumulative viewing interval of 900 μs out of a total reverberation time of 8 ms. A typical data collection sequence consists of a sounder mode run, followed by a prober mode run, followed by a second sounder mode run.

A comprehensive way of presenting the sounder mode (narrow-band) data is in terms of an ionogram, an example of which is shown in Fig. 1. The most prominent feature of this fall morning ionogram is the groundwave which is located at an arbitrary delay of 100 μs. Also shown are the E-layer, the one-hop-F2 and the two-hop-F2 skywave modes. The interaction between a linearly-polarized HF wave and the ionospheric plasma results in the propagation of 2 distinct elliptically-polarized waves of opposite polarizations—the so-called *ordinary* (O) and *extraordinary* (X) components. In Fig. 1, both components are clearly distinguishable in the one-hop F2 mode. The ionograms are mainly used for characterizing the state of the ionosphere at the time of the wide-band measurements.

A comprehensive way to examine the prober mode (wide-band) data is by means of a three-dimensional delay-power-time plot, as shown in Fig. 2. The data in Fig. 2 are for a single frequency of 6.5 MHz and cover a much more limited delay interval than Fig. 1. The delay interval brackets the skywave return for a winter morning for the one-hop-F2 layer. The O- and X-traces are clearly visible, with the X arriving later. The O-trace is dispersed while the X-trace is sharp for

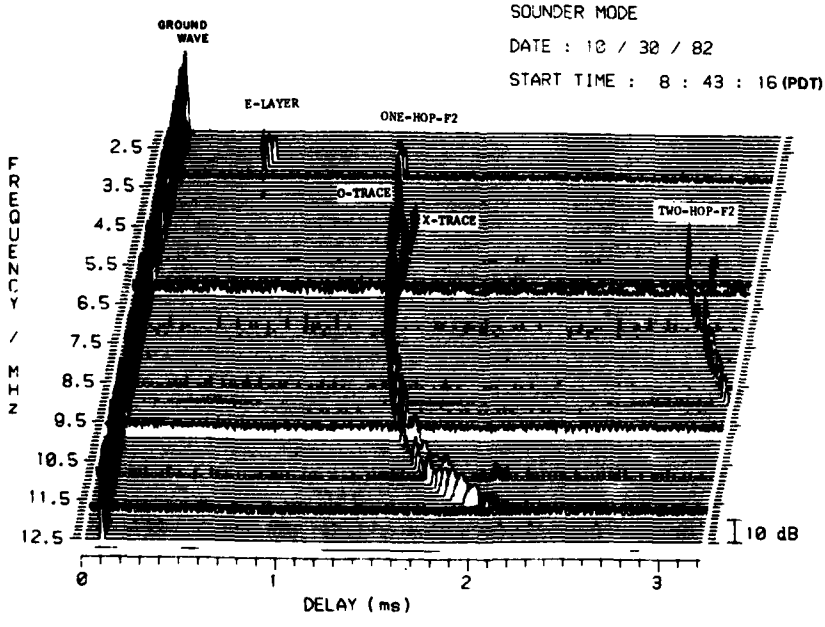

Fig. 1 — Morning ionogram; October 1982

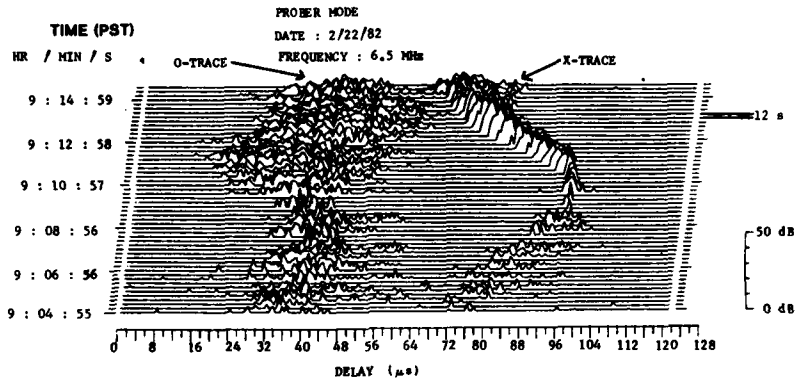

Fig. 2 — Wideband delay-power time history; one-hop-F2 at 6.5 MHz

most of the observation period. The O-trace exhibits a modulation of pulse spread as well as a barely perceptible delay variation. The X-trace shows an oscillation in delay of approximately 24 μs and a marked modulation of pulse spread. These observations suggest the presence of a traveling ionospheric disturbance or some other wavelike disturbance of the upper atmosphere which has the effect of distorting the normal contours of the ionosphere.

At times, the channel pulse-response is very complex. A high resolution snapshot of the wide-band data for a summer night is shown in Fig. 3 for 2.5 MHz. As in Fig. 2, the delay interval brackets the sk:wave return for the one-hop-F2 layer. The delays of the O- and X-traces overlap causing interference fading in the region of the overlap. The spread of the composite return is quite broad, ranging between 70 and 100 μs.

Evidence of nighttime sporadic-E during the spring of 1982 is shown in Fig. 4. The frequency is 3.5 MHz. The earlier return shows a pronounced scatter tail and a slight undulation in delay. The later return appears to be more complicated, possibly resulting from thin, closely spaced multiple layers or an extended patch of small irregularities. It is followed by an extended scatter-tail which is probably related to the irregular structure of the layers. The effective duration of the sporadic-E return ranges from 4 to 10 μs.

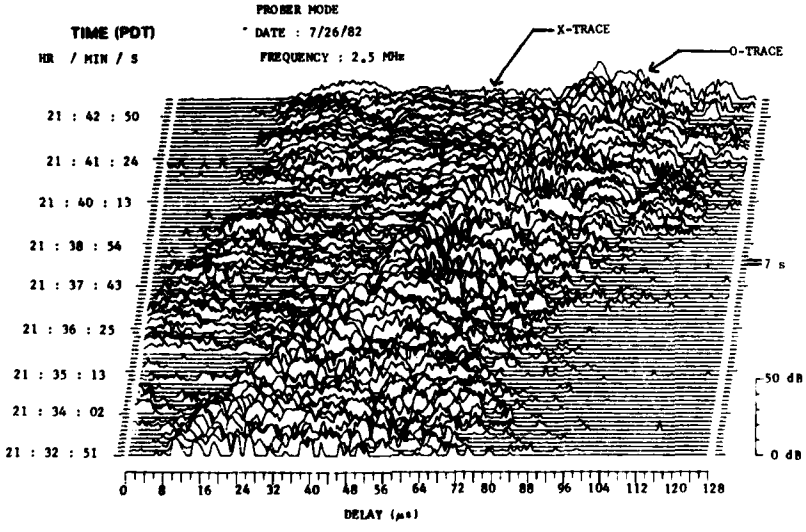

Fig. 3 — Wideband delay-power time history; one-hop-F2 at 2.5 MHz

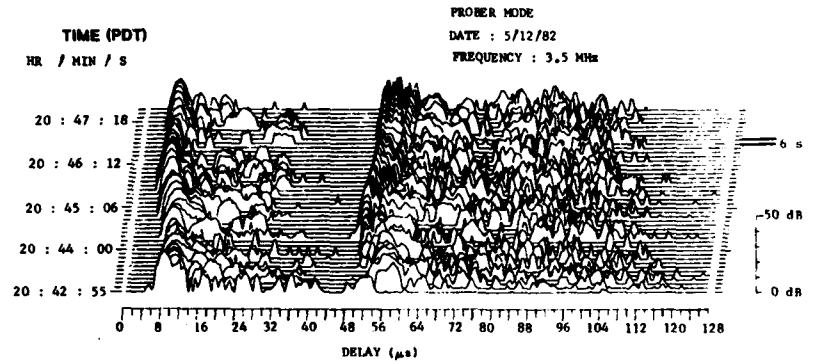

Fig. 4 — Wideband delay-power time history; sporadic-E at 3.5 MHz

The results shown here represent a small fraction of the available data, but they serve to illustrate the capabilities of the present equipment and to provide some idea of what one may expect in the way of sky-wave mode characteristics. Future plans for this program include additional measurements at longer propagation path lengths and careful analysis of the data in order to characterize the HF channel and to study the behavior of the ionosphere.

[Sponsored by ONR]

REFERENCE

1. L.S. Wagner, J.A. Goldstein, E.A. Chapman, "Wideband HF Channel Prober-System Description," NRL Report 8622, July 1982.

Phenomenology of Ionospheric Irregularities by E.P. Szuszczewicz, *Space Science Division*

We have been conducting a program of *in situ* measurements designed to map the Earth's geoplasma environment; to identify domains of highly irregular structure; to determine associated physical mechanisms; and to assess the potential effects on command, control, communications, and intelligence systems (C^3I). By making direct measurements of plasma density and energy distribution functions using instruments on rockets, satellites and the space shuttle we can obtain complete and unambiguous distributions of ionospheric irregularities covering a range of sizes from the planetary scale of thousands of kilometers to the smallest detectable features on the scale of meters. These measurements provide direct clues to active geoplasma processes, stimulate the development of computational models, and help to establish operational guidelines for systems affected by the ionosphere, such as VHF → EHF communications and synthetic-aperture-radars [1,2].

We have recently succeeded in obtaining complete spectral distributions of irregularities in the nighttime equatorial ionospheric regime, an unstable geoplasma condition called *equatorial spread-F*. Figure 5 gives the power spectrum characteristic of this condition. The features of this spectrum throw light on the various physical processes at work.

Equatorial spread-F is triggered in the density gradient on the underside of the F-layer by large-scale disturbances (on a scale of tens of kilometers) which have evolved either from

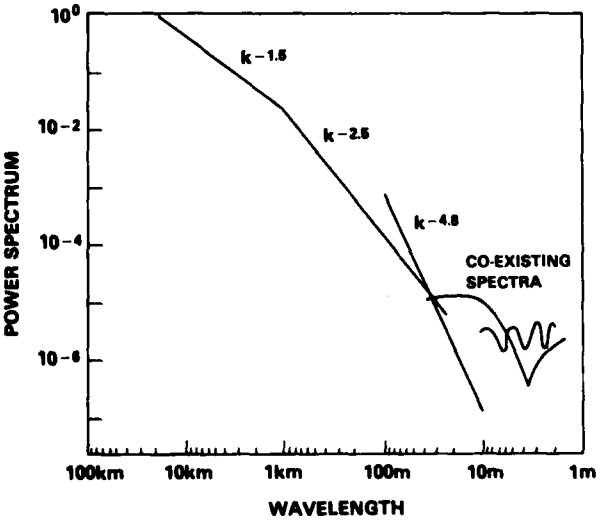

Fig. 5 — Spectral distribution of irregularities in the ionospheric electron density in the nighttime equatorial domain under conditions of spread-F.

planetary scale waves associated with solar activity or, more frequently, from meteorological phenomena in the Earth's atmosphere and ionosphere. A two-fluid process, interacting with the background density gradients, results in a turbulent cascade with a spectrum of medium-scale irregularities (from 2 → 20 km), proportional to $k^{-1.5}$, where k is the wavenumber. The medium-scale macrostructure on the underside of the F-layer can then become unstable to Rayleigh-Taylor instabilities; this fills the intermediate wavelength region with a $k^{-2.5}$ spectral distribution.

In the next wavelength domain ($\lambda \lesssim 200$ m) a steeper $k^{-4.7(\pm.3)}$ spectral distribution has been found, and has been identified with the universal drift instability driven by gradient scale lengths $L_n \lesssim 200$ m. This conclusion is supported by the experimentally observed coexistence of $L_n \leqslant 200$ m and $k^{-4.7(\pm.3)}$ domains. At still shorter wavelengths ($\lambda \lesssim 20$ m) the irregularities cannot be described by a single (or uniform) spectral distribution but are more characteristic of a resonance distribution. The short wavelength results are consistent with a lower-hybrid drift mode but point more strongly to a resonant mode-coupling process.

Our interest is now being focussed on the distribution of irregularities in the high-latitude ionosphere (Fig. 6) where diffuse aurora, discrete arcs, polar cap phenomena and cusp particle precipitation cause irregularities to exist almost all the time. We expect that the S3-4 satellite program, augmented by supporting theoretical and experimental efforts, will lead to an improved understanding of the extensive spectrum of high-latitude irregularities. When combined with the existing understanding of plasma processes at equatorial and mid-latitudes this should provide an ionospheric model covering the entire globe.

[Sponsored by ONR]

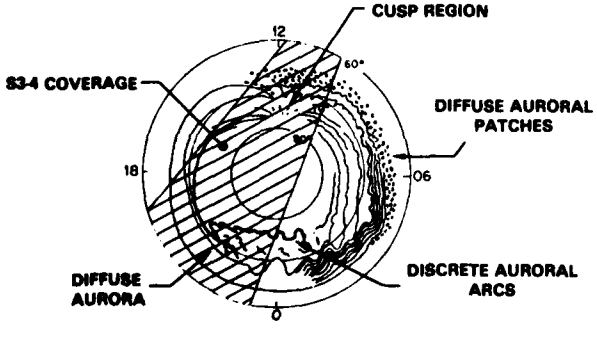

Fig. 6 — A phenomenological source-term map of high-latitude ionospheric irregularities showing regions covered by the S3-4 satellite. (Adapted from S. I. Akosofu, Space Science Rev. 19, 169 (1976)). The diagram shows major phenomenological elements in dipole-MLT coordinates.

REFERENCES

1. E.P. Szuszczewicz, J.C. Holmes and M. Singh, "The S3-4 Ionospheric Irregularities Satellite Experiment: Probe Detection of Multi-ion Component Pressures and Associated Effects on Instability Processes," *Astrophysics and Space Science* **86**, 235, (1982).

2. E.P. Szuszczewicz, M. Singh, P. Rodriguez, and S. Mango, "Ionospheric Irregularities and Their Potential Impact on Synthetic Aperture Radars," NRL Memorandum Report 4999 (1983); *Radio Science* (1983, in press).

Relative Humidity Measurements in Fog, by H. Gerber, *Environmental Sciences Divisions*

The phase transition in the atmosphere between water vapor and liquid water depends primarily on the value of the ambient relative humidity (RH). Even under dry conditions some vapor is condensed on hygroscopic particles in the atmosphere to form small droplets. This effect becomes more important as RH increases and can lead to dense hazes. When RH exceeds 100% (*supersaturation*), the haze droplets undergo explosive growth and evolve into the much larger droplets found in fogs and clouds.

We need to understand the formation of hazes and fogs, because of their adverse effect on naval operations. Progress in this area has been hampered by the inability of existing instruments to provide accurate measurements of high values of RH. Errors become excessive above RH ~95%, and no direct measurements have been made in supersaturated conditions. The strongest optical effects in the atmosphere arising from the vapor-liquid phase transition are found in the range of RH values centered about RH = 100%.

The strong dependence of haze-droplet size on RH forms the basis of a novel technique which we have developed for precisely measuring RH in this most important range. A cross section of the new instrument, a saturation hygrometer, is shown in Fig. 7. The sensing element consists of a thin 1- by 1-cm mirror on which hygroscopic

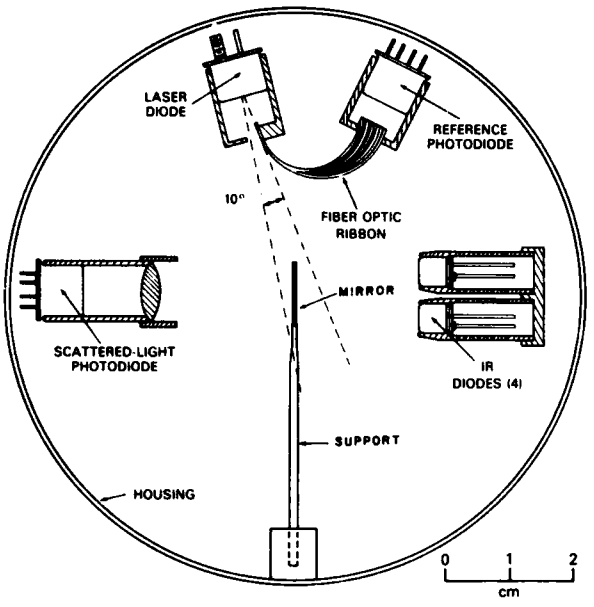

Fig. 7 — Sensor head of the saturation hydrometer

salt particles have been deposited. Droplets form around the particles whenever the ambient RH exceeds the deliquescent point of the salt (≃80% for the $(NH_4)_2 SO_4$ particles used here) and the size of the droplets is directly related to the ambient RH. The size and the concentration of the particles on the mirror are chosen so that a minimum amount of coagulation takes place between the droplets as they swell with increasing RH. The average droplet size is measured by the scattering of light from a laser diode; the intensity of scattered light is related to the ambient RH up to a value of RH = 100%. Above RH = 100%, the mode of operation of the instrument changes and becomes similar to that of the familiar dew-point hygrometer, except that the mirror is heated instead of being cooled. Heat is applied to the mirror from infrared diodes and controlled by a feedback loop to keep the haze droplets at the size corresponding to RH = 100%. The temperature increase of the mirror is then directly related to the amount by which the ambient RH exceeds 100%. By maintaining RH = 100% at the mirror, the haze droplets are prevented from growing explosively when the ambient RH exceeds 100%, thus preserving the calibration of the droplet deposit. Calibration is easily accomplished by measuring the instrument's response in an insulated sealed box with interior walls wetted with distilled water; this produces an environment with RH = 100%. Laboratory and field trials of the hygrometer have shown that the haze droplet deposit on the mirror has a strong resilience to change, which is important for the successful application of this technique.

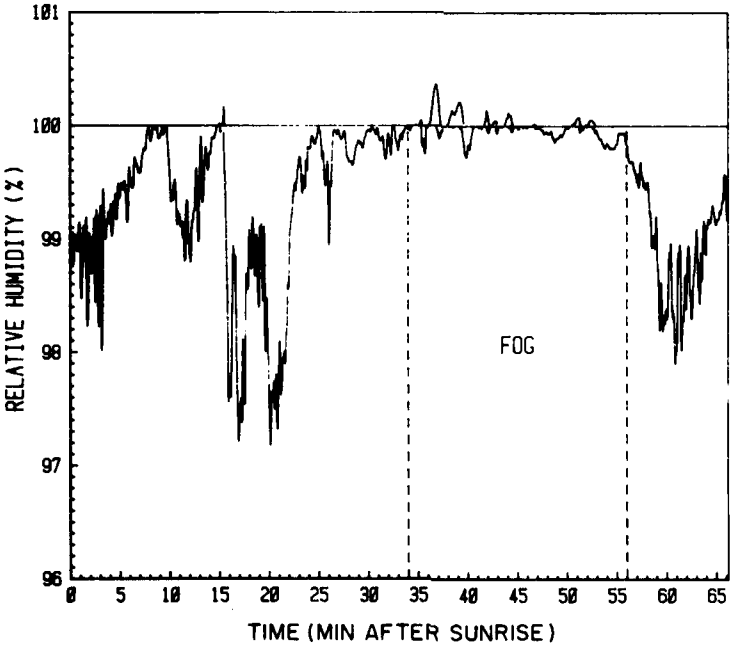

Fig. 8 — RH measured with the saturation hygrometer in a radiation fog which occurred after sunrise at Albany County Airport on Oct. 6, 1981

The first application of the hygrometer was to measure RH in fog formed by the radiative cooling of the atmosphere near the ground [1]. Figure 8 gives a typical example of such a measurement; the accuracy is one order of magnitude greater than possible with other techniques, and the results include the first direct measurements of supersaturation. This first detailed look at the RH structure near 100% gave new insights into the physical nature of radiation fogs. An unexpected observation was that rapid changes between supersaturation and values of RH less than 100% occurred during the fog episode. This suggests that turbulence plays a larger role in the formation of these fogs than had been previously thought. The usual procedure in fog modelling has been to assume a low, constant value of supersaturation; it now appears that we should treat radiation fogs as consisting of small patches with high values of supersaturation (and rapidly growing fog droplets) separated by patches of stable haze droplets. Turbulence also appears to be the trigger for fog formation, although the radiative cooling of the air near the ground remains a necessary condition. This effect is demonstrated in Fig. 8 where the dense fog formed 30 min after sunrise when the ground had warmed sufficiently to cause turbulent mixing in the previously stable boundary layer.

It is planned to use the hygrometer to make measurements in maritime fogs. A better understanding of these fogs should lead to improved prediction of their occurrence and thus benefit naval operations.

[Sponsored by NAVAIR]

REFERENCE

1. Gerber, H.E., 1981: "Microstructure of a Radiation Fog.," *J. Atmos. Sci.*, **38**, 454 (1981).

SPACE SCIENCE and TECHNOLOGY

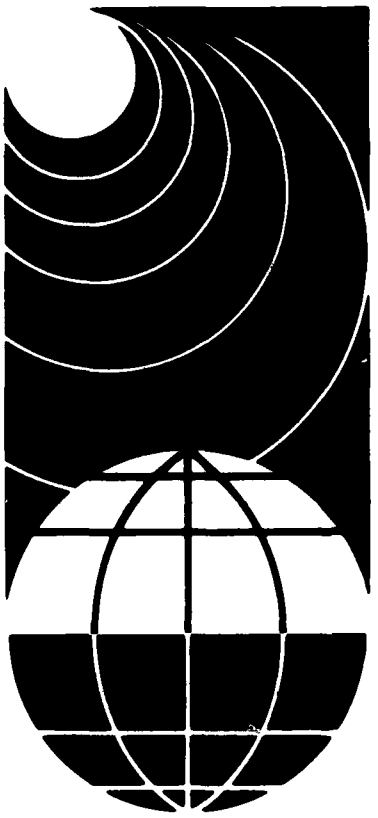

SPACE SCIENCE AND TECHNOLOGY

Space research is represented by these six articles covering a wide range of extraterrestrial projects. Events taking place far from the earth, such as solar flares, can affect the ionosphere and this in turn affects communications. NRL has been a pioneer in the field of x-ray astronomy and continues its contribution to the national space program.

Submicrosecond Time Synchronization Using GPS Satellites, by J.A. Buisson and O.J. Oaks, *Aerospace Systems Division*

The NAVSTAR Global Positioning System (GPS), when fully operational, will consist of a constellation of 18 to 24 satellites able to provide navigation signals to users worldwide. GPS, which evolved from the NRL TIMATION and Navigation Technology Satellites (NTS) programs, currently consists of five operational satellites. Each satellite transmits a signal which allows a user to compute the position of the satellite and time relative to GPS master time. Navigation users receive signals from four different satellites simultaneously to determine their own position and time. A time-transfer user, whose position is known, determines time relative to GPS by receiving and processing a signal from any one satellite. The receivers for the time-transfer function alone are much simpler than the navigation receivers.

NRL has performed time transfer by satellite since the late 1960's. Initial experiments with the TIMATION satellites demonstrated synchronization of less than 1 μs over trans-Atlantic baselines. More recently, the Laboratory has designed a time-transfer receiver for use with GPS satellites. In a test conducted in April 1982, the NRL-built prototype receiver provided time transfer well within the accuracy goal of 100 ns (rms). Since then, units have been delivered to NASA and deployed worldwide for operational use.

To measure the offset between his own clock and GPS time, maintained in the designated GPS ground control station, a user makes measurements of *pseudorange*, that is, a time interval that starts with a specific epoch in the user's clock signal and stops with receipt of the corresponding epoch in the signal from a GPS satellite. The pseudorange is essentially the time difference between the satellite clock and the user clock plus the propagation time between the satellite and the user. With the satellite position data provided by the satellite signal and the knowledge of his own position, the user calculates the propagation time and subtracts it from the pseudorange to obtain the offset between his own clock and the satellite clock. The difference between GPS time and the clock on each satellite is also provided by that satellite's signal, and the user employs this to reference his clock to GPS time.

GPS users can synchronize their clocks by several methods depending on the application and the degree of accuracy required. Figure 1 illustrates three of the more common methods. In the first, a single user synchronizes a clock to GPS master time using the procedure described above. Errors in this method include 50-100 ns due to uncertainties in the ionosphere and the satellite orbit, plus any errors in relating satellite time to GPS time. Two stations can synchronize to each other more accurately if they can each take measurements simultaneously from the same satellite and compare differences. In this second method, designated the *common view method*, the errors due to uncertainties in relating satellite time to GPS time are eliminated and errors due to satellite orbit uncertainties are reduced. Accuracy of better than 50 ns can be achieved by this method. Stations wishing to synchronize clocks to each other, and not having simultaneous views of GPS satellites, must use a less accurate third method: comparing their offsets from GPS time to get the differences from each other.

The NRL time-transfer receiver is a microprocessor-based system that tracks the course/acquisition pseudonoise-coded signal which is modulated on the L1 frequency (1575.42 MHz). It uses an omnidirectional antenna and can track GPS satellites from horizon to horizon. Figure 2 is a block diagram of the NRL system. The microprocessor controls the hardware functions, decodes the navigation message, and calculates the time offsets. The results are displayed on a cathode ray tube and recorded on a flexible disk once every six seconds.

In April 1982, the time transfer receiver was tested at the GPS Vandenberg monitor station (VMS) in Vandenberg, California. For the test,

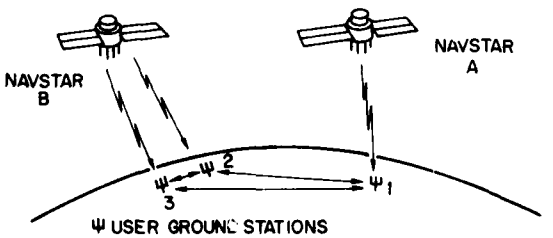

Fig. 1 — Time synchronization between ground stations using GPS satellites. NAVSTAR-A provides user 1 with a time synchronization to GPS time with an independent measurement. Users 2 and 3 synchronize to each other by comparing NAVSTAR-B measurements taken simultaneously. All three users can synchronize to each other by comparing the offset of each station to GPS time.

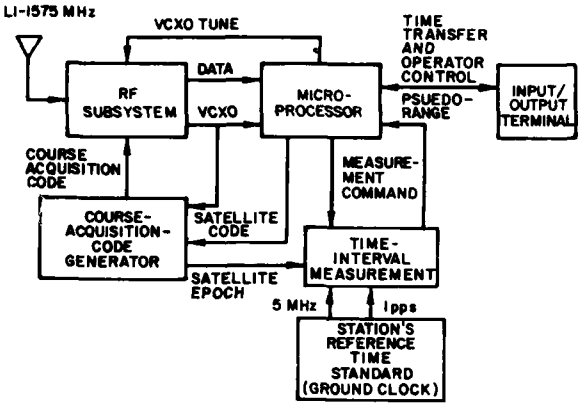

Fig. 2 — NRL time transfer receiver. The receiver is microprocessor-controlled and uses the course/acquisition signal at the L1 frequency (1575 MHz) to determine the time difference between a user's ground clock and GPS time.

the NRL receiver was controlled by the VMS clock which was also the frequency standard for GPS time. Figure 3 shows time-transfer results between the VMS clock and GPS master time using four GPS satellites: NAVSTAR 3, 4, 5, and 6. A linear least squares fit to the data results in a standard deviation about the known mean of 41 ns (rms). This is well within the original goal of 100 ns.

Additional receivers are scheduled for deployment in 1983. These will have some improvements in the design, including a time correction which allows a user to reference his ground clock not only to GPS time but also to the U.S. Naval Observatory master clock by using a correction provided by the GPS spacecraft. The improved receiver will be evaluated and tested in 1983. It is anticipated that this will have an accuracy of less than 50 ns over transcontinental distances using the common view method.

[Sponsored by NASA]

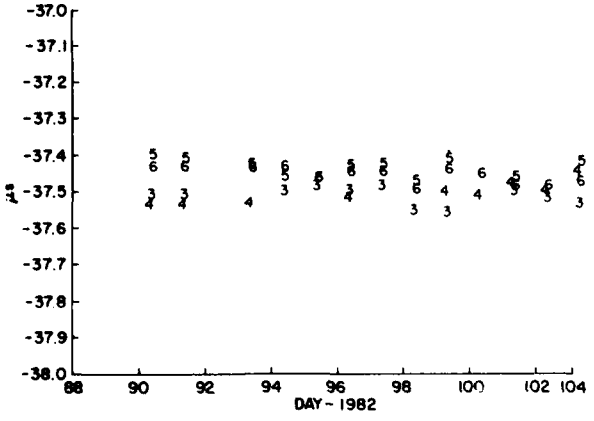

Fig. 3 — NRL receiver time transfer results comparing the VMS clock with GPS time using NAVSTARS 3, 4, 5, and 6. The bias of about 37.5 μs is an artifact in the definition of GPS time. The data have a 41 ns standard deviation about this known bias.

Analytic Orbit Prediction, by S.L. Coffey and K.T. Alfriend, *Aerospace Systems Division*

Today's satellite tracking systems use numerical integration programs for accurate orbit determination and ephemeris predictions. These programs are calculation-intensive and require the capabilities of large computer systems. On the other hand, an analytic orbit prediction program requires substantial theoretical development and complex algebraic manipulations to produce the equations of motion, but once the program is available, it can perform the tasks of orbit determination and prediction with modest computational requirements within the capabilities of today's microcomputers. The use of analytic orbit prediction has been limited to date principally because current theories do not provide sufficient accuracy.

NRL is developing an analytic orbit prediction program for broad applications in orbit research, system design and analysis, and for operational use in satellite tracking systems. Two aspects of the project are the development of the analytic theory and the implementation of the theory in an operational program. Early in 1982, work was completed on an analytic second-order solution to the zonal satellite problem. The resulting theory can accomodate any combination of zonal harmonics in the earth's gravitational potential [1]. Implementing the theory was emphasized during the remainder of the year. This effort has resulted in an automated procedure which transcribes the computer files representing the theory into compact forms which can be incorporated into self-contained programs tailored to specific applications.

The analytic theory involves a number of transformations of coordinates starting from the osculating coordinates (epoch coordinate system) and ending in an averaged coordinate system. The literature contains many references to methods of initializing the averaged elements. It is a common practice for first-order theories to use a differential correction procedure on the

AD-A136 193 1982 NAVAL RESEARCH LABORATORY REVIEW(U) NAVAL RESEARCH 2/3
LAB WASHINGTON DC A E ROBSON ET AL. 1983

UNCLASSIFIED F/G 14/2 NL

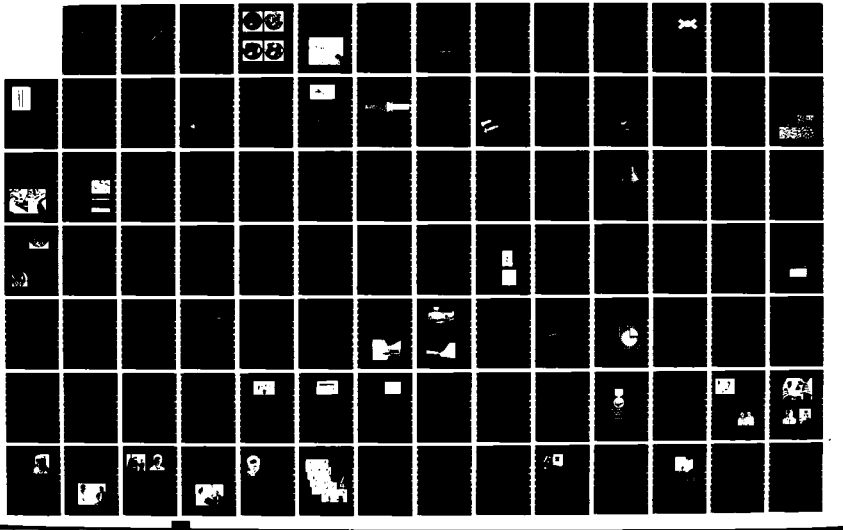

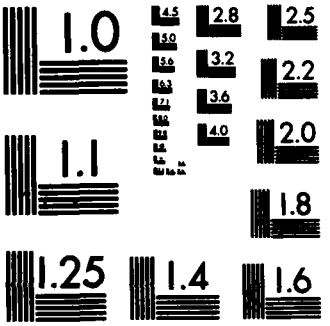

averaged coordinates to force the osculating coordinates into a best fit to a reference orbit over some time span. The adjusted averaged coordinates are then used to propagate the orbit. A second-order theory such as ours can obviate the need for such a procedure, the averaged coordinates being calculated from the second-order transformation equations.

A two-stage process was developed to implement the theory. To provide users with the utility of a general purpose program, a program generator called a *metaprogram* was written. The metaprogram forms a mechanized interface between the theory and the operational orbit programs (Fig. 4). The metaprogram automatically writes orbit prediction programs in FORTRAN IV. In the second stage of the implementation process, the output orbit program is optimally tailored by the metaprogram to the specifications of the intended application. The metaprogram forms the link between the theory and the operational orbit programs, a role normally occupied by human programmers. The instructions for the metaprogram are passed through a program template which is completed by the user during a short interactive session at a terminal. The user designs the output program by choosing from two versions of the theory and specifying the order of the theory, the form of the input, the form of the output (either numerical or plotted), the type of computer on which the orbit program is to be run, changes in physical parameters, and a number of other options. Even the largest versions of the orbit program can easily be run on current personal computers with 64K of memory. This provides researchers with an analytical orbit predictor which can be used as a tool in the same way that small preprogrammed packages are used on hand-held calculators.

To verify the accuracy of the theory, extensive comparisons were made with orbits computed by the Cowell numerical integration algorithm provided in the Goddard Trajectory Determination System (GTDS). The force field used for the numerical integration was identical to that used in the analytic theory. The results of one such comparison are given in Fig. 5, which gives

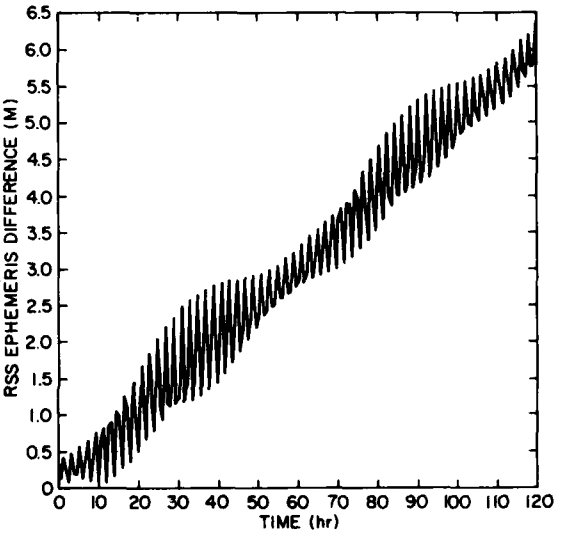

Fig. 5 — Difference in the predictions of the analytical model and numerical integration. The rapid oscillations are due to trigonometric terms in the short-period transformations. Second order analytic theory with zonals J_2, J_3, J_4 was used.

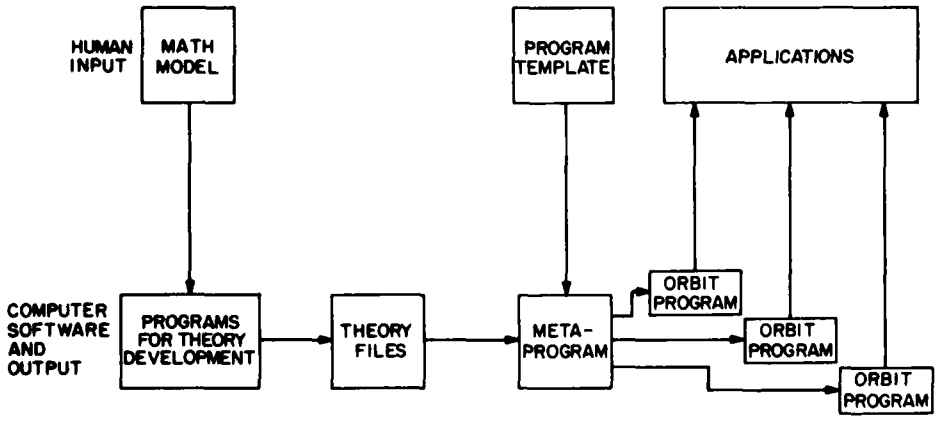

Fig. 4 — Model of man-computer interaction leading to orbit prediction programs for specific applications

the difference in an ephemeris prediction as a function of time after the start of the computation. The difference is seen to be small.

Further work in this area will broaden the mathematical model to include more of the forces, such as drag and lunisolar terms, that perturb satellite motions. A convenient distribution process for dissemination of the ephemeris programs is also envisioned.

[Sponsored by ONR]

REFERENCE

1. S.L. Coffey and K.T. Alfriend, "AOPP: An Analytic Orbit Prediction Program," AIAA paper no. 83-0193 presented at AIAA 21st Aerospace Sciences Meeting, 1983.

Magnetic Flux Transport on the Sun, by C.R. DeVore, J.P. Boris, and T.R. Young, Jr. *Laboratory for Computational Physics* N.R. Sheeley, Jr. *Space Science Division*

The sun displays a variety of phenomena involving the activity of magnetic fields, some of which can affect the earth's environment. Magnetic phenomena occur at all depths in the solar atmosphere and span a wide range of temporal and spatial scales—from the explosive, concentrated release of energy in a solar flare to the reversal of the sun's global magnetic field over the 11-year sunspot cycle. Underlying this cyclical activity is the evolution of bipolar magnetic regions, loops of magnetic field and plasma anchored in the photosphere and extending out into the corona. The pattern of emergence of these regions on the surface of the sun couples with the characteristics of fluid flows in the photosphere to determine the large-scale structure of the solar magnetic field. We have developed a computer simulation model to study these aspects of the sun's magnetic activity.

The evolution of bipolar magnetic regions is governed by differential rotation, meridional currents, and turbulent diffusion. Differential rotation, the variation of the surface rotation rate with latitude, causes a shearing deformation of active regions. Meridional currents are latitude-dependent flows which displace the magnetic regions in the north-south direction. Turbulent diffusion arises from photospheric structures known as granulation and supergranulation convection cells, and results in the dispersal of the magnetic flux over the solar surface. Our model simulates this convective-diffusive transport of magnetic flux over the entire sun.

The magnetic sources for the model are taken directly from observational data. The subsurface dynamics responsible for the generation and emergence of active regions are not well understood, and prediction of the precise time, location, and other characteristics of the eruption of new magnetic flux is not presently feasible. However, once a new region has emerged its further development is determined by the convection and diffusion on the surface, and the resulting flux distribution is subject to direct observation. We are testing and refining our model by comparing the predicted and observed characteristics of evolving bipolar magnetic regions.

Our present objective is to determine the optimum values for the solar parameters which characterize the velocity fields. These parameters—the differential rotation profile, the meridional flow profile, and the turbulent diffusion coefficient—are subject to observational uncertainties large enough to permit a wide range of possible solar magnetic behavior. To find the set of parameters that best represents the sun, we are conducting detailed numerical simulations of several large, isolated active regions using digital data provided by K. L. Harvey of the Kitt Peak National Observatory. Figure 6 shows the evolution of a bipolar magnetic region, at successive solar rotations, as measured directly (top) and as predicted by the simulation model (bottom).

Our ultimate goal is to predict the large-scale features of the sun's magnetic field. Given an initial distribution of magnetic flux, can we accurately predict, in the absence of new sources, the global structure of the field weeks or months hence? One indication that this may be possible came early in our investigation, when the simulation showed the formation of a large photospheric magnetic region with a structure associated with coronal holes—known sources of high-speed solar wind streams and their associated geomagnetic activity. This region was in fact the origin of the first low-latitude coronal hole of the present sunspot cycle. We are also exploring extensions of the model which will enable us to infer properties of the subsurface magnetic fields and, possibly, to predict the eruption of new active regions. A successful predictive model of the sun's global magnetic flux distribution would be a valuable scientific and technological tool.

[Sponsored by NASA and AFGL]

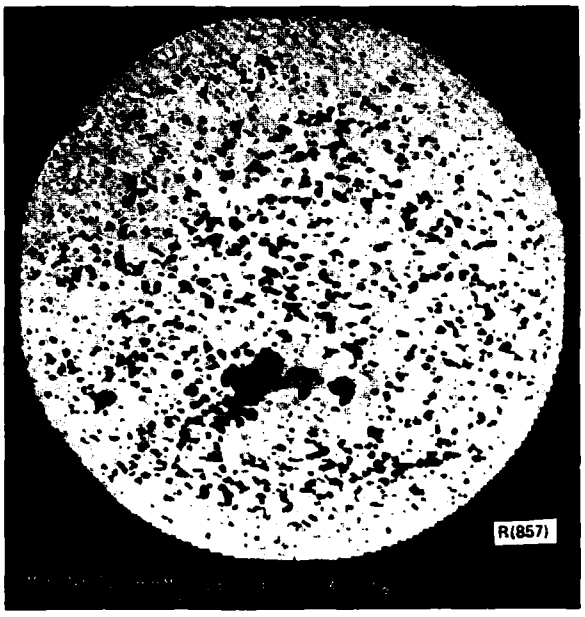

(a)

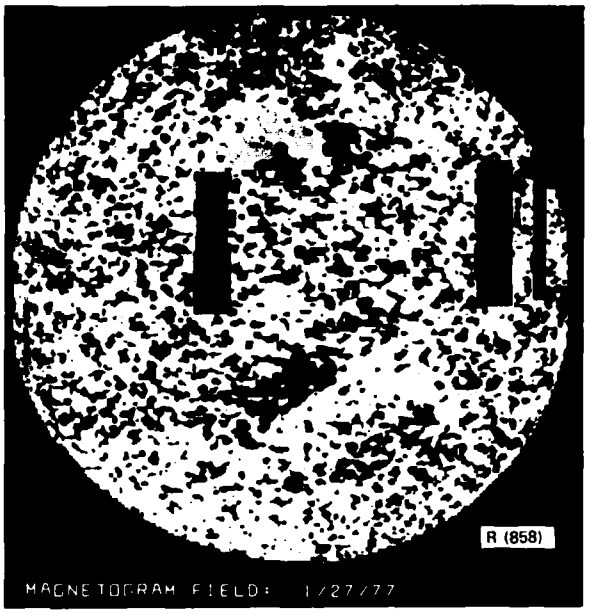

(b)

(c)

(d)

Fig. 6 — A large active region appearing in the southern hemisphere of the sun on 30 December 1976 (upper left) is put into the simulation model (lower left), and its flux distribution at the succeeding solar rotation, as observed (upper right) and as computed (lower right), is shown. The bars in the 27 January 1977 magnetogram are data gaps caused by clouds.

Dynamics of the Solar Atmosphere, by J.T. Mariska, *Space Science Division,* and J.P. Boris, *Laboratory for Computational Physics*

All of the energy that the sun eventually radiates into space is produced in the innermost one third of its radius. From there the energy slowly diffuses outward through layers of decreasing temperature and density. Above the photosphere, or visible surface of the sun, this trend reverses and after reaching a minimum value of about 4300° K the temperature begins to increase. It rises gradually at first in the chromosphere to a value of about 10,000° K. Above the chromosphere it increases sharply to a value of over one million degrees K in the corona. One of the major unsolved problems of solar physics is the nature of the physical processes that produce and maintain these high temperature regions.

Over the last decade some progress has been made toward solving this problem, primarily through high-resolution observations of these layers from space. These observations, such as the extreme ultraviolet picture of the sun in Fig. 7, have shown that the upward extension of the sun's magnetic field above the visible surface plays a crucial role in determining the structure of the outer layers of the atmosphere. As the figure suggests, the plasma of the solar corona is confined to follow the magnetic lines of force in the outer layers of the sun's atmosphere. Thus, the basic structural unit of the corona is a magnetic flux tube and the plasma contained within it. Time-resolved observations show that the structures in Fig. 7 are highly dynamic. In fact, virtually every structure in the outer layers of the solar atmosphere is in motion. Despite the obvious importance of the structuring introduced by the magnetic field and the dynamic nature of the atmosphere, very little theoretical modelling has included either of these effects.

We are developing computer programs to simulate dynamic phenomena in magnetic flux tubes. In the past year, we have carried out a series of calculations designed to examine the dynamics of plasma confined within a small

Fig. 7 — An example of coronal loops on the sun. These loops were photographed in the light of Ne VII with the NRL spectrohellograph on Skylab.

coronal loop. The loop is modelled as a semicircular tube of constant cross-sectional area. Inside the tube we construct a model of the solar atmosphere which is stationary and in which the amount of energy leaving the system as radiation is exactly balanced by heating. The radiation comes predominantly from the region of the atmosphere just above the top of the chromosphere, where the temperature is around 20,000° K. The heating is modelled as a constant energy input in each unit of plasma volume. This is the initial state of the numerical model and is in static equilibrium.

We have been studying how this initially static model atmosphere evolves in response to changes in the energy input necessary to maintain it. We have examined the response of the atmosphere to changes in the amount and the location of the heating. Changes in the amount of energy being deposited have a surprisingly small effect. The atmosphere simply restructures itself to provide enough material in the region of peak radiating efficiency just above the chromosphere to radiate away all of the energy deposited. There are some mass motions associated with these changes, but they are small and damp very quickly.

Changes in the *location* of the energy deposition have a much greater effect on the atmosphere. When the total amount of energy being deposited per unit time is held constant, but the deposition is changed from being uniformly distributed in the loop to being localized in a smaller region, the atmosphere responds by setting up a flow of material from the heated side of the loop to the unheated side. An example of this is shown in Fig. 8. This flow carries energy and serves to reestablish the balance in the heating which was disrupted by the change in the heating location. The flow in this case does not damp with time, but rather represents a new steady-state solution of the equations that describe the system. Note that although there are large velocities present in the model the temperature and density as a function of position in the loop are hardly changed at all.

Observations of Doppler shifts of spectral lines formed in corresponding regions of the solar atmosphere show that steady flows are ubiquitous phenomena on the sun. Our calculations suggest that these flows may simply be the natural consequence of the nonuniformity of the heating that maintains the atmosphere. Since the nature of the flows appears to be related to the location of the heating, it may be possible to obtain information about the still unknown heating mechanism by carefully studying the flows in these regions of the solar atmosphere. We are continuing to study dynamic phenomena in magnetic flux tubes with this goal in mind.

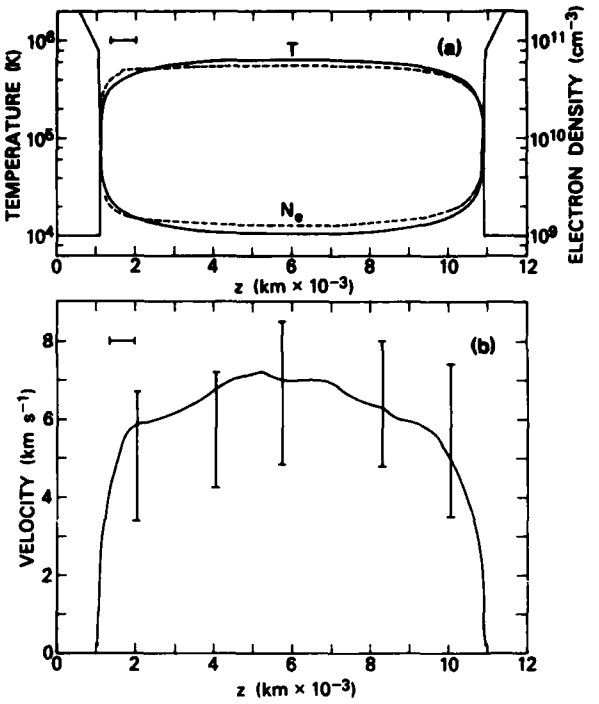

Fig. 8 — (a) Initial (solid) and final (dotted) temperature and electron-density profiles and (b) final velocity profile for an asymmetrically heated loop. The horizontal bars in the upper left corners of each panel show the location of the asymmetrical heating.

[Sponsored by NASA and ONR]

REFERENCES

1. J.T. Mariska, J.P. Boris, E.S. Oran, T.R. Young, Jr., and G.A. Doschek, "Solar Transition Region Response to Variations in the Heating Rate," *Astrophys. J.*, **255**, 783 (1982).

2. J.P. Boris and J.T. Mariska, "An Explanation for the Systematic Flow of Plasma in the Solar Transition Region," *Astrophys. J. Letters*, **258**, L49 (1982).

Efficient Imaging X-ray Detector, by G.G. Fritz, *Space Science Division*

X-rays can be detected by the blackening they produce on photographic film, by the ionization of gases, and by the photoelectrons emitted from solids. The last two processes are generally much more efficient, and can be made all-electronic, which has definite advantages where rapid analysis or remote detection is required. In the field of space science, spectacular and revealing pictures of the x-rays from the sun's outer atmosphere were recorded on film during the Skylab mission. X-ray astronomy, on the other hand, has had to rely almost exclusively on ionization or photoelectric detection of x-rays from nonsolar sources, because the fluxes are orders of magnitude smaller than from the sun.

The most sensitive x-ray astronomy instruments to date were on board the Einstein Observatory, launched by NASA in late 1978 as the second high energy astrophysical observatory (HEAO-2). The successes of the Einstein Observatory have been well publicized [1], and include discoveries about objects ranging from nearby ordinary stars to the most distant quasars. However, the detecting instruments involved a serious compromise. The gas-filled imaging proportional counters operated with an x-ray efficiency approaching unity, but had spatial resolution some ten times worse than the telescope; on the other hand, the high resolution imager (HRI) matched the telescope resolution, but at the expense of low efficiency.

Several years ago, we set out to develop an x-ray imaging device that would combine high efficiency with high resolution, and that would serve as one of the primary detectors for the next generation of space x-ray experiments. The result of this effort is the efficient x-ray imager (EXI), an electronic, solid-state x-ray detector which rivals the efficiency of gas ionization detectors while approaching the resolution of film.

The operation of the EXI, shown schematically in Fig. 9, is based on the use of microchannel plates (MCP). These are plates of special glass, about 1 mm thick and 25 to 100 mm in diameter, containing millions of holes which are typically 15 μm in diameter. An electric field applied to the MCP stack causes an electron entering a hole to cascade and multiply, so that roughly 10^7 electrons emerge from the other side of the plates. The technology of MCP devices has advanced dramatically in the last ten years, and their use in optical image intensification is becoming widespread [2]. The problem with x-rays is to produce an x-ray photocathode that will efficiently convert x-ray photons to free electrons for amplification by the MCP, and then to measure electronically the position of each electron bundle emerging from the MCP.

Many substances will emit photoelectrons when struck by x-rays in the 0.1-10 keV range,

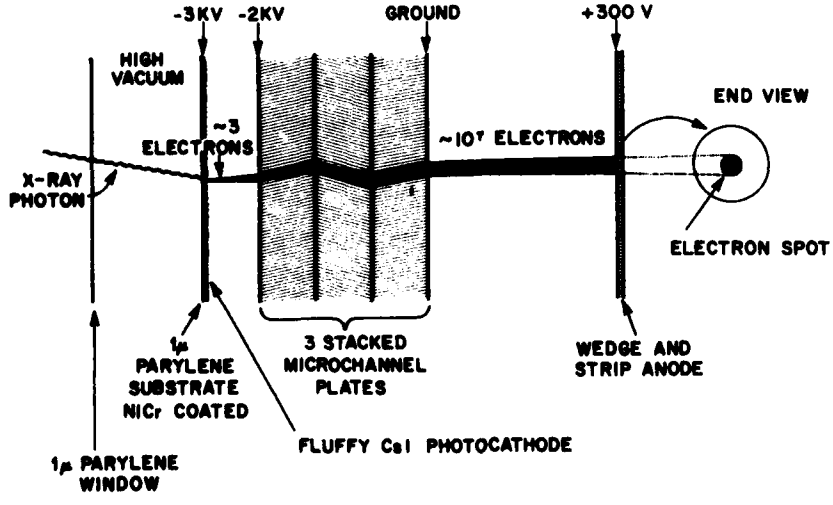

Fig. 9 — Cross-section schematic of EXI. An x-ray photon enters from the left and ejects several electrons from the photocathode, which are then multiplied by the MCP stack. The resulting electron spot produces pulses in a collecting anode which are used to determine the position of the incoming x-ray.

but in general, the electrons are immediately absorbed by the solid material. This is simply because the absorption depth for x-rays is much larger than the range of the electrons. We have found a clever way around this problem by preparing the photocathode in a fluffy form, which on a microscopic scale somewhat resembles a ball of cotton. The strands of photocathode material are sufficiently thin that electrons can escape efficiently, and yet the total density of the layer is adequate for x-ray absorption. The result of an extensive study at NRL has shown that cesium iodide, (CsI) a photocathode material used principally at ultraviolet wavelengths, can be evaporated in an inert gas to produce fluffy x-ray photocathodes of remarkable efficiency. These have been built into detectors using MCP electron multiplication, as shown in Fig. 9. The efficiency of a typical EXI detector, in this case one prepared for an x-ray astronomy experiment on a sounding rocket, is shown in Fig. 10. For comparison, the efficiency of the HRI detector on the Einstein Observatory, a state-of-the-art MCP x-ray detector just a few years ago, is also shown. In the important region around 1-2 keV, the EXI is superior by about a factor of 4, and more recent work has extended this factor to 6. Such improvements in efficiency are important in x-ray astronomy where sensitivity is a critical factor. They are equivalent to building a much larger telescope, and will permit the observation of fainter objects and weaker spectroscopic lines.

The spatial resolution of an MCP detector is ultimately limited by the size of the holes in the plates. In the EXI, the electrons from the fluffy CsI photocathode are proximity-focussed onto the MCP; that is, a high voltage is placed across a narrow gap to limit sideways motion of the electrons. This arrangement has a resolution close to that of the MCP alone. Finally, the position of each bundle of electrons from the output side of the MCP must be measured. From a variety of techniques available or under development [2], we have chosen the wedge and strip anode as most promising. The electron spot falls on a regular geometrical pattern of conductors, and the x and y position of the x-ray event is then determined from the charge division among the conductors. An initial version of the anode, which consists of gold electrodes on a sapphire substrate, has been produced and tested at NRL. The complete EXI allows a computer to calculate the position of each detected x-ray event, and to build up an x-ray image in the computer's memory. An imaging system consisting of the EXI and a microcomputer is nearing completion for laboratory tests and will be adapted to future space experiments.

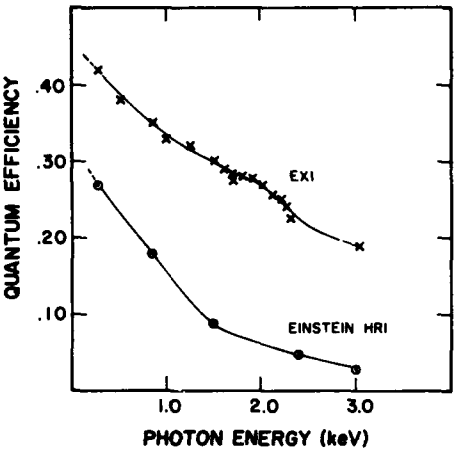

Fig. 10 — Detection efficiency versus x-ray energy for the NRL EXI detector and the high resolution imager carried on the Einstein Observatory (1978-1980).

[Sponsored by ONR and NASA]

REFERENCES

1. R. Giacconi, "The Einstein X-ray Observatory," *Scientific American* 242, 80 (1980).

2. M. Lampton, "The Microchannel Image Intensifier," *Scientific American* 245, 62 (1981).

Transient Hard X-Ray Emission From the Crab Pulsar, by M.S. Strickman, J.D. Kurfess and W.N. Johnson, *Space Science Division*

X-ray and gamma-ray observations of the Crab Pulsar afford the opportunity to observe physical phenomena in an environment so exotic that it is impossible to duplicate in the laboratory. Like all pulsars, the Crab is a rapidly spinning neutron star which is the result of a supernova explosion. The rotation of its intense magnetic field ($\sim 10^{12} - 10^{13}$ gauss) generates large electric fields near the surface of the star which accelerate charged particles to very high energies. Observations of the radiation emitted by these particles can throw light on the emission mechanisms of the pulsar system as well as the behavior of relativistic particles in a strong magnetic field in general.

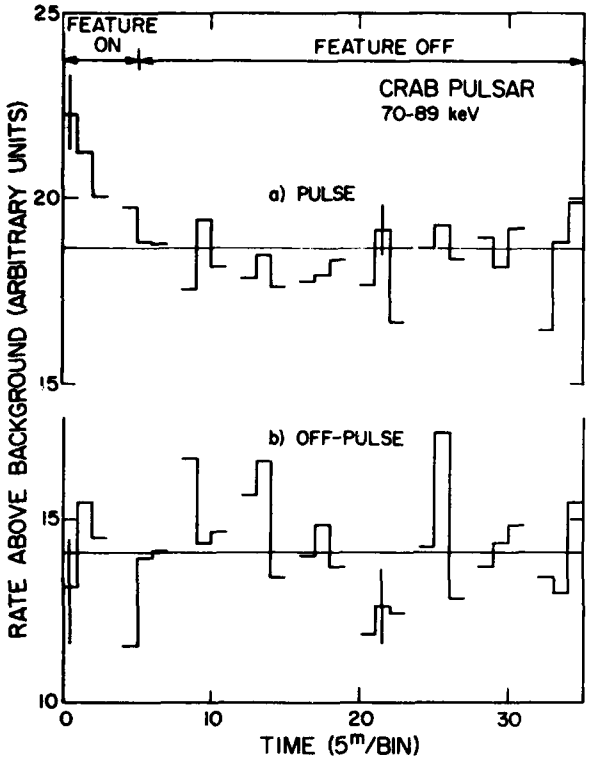

Fig. 11 — Time histories of the pulsar ("Pulse") and background ("Off-Pulse") emission in the energy band including the emission line

The NRL balloon-borne hard x-ray observatory observed the Crab Pulsar on 11 May 1976 in the 15-250 keV energy band. Spectral measurements within this band were made with a large area (765 cm^2) NaI(Tl) scintillator having a 10° field-of-view. NaI(Tl) detectors have moderate spectral resolution: a very narrow spectral emission line at 60 keV would appear to be ~15 keV wide. The data were pulse-height analyzed into 128 spectral channels. The pointing of the detector was controlled automatically by a microprocessor system which could track the source with a minimum of commands from the ground.

An initial analysis of data from the 1976 balloon observation of the Crab was presented in the 1979 *NRL Review*. More recent analyses have indicated the presence of a transient emission line at 77 keV superimposed on the power-law continuum. The line is present in the spectrum at the start of the observation and gradually diminishes in intensity until it drops below the sensitivity of the detector after about 25 min (Fig. 11). The feature does not reappear during the three-hour observation period.

Figure 12 presents two pulsar spectra. The first is integrated over the 25-min duration of the line, and the second is integrated over the following 40 min. For each spectrum, the effects of the atmosphere and detector response have been unfolded, but the broadening of line features arising from of the detector's resolution has been left

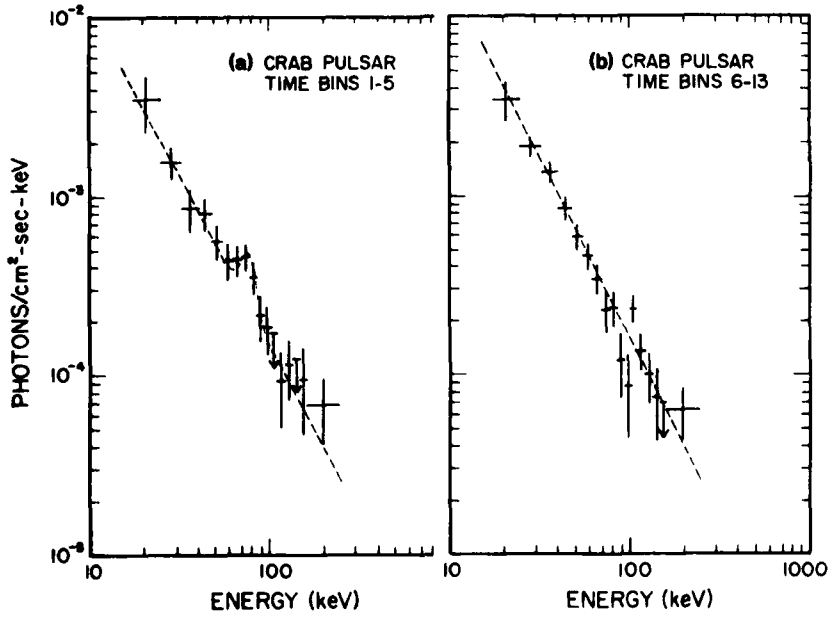

Fig. 12 — Pulsar spectra during (a) and after (b) the emission line outburst

in. The observed width of the line feature is consistent with the broadening of a narrow line by the instrument resolution, as indicated by the best-fit model (dashed line). In both cases, the underlying pulsar continuum is well represented by the same power-law model but the line feature is visible only in the first spectrum.

This observation is the first direct measurement of the variability of a hard x-ray line feature in the Crab Pulsar spectrum. Some previous measurements by other instruments have suggested the presence of such a feature, while others have not. The flux range occurring during our observation is consistent with previous results and lends credance to the reality of the feature.

The observation also has important theoretical implications. When electrons circulate in an intense magnetic field, they are constrained to move in distinct quantum orbits. Quantized cyclotron emission from radiative transitions between low-energy-level orbits is the most likely source of a line in the hard x-ray range. If this is the origin of our observed line, the line energy gives a direct measurement of the magnetic field strength in the emission region. The resultant value is 8×10^{12} gauss, assuming a reasonable value for gravitational redshift in the gravitational field of the neutron star. Assuming a dipole magnetic field structure, this means that the emission region must be very close to the surface of the neutron star.

The transient nature of the feature is difficult to explain within the context of current pulsar models. Long-term observations of the emission are clearly necessary. These observations would determine the frequency of recurrence of line emission, variation of line characteristics from occurrence to occurrence, and, with coordinated observations at other frequencies, the correlation of x-ray-line outbursts with any other transient phenomena from the pulsar. We expect to make these extended observations in 1984 or 1985, when the NRL observatory will be carried on longer-duration (~30 days) balloon flights provided by NASA and the National Scientific Balloon Facility.

[Sponsored by ONR and NASA]

REFERENCE

1. M.S. Strickman, J.D. Kurfess, and W.N. Johnson, "A Transient 77keV Emission Feature from the Crab Pulsar," *The Astrophysical Journal Letters* **253**, L23 (1982).

HIGH-POWER RADIATION SOURCES and PULSED POWER TECHNOLOGY

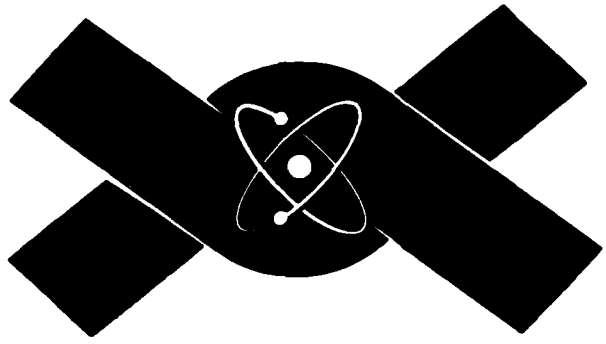

HIGH-POWER RADIATION SOURCES AND PULSED POWER TECHNOLOGY

The study of ionized matter, or plasma, is relevant to possible future Naval applications of high-power directed energy systems using either electromagnetic radiation or particle beams. NRL's involvement in this forward-looking area is represented by the following articles.

The Plasma Antenna, by J.R. Greig, R.E. Pechacek, and M. Raleigh *Plasma Physics Division*

A ship's antennas are among its most vulnerable components. Some years ago it was suggested that this vulnerability might be reduced if the antennas were made of ionized air (plasma) instead of solid metal, but no demonstration of this idea has been reported. We have recently developed techniques for guiding long electrical discharges in the atmosphere using lasers. The path of the discharge is designated by the laser and may be quite different from the natural path, which is usually the shortest distance between the electrodes. Using these techniques we have made a plasma antenna and used it in a proof-of-principle experiment to transmit and receive radio frequency signals [1]. In carrying out this experiment we had the enthusiastic collaboration of LCDR J.M. Perin of the USNA, Annapolis.

The experiment is shown schematically in Fig. 1; A_1 represents the plasma antenna, used in this case as the transmitter. A folded monopole geometry was chosen because both ends of the antenna must be accessible in order to be compatible with the plasma-formation techniques. The receiving antenna, represented by A_2, was a folded monopole antenna made out of copper pipe. The plasma antenna consisted of two vertical plasma columns, P_1 and P_2, whose positions were designated by beams from an Nd:glass laser, The two plasma columns intersected with a short copper wire that was suspended at the desired height ($\lambda/4$) above the ground plane, G. The electric discharge that created the plasma was driven by the high-voltage power supply, D, and terminated in the discharge ground, G_2. The RF signal from the transmitter T, was injected near the discharge ground, G_2, and terminated in the RF ground, G_1.

The Nd:glass laser had an output of 100 J in a 40-ns pulse. The beam was split into two vertical beams, 10 cm apart, and used to designate the two arms of the antenna, which were 67 cm tall. The initial electrical discharge was created by a small 360-kV Marx generator. This discharge lasted only ~ 7 μs and deposited about 3 J/cm along the length of the plasma. This is significantly more energy than deposited by the laser and by any subsequent RF heating. To extend the useful lifetime of the plasma the initial discharge was followed by a sustaining discharge having a peak current of about 1 kA and a duration of about 2 ms. The second discharge followed the path established by the laser/Marx discharge (Fig. 2). The experiment was performed on the roof of a building which provided a flat unobstructed area almost 61 meters square. The laser beams and the high-voltage power were brought through a hole in the roof. The second antenna, A_2, was placed ~ 17 m from the plasma antenna.

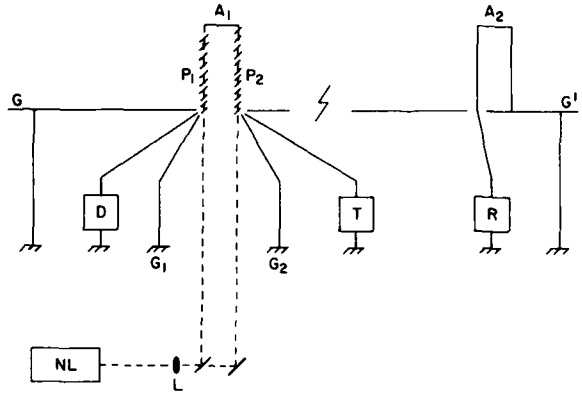

Fig. 1 — The RF propagation experiment. A_1 is the plasma antenna rising above the local ground plane, G. A_2 is a second antenna rising above its local ground plane, G'. *NL* is the Nd-glass laser. *L* is a long focal length lens. *D* is the high-voltage system which goes to ground at G_2. *T* is the RF transmitter and G_1 the RF ground. *R* is the receiver.

Radio frequency propagation experiments were conducted using 0.2 W of rf power at a frequency of 112 MHz (λ = 268 cm) with a bandwidth of 1 MHz. The plasma antenna was used as either a transmitting or a receiving antenna, and in each role its performance was compared with that of a solid copper reference antenna having the same dimensions. Using signal modulation at frequencies up to ~ 1 MHz, RF signals were clearly recognizable during the lifetime of the plasma antenna. The useful lifetime of the antenna produced by the laser/Marx discharge alone varied between 200 and 300 μs. During this time, the signal received from the transmitting plasma antenna fell to about 2 dB below that received from the copper reference antenna. The useful lifetime of the antenna produced by the long duration discharge was approximately 2 ms.

Using the plasma antenna as the receiver, the signal received was about the same as that received on the reference antenna. The background noise on the receiving system was equivalent to $\sim 10^{-10}$ W/MHz at the antenna when the copper reference antenna was used.

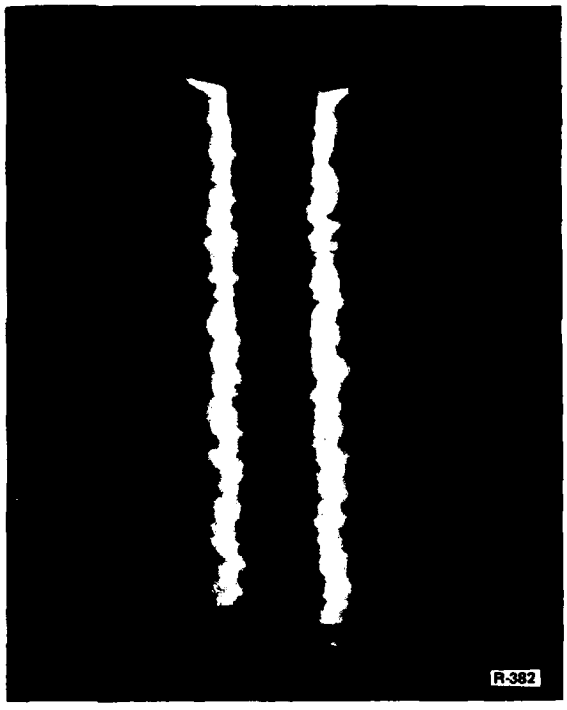

Fig. 2 — Open shutter photograph of the plasma antenna sustained with a secondary discharge

Using the plasma antenna as the receiving antenna, the background noise was $\sim 10^{-9}$ W/MHz.

Finally, to demonstrate that the plasma antenna could be created without using a copper conductor suspended above the ground plane, the suspended wire was removed and the two laser beams were tilted so that they intersected. There was no difficulty making the initial discharge track up one laser path, jump the gap, and come down the other laser path. However, because the two laser beams were so close together—less than the distance that the Marx discharge could jump without laser-guiding—the height of the antenna was difficult to control.

These experiments have shown that the efficiency of a folded monopole plasma antenna when transmitting or receiving is very nearly as good (-1 ±1 dB) as that of a copper antenna of the same dimensions. With the presently- available laser and high-voltage equipment, the frequency range over which the plasma antenna can be tuned is limited by the length of the laser-guided discharge to $\geqslant$ 75 MHz. But results obtained so far suggest that the lower frequency limit could be extended to $\sim$10 MHz or even lower. Furthermore, there appears to be no obvious reason why the sustaining discharge should not be repeated to produce a plasma antenna that would be available on a repetitive basis.

[Sponsored by ONR]

REFERENCE

1. T. Dwyer, J.R. Greig, D.P. Murphy, J.M. Perin, R.E. Pechacek, and M. Raleigh, "Characteristics of an Atmospheric Discharge Plasma as an RF Antenna," NRL Memorandum Report 4815 May 1982.

Relativistic Electron-Beam Propagation, by M. Lampe and G. Joyce, *Plasma Physics Division*

High-energy charged-particle beams propagating through air are subject to a variety of instabilities and other pathologies that preclude orderly and predictable propagation unless beam parameters are carefully chosen. For several years, NRL has been engaged in a comprehensive theoretical and computational study of the equilibrium and stability of high energy electron beams and of the associated heated air channel, with the ultimate objective of determining whether long-range propagation is feasible. This work has been coordinated with experimental propagation studies at NRL and the Lawrence Livermore National Laboratory as well as other laboratories; however, the experiments to date have been performed with beams that have relatively low particle energy (few MeV) and are otherwise in beam parameter regimes far removed from those required for long-range propagation; they have been useful chiefly to elucidate basic phenomena and verify theoretical models. A major advance in experimental capability is expected during 1983 with the completion of the 50-MeV Advanced Test Accelerator at Livermore and NRL is deeply involved in the planning for this new experimental phase. One important aspect of our work is the analysis of beam instabilities.

To propagate long distances, it is necessary that a charged particle beam remain tightly collimated. Within the atmosphere this can be accomplished only if the beam ionizes the ambient air sufficiently for the beam space charge to be neutralized by the conducting air plasma. This leaves the powerful magnetic field generated by the beam current as the dominant force on the beam, which reaches a *self-pinched* equilibrium

under the influence of this force. Unfortunately, the equilibrium is unstable: small perturbations from cylindrical symmetry, fed by the free energy of the magnetic field, can grow into large scale distortions and disruptions. Three types of instability, the *hose*, *sausage*, and *hollowing* modes, are illustrated in Fig. 3. In the hose mode, the beam thrashes around like an agitated snake (or a firehose). In the sausage mode, the beam is alternately puffed out and pinched in, like a string of sausages. In the hollowing mode, the cross-sectional profile of beam density is redistributed, alternately hollowing out in the center and then peaking sharply on axis. The hose instability has been observed (often to his sorrow) by nearly every electron beam experimenter; the other two instabilities have not been identified in experiments, but have been predicted by various theories and computer simulations.

In 1982, a major advance occurred when an improved theory developed at NRL showed that the sausage mode should not, after all, be unstable for a beam freely propagating in air. Previous theories, including our own, had neglected an important stabilizing effect associated with the tendency of the air conductivity profile to adjust to beam distortions. The new result is consistent with available experimental data and, after careful reexamination, with the simulations. So we were left with two instabilities to be concerned about instead of three.

The hollowing instability has been resistant to analytic theory, but a great deal was learned about it in 1982 by using our particle simulation code SIMMO in an extensive series of computer experiments. Previously it had been thought that this instability would always occur when there is a large return current flowing in the air plasma channel, but we found that this is only one of several conditions needed to trigger the instability. When this instability occurs, it proceeds with great violence and rapidity. However, the instability could be completely avoided by careful choice of parameters, such as the beam radius and rise time. Our results indicate that experiments to date should be stable to this mode, which is probably why it has not been observed. However, the instability is likely to occur in the next generation of experiments, unless parameters are adjusted to control it.

The hose instability has been studied at many laboratories over the last ten years. Theory indicates that it cannot be completely stabilized. The object of investigation is to determine the best choice of beam parameters to minimize the growth rate of the instability, and thus permit the use of the longest possible beam length (since the instability is convective and grows from the head of the beam back toward the tail). With the collaboration of Drs. R. Hubbard and S. Slinker of Jaycor, and Dr. W. M. Sharp of Science Applications, Inc., we have developed the first exact (Vlasov) treatment of hose particle dynamics as well as carefully benchmarked approximate models, and are presently engaged in extensive surveys of prospective parameters, comparison with available experimental data, and preparation for the next generation of experiments.

[Sponsored by DARPA]

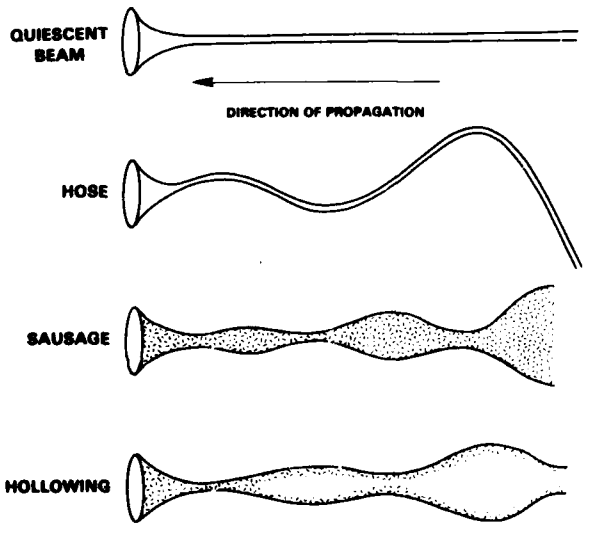

Fig. 3 — Types of beam instabilities. The trumpet shape is a characteristic of the head of the beam before the space charge has been neutralized by ionization of the air.

REFERENCES

1. W.M. Sharp, M. Lampe and H.S. Uhm, "Multi-component Model of the Resistive Hose Instability," *Phys. Fluids* **25**, 1456 (1982).

2. G. Joyce and M. Lampe, "Numerical Simulation of the Axisymmetric Hollowing Instability," NRL Memorandum Report 5053, April 1983.

Radiation Dynamics of Laser-Heated Plasmas, by D. Duston, R.W. Clark, J. Davis, and J.P. Apruzese, *Plasma Physics Division*

The interaction of an intense laser beam with a thin planar target results in the creation of a hot, dense plasma which radiates strongly over a broad band of frequencies. Previous theoretical models of laser-target interaction have tended to concentrate on the fluid aspect of the problem and have relegated radiation to a secondary role. Since the plasma is optically thick to much of its emitted radiation, that is, photons are absorbed and re-emitted many times before they escape, the transport of radiation can play a major role in the overall dynamics. We have therefore constructed a radiation-hydrodynamics model [1] of a laser-heated plasma in which a detailed description of the ionization-radiation dynamics is solved self-consistently with the equations of hydrodynamics on a one-dimensional numerical grid.

Our ionization model [2] calculates the population densities of the ground state and many excited states of each target ion using a system of rate equations with accurate atomic collisional rate coefficients. The radiation transport calculation treats radiation from three sources: line emission, from bound-bound transitions; recombination radiation from bound-free transitions; and bremsstrahlung, from free-free transitions. In transporting the line photons, the effect of line shape, which at lower densities is Doppler-broadened and at higher densities is collisionally broadened, is taken into account.

Photon collisions with the inner-shell electrons of the target ions are treated in an innovative way. Since this model explicitly tracks the population density of each ionization state in time and space, it uses photoionization absorption edges that are functions of the ionic charge state. This allows it to calculate the photon absorption more accurately than the more usual cold plasma approximation in which absorption edges characteristic of the neutral atom are used. At present, the model is capable of describing planar targets of carbon or aluminum, and an iron model is nearing completion.

Figure 4 illustrates several of the more important physical processes that play a role in laser-plasma interaction experiments. Initially, an intense laser beam is incident on a planar target. The laser light is strongly absorbed at the critical surface of the resulting plasma: this is where the laser frequency matches the electron plasma frequency. Strong local heating occurs in this region, producing highly ionized atoms which radiate x-rays into and away from the target. Electron thermal conduction, shock waves, and x-rays transport energy beyond the critical surface; this causes the target material to ablate into the blow-off region and creates a steep density

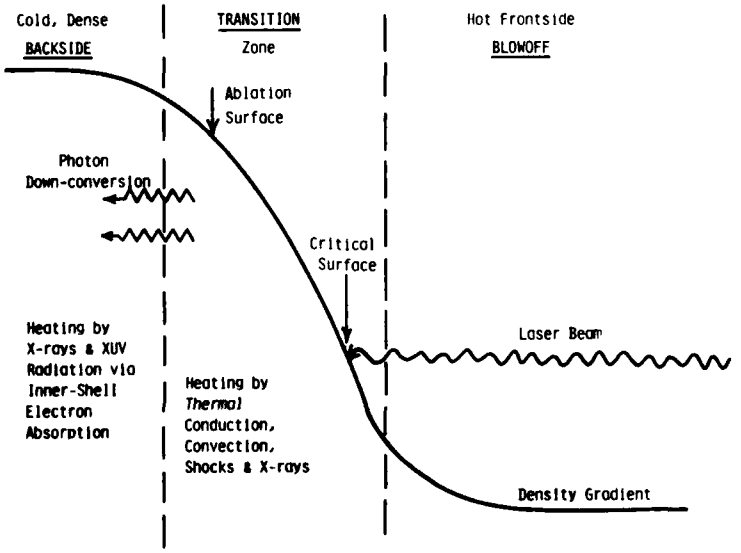

Fig. 4 — Major physical processes taking place in laser-foil interaction at low irradiances

gradient in the plasma. Our simulations have shown that radiation becomes the dominant heating mechanism past the ablation surface. This radiation consists not only of x rays emanating from near the critical surface, but also of secondary photons down-converted in frequency, created when x rays from the front surface are reabsorbed in the transition zone. The cold, dense, backside region absorbs this incident radiation predominately by inner-shell electron photoionization.

A major advantage of our detailed ionization-radiation model is that it allows us, for the first time, to calculate self-consistently the broadband radiation spectrum from the backside as well as from the frontside of the target. In Fig. 2 the time-integrated frontside spectrum is shown for a 3-ns Nd:glass laser pulse ($\lambda = 1.06\ \mu$m) of intensity 10^{13} W/cm^2 incident on an 8 μm-thick aluminum foil. The spectrum has many emission lines superimposed on a continuum. The free-free and bound-free components of the continuum are shown as broken lines. The isolated group of lines around 2.0 keV are the Lyman series lines of the *K*-shell ions, Al XII and Al XIII. The remaining lines are from bound-bound transitions in *L*-shell ions.

Figure 6 shows the full time-integrated rearside spectrum. Since photons from the frontside of the foil must pass through cold, dense plasma to escape in this direction, only photons above 1.0 keV can shine through the foil; almost all those below 1.0 keV are reabsorbed by inner-shell

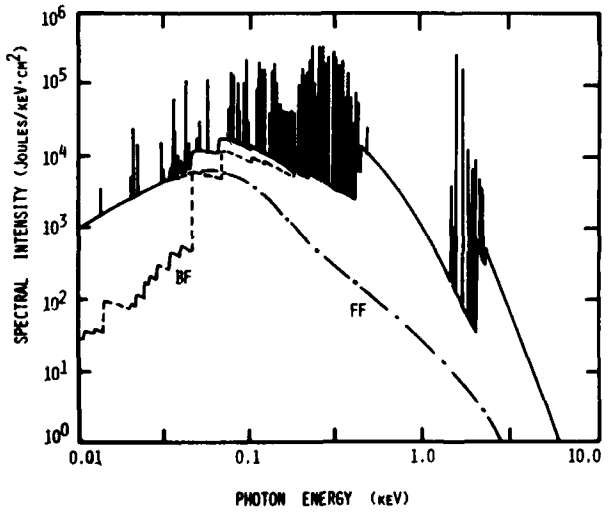

Fig. 5 — Full time-integrated spectrum from the frontside of a laser-heated aluminum foil. The bound-free (BF) and free-free (FF) components of the radiation are identified.

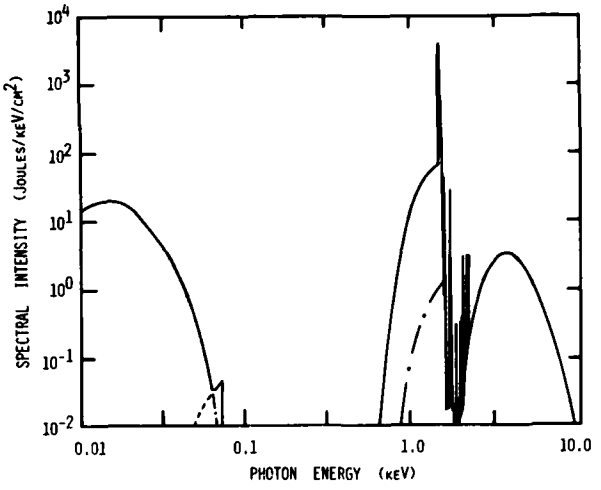

Fig. 6 — Full time-integrated spectrum from the rearside of a laser-heated aluminum foil

photoionization. The radiation at low photon energies is actually emitted from the low temperature backside region, and resembles a blackbody spectrum at about 5 eV.

The model has also helped to explain an observation which has perplexed previous workers. It was believed that the backside of the foil was heated by x rays from the front, and it was expected that the backside temperature would rise with the laser pulse, and fall soon after the pulse ended. In experiments, the temperature rise was delayed with respect to the beam pulse, and persisted after the laser beam terminated. Our model explains this as being due to *ionization burn-through* of the dense plasma. X rays from the frontside are stopped in a relatively thin layer, dictated by the *K* absorption edge. As the plasma heats and ionizes, the edge shifts, and the layer becomes transparent to the x rays. In this way, the x rays burn their way through the plasma, and the time they take to do so accounts for the delay in the heating of the backside.

Our model could readily be modified to include heating effects from drivers other than lasers, such as ion or electron beams and noncoherent radiation sources. This extends the capabilities of the model to many problems associated with heated plasma foils or slabs. In addition, we are extending the model to other materials to allow greater flexibility in the types of problems we can address using this powerful new computational tool.

[Sponsored by DNA]

REFERENCES

1. D. Duston, R.W. Clark, J. Davis and J.P. Apruzese, "Radiation Energetics of a Laser-produced Plasma," *Phys. Rev.* **A27**, 1441 (1983).

2. D. Duston and J. Davis, "Soft x-ray and x-ray Ultraviolet Radiation from High-density Aluminum Plasmas," *Phys. Rev.* **A23**, 2602 (1981).

Field Distribution for a Focused Reflected Gaussian Beam, by W.H. Carter, *Space Systems Division* and T.J. Wieting, *Condensed Matter and Radiation Sciences Division*

An understanding of the phenomena associated with absorption of high-power electromagnetic waves by surfaces is important for many applications; for example, damage effects of laser weapons; damage in laser mirrors; welding and cutting of metals with laser beams; and the annealing of semiconductor materials. Some of the important interaction processes take place in the air just outside the surface. In an experiment at NRL in which microwaves were focused onto a surface, the electric fields were large enough to cause breakdown of the adjacent air and much of the electromagnetic energy went into the resulting air plasma.

The experiment (Fig. 7) was designed to measure the coupling of energy from a 35-GHz pulsed-microwave beam focused onto a plane metal surface inclined at 45° to the beam. A plasma having a distinct spatial structure was seen in front of the surface (Fig. 8.)

In support of this experiment, we have performed an analysis of the electric field distribution in the neighborhood of the irradiated surface. To simplify the algebra, the incident beam was assumed to be a Gaussian beam corresponding to the output of a laser operating in its lowest order mode. The incident beam was represented by an angular spectrum of homogeneous plane waves. The plane wave amplitudes were calculated analytically using the asymptotic expression for the superposition integral in the far field (many wavelengths from the focal point) and the assumed Gaussian far-field angular dependence. The complex plane-wave amplitudes calculated in this manner were substituted into the superposition integral to calculate numerically the field distribution in the near field about the focal point. The beam was then assumed to be incident on a perfect conductor at 45° and focused onto the surface.

We first calculated the amplitude of the transverse component of the electric field in the plane of incidence for the incident beam alone. Using the well-known boundary conditions for this field component at the surface, and assuming that the beam was reflected without loss, we calculated the field of the reflected beam. The fields of the incident and reflected beams were then

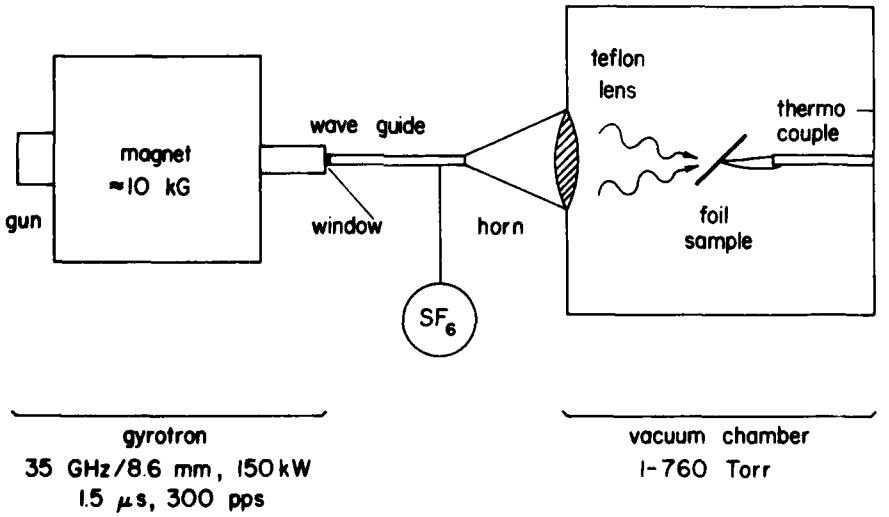

Fig. 7 — The experiment

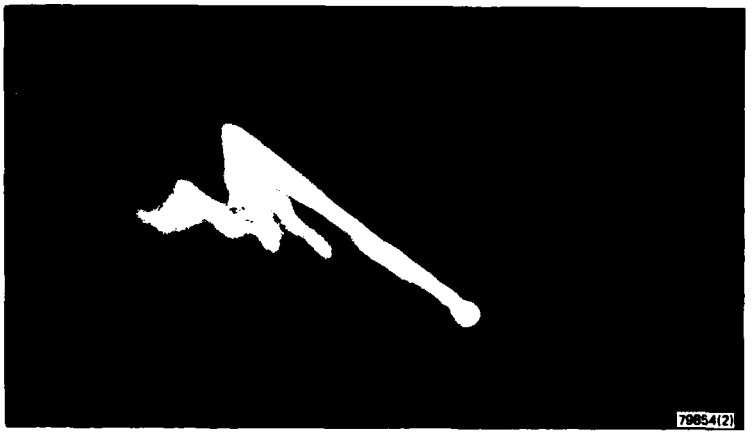

Fig. 8 — Air plasma created by microwave beam incident on surface at 45°

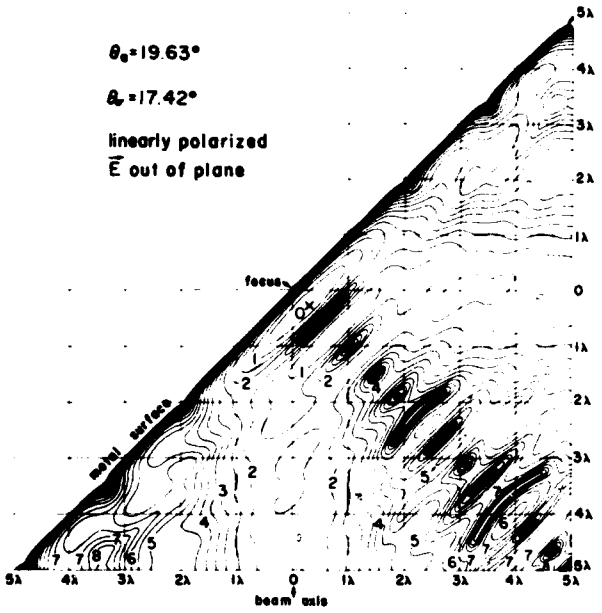

Fig. 9 — The magnitude of E_y in the interference pattern near the surface of the reflector. The contours represent loci of constant intensity. The intensity is proportional to exp (-n/2), where n is the contour symbol.

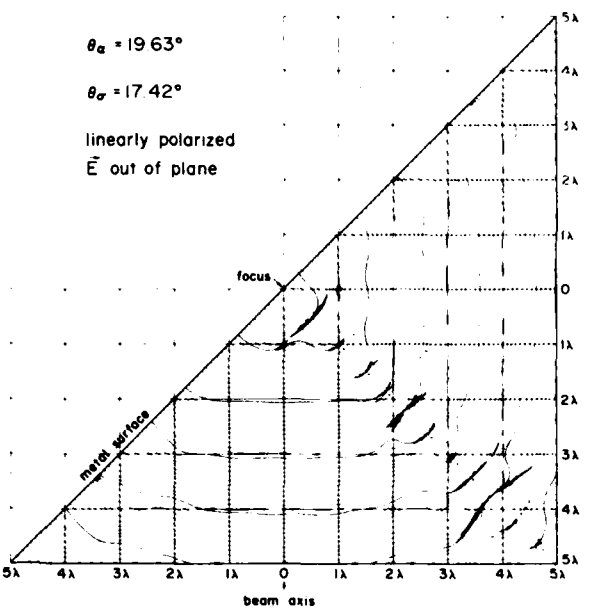

Fig. 10 — The phase of E_y in the interference pattern near the surface of the reflector. The contours indicate the loci of constant phase at 30° intervals.

added numerically and plotted to obtain the standing wave patterns shown in Figs. 9 and 10. The location of the plasma in the experiment corresponded closely to the regions of high electric field in Figs. 9 and 10, a strong indication that the plasma is the result of air breakdown due to the fields near the surface.

The experiments are continuing and we shall extend the calculations to include the effects of the longitudinal component of the electric field, near-field effects, and polarization in the plane of incidence.

[Sponsored by ONR]

REFERENCE

1. W.H. Carter and T.J. Wieting, "The Field Distribution of a Focussed Gaussian Beam Reflected at 45° for a Conducting Plane and its Effect in Plasma-Ignition Experiments," *J. Appl. Phys.* **54**, 519 (1983).

MATERIALS MODIFICATION and BEHAVIOR

MATERIALS MODIFICATION AND BEHAVIOR

The properties of materials determine the performance of all devices, machines and structures. The properties of common materials can often be modified to give greatly increased performance, as shown by these examples of NRL research.

Radiation-Thermal Aging of Polymers, by F.J. Campbell, *Condensed Matter & Radiation Sciences Division*

To select the most suitable polymers for service as wire insulation in nuclear power plants, it is necessary to understand the synergistic reaction that can occur when the materials are exposed simultaneously to radiation and heat. We have studied this effect as part of a larger program to develop methods for rating thermal endurance of electrical insulation for shipboard motors and generators. The aim of the study was to determine whether the life expectancy of these materials could be accurately predicted by the conventional practice of selecting these materials on the basis of their thermal aging ratings and reported radiation tolerances.

Experiments were conducted in which the materials were exposed simultaneously to heat and radiation. The test samples consisted of insulated magnet wires that are used in the windings of stators and rotors of rotating machinery in naval vessels. The thermal aging characteristics of these materials had been studied previously at NRL [1]. The NRL ^{60}Co Source was used to expose the wires to gamma radiation at exposure rates ranging from about 10^3 to 10^6 Roentgens per hour. A specially designed oven (Fig. 1) allowed the samples to be heated to 300°C while being irradiated.

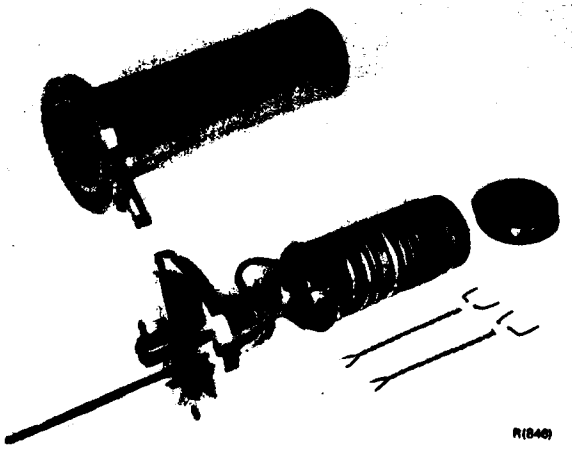

Fig. 1 — Radiation-thermal exposure assembly. The test samples, in the form of twisted insulated wires (lower right) fit into the oven (center) which then goes into the test cell (upper left). The whole assembly is then placed in the shielding pool of the NRL ^{60}Co source.

Each of the wires was coated with a different polymer enamel; namely, polyimide, polyester, polysiloxane, polyvinyl formal, and fluorocarbon. Aging temperatures and approximate exposure times per test cycle were selected from the thermal life curves available on these insulated wires. Ten samples in the form of twisted pairs were tested for each data point. After each exposure the integrity of the polymer insulation was tested by applying 1000 V to the wires.

The results of these experiments are shown in Table 1. In environments combining radiation and high temperatures, the lifetimes of insulating polymers differed greatly from lifetimes in either the heat or radiation environment alone or when exposed to heat and radiation sequentially. The lifetime of each polymer was affected differently; some lifetimes were shortened, others lengthened by exposure to certain environmental combinations. For example, the simultaneous exposure of polyimide, polyester, polysiloxane, and polyvinyl formal insulations to heat and radiation produced considerably longer lifetimes than were recorded for thermal exposure alone. The radiation exposure rate also affected the results. At the same temperature, the life of polyvinyl formal decreased as the exposure rate increased; on the other hand, the life of polyester increased with the exposure rate. These results indicate the need to duplicate the complete environment when evaluating the suitability of polymeric materials. It is not sufficient to select materials on the basis of tests in which radiation exposure precedes or follows thermal aging.

It is possible to explain why equivalent exposures affect each polymer differently by considering the chemical reactions that occur in the polymers. The addition of energy to a polymer chain creates excited states, bond ruptures, and free radicals. The recombination of the free radicals will occur in different formations, depending upon the structure of the molecule. Polymeric molecules can undergo either *crosslinking* into a large network or *chain scission*, that is, degrading into many shorter chain fragments. These mechanisms can occur simultaneously in many kinds of structures. The predominance of one mechanism over the other determines the change in the properties of the material. It is reasonable to expect that for some materials the right combination of heat and radiation could produce a kinetic balance between crosslinking and scissioning, so that the corresponding physical or electrical properties would be only minimally affected, if

Table 1 — Effects of Thermal Environment and Combined Thermal and Radiation Environments on Magnet Wire Insulation

Insulation Material	Thermal Aging		Simultaneous Radiation and Thermal Aging			
	Aging Temp. (°C)	Life (H)	Exposure Rate (MR/H)	Total Exposure (MR)	Life (H)	Percent of Thermal Life
Polymide	300	940	0.37	2900	7750	820
Polyester	200	3160	0.40	2540	6350	200
	200	3160	0.02	25	1260	40
Polysiloxane (Modified)	240	350	0.50	290	570	160
	240	500	0.40	124	310	60
Polyvinyl Formal	160	630	0.40	2200	5510	870
	180	280	0.50	280	560	200
	200	90	0.40	120	300	330
	180	280	0.09	900	>10,000	>3500
Fluorocarbon	180	>10,000	0.014	1.50	105	<1.0
	270	>10,000	0.015	0.75	50	<0.5
	13	∞	0.015	34.00	2280	-
	13	∞	0.320	240.00	760	-

at all. This appears to be borne out by the results of our study.

Further work should lead to a better understanding of these mechanisms and the construction of kinetic models which could be used to develop reliable accelerated aging procedures.

[Sponsored by NAVSEA]

REFERENCE

1. E.L. Brancato, L.M. Johnson, F.J. Campbell, and H.P. Walker, "Reliability Prediction Studies on Electrical Insulation: Navy Summary Report." NRL Report 8095. July 13, 1977

NMR Spectroscopy of Synthetic Metals, by H.A. Resing, M.J. Moran, and D.C. Weber, *Chemistry Division*

There is a continuing search for materials that would combine the electrical conductivity of metals with the favorable properties of polymers, such as flexibility, high strength-to-weight ratio, ease of fabrication and low cost. Such *synthetic metals*, with a conductivity of up to two-thirds the conductivity of copper, have been produced in the laboratory by the action of certain very reactive chemicals on a broad variety of polymeric materials. To develop technically useful synthetic metals, we need analytical techniques to understand the chemistry and physical methods to determine the electronic structure and conductivity of these materials. To this end we have been applying nuclear magnetic resonance spectroscopy (NMR) to the study of conducting polymers.

A conducting polymer may be produced either by adding electrons to a framework through the use of a *donor* dopant or by withdrawing electrons from the framework by means of an *acceptor* dopant. The electron transfer is accompanied by the incorporation of part of the reagent responsible for the doping into the body of the polymer. In layered hosts, such as graphite, the doping process is known as *intercalation.* Our principal interest is in the acceptors because of their controversial mode of action and also because they appear to offer the best hope for chemically stable, and therefore technically useful conductors. In particular, we have been using our NMR facilities to study intercalated graphite.

NMR spectroscopy involves the application of a radiofrequency (RF) magnetic field to a sample in a uniform, static magnetic field and the detection of resonances in the absorption curve as a function of frequency. The resonances allow the identification of chemical elements in the sample and provide information about the chemical arrangement. Difficulties arise when NMR is applied to conductors because eddy currents are induced which shield the interior of the sample from the RF field; this results in weak NMR signals. In intercalated graphite, the conductivity

perpendicular to the layers is often much lower than the conductivity in the plane of the layers; thus, by aligning the magnetic vector of the R.F. field in the graphite plane the shielding by eddy currents is greatly reduced. This is illustrated in Fig. 2. A 16-times greater gain is required to obtain the ^{19}F signal from AsF_5 intercalated in graphite when the magnetic vector is perpendicular to the graphite plane than when it is in the plane. This measurement actually allows us to determine the conductivity in the graphite planes.

Graphite compounds with reagents such as NO_2PF_6 or NO_2AsF_6 are well understood systems. NO_2PF_6 oxidizes the graphite by the reaction:

$$NO_2\,PF_6 + C_{20} \rightarrow NO_2\ (\text{gas}) + C_{20}^{+}\,PF_6^{-}. \quad (1)$$

The PF_6^- ions create a space for themselves between adjacent layers of the graphite, thus separating the graphite sheets. The NO_2^+ ion takes an electron from the graphite and bubbles off as gas. The ^{19}F and ^{31}P NMR spectra in Fig. 3 show that this reaction truly deposits PF_6^- ions in the graphite; the spectra are identical to those seen for PF_6^- in solution. Both ^{19}F and ^{31}P have nuclear spin 1/2. The ^{19}F doublet shows that all the fluorine nuclei are chemically equivalent and bound to a nucleus of spin 1/2; the ^{31}P septet shows that only one isotope of phosphorous is present and that it is bound to six nuclei of spin 1/2, that is, to six fluorine atoms. NMR spectroscopy thus gives a very clear picture of the intercalation process.

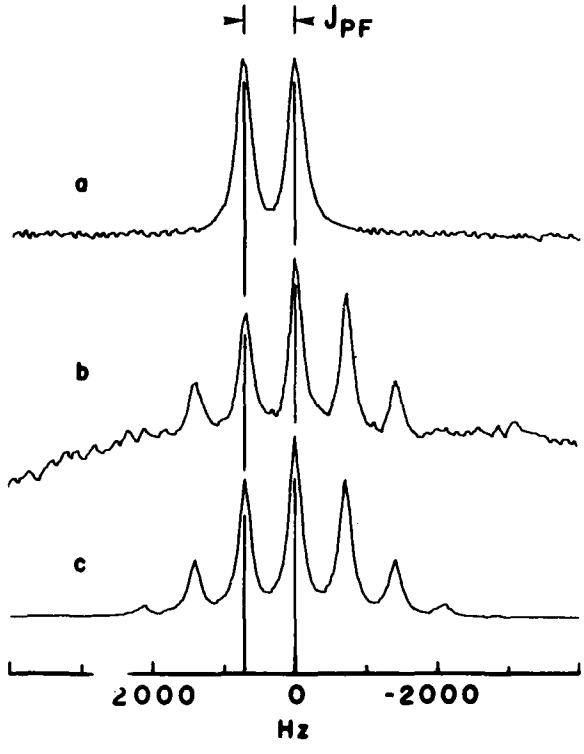

Fig. 3 — NMR spectra of graphite intercalated with $NO_2\ PF_6$. Fluorine doublet shows bonding to one phosphorus atom. Phosphorus septet shows bonding to six fluorine atoms.

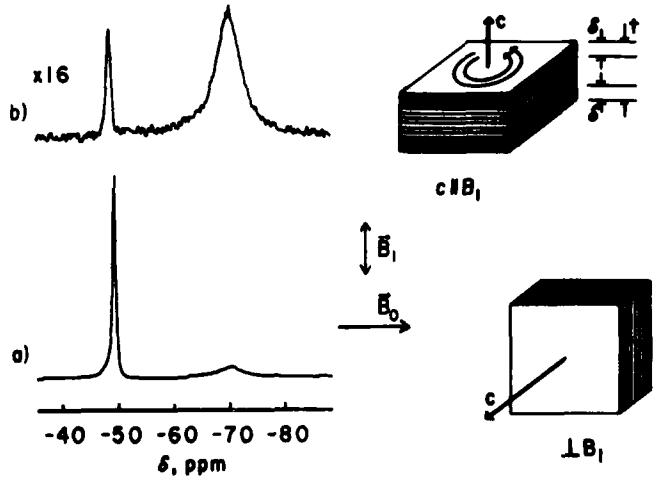

Fig. 2 — ^{19}F NMR spectra for AsF_5 intercalated in highly- oriented pyrolitic graphite. The peak at −49 ppm is from AsF_5 within graphite and the peak at -70 ppm is from AsF_5 gas. Steady magnetic field B_0 is parallel to the graphite planes. Oscillating magnetic field (B_1) is parallel (a) or normal (b) to planes.

With the substitution of NO_2AsF_6 for NO_2PF_6, the reaction shown in Eq. (1) was again carried out on graphite. Following the reaction, the system was exposed to AsF_3 gas. The ^{19}F NMR spectrum of this graphite compound is shown in Fig. 4. Having nuclear spin 3/2 makes the central ^{75}As of the AsF_6 ion sensitive to inhomogeneous electric fields; instead of the uniformly intense quartet expected for the ^{19}F NMR spectrum of the AsF_6^- ion in solution, we see a broad doublet for the intercalated AsF_6^- ion, and we accept this as the signature of AsF_6^- in the intercalated state. The relatively sharp lines of the 1:2:1 triplet belong to AsF_3. The AsF_6^- spectrum is essentially the same whether AsF_3 is present or not.

The intercalant AsF_5 leads to graphite compounds or polyactylene compounds of the highest conductivity. However, the mode of action is controversial; it is unclear whether there is a simple charge transfer or whether the reaction is:

$$3\ AsF_5\ (gas) + 2\ C_n \rightleftarrows 2\ C_nAsF_6 + AsF_3. \quad (2)$$

The ^{19}F spectrum for graphite intercalated with AsF_5 is given in Fig. 2. Intercalated AsF_5 shows a single sharp line, while that of the external gas is somewhat broader. But if the reaction shown in Eq. (2) goes to completion, AsF_6 and AsF_3 should be present, and we have seen what to expect in Fig. 4. Clearly, it makes a difference if one starts on the left or on the right of reaction (2). Electrical conductivities are the same, but the NMR spectra are different.

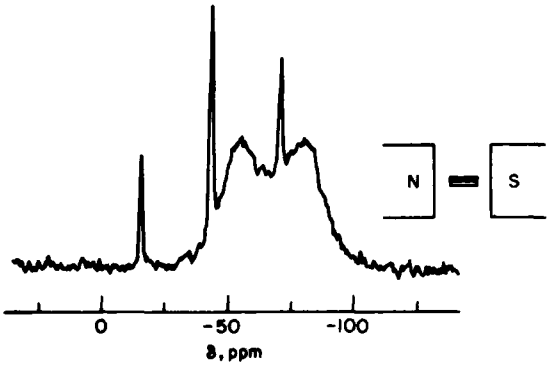

Fig. 4 — The 56.4 MHz ^{19}F NMR spectrum, of a second-stage graphite intercalation compound of AsF_6^-, (broad doublet) subsequently intercalated with AsF_3 (sharp triplet). The two species do not exchange fluorine atoms rapidly enough to give a single sharp line, as in Fig. 2.

The goal of this research is to understand the conduction mechanism in highly conducting polymers. So far we have concentrated on measuring the concentration of the species intercalated between the layers. We also use two other NMR techniques, each of which gives a measure of the hole carrier concentration in the AsF_5- graphite system:

1. the ^{13}C NMR shift which may be calibrated by compounds with known concentration (for example, compounds containing AsF_6^- as the only charged intercalated species)

2. a low frequency electron spin resonance (ESR) technique by which the density of states at the Fermi level is measured.

[Sponsored by ONR]

The Piezoelectric Properties of Oxygen-Modified Antimony Sulfur Iodide, by R.Y. Ting, *Underwater Sound Reference Detachment*

Antimony sulfur iodide (SbSI) is a potentially important material for Navy underwater sound transducers. Its piezoelectric *g*-constant (electric field generated per unit applied pressure), its mechanical strength and several other properties far exceed those of traditional materials such as barium titanate and PZT. However, the Curie temperature, above which piezoelectric activity disappears, is only 20°C which makes SbSI unsuitable for most underwater sound applications. Recent studies at NRL have shown that this transition temperature can be significantly increased by the technique of molecular alloying.

The approach is to replace one of the atoms in the SbSI molecule with another one from the same valence group. This substitution directly alters the unit cell dimensions by changing the length of the chemical bonds, and consequently affects the properties of the material. So far, the most promising substitution has been to replace sulfur with oxygen. A comprehensive range of ferroelectric and piezoelectric measurements on oxygen-modified SbSI have been carried out as a function of temperature and hydrostatic pressure using an acoustic reciprocity technique. Figure 5 shows the measured piezoelectric *g*-constant of a series of $SbS_{1-x}O_xI$ samples, where x denotes the weight fraction of the oxygen that replaces the sulfur. At low temperatures, the addition of 4%

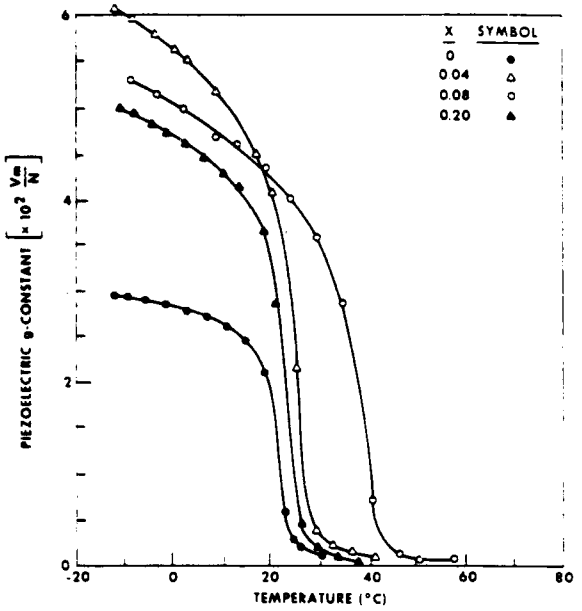

Fig. 5 — Piezoelectric *g*-constant of oxygen-modified SbSI as a function of temperature

oxygen resulted in almost a two-fold increase in the *g*-value over that of pure SbSI. The rapid decrease of *g* with increasing temperature is characteristic of the material, and is related to the Curie transition. This transition temperature was increased by the addition of oxygen; the optimum oxygen concentration seems to be between 4% and 8%.

SbSI is a ferroelectric material having axial polarization. A phenomenological model was developed for this material based on the theory of Landau and Devonshire for alloys. The simplified form of Landau-Devonshire free energy was modified by adding an electrostriction term to account for the piezoelectricity of SbSI. The expression was a weighted sum of the free energies of the constituents and an interaction term that is quadratic in the concentration of the constituents. The interaction coefficients in the model were shown to represent a complete set of properties of an interacting ferroelectric material. The experimental results were used to fit this model, which was then applied to predict the properties of any alloy of $SbS_{1-x}O_xI$ within the range of $0 < x \leqslant 0.2$. The agreement between experimental results and the theoretical prediction was excellent, as shown in Fig. 6 where the Curie temperature is plotted against the oxygen concentration. The molecular alloying technique increased the Curie temperature to a maximum of 34°C for $SbS_{0.96}O_{0.04}I$.

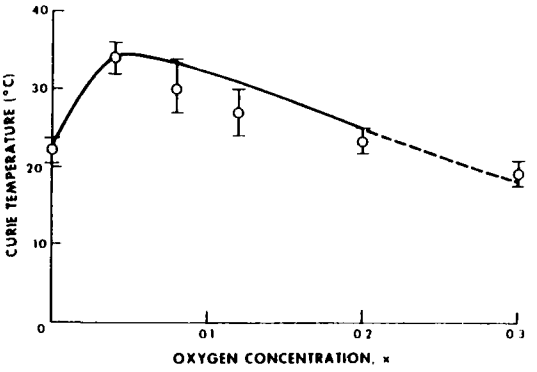

Fig. 6 — The dependence of Curie temperature on oxygen concentration in $SbS_{1-x}O_xI$ alloys. Theory — Experimental results.

Research continues at NRL on more complex molecular systems in an attempt to raise the Curie temperature to 50°C. This would make the material a viable candidate for underwater acoustic applications.

[Sponsored by ONR]

Oxidation of Yttrium-Bearing High-Temperature Alloys, by J.A. Sprague, G.R. Johnston, V. Provenzano and F.A. Smidt, Jr., *Material Science and Technology Division*

Alloys of the MCrAlY-type (where M = Co, Ni, Fe or combinations thereof) are used widely as protective coatings on hot-stage components of gas turbines. The durability of such coatings in the extremely aggressive atmospheres that exist in these engines depends critically on the morphology and adherence of the surface oxide. The high temperature oxidation of these alloys has been extensively studied at NRL and other laboratories, mostly in the temperature range 1000 to 1200°C. However, the principal concern for gas turbines operating in a marine environment is hot corrosion by sulphate salt deposits which form during engine operation at temperatures between 700 and 850°C. We have been conducting a research program in collaboration with the University of Pittsburgh to elucidate the mechanisms of both oxidation and hot corrosion in the temperature range 700 to 1000°C. Part of our 1982 program has focused on the effects of yttrium on the oxidation of the alloy Co-22%Cr-11%Al.

Yttrium, or other highly active elements such as hafnium and cerium, are added to coating alloys to improve oxidation resistance, principally by promoting adherence of the protective oxide to the surface of the alloy. There have been a number of suggestions as to how the active element brings this about. These include: pegging of the oxide scale to the alloy surface by protrusions extending into the alloy; eliminating voids at the oxide/metal interface; increasing the plasticity of the oxide scale; or altering the diffusivity of oxygen in the oxide. However, it is obvious from a review of the recent literature that no one mechanism adequately explains the role of the active element, and furthermore, that no one mechanism is agreed upon by the researchers in the field of high-temperature oxidation.

We have studied cast alloys of Co-22Cr-11Al (CoCrAl) and Co-22CR-11Al-0.5Y (CoCrAlY). The castings had microstructures similar to those found in vapor-deposited CoCrAl coatings (*1981 NRL Review*, pp. 131-132). The CoCrAl microstructure consisted of a matrix of β-CoAl (an ordered cubic phase) and precipitates of a solid solution of 25% Cr and 2% Al in Co (α-phase). The CoCrAlY microstructure had a complex yttride phase which was isolated at a small fraction of the grain and phase boundaries.

In the earlier part of this study, oxide films which formed on cast CoCrAlY oxidized at 700°C for up to 50 min were examined by transmission electron microscopy (TEM) and x-ray microanalysis. The oxide layer was found to be thinner over the β-phase and thicker over the α-phase. While the oxide films themselves contained no detectable yttrium concentrations, yttrium-rich pegs formed on the preexisting yttride precipitates and extended from the oxide film into the alloy. Further examination of oxidized CoCrAlY (Fig. 7) and CoCrAl (Fig. 8) by both TEM and scanning electron microscopy (SEM), has revealed the presence of voids at the oxide/metal interface. When either the time of oxidation or the temperature was increased the size of the voids also increased while their number density decreased (Fig. 7). In both CoCrAl and CoCrAlY, the voids formed preferentially over the α-phase in the alloys, particularly at the boundaries between α- and β-phases. This observation refutes the theory that yttrium increases the oxide adherence on CoCrAl by eliminating these voids.

To examine further the effect of yttrium on the oxidation process, specimens of CoCrAl were

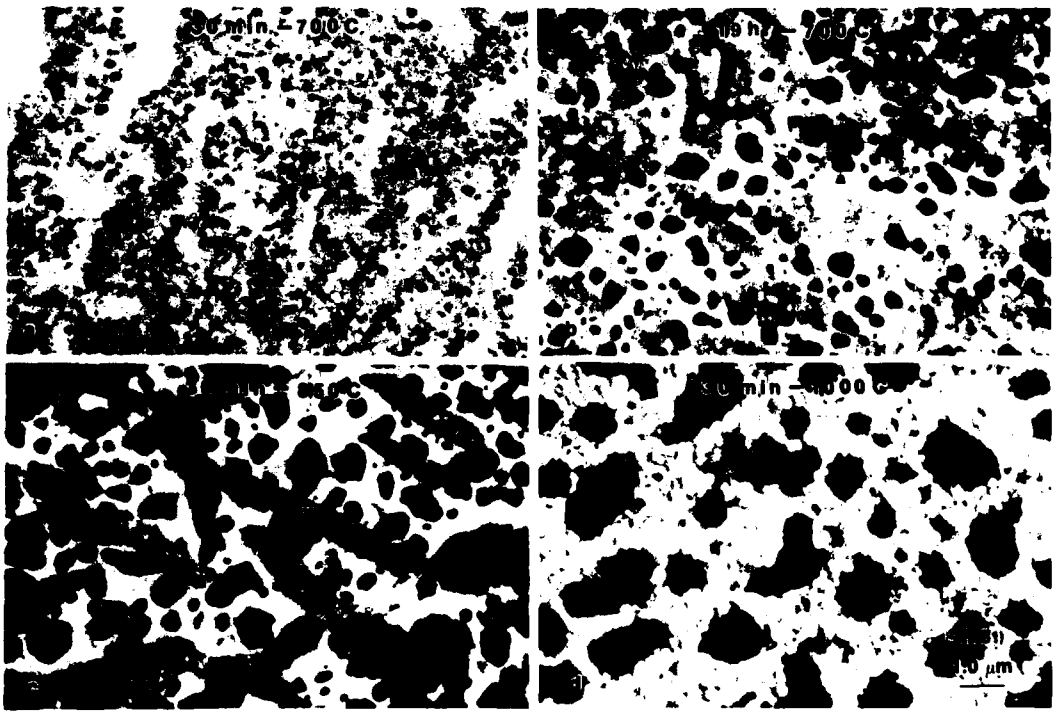

Fig. 7 — Secondary electron micrographs showing the development of interfacial voids (dark areas) during oxidation of Co-22Cr-11Al-0.5Y

implanted with yttrium ions (with 150 keV energy, 2×10^{16} ions/cm^2 dose rate) which produced a supersaturated solid solution of yttrium on both α- and β-phases. All the yttrium was located within 100 nm of the implanted surface, with a peak concentration of approximately 2% at 50 nm depth.

The oxidation behavior of the Y-implanted CoCrAl was quite different from that of the cast CoCrAlY. Figure 8a-c shows a series of scanning electron micrographs of a Y-implanted CoCrAl specimen which had half of its surface masked during implantation, and was then oxidized for one hour at 700°C. The unimplanted region of the specimen exhibits a similar degree of void formation to that observed for CoCrAlY (Fig. 7) but in the Y-implanted region the void formation is almost completely suppressed. TEM analysis showed that Y_2O_3 was present in the oxide films formed over both α-and β-phases, and that no yttrium-rich pegs were formed under the oxide.

In addition to changing the composition of the near-surface regions of an alloy, ion implantation also produces radiation damage, displacing atoms from their normal sites. To examine this effect, specimens of CoCrAl were implanted with 5×10^{16} cobalt ions/cm^2 (also at 150 keV) to produce damage levels similar to those produced by the yttrium implantation. Figure 8d shows that voids were formed in the Co-implanted specimen, although they were smaller and more numerous than in the unimplanted CoCrAl. This indicates that void suppression by Y-implantation is a chemical effect and not a consequence of radiation damage.

These observations suggest that the effect of yttrium on the oxidation of CoCrAl is a sensitive function of the distribution of the element in the alloy. It follows that the effect of yttrium in a vapor-deposited coating is likely to be strongly affected by the processing of that coating.

Further NRL work will attempt to characterize more fully the role of yttrium and other active elements on the oxidation and hot corrosion of CoCrAl alloys. This work should provide a scientific basis for new processes that could lead to better protective coatings.

[Sponsored by ONR]

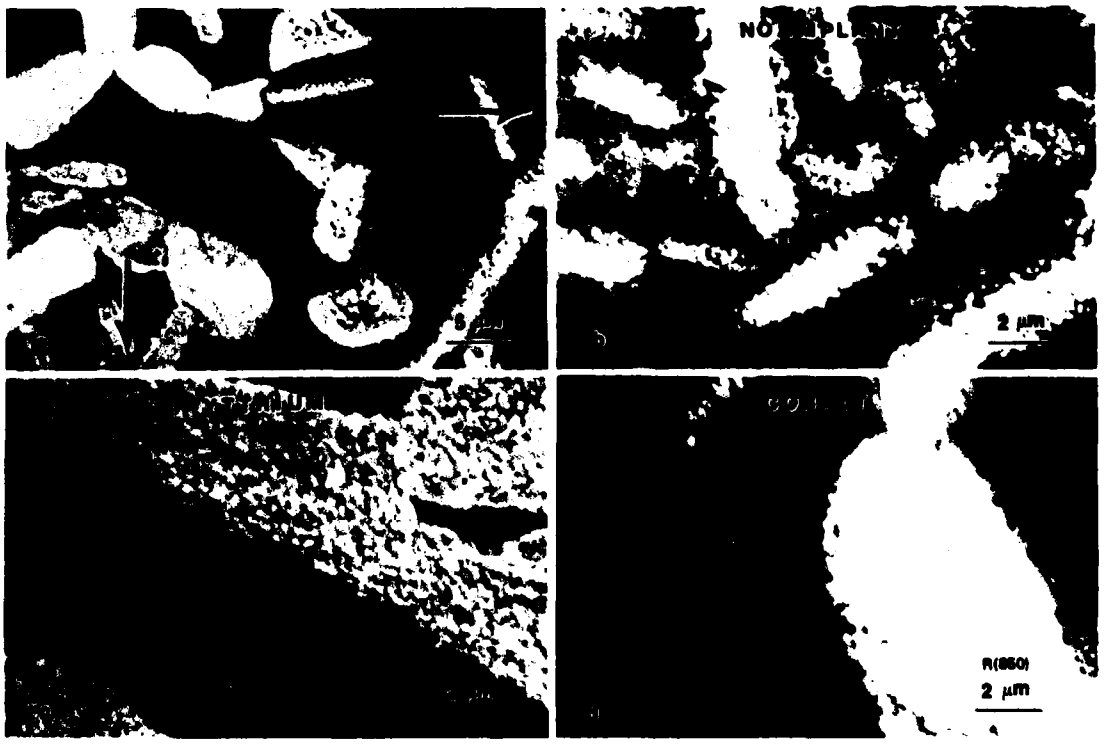

Fig. 8 — Effects of ion implantation on interfacial void formation during oxidation of Co-22Cr-11Al at 700°C for 60 min. (a) Unimplanted (right) and yttrium-implanted (left) areas, low magnification; (b) Close-up of unimplanted area of (a); (c) Close-up of yttrium-implanted area; (d) Close-up of cobalt-implanted area;

Electrodeposition of Refractory Carbide Coatings, by K.H. Stern, *Chemistry Division*

The Navy needs to protect structural alloys against wear and corrosion, especially under the severe conditions that are encountered, for example, in drive shafts and parts of gas turbines. A novel technique for depositing refractory carbide coatings on these alloys has been developed at NRL and is a significant improvement over existing technology.

Refractory carbides possess the required hardness for wear resistance and are not oxidized appreciably below 500°C but they lack the desirable ductility of metals. Consequently, materials scientists have tried several techniques to combine the hardness of carbides with the ductility of metals. One well-known technique is hardfacing, the incorporation of carbide particles into a bulk metal. Other techniques produce carbide coatings on metals, but existing coating methods have not been entirely successful. Plasma spraying, which involves impinging the carbide powder onto the surface to be coated, requires temperatures near 1500°C, is a line-of-sight technique, and tends to produce somewhat porous coatings. Chemical vapor deposition combines two reactive gases to produce the carbide at the surface, but coatings made in this way are usually quite thin.

Because some carbides had previously been prepared electrochemically as small crystals, we believed that refractory carbide coatings might be electrodeposited. We therefore set out to modify techniques used to electrodeposit refractory metals so that the carbide would be deposited instead. The metal-plating procedure consists of dissolving a suitable compound of the desired metal in an alkali fluoride melt, and plating between an anode of the metal and the substrate. For example, when plating tantalum, the metal-bearing compound K_2TaF_7 would be dissolved in FLINAK, the ternary eutectic of LiF, NaF and KF. Critical features of the process include removal of water and hydroxide impurities from the melt, containment in a material (usually nickel) not attacked by the highly corrosive melt, and operation in an inert atmosphere. The usual temperature range is 750-800°C.

Our modification of this method was to add an alkali metal carbonate to the melt, in the expectation that the carbonate would be reduced electrochemically to carbon, which would then react with the metal to form the carbide. It was by no means clear that this would be the only path for reduction of the carbonate, but the initial experiments with tantalum as the metal did indeed produce tantalum carbide coatings on nickel, although the quality was poor. Subsequent improvements in melt purification and adjustments to solute concentration and electrical parameters produced dense, adherent, and hard coatings (Knopp numbers in the 1000-1500 range) with excellent abrasion resistance, and resistance to oxidation in air at temperatures up to 500°C [1]. Figure 9 shows the surface and cross-section of the coating. The composition of the coating is ditantalum carbide (Ta_2C) over a wide range of plating conditions, and the current efficiency of the process is close to 50%. An attractive feature of Ta_2C is its low coefficient of friction, shown in Fig. 10. Tantalum carbide (TaC) has also been plated, but at lower current efficiency.

Fig. 9a — Tantalum carbide (Ta_2C) coating on nickel. The dense and crystalline nature of the coating surface is self-evident.

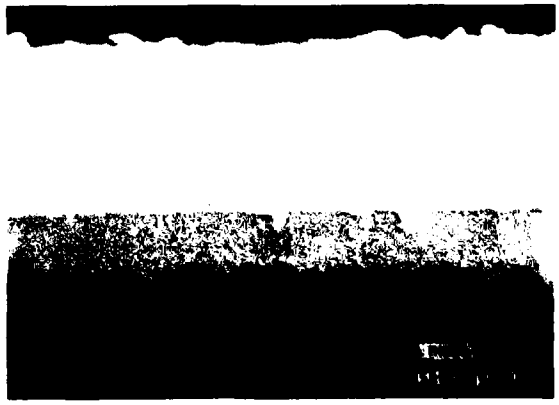

Fig. 9b — Cross section of the Ta_2C coating. The 20-μm-thick coating is bonded to the surface by a 10-μm-thick nickel-tantalum interdiffusion layer (darker gray).

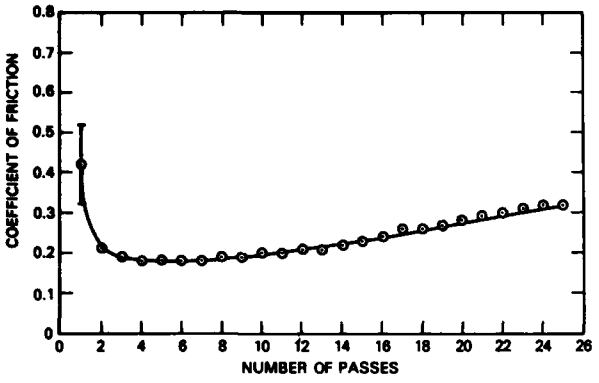

Fig. 10 — Friction coefficient of ditantalum carbide (Ta_2C) on nickel. Each pass represents one measurement.

Tungsten carbide coatings, usually W_2C, with characteristics similar to those of Ta_2C, have also been plated, and in the course of this work the conventional method for plating metallic tungsten has been simplified. Attempts to produce chromium carbide coatings proved unsuccessful because the chromium and carbon did not react below 850°C, and above this temperature the melt evaporated too rapidly.

Our work has opened a new and promising path to the production of hard, wear-resistant coatings which are thermally stable up to 500°C. The advantages of the electrochemical method are the ability to coat complex shapes to virtually any thickness, and the relatively low temperature required. Future work will be directed towards a better understanding of the plating process, further improvements in the properties of the coatings and studies of plating on metals other than nickel.

[Sponsored by ONR]

REFERENCE

1. K.H. Stern and S.T. Gadomski, "Electrodeposition of Tantalum Carbide Coatings from Molten Salts," *J. Electrochem. Soc.* **130**, 300 (1983).

Improved Scuffing Resistance of Gear Steel by Ion Implantation, by N.E.W. Hartley, J.K. Hirvonen and G.K. Hubler, *Condensed Matter and Radiation Sciences Division*

Scuffing is a term used to describe the severe adhesive wear that can occur in high-performance hardened steels under arduous load conditions. This phenomenon is troublesome because of its unpredictable sudden onset, and because of the catastrophic damage which can occur rapidly after scuffing begins, for example, in a helicopter gear box. The beneficial effect of ion implantation in reducing friction and wear in a variety of steels is now well known, but there is little information on how this technique affects resistance to scuffing.

We have investigated the friction and wear behavior of ion implanted AISI 9310 steel under simulated scuffing conditions using a standard Falex friction and wear tester (Fig. 11, inset). AISI 9310 is a case-hardened gear steel containing 3.0% Ni, 1.4% Cr and 0.55% Mn. Conventional wear tests were conducted at low load, and tests were conducted at high load to produce scuffing conditions. Tantalum and molybdenum ions were chosen for implantation into the 9310 steel because they are used conventionally as anti-scuffing additions to alloy steels.

The objective of the low-load tests was to observe the effects of Ta^+ and Mo^+ implantation on the friction and weight loss of 9310 steel. The implantation produced Mo^+ or Ta^+ ion concentrations of 20 at-% in the first 30 nm of the steel surface. The low-load test measures the long-term wear performance and requires a load of 91 kg to be maintained on the rotating pin of the tester for 90 minutes. Figure 11 shows the friction coefficient for 9310 steel as a function of time for Mo^+ and Ta^+ implanted samples and for an unimplanted sample. The rate of weight loss from the pin is tabulated in the inset. Clearly, ion implantation results in a considerable reduction in both wear and friction. For Ta^+ implantation in particular the wear rate was reduced by a factor of 28. A Dektak surface profilometer was used to measure the surface roughness of the worn and unworn zones of the pins. The results (Fig. 12) show that the surface of the Ta^+-implanted sample is considerably smoother than the unimplanted sample. The Mo^+-implanted sample shows a similar improvement, but to a lesser degree.

The objective of the high-load test was to subject the sample to severe scuffing conditions in accordance with ASTM procedures for evaluating lubricants. After an initial wear-in period of 5 min at 114 kg, the load was increased to 318 kg for a further 15 min. Under these conditions the unimplanted steel showed occasional rapid fluctuations in the friction coefficient accompanied by audible squeaking, indicating scuffing events.

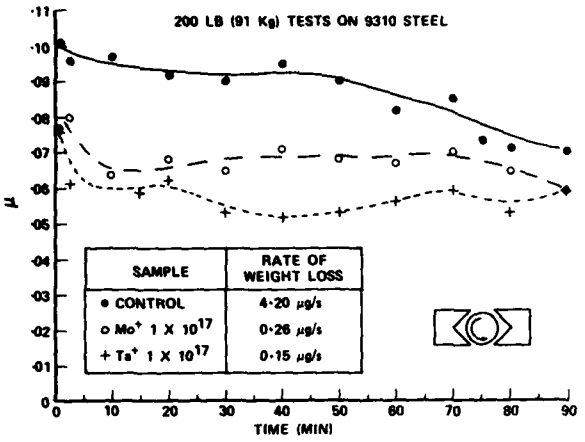

Fig. 11 — Friction coefficient of carburized 9310 gear steel as a function of time for Mo^+ and Ta^+ implantations. Falex wear testing was done in Hercolube A lubricating oil.

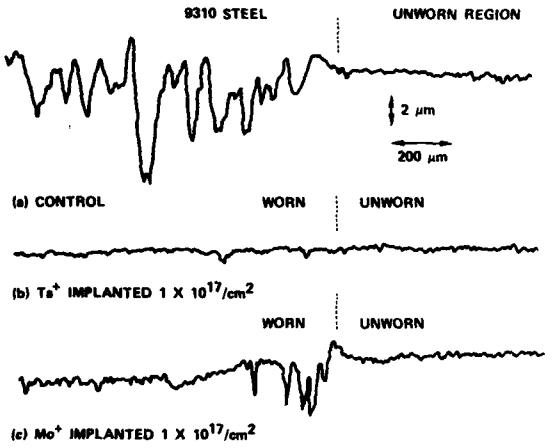

Fig. 12 — Dektak surface profiles of wear zones on implanted and unimplanted test pins of AISI 9310 steel after low load (91 kg) testing

For these high-load scuffing tests, Mo^+ implanted into AISI 9310 steel neither decreased the friction coefficient nor reduced scuffing events significantly relative to the unimplanted samples. However, Ta^+ implantation was quite effective in lowering the friction coefficient, eliminating scuffing events, and preventing excessive wear of the V-blocks and pins. Profilometer traces of the worn surfaces on the pins for the Ta^+ and Mo^+ implants are shown in Fig. 13 relative to the unimplanted control. The profilometer trace of the Ta^+-implanted sample shows a dramatic reduction of wear and an impressively smooth surface.

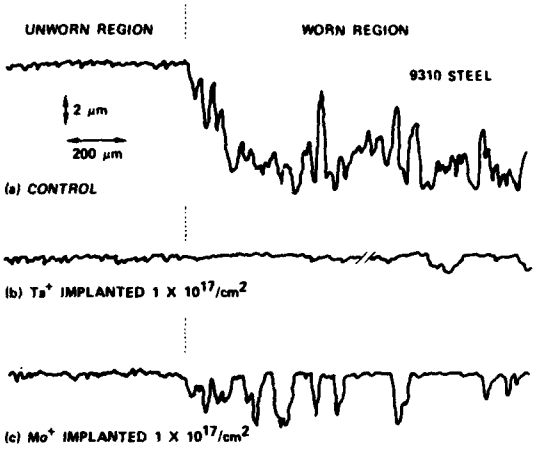

Fig. 13 — Dektak surface profiles of wear zones on implanted and unimplanted test pins of 9310 steel after high-load (114/318 kg) testing

Because scuffing is initiated by very localized plastic flow, the problem reduces to avoiding metal-to-metal contact and eliminating gross deformation. The three ways (either singly or in combination) to prevent scuffing are: to increase the surface hardness; to use extreme pressure additives in the lubricant; and to avoid the formation of the more ductile (austenitic) phase of ferrous alloys. Some of the hardness of case-hardened 9310 steel arises from the trapping of carbon atoms as carbides. Tantalum and molybdenum both form more strongly bonded carbides than either $Cr_{23}C_6$ or Fe_3C. In addition, molybdenum forms a range of oxides which have beneficial lubricious properties. The lowered friction and decreased wear rate observed in ion-implanted 9310 steel may be attributable to these effects.

These results are consistent with other NRL work on 52100 steel carried out by Singer et al. of the Chemistry Division [1]. They found that Ta implantation leads to a large improvement in unlubricated sliding wear resistance. Careful surface analysis by Auger electron spectroscopy showed that the surface was enriched in carbon, and that the Ta was appreciably bonded with the C in TaC. In this case the carbon came from residual hydrocarbons in the vacuum system and combined with Ta at the surface during Ta ion-implantation (gettering). AISI 9310 steel contains considerably more carbon for the Ta to react with, but it is likely that considerable gettering of C occurs as well. Surface concentrations of Ta and C of 20 at.% have been measured in 52100

steel, indicating that a substantial degree of surface hardening by TaC formation has occured [1].

Wear tests of actual Ta-implanted gears are planned. If the tests bear out the laboratory predictions, the reliability of gears used in the Fleet could be substantially improved by ion implantation.

[Supported by NAPC]

REFERENCE

1. I.L. Singer, C.A. Carosella, and J.R. Reed, "Friction Behavior of 52100 Steel Modified by Ion Implanted Ti," *Nuclear Instruments and Methods*, **181/182**, 923 (1981).

Control of Fatigue in Steels, by G.R. Yoder, L.A. Cooley and T.W. Crooker, *Material Science and Technology Division*

The growth of fatigue cracks can lead to premature or even catastrophic failure in structural components that are subjected to repeated (cyclic) loads. We would like to extend the useful lifetime of components under these conditions, and to prevent catastrophic failures altogether. Recent work at NRL has provided a breakthrough which brings closer the attainment of these two objectives for a broad variety of steels. The breakthrough was the identification of the metallurgical parameters that control the resistance of an alloy to the growth of fatigue cracks. Through appropriate choice of these parameters, this resistance may be improved by two or three orders of magnitude, thus significantly extending the useful lifetime of structural components. Moreover, the threshold level of fatigue resistance (below which cracks cannot grow) can now be raised significantly by metallurgical means.

To describe our new results, it is necessary to use the methodology of fracture mechanics in which the stress-intensity factor, K, is a primary parameter. K is related to the applied load or stress level and to the crack length. Under conditions of cyclic stressing, the stress-intensity factor range, ΔK, is the relevant parameter, and in particular its value ΔK_{th} at the fatigue threshold.

Analysis of fatigue crack growth in many different steels makes it clear that apparent values of ΔK_{th} can vary widely. Although in many instances actual values of ΔK_{th} are difficult to define rigorously, a pronounced transition point (knee) is apparent in the near-threshold region of fatigue crack growth. This is illustrated in Fig. 14, where the conventional logarithmic plot of fatigue crack growth rate (da/dN) as a function of ΔK exhibits the characteristic bilinear form, with a knee at ΔK_T. The position of the knee is predictable from the cyclic plastic zone model of fatigue crack growth established in prior NRL work with titanium alloys [1]. Within the confines of the cyclic plastic zone, the material yields in both tension and compression during each fatigue loading cycle. As illustrated in Fig. 14, the size of the cyclic plastic zone lobe, r_y^c, increases with ΔK until at ΔK_T it is comparable to the effective grain size, $\bar{l}$, of the material. Thus in the lower limb of the curve, where $r_y^c < \bar{l}$, the mode of fatigue crack growth is sensitive to the structure but in the upper limb, where $r_y^c > \bar{l}$, it is not. It follows that ΔK_T is directly proportional to the parameter $\omega = \sigma_{ys}\sqrt{\bar{l}}$, where σ_{ys} is the yield strength of the material. Experimental confirmation of this relationship is shown in Fig. 15, where measured values of ΔK_T are compared with predictions of the model for several steels and titanium alloys. It follows that

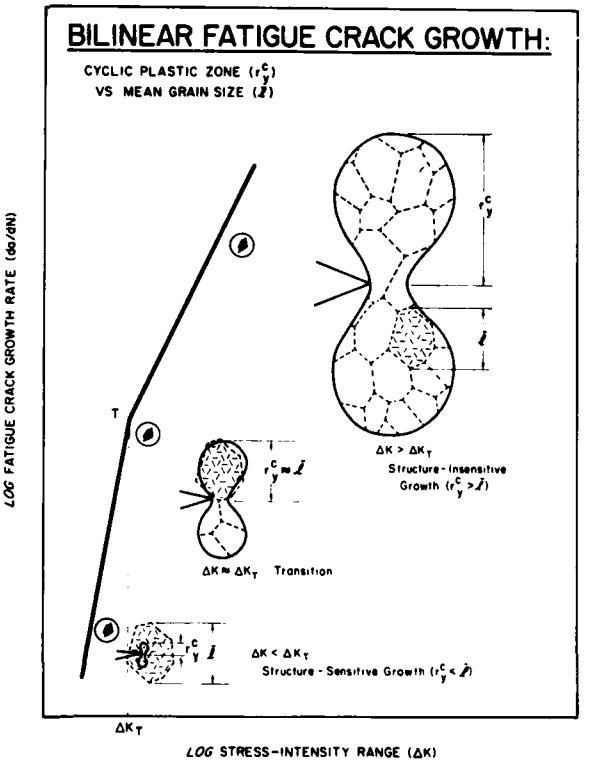

Fig. 14 — Influence of the ratio of cyclic plastic zone size (r_y^c) to grain size ($\bar{l}$), upon development of bilinear fatigue crack growth behavior

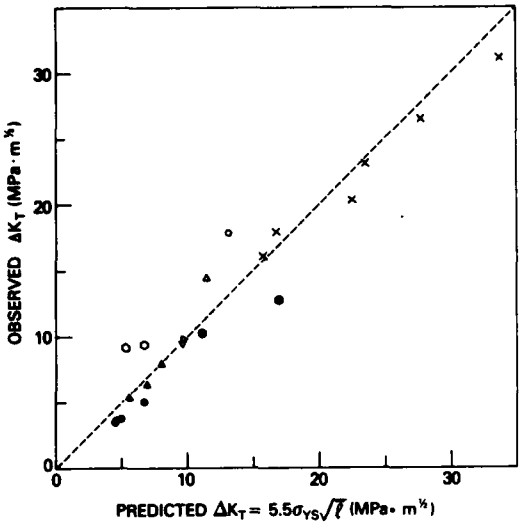

Fig. 15 — Comparison of actual values of transitional stress-intensity range (ΔK_T) with model predictions for several different steels and titanium alloys

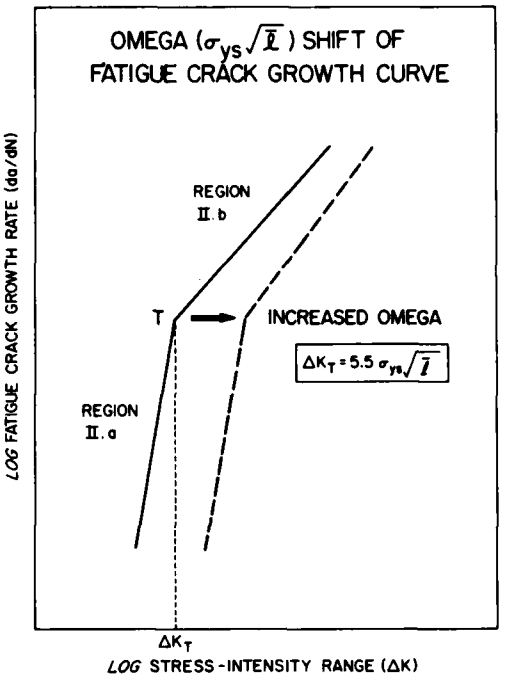

Fig. 16 — Shift in the fatigue-crack growth rate curve arising from an increase in the value of ω based on cyclic plastic zone model of fatigue crack growth

by metallurgical control of σ_{ys} and $\bar{l}$ the position of ΔK_T and the whole crack growth rate curve may be shifted to higher ΔK, as illustrated in Fig. 16.

This work should have a significant impact on the fundamental understanding of fatigue as well as on practical applications. Not only does it elucidate the basic metallurgical principles by which threshold levels for fatigue-crack growth may be raised, but it also provides a straightforward, inexpensive method for estimating these thresholds, which until now have had to be measured directly by costly and time-consuming procedures. Estimation of fatigue thresholds (ΔK_{th}) for steels is now practicable because of the steep slope in the lower limb of the fatigue-crack growth rate curve, so that ΔK_T approximates ΔK_{th}. The shift in growth-rate curves illustrated in Fig. 16 can be very significant because values of ΔK_T or ΔK_{th} for steels can span roughly an order of magnitude. Even if a structural component is designed for cyclic levels above ΔK_{th}, its useful lifetime can be extended greatly since the shift can reduce levels of da/dN by two to three orders of magnitude at a specific level of ΔK in the near-threshold region. Further work at NRL will explore the applicability of this approach to new advanced alloy systems.

[Sponsored by ONR]

REFERENCE

1. G.R. Yoder, L.A. Cooley, T.W. Crooker, "Observations on the Generality of the Grain-Size Effect on Fatigue-crack growth in $\alpha + \beta$ Titanium Alloys," *Titanium '80, Proc. 4th Int. Conf. on Titanium,* Kyoto, Japan, H. Kimura, O. Izumi, eds., Vol. III, May 19-22, 1980, pp. 1865-1873.

Sulfur Detrimental to SCC Resistance of Steel Welds, by C.T. Fujii, *Material Science and Technology Division*

Stress-corrosion cracking (SCC) is likely to occur with greater frequency as the use of higher strength materials increases to meet the growing performance requirements of modern structures. Naval structures are especially vulnerable because they are constantly exposed to a particularly aggressive environment which provides conditions conducive to corrosion-cracking damage. Many of these structures are fabricated by welding, and because weldments are frequently more

vulnerable to SCC than the corresponding base plates, the welded zones are potential weak points in the structure. Improvements in weldment properties would greatly increase the reliability of high-performance structures using welded high-strength materials.

To a large extent, the metallurgical and microstructural characteristics of deposited weld metals are determined by the welding process. The thermal cycles associated with multipass welding invariably produce a distribution of tempered material and residual stresses which affect the mechanical and SCC behavior of weldments. The shielded-metal-arc (SMA) and the gas-metal-arc (GMA) processes have been routinely used for welding metals in the Navy's HY-series of steels (HY-80, HY-100, and HY-130). During the development of standard welding practice, it became increasingly apparent that SCC of the welds could be a major problem. This stimulated research on the SCC behavior of welds with the aim of improving SCC properties. Two major Navy programs evolved and NRL has played a major role in each. These are the HY-130 Program and the Weld Metal Improvement Program. In one phase of the Weld Metal Improvement Program, welds produced by the high-cost gas-tungsten-arc (GTA) welding process generally produced cleaner (that is, with less oxygen), more fine-grained, and more highly tempered weld material with improved fracture toughness than either GMA or SMA welding. However, the SCC properties of all weld metals were shown to be affected not only by microstructural and metallurgical factors but also by the amount of sulfur present as an impurity.

The role of sulfur in SCC is an indirect one, and appears to be associated with sulfur's recognized ability to inhibit catalytically the recombination of adsorbed hydrogen, $H_{ad} + H_{ad} \rightarrow H_2$. Thus, sulfur enhances the effective concentration of H_{ad} and thereby increases absorption of nascent hydrogen (H_{ab}) by the bulk metal. In the critical zone of maximum triaxial stress at the crack tip, the increased absorbed hydrogen lowers the stress intensity factor K_{Iscc}. This explanation appears adequate to account for experimental observations at NRL that weld metals with lower K_{Iscc} contain higher concentrations of sulfur [1].

Figure 17 summarizes the variation of K_{Iscc} with sulfur content in GTA weld metals obtained under two different environmental conditions. The curves show that K_{Iscc} is enhanced if the sulfur contents are below 50 ppm and 30 ppm under

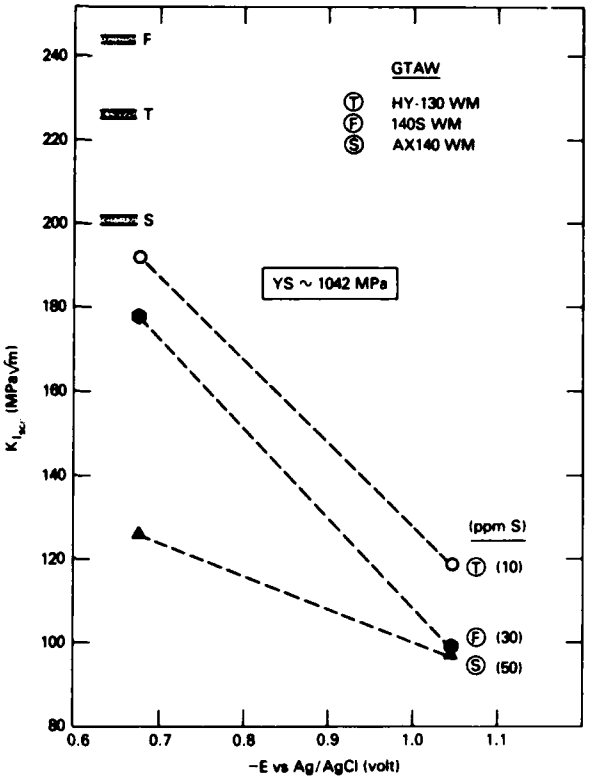

Fig. 17 — Stress intensity factor (K_{Iscc}) of four high-strength steel GTA weld metals relative to sulfur content and environmental conditions

free-corroding and zinc-coupled conditions, respectively. At higher sulfur concentrations, K_{Iscc} remains constant for a given environmental condition. Significant improvements in K_{Iscc} can be expected if sulfur contents can be reduced to below some minimum level which appears to be specific to a given combination of metal system and environmental condition. Improvements in K_{Iscc} arising from a change in the welding process can be offset by the deleterious effect of sulfur.

Figures 18 and 19 compare the SCC properties of weld metals having similar microstructures and yield strengths, eliminating these as factors affecting K_{Iscc} and isolating the effect of sulphur content. Figure 18 shows the effect of sulfur content on K_{Iscc} of GTA welds under freely-corroding and zinc-coupled conditions defined, in this case, by the electrochemical potential. The spread in K_{Iscc} values is clearly greater under freely corroding conditions (−0.68 V) than under zinc-coupled conditions (−1.05 V), an indication that both electrochemical potential and sulfur are affecting nascent hydrogen levels and hence K_{Iscc}.

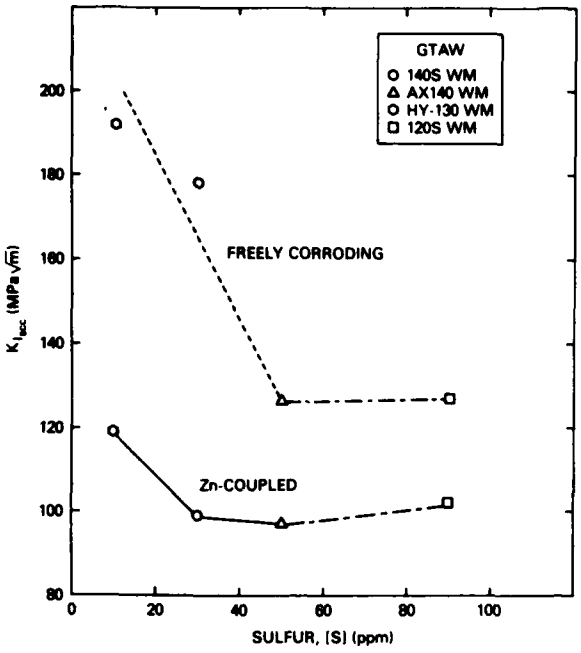

Fig. 18 — The influence of sulfur content on the effects of electrochemical potential on K_{Iscc} of the GTA weld metals at a yield strength of 1042 MPa

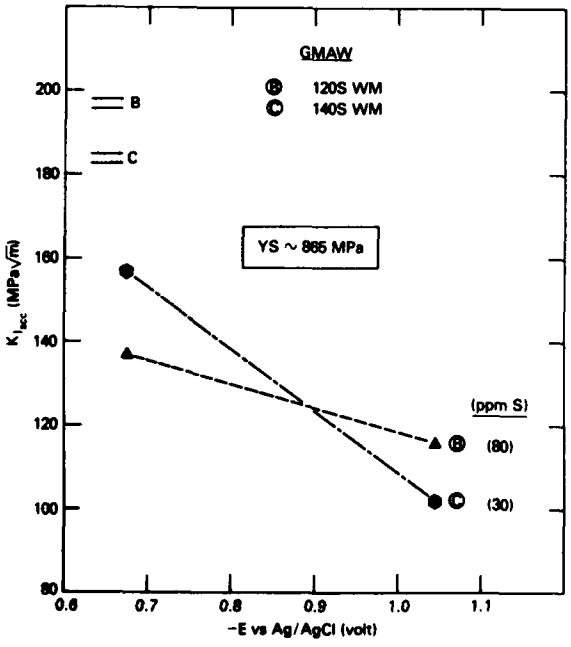

Fig. 19 — The influence of sulfur content on the effects of electrochemical potential on K_{Iscc} of the GMA weld metals at a yield strength of 865 MPa

The potential is dominant in determining hydrogen availability at −1.05 V whereas sulfur is relatively more effective at −0.68 V. Figure 19 shows similar behavior in GMA weld metals, Codes B and C, both at a yield strength of approximately 865 MPa. The somewhat lower K_{Iscc} of weld metal C under zinc-coupled conditions (−1.05 V) indicates a greater sensitivity of this GMA weld metal to hydrogen than weld metal B. However, under freely-corroding conditions (−0.68 V) the difference in the sulfur content between the two weld metals presumably causes more nascent hydrogen to be available to weld metal B, thus lowering its K_{Iscc} below that of weld metal C and creating the observed crossover in the curves.

The suggestion that sulfur plays a negative catalytic role in the electrochemical production of hydrogen is consistent with the increasingly accepted view that hydrogen is the principal cause of SCC in steels. The precise mechanism by which sulfur participates in the SCC process is still unresolved and will be the subject of future work at NRL.

[Sponsored by ONR and NAVSEA]

REFERENCE

1. C.T. Fujii, "Factors Influencing Stress-Corrosion Cracking of High-Strength Weld Metals," *Metall. Trans.*, **A12**, 1099 (1981).

Radiation Resistance of Ferritic Stainless Steels, by J.R. Hawthorne, *Material Science and Technology Division*

Ferritic stainless steels are receiving increased attention as possible structural materials for use at high temperatures in a high neutron flux. Potential applications would be as the first wall of a magnetic fusion reactor or as components of advanced fission reactors. Ferritic stainless steels are attractive because of their low cost, high strength, ease of fabrication and low neutron absorption. They have recently been found to possess excellent resistance to radiation-induced swelling and to exhibit low creep rates under neutron irradiation. However, their ability to retain sufficient fracture resistance in long term service is a major uncertainty. Radiation exposure typically causes a progressive

elevation in the brittle/ductile (B/D) transition temperature of structural steels by an amount which normally depends on service temperature and fluence (total neutrons/cm^2). Radiation also can cause a reduction in fracture resistance at temperatures above the B/D transition temperature. The level of the ductile performance (the fracture resistance plateau) is also important for fracture-safe design. Until recently, the fracture resistance of ferritic stainless steels had not been investigated in detail for either the irradiated or the unirradiated condition. We have initiated studies on two promising steels, Alloy HT-9 and Alloy 9Cr-1Mo (Modified), to determine their fracture resistance and other properties under a variety of conditions.

Figure 20 presents some of our experimental findings for Alloy HT-9 [1]. The data depict Charpy-V (C_v) notch ductility behavior before and after irradiation at a temperature of 427°C to a fluence of 10^{22}n/cm^2. (Service fluences as high as 10^{23} n/cm^2 are anticipated for some fusion reactors. Alloy screening evaluations typically use lower fluences because of the long time necessary to achieve high fluences in test reactors.) The irradiated samples show a relatively small elevation in the B/D transition temperature and only a small reduction in fracture resistance. The B/D transition remains well below the simulated service temperature of 427°C. Companion tests of fatigue-precracked C_v specimens revealed that the increase in dynamic fracture toughness with temperature coincides approximately with the increase in C_v energy absorption with temperature (See Fig. 21). This coincidence has great importance for structure design because fracture toughness data needed for choosing materials are often unavailable. Measured fracture toughness levels for the upper shelf regime, like the C_v data of Fig. 20, clearly indicate high fracture resistance qualities for Alloy HT-9 for the indicated exposure. On the microscale, the failure mode of ductile rupture by microvoid coalescence was apparently unchanged by irradiation. Exploratory assessments using irradiation at lower temperature show that the material may also be suitable for high fluence applications at 290°C but not at 100°C. At 100°C, a fluence of only 1×10^{20} n/cm^2 raised the B/D temperature to the simulated service temperature. Significantly, tests of fatigue-precracked C_v specimens consistently demonstrated a coincidence of the fracture toughness transition with the C_v energy transition after irradiation (see Fig. 21). Thus the studies have identified a general trend which will allow a cross application of notch ductility and fracture toughness data in design and materials analyses.

The effects of radiation on material subjected to the heat of welding were also studied in view of the probable need for welding in fabrication. Tests by the C_v method indicate that the B/D transition of the heat-affected zones after irradiation at 290°C will be no higher than the B/D transition of base material, therefore, heat-affected zones should not represent weak points in welded Alloy HT-9 structures.

Some important differences among ferritic stainless steels have been found. Initial results indicate that Alloy 9Cr-1Mo (Modified) with 9%

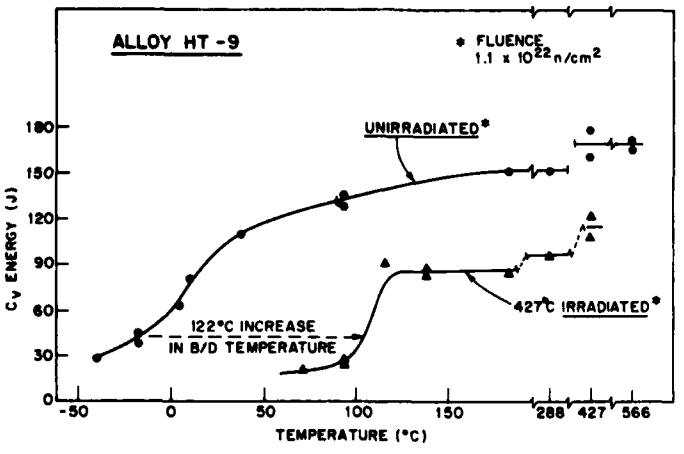

Fig. 20 — Radiation resistance of Alloy HT-9 as evidenced by C_v notch ductility properties before and after neutron irradiation at 427°C.

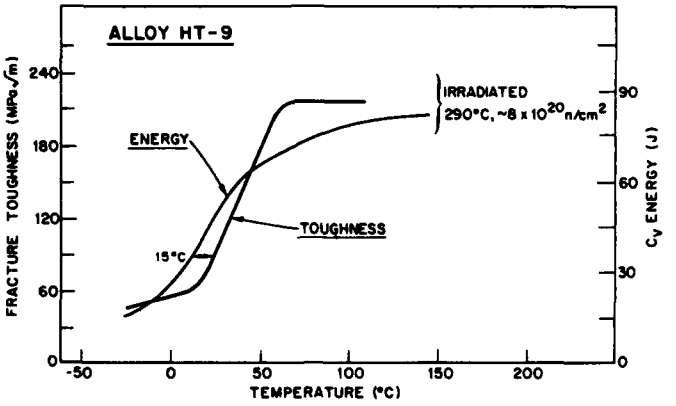

Fig. 21 — Similarity in temperature of fracture toughness and notch ductility B/D transitions for Alloy HT-9 after irradiation at 290°C. The similarity has also been observed for 100°C and 427°C irradiation conditions.

chromium is more resistant to radiation than Alloy HT-9 with 12% chromium. This difference in behavior may be related to differences in the microstructure of the two materials, that is, between tempered lower bainite and tempered martensite. This observation is of special interest because it suggests that the alloy may be optimizated for first-wall service. Similar observations in the past led to the successful development by NRL of highly radiation-resistant steels for the pressure vessels of the current generation of power reactors. Tests of Alloy 9Cr-1Mo (Modified) by C_v and fatigue precracked C_v methods revealed that, unlike Alloy HT-9 after irradiation, the increase in the B/D transition for fracture toughness does *not* coincide with the increase in the B/D transition for C_v energy absorption. Thus projections of fracture resistance for Alloy 9Cr-1Mo (Modified) should not be based solely on C_v notch ductility tests.

Further research efforts will include assessments of the alloys by subjecting them to higher neutron fluences at temperatures above 300°C and to low fluences at intermediate irradiation temperatures of about 150°C. Exploratory tests of appropriate weld metal compositions are also planned. The search for experimental correlations between radiation-induced changes in fracture toughness and C_v notch ductility will continue.

[Sponsored by DOE]

REFERENCE

1. J.R. Hawthorne, "Postirradiation Notch Ductility and Fracture Toughness Behavior of AOD Heat of Alloy HT-9," Department of Energy Report DOE/ER-0045/8, September 1982.

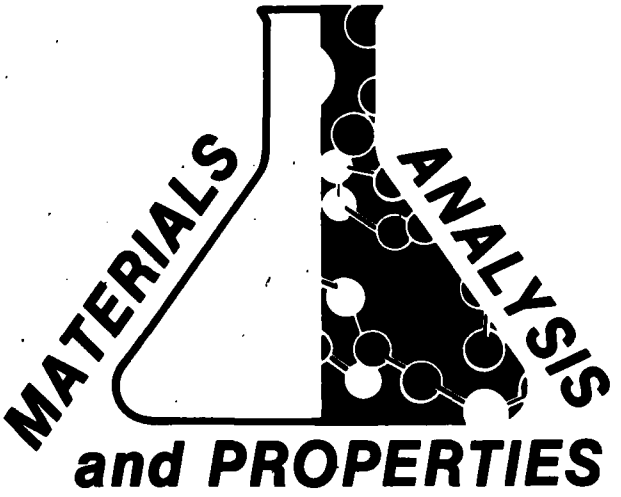
MATERIALS
ANALYSIS
and PROPERTIES

MATERIALS ANALYSIS AND PROPERTIES

Before new materials can be developed, it is necessary to understand the physics and chemistry that determine their properties. Sometimes this calls for new methods of analysis, as illustrated by the following examples of NRL work.

Acoustoelastic Stress Measurements, by A.V. Clark, R.B. Mignogna, and R.J. Sanford, *Marine Technology Division*

Acoustoelastic stress measurement is an emerging new technology in the field of nondestructive evaluation. High frequency sound waves are used as a probe to determine stresses either in the bulk or on the surface of structural components subjected to residual or applied stress. The presence of stress causes small changes in the phase velocities of the propagating sound waves (acoustoelastic effect). The difference between the phase velocities of two orthogonally polarized shear waves is known as the *acoustical birefringence.* With highly accurate velocity (time) measurement systems, this birefringence can be measured and the stress determined. Knowledge of the stress within a structure allows decisions to be made in regard to its structural integrity and probable service life.

For a homogeneous, isotropic material in a state of plane stress, the relationship between the birefringence and the stress field is well known. However, most common structural materials are not isotropic, exhibiting some anisotropy, or *texture,* due to the forming process. In particular, rolled plates of aluminum and mild steel are anisotropic even in the absence of applied stress. A new theory has been developed which accounts for the effect of texture on birefringence. The theory states that the birefringence is proportional to the in-plane shear stress. The proportionality factor is one of three acoustoelastic constants of the plate material.

To test the theory, we have used a version of the pulse-echo-overlap method [1] to determine the acoustic birefringence in uniaxial tension specimens cut from rolled 2024-T351 aluminum plate at various angles. Measurement of round-trip travel time with this system had an accuracy of 10 ppm. A fit was made to the experimentally obtained birefringence as a function of stress to determine the acoustoelastic constants. As shown in Fig. 1, the theoretical results agree with the measurements.

The acoustoelastic theory was also applied to a case of more practical interest; namely, an aluminum plate with a simulated crack, as shown in Fig. 2. This is a well-characterized fracture specimen with a known stress intensity factor K_I. The stress field in the plate is represented by a series expansion of stress functions which satisfy the stress equilibrium equations. The coefficients in the series expansion allow the boundary conditions to be satisfied; the stress intensity factor K_I is proportional to the coefficient of the leading term in the series. The coefficients have been determined by Sanford et al. [2] using photoelasticity. Contours of constant shear stress using these coefficients are shown in Fig. 3; note the large stress gradients around the crack tip.

To verify that the acoustoelastic stress measurements would reproduce this stress field, the acoustic birefringence B was measured at sample points in a square centered on the crack tip.

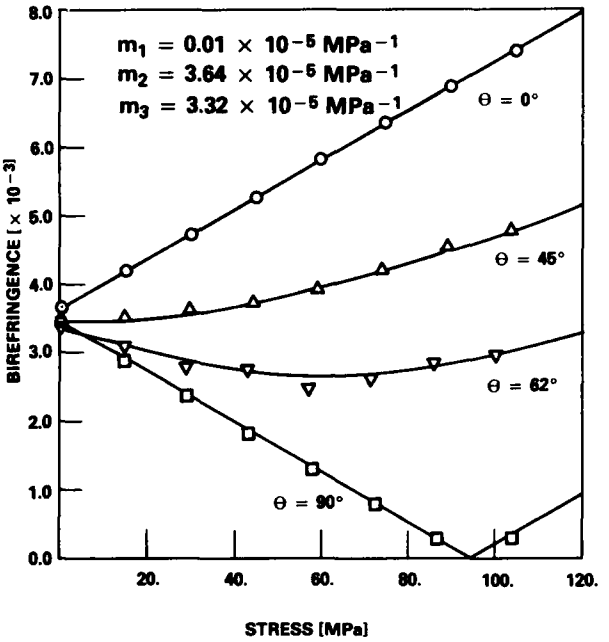

Fig. 1 — Acoustic birefringence as a function of stress for uniaxial tensile specimens for θ = 0°, 45°, 62°, and 90°. θ is the angle between perpendicular to rolling direction, and direction of uniaxial tension. Theory ———, data. ○, △, ▽, □.

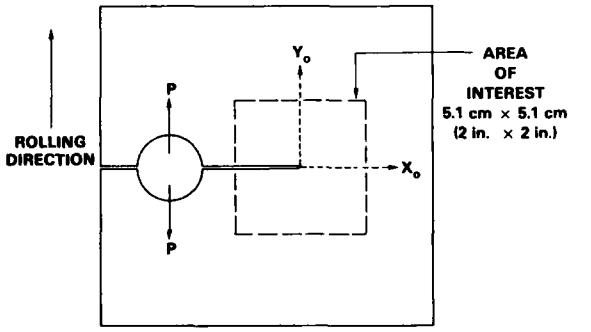

Fig. 2 — Tensile specimen with simulated crack. Acoustic measurements were made in "area of interest." X_0 and Y_0, are the unstressed acoustic axes, P is the applied force.

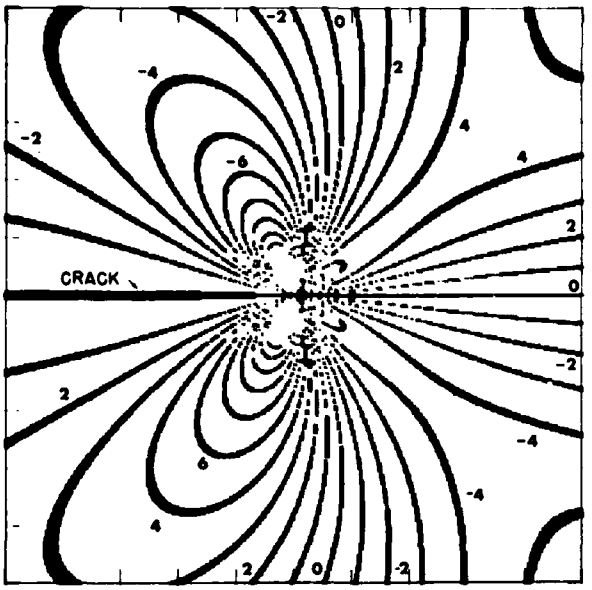

Fig. 3 — Theoretical shear stress contours within a 51-mm × 51-mm region of the specimen, centered at crack tip. Theoretical contours generated from optical birefringence data of [2]. Contours plotted for $\sigma_{12} = (6.9N \pm 0.55)$ *MPa*, N=0, 1, 2....

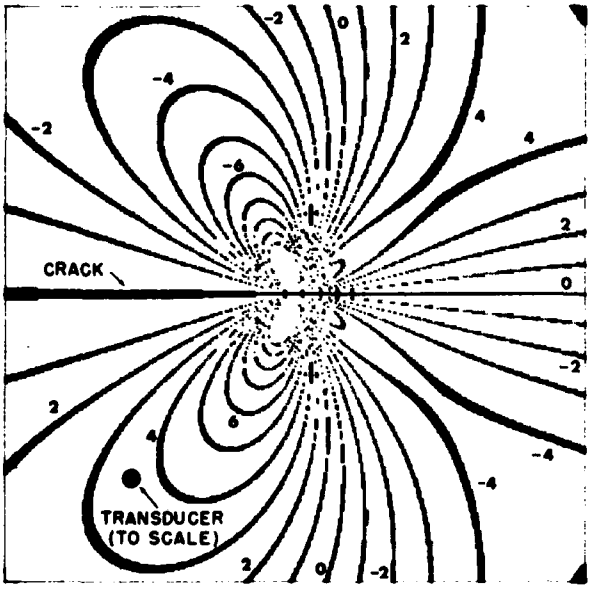

Fig. 4 — Experimental shear stress contours within a 51-mm × 51-mm region of specimen centered at the crack tip. Experimental contours were generated from acoustoelastic data. The size of the tranducer used in experiment is also shown. Contours plotted for $\sigma_{12} = (6.9N \pm 0.55)$ *MPa*.

Values of the shear stress σ_{12} were then determined from the theory. The coefficients were obtained by a least squares fit to the acoustoelastic data. Contours of constant shear stress calculated using these coefficients are shown in Fig. 4. The similarity between this figure and the theoretical contours of Fig. 3 indicate good agreement. The acoustoelastically determined stress intensity factor also agreed with the theoretical value to within 2%.

The feasibility of the birefringence method for plane stress problems has thus been demonstrated, even in the presence of anisotropy and large stress gradients. Work is underway to extend the method to three-dimensional stress fields.

[Sponsored by ONR]

REFERENCES

1. E.P. Papadakis, "Ultrasonic Phase Velocity by the Pulse-Echo Overlap Method Incorporating Diffraction Phase Corrections," *J. Acoust. Soc. Am.* **42**, 1967 pp. 1045-1057.

2. R.J. Sanford et al., "A Photoelastic Study of the Influence of Non-Singular Stresses in Fracture Test Specimens," University of Maryland, NUREG/CR-2179, Aug. 1981.

A Rayleigh-Wave Technique to Size Surface Cracks, by R. Hughes and J. Waskey, *Marine Technology Division*

Surface-breaking cracks in amorphous solids are serious defects that can lead to failures in naval structures. The most significant characteristic for predicting failure is the *crack height* (the distance the crack extends into the material). Many ultrasonic nondestructive techniques have been used to measure crack height and new approaches and refinements continue to appear in the literature. Most of these methods are based upon time-of-flight or amplitude measurements of various elastic waves; their accuracy is typically about 20%.

A new method which is being developed at NRL in collaboration with C. P. Burger of Iowa State University uses ultrasonic Rayleigh (surface) waves to determine the crack height of surface-breaking cracks. This method is based upon frequency measurements and uses the special property of Rayleigh waves that their frequency distribution depends on their depth beneath the surface of the solid. Specifically,

material particles at the surface of a solid are subjected to all frequency components of the incident wave, whereas particles near the full depth of the crack are subjected primarily to the lower frequency components. By measuring the frequency content of Rayleigh waves transmitted past a surface-breaking crack, the height of the crack may be determined. The crack acts as a low-pass filter for Rayleigh waves; the higher frequency components are reflected back towards the ultrasonic source, while the lower frequency components are transmitted past the crack. By deconvolving the transmitted wave with the incident wave, a cutoff frequency may be determined. This cutoff frequency is then used to calculate the crack height.

A limitation of this method is that displacement measurements made at the surface include not only the desired Rayleigh wave but also waves resulting from mode conversions at discontinuities. We have made significant progress in delineating the various mode-converted waves associated with a Rayleigh wave propagating in the vicinity of a crack. Photographs taken with a high resolution dynamic photoelastic camera developed at NRL have shown the details of Rayleigh waves incident on specific boundaries associated with crack geometries.

One of our first applications of these techniques has been to study steps (representing half of a crack) in a free surface. The top surface in Fig. 5 is the free surface of a solid in which there is a 5-mm step. This surface was subjected to an impulse load to the left, and the stress contours in the photograph are the result of a Rayleigh wave propagating to the right. Figure 6 shows the waves resulting from the interaction of this Rayleigh wave with the step; a transmitted and a reflected Rayleigh wave can be seen. Spectral

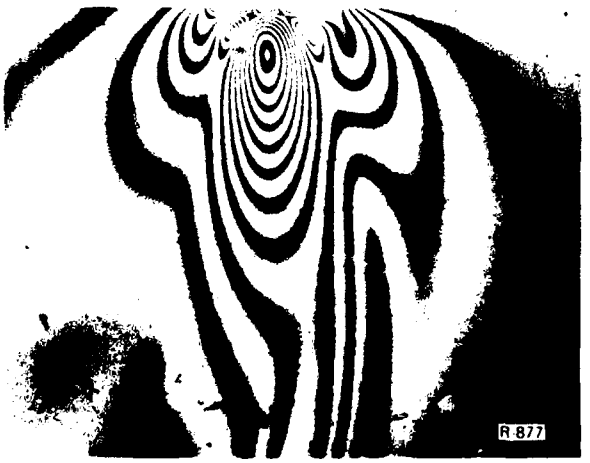

Fig. 5 — Stress contours produced by a Rayleigh wave propagating from left to right along a free surface (top of photograph)

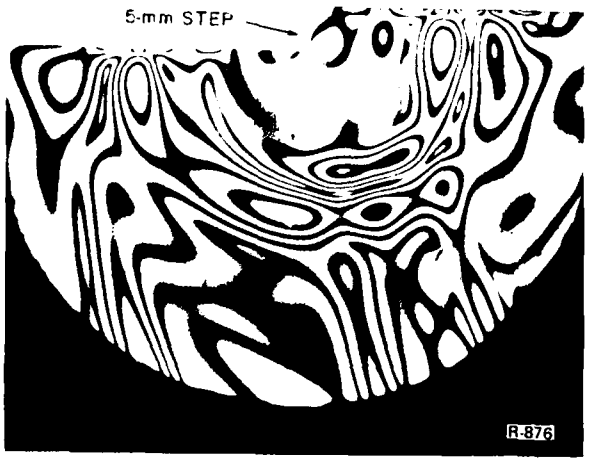

Fig. 6 — Stress contours produced by a Rayleigh wave reflected by (top left) and transmitted past (top right) a 5-mm step in a free surface (off the figure to the right)

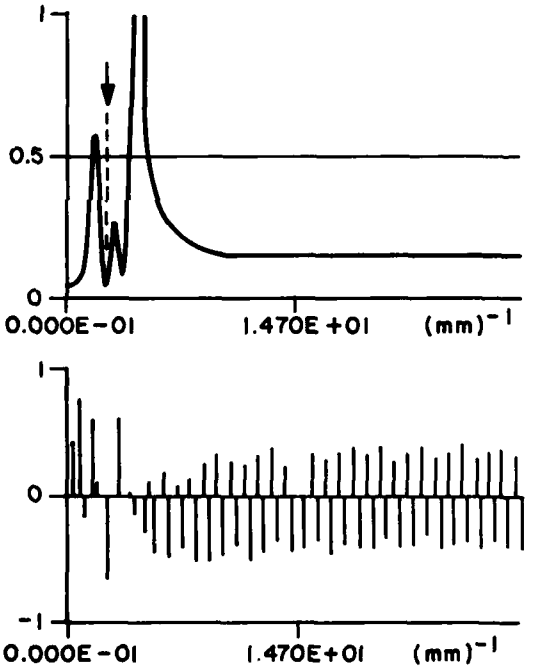

Fig. 7 — The transfer function of a Rayleigh wave transmitted past the 5-mm step in Fig. 6. (a) Normalized amplitude vs spatial frequency (mm^{-1}). The arrow marks the minimum at 0.196 mm^{-1}. (b) Normalized phase vs spatial frequency (mm^{-1}).

densities were determined from these photographs using a digital image processing system. The transfer function depicted in Fig. 7 was determined from these spectra. Note the definite pattern in the amplitude distribution and the random phase distribution. The low-frequency nature of the transmitted wave is well illustrated. The minimum following the first peak of the transfer function occurs at an inverse length of 0.196 mm^{-1} from which a step size of 5.1 mm is deduced.

Further study is underway to interpret the transfer functions for other boundary conditions associated with surface-breaking cracks. We plan to correlate the results obtained with ultrasonic measurements, numerical models, and visualization studies. The ultimate objective is to establish an ultrasonic method which can reliably size surface-breaking cracks and be less sensitive than existing methods to operational variables.

[Sponsored by ONR and NAVSEA]

Predicting the Properties of Chain Polymers, by C.T. White and J.W. Mintmire, *Chemistry Division*

Electroactive and piezoelectric polymers are likely to become increasingly important to the Navy. In principle, it should be possible to tailor their properties to specific Naval applications, such as lightweight batteries, conductive coatings, and acoustic devices. Although used in bulk formulations, the effectiveness of these polymers for particular applications depends on their microscopic qualities, for example, their electronic structure and crystal orientation. At the present time, the relationship of many of the useful macroscopic properties of these materials to their microscopic properties is not well understood. We have made significant progress in defining this important relationship.

In general, most current theoretical methods of predicting the electronic structure of polymers use a solid-state based theory which relies on knowledge of the geometry of the system. This is unfortunate since with quasi-one-dimensional polymers, the details of the intrachain geometry often are not well-known experimentally because of the difficulties in preparing single crystals of these materials for x-ray crystallographic analysis. However, such details can be important for a satisfactory understanding of semiconducting polymers because they often determine the semiconducting properties of the material.

We have concentrated on developing from first principles a new computational approach for determining both the electronic structure, total energy, and dielectric response of chain polymers. The method assumes a chain geometry and then calculates the total energy, band structure (electronic excitation spectra), and the one-electron wavefunctions of the system. The geometry of the polymer is derived from a set of total energy calculations at different geometries which can be used to locate the minimum energy of the material as a function of geometry. For the prototype chain polymer, polyacetylene, this approach [1] resulted in a geometry with short and long bond lengths of 1.377 Å and 1.434 Å respectively and a total unit cell length of 2.435 Å. These results agree well with recent experimental data. The calculated band structure of polyacetylene was used to generate the density of states and x-ray and ultraviolet photoelectron spectra of the material. As shown in Fig. 8, these

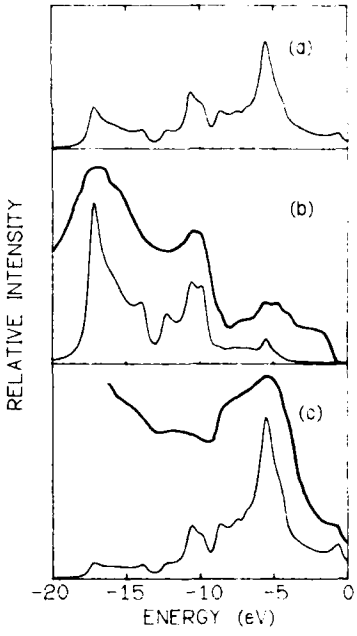

Fig. 8 — Properties of all-trans polyacetylene. (a) Density of valence states, (b) theoretical and experimental x-ray photoelection valence spectra, and (c) theoretical and experimental ultraviolet photoelectron spectra. Upper lines in (b) and (c) represent experimental results and lower lines represent theoretical results. The background has not been subtracted from the experimental results.

calculated results compared well with the corresponding experimental data. In addition, the one-electron wavefunctions and band structure were used to make a theoretical prediction of the dielectric function of polyacetylene [2] as a function of wave vector and frequency. The dielectric function is a measure of the response of a system to external electric fields; thus, it describes properties such as the reflectivity, conductivity, and electron energy-loss spectra. Again, the predictions agreed well with experiment, even to the correct prediction of the observed anomalous collective electron resonant dispersion frequencies.

Our methods provide a description from first principles of semiconducting, metallic, and piezoelectric chain polymers with a degree of sophistication that previously was achieved only for molecules. The demonstrated predictive power of the approach should result in a significant savings in the money and time needed to develop polymers with specific properties. These techniques will next be applied to other electroactive and piezoelectric polymers of Naval interest such as polypyrrole, polyparaphenylene, and polyvinylidene difluoride, with particular attention is to the properties arising from different substituents attached to the carbon backbone of these polymers. The new theoretical methods should make it possible to predict many of the electronic properties of new electroactive and piezoelectric properties even before they have been synthesized experimentally.

[Sponsored by ONR]

REFERENCES

1. J.W. Mintmire and C.T. White, "$X\alpha$ Approach for the Determination of Electronic and Geometric Structure of Polyacetylene and Other Chain Polymers" *Phys. Rev. Lett.* **50**, 101 (1983).
2. J.W. Mintmire and C.T. White, "Theoretical Treatment of the Dielectric Response of All-*trans*-Polyacetylene" *Phys. Rev.* **B27**, 1447 (1983).

Secondary Ion Mass Spectrometry of Organic Adsorbates, by M.M. Ross and R.J. Colton, *Chemistry Division*

Carbon-based particulate matter is generated by many sources including some power plants and diesel engines. Organic compounds, such as polycyclic aromatic compounds (PAC), which are also products of hydrocarbon fuel combustion, have been shown to adsorb onto the surface of carbon particles. Many of these organic compounds are carcinogenic, mutagenic, or have other biologically adverse effects. The organic adsorbate/carbon adsorbent system is also produced when activated carbons are used to scavenge pollutants from the air or water. Realizing the difficulties inherent to the analysis of adsorbates on carbon and the widespread use of diesel engines and charcoal adsorbents by the Navy, we have investigated the use of secondary ion mass spectrometry (SIMS) for the direct and rapid analysis of organic compounds such as PAC, adsorbed on carbon.

Molecular SIMS has become a popular method of studying nonvolatile and thermally labile organic compounds [1]. The compound is usually deposited on a metal surface such as silver and bombarded with energetic Ar^+ ions. Secondary ions of the type M^+, $[M + H]^+$, $[M - H]^-$, or $[M + Ag]^+$ where M represents the intact molecule, are emitted and are then analyzed by the mass spectrometer. Certain compounds are difficult or impossible to analyze from solid metal surfaces; we have successfully used carbon and liquid metal surfaces as alternative substrates.

The first part of this work used SIMS to study several monocyclic and polycyclic aromatic compounds including benzene, methyl-substituted benzenes, naphthalene, anthracene and pyrene [2]. These compounds were burnished directly onto silver foil or adsorbed from chloroform solutions on carbon particles which were subsequently burnished onto silver. Secondary ion mass spectra were obtained with a double-focusing instrument using a primary ion beam of 4.4 keV Ar^+ ions with a current density of 4 to 8 $\times$ 10^{-8} A/cm^2.

No secondary ions characteristic of the organics were detected when silver alone was the sample substrate, but when toluene, xylene, and mesitylene were absorbed on carbon, $[M + Ag]^+$ ions were detected. The heats of adsorption of organic compounds on carbon are higher than their corresponding heats of adsorption on metal surfaces allowing the carbon substrate to hold some volatile compounds long enough for SIMS analysis. Since toluene is detected but benzene is not, we infer that the minimum organic/carbon adsorption energy necessary to permit detection is the heat of adsorption for toluene (~11 kcal/mole). When the carbon is initially

saturated with toluene, the molecular ion emission can last as long as an hour.

Larger PACs are also difficult to analyze with SIMS when adsorbed on metal surfaces, but when these PACs are adsorbed on carbon, M^+ and $[M + Ag]^+$ ions are readily detected. We believe that the high surface area and porosity of the carbon provides a three-dimensional surface over which the sample molecules are dispersed and from which ions can be emitted for extended periods of time. For example, a sample as small as 2 μg of a PAC on carbon emitted $[M + Ag]^+$ ions for over one hour. A sample of only ~1 ng of phenanthrene on carbon was detected under the same conditions.

We have also investigated liquid metal substrates for dynamic SIMS analysis of organic compounds. Microgram quantities of the 3- and 4-ring PACs were dispersed on a liquid gallium-indium alloy surface which was bombarded with a dynamic ion beam (5×10^{-5} A/cm^2, O_2^+). A CAMECA IMS 300 ion microscope was used to observe the ionic species emitted from the surface.

The intensity of the molecular ion, M^+, signal is initially high, ~10^4 cps. After one or two minutes it decreases by about an order of magnitude to a steady level of ~10^3 cps which is maintained for more than 30 minutes if the original sample concentration is high enough. During ion bombardment, aggregates of the sample molecules can be seen with an optical microscope moving across the gallium-indium surface. The continuous migration of these sample molecules to the beam area causes the ion emission to be long-lived and readily detected by the CAMECA

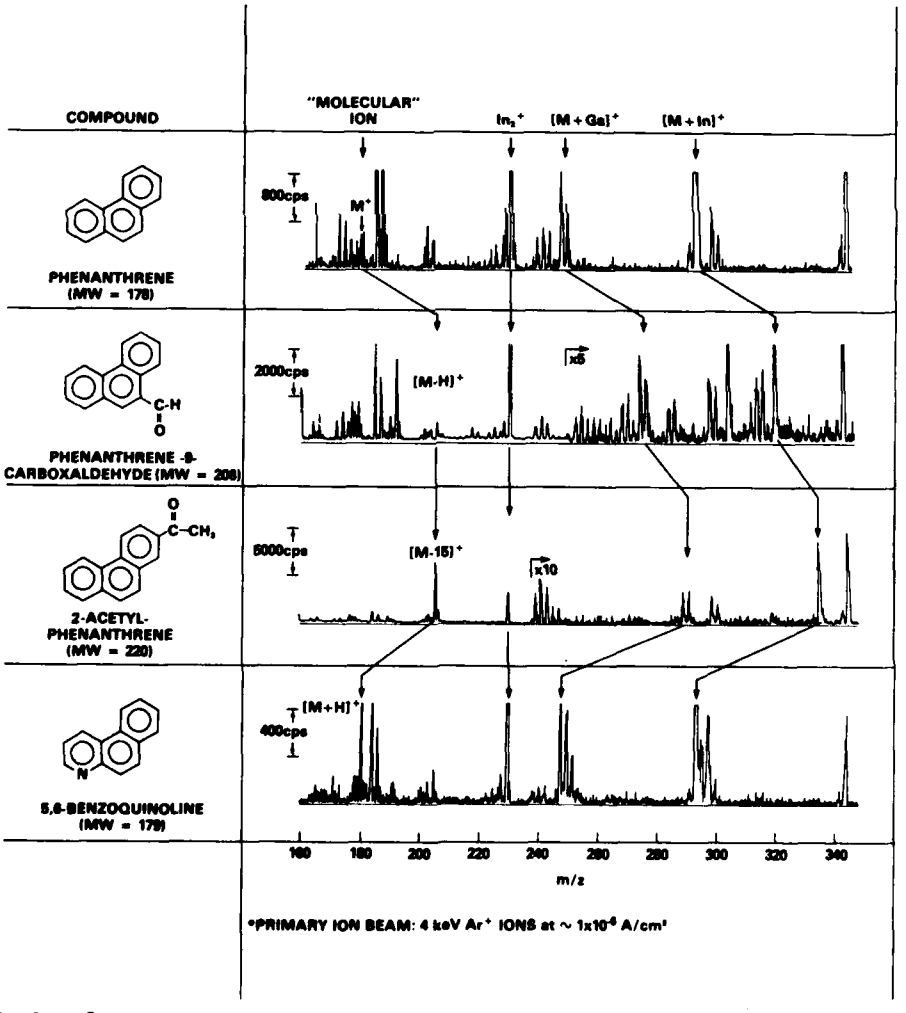

Fig. 9 — Secondary ion mass spectra of PAC on liquid metal. The samples ranged from ~10 to ~20 μg in mass. SIMS can detect different molecule-like ions for related PACs that have different functional groups.

microscope. Under the same conditions, no molecular ions were observed from PACs deposited on solid silver or indium surfaces.

To achieve a higher mass range than possible with the CAMECA, secondary ion mass spectra were obtained using the double-focussing SIMS instrument operated at a high primary ion current density (dynamic mode). Figure 9 shows that different molecular-like ions M^+, $[M - H]^+$, $[M - 15]^+$, or $[M + H]^+$ for related PACs having different functional groups are detectable, as well as $[M + Ga]^+$ and $[M + In]^+$ cationized by the substrate.

These preliminary results show liquid gallium to be an effective substrate for the analysis of the nonpolar organic compounds with dynamic SIMS and suggest that liquid metals may be useful in other SIMS applications.

[Sponsored by ONR]

REFERENCES

1. R.J. Colton, "Molecular Secondary Ion Mass Spectrometry (SIMS)" *J. Vac. Sci. Technol.* **18**, 736 (1981).

2. M.M. Ross and R.J. Colton, "Carbon as a Sample Substrate in Secondary Ion Mass Spectrometry" *Anal. Chem.*, **55**, 150, (1983)

Unique Properties of Europium Molysulfide, by S.A. Wolf and W.W. Fuller, *Condensed Matter and Radiation Sciences Division*

The Navy is interested in the development of superconducting materials because of their use in electromagnetic sensors, communication devices, and navigation systems and their potential application to electrical machinery and power transmission lines. If superconducting materials are to be used efficiently, it is necessary to have a fundamental understanding of the interactions among their structural components. For this reason, NRL scientists have been studying the properties of certain exotic superconducting materials which could lead to dramatic improvements in the design and application of superconducting wires.

One such material, europium molysulfide ($EuMo_6S_8$), in a structure called the *chevrel phase* (eight cubes of molybdenum and sulfur surrounding the europium atom) has exhibited several remarkable and unexpected properties. Although this sulfide was expected to be a superconductor similar to other rare earth chevrel phase materials, it showed no evidence of superconductivity, even down to a temperature of 0.01° K above absolute zero. The absence of superconductivity was attributed to an anomalous temperature dependence of resistance (Fig. 10). It was suggested that $EuMo_6S_8$ was either a narrow-gap semiconductor or exhibited low-temperature magnetic scattering (Kondo effect) due to the magnetic moment of the Eu atoms.

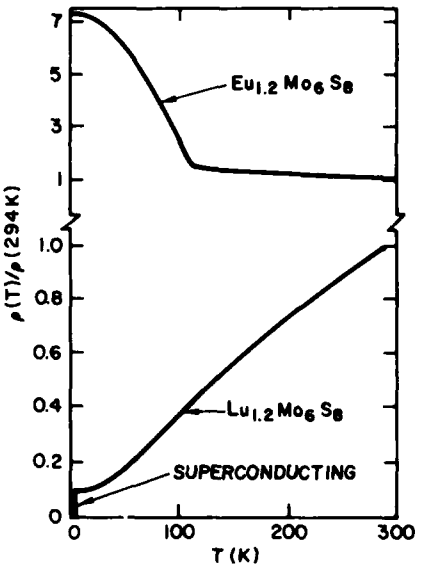

Fig. 10 — Normalized resistivity (ρ) as a function of temperature T for $Eu_{1.2}Mo_6S_8$ and $Lu_{1.2}Mo_6S_8$. The behavior of the Lu chevrel is similar to that of a metallic superconductor.

Several groups outside NRL independently discovered that if a hydrostatic pressure above 6 kbar is applied to this material it becomes superconducting with a transition temperature (T_c) which increases rapidly with pressure to a maximum of about 10°K at 12 kbar. We have measured the thermoelectric power as a function of temperature and the resistance as a function of temperature and pressure. From these observations we deduced that the anomalous behavior of the resistance at low pressures is caused by a phase transition which reduces the number of electrons that are available for conduction, and hence for superconduction. As the pressure is increased, the transition temperature is reduced and the number of electrons available for conduction is increased. At higher pressures, the transition is completely suppressed. Almost simultaneously with our observations another non-NRL group using x-ray diffraction discovered a lattice distortion occurring at the temperature that we

had deduced was the phase transition temperature. Yet another group discovered an anomaly in the heat capacity at the same temperature, also a sign of a phase transition. Thus the mystery of why $EuMo_6S_8$ is not a superconductor was solved: distortion of the chevrel phase structure at low temperatures results in a much lower electron density than in the chevrel phases of the other rare earths. The electron density is also much lower than predicted by band-structure theory based on the undistorted chevrel structure. It is now possible to predict the pressure dependence of the transition temperature on the basis of a theoretical model which takes the distortion into account. The results of this model (Fig. 11) show good agreement with experienced data.

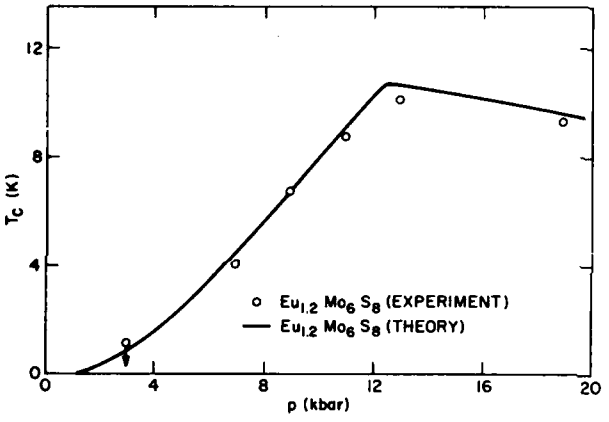

Fig. 11 — Superconducting transition temperature T_c as a function of pressure p for $Eu_{1.2}Mo_6S_8$.

The magnetism associated with the Eu atom also has a strong influence on the superconducting properties of this material. In most cases, magnetic moments degrade superconductivity because a magnetic field acting on superconducting electrons tends to make them nonsuperconducting. If magnetic moments are present, an applied magnetic field will usually align these moments and increase the internal field acting on the superconducting electrons. This usually decreases the critical applied field H_c at which superconductivity is suppressed. In some special cases in which the atoms that contribute the magnetic moment are separated from the atoms that provide the electrons for superconductivity, it is possible for the field of the magnetic moment to be opposed to the applied field at the site of the superconducting electrons. This is called the *compensation effect* and can give rise to very high critical fields. We have observed this compensation effect in measurements of the critical field of $EuMo_6S_8$ as a function of pressure. At low pressures, (the distorted phase) the field of the moments acting on the superconducting electrons is so strong that it overwhelms the applied field at low temperatures, leading to a reduction in the critical field. At higher pressures, (the undistorted phase) the internal field of the moments cancels the applied field and the critical field becomes very large [2]. These features are apparent in Fig. 12 where the re-entrant behavior of the critical field vs temperature curve at low pressures changes to a curve rising to anomalously large H_c at 13 kbar. This drastic change in behavior is associated with the suppression of the lattice transformation above 12 kbar. Thus although the behavior of $EuMo_6S_8$ is anomalous in many respects we have been able to put together a selfconsistent picture from a series of complementary measurements.

[Sponsored by ONR]

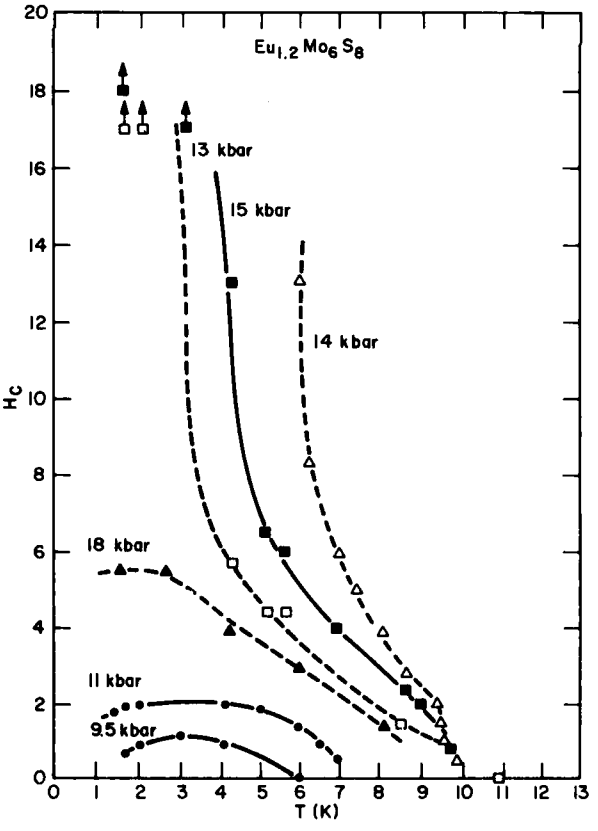

Fig. 12 — Critical magnetic field H_c as a function of temperature T for a range of pressures

REFERENCES

1. R.C. Lacoe, S.A. Wolf, P.M. Chaikin, C.Y. Huang, and H.L. Luo, "Partial Gapping of the Fermi Surface and Superconductivity in $Eu_xMo_6S_8$" *Phys. Rev. Lett.* **48**, 1212 (1982).
2. C.Y. Huang, D.W. Harrison, S.A. Wolf, W.W. Fuller, and H.L. Luo, "Study of $Sn_xEu_{1.2-x}Mo_6S_8$ under High Pressure and High Magnetic Field," *Physica* **109** and **110B**, 1649 (1982).

Photoacoustic Spectroscopy of Piezoelectric Polymers, by E. Balizer, *Acoustics Division*

Semicrystalline polymers, composed of amorphous and crystalline fractions, have a variety of important piezoelectric and mechanical applications as acoustic transducers and as coatings for fiber optics to enhance their performance as sensors. Two types of such polymers, a copolymer of vinylidene fluoride and tetrafluoroethylene (VDF-TFE), and polyethylene terephthalate (PET) are of particular interest for these applications. Since the mechanical and electrical properties of these polymers are directly related to their crystalline composition (the degree of crystallization and the orientation of the crystals), a reliable and sensitive method of measuring this composition is required. Standard methods of infrared transmission, x-ray diffraction, and calorimetry suffer from the disadvantage of requiring special sample preparation or destructive tests which are not always possible on devices or intact coatings.

As an alternative measurement method, NRL, in collaboration with the University of Pennsylvania and the Digilab Corporation, has applied the recently-developed technique of photoacoustic spectroscopy. This technique provides a nondestructive and quantitative method of determining the crystallinity of prototype polymer coatings without restriction on the geometry of the sample and without the need for special preparation. Photoacoustic spectroscopy involves focussing a chopped light source at the particular wavelength of interest onto a sample in a gas filled cell which also contains a microphone. An acoustic signal is generated when the light absorbed by the solid is converted to heat and causes the surrounding gas to expand. The strength of this signal depends upon the amount of energy absorbed which in turn depends on the radiation absorption properties of the sample at that wavelength. With all other parameters held constant, the strength of the signal is proportional to the material composition, in this case the degree of crystallinity. Thus, a quantitative measure of the polymer crystalline fraction can be obtained from the ratio between the absorption lines associated with the crystalline component and the absorption lines intrinsic to the material whether crystalline or not.

In the case of the VDF-TFE copolymer, the crystalline and highly polarized (and therefore piezoactive) β-phase has a crystallinity spectral line at 510 cm^{-1}. Mixing low and high molecular weights of this polymer makes it especially easy to process electroactive coatings. A series of such mixtures was prepared as prototype samples for coatings and analyzed by the photoacoustic method for crystalline content. The photoacoustic spectra were taken with a Digilab Fourier transform infrared spectrometer and photoacoustic cell. The crystallinities of the copolymer blends were determined from the ratio of the intensities of the 510 cm^{-1} crystallinity spectral line to that of an intrinsic material line at 530 cm^{-1}. Only a slight variation in the crystalline fraction for the blends was found, indicating that the proportion of different molecular weights did not significantly alter the final crystallization of the samples. This result is attributed to the very

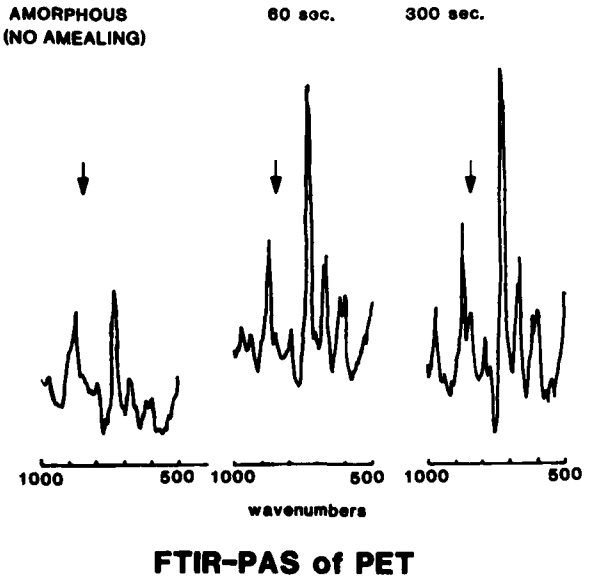

Fig. 13 — Fourier-transform infrared photoacoustic spectra of PET showing growth of the 848 cm^{-1} crystalline band

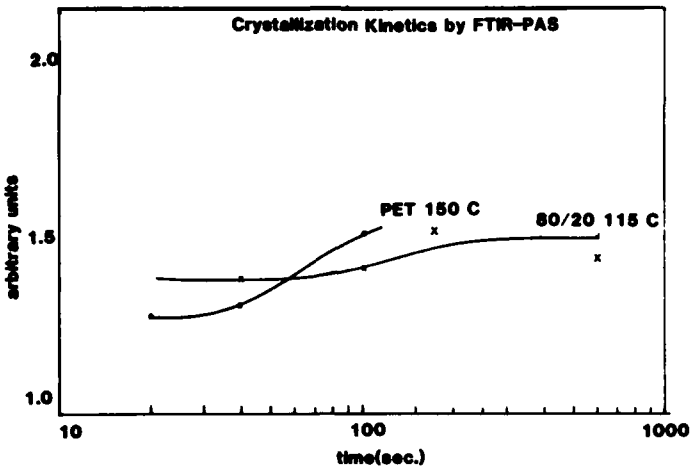

Fig. 14 — The kinetic curves for PET crystallized at 150°C and its 80/20 blend, at 115°C

rapid crystallization which occurs when the samples are cooled from the temperature of crystallization.

A more illuminating study was performed on polyethylene terephthalate (PET) and a mixture of 80% by weight of PET with 20% of polybutylene terephthalate. For these two systems the slower rates of crystallization can readily be followed by photoacoustic spectroscopy. This is illustrated by comparing the spectrum of PET in the unannealed and therefore amorphous, (non-crystalline), state with spectra of PET that has been annealed for 60 s and 300 s, as shown in Fig. 13. All the absorption lines show more definition and growth as the annealing time is increased, but the appearance of the 848 cm^{-1} line is due only to the onset of crystallinity.

The ratio of intensities of the 848 cm^{-1} line and a reference line at 632 cm^{-1} is plotted vs annealing time in Fig. 14 for PET crystallized at 150°C and for the 80/20 mixture crystallized at 115°C. Both kinetic curves of the crystallization have the same characteristic sigmoidal shape indicative of a phase change. Similar sets of kinetic curves were then obtained from the more conventional technique of infrared transmission spectroscopy. These had a greater spread in intensity values with crystallinity but the characteristic half times (in which half of the crystallization occurs) agree within a few percent for the photoacoustic and infrared methods. This close agreement indicates that photoacoustic spectroscopy is a sensitive way to examine the polymer crystallization processes.

We are presently investigating the effects of sample thickness on crystallinity and crystal orientation for both polymer systems; the results will be correlated with the response of polymer-coated sensors.

[Sponsored by ONR]

REFERENCE

1. E. Balizer and H. Talaat, "Photoacousic Study of Polymer Blends of VDF-TFE and PET/PBT" *1982 IEEE Ultrasonics Symp. Proc.*, (1982) p. 571. (1982).

The Effect of Porosity and Grain Size on Wear in Ceramics, by C.C.M. Wu and R.W. Rice, *Material Science and Technology Division*

Many ceramic materials, with their high hardness and low coefficient of friction, show moderate to high resistance to wear. Furthermore, many of these materials can be used at high temperatures and in corrosive environments. These characteristics have led to the selection of ceramics to replace conventional hard-face materials for shaft seals in *Trident* submarines.

The seal on a submarine propulsion shaft is provided by mating two flat surfaces or *faces.* The rotating face is usually made from a hard material such as stellite (31% Cr, 12% W, 2.5% C, and 54.5% Co); the stationary face is made of a soft material such as a carbon composite. In service these seals have shown considerable variation in leakage accompanied by high wear on one or both surfaces. Their reliability and operational life is not adequate for the high performance required of the Navy's submarines.

The properties that determine the usefulness of ceramics in this application depend, to a very large extent, on the microstructure of the material. We have undertaken a thorough study of the key microstructural factors that affect the performance of ceramics so that we may establish guidelines for the selection and development of the most suitable ceramics for a particular application. Two of the most important microstructural factors under study are porosity and grain size.

A major factor in the wear of surfaces moving relative to each other is the roughness caused by asperities (protruberances) which dig into the opposing surface or are sheared off by the relative motion. Two different tests are used in our studies. The first is the pin-on-disk (POD) test in which a diamond pin with a 90° conical point (0.0762 mm radius at the point) slides on a polished surface under a predetermined dead weight load (Fig. 15a). This microscale test is a first approximation to a single asperity interacting with a surface. The wear track is characterized in terms of its cross-sectional area (material lost), the nature of the track surface and related damage. The second test uses a Taber Tester abrader, a commercial instrument with two rotating multipoint diamond wheels which abrade the specimen under a known load (Fig. 15b), the debris being removed continuously. This macroscale test provides many asperities moving over a large area of the surface. Weight loss, depth of abrasion, and especially the character of the wear

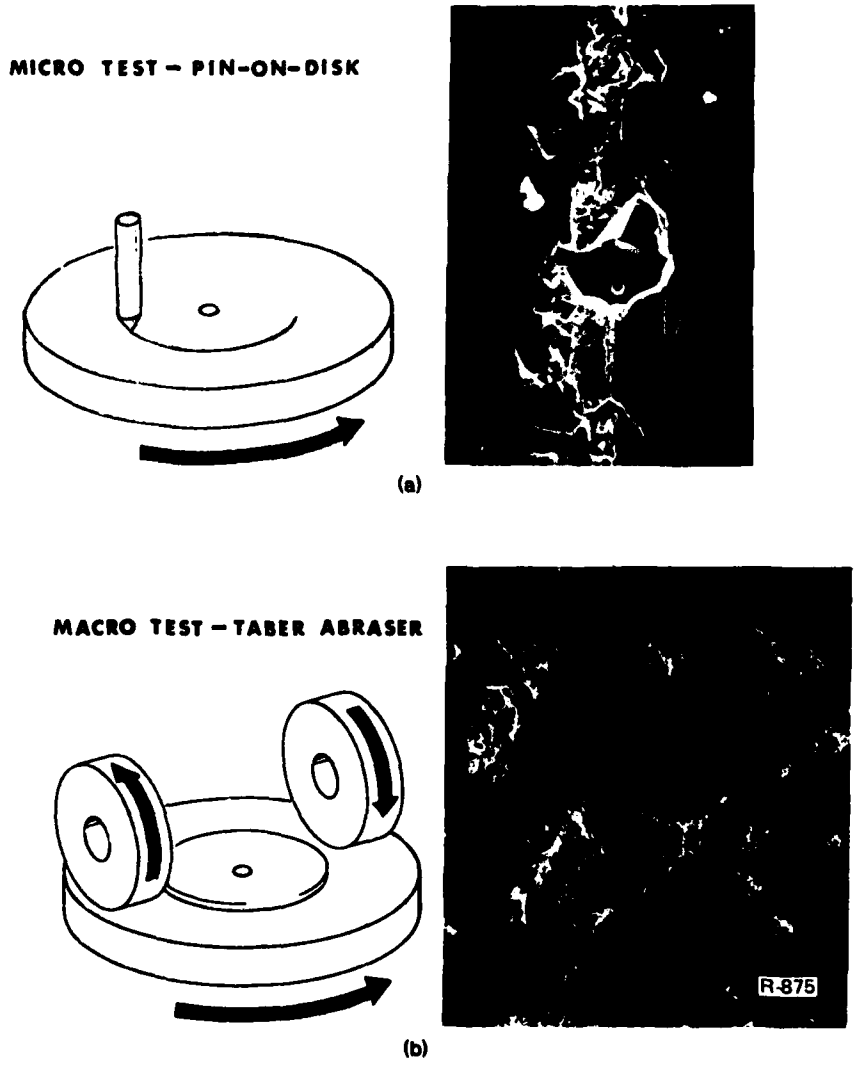

Fig. 15 — (a) Pin-on-disk apparatus with wear track on Al_2O_3 sample; (b) Abrader with abrasion pattern on B_4C sample

surface are noted. The two tests are correlated to provide a broader understanding of wear mechanisms.

Hot-pressed Al_2O_3 and B_4C bodies with fine grains (~2 μm and 5 μm respectively) and different porosities have been tested with the POD apparatus. The cross-sectional area of the wear track for Al_2O_3 is plotted as a semilog function of the porosity P and shows a family of parallel lines for different applied loads; all lines show a significant change of slope at a porosity of about 20% (Fig. 16). There is a suggestion that the change in slope occurs at lower porosity under higher loads. When the results are plotted with the load divided by the cross section of the wear track as the ordinate (as in a conventional hardness test) a single curve is obtained consisting of two straight lines with slopes of about 3 for $P < 20\%$ and about 11 for $P > 20\%$ (Fig. 17). The change of slope may indicate that the wear mechanism changes to a crushing mechanism at higher values of P. The hardness of these same Al_2O_3 bodies, measured with a Vickers indenter, gave a linear semilog plot with a slope of 6.5, intermediate between the two wear slopes.

Results of POD tests on B_4C (Fig. 18) also showed a linear semilog dependence on P, but in this case both hardness and wear had a single slope (~7.5) up to the limit of the porosity tested (~14%). This slope is similar to the hardness dependence of Al_2O_3, but much greater than the slope of the Al_2O_3 wear curve at low P.

Studies of dense Al_2O_3 bodies of varying grain size with both the POD and Taber testers show wear rates which increase with increasing grain size; the POD test shows a greater increase than the Taber test. However, the effect of grain size is substantially less important than the effect of porosity.

Examination of the wear tracks indicated that wear damage, mainly cracks, usually extends far beyond the direct contact region. The interaction of these cracks with one another, and with the microstructure of the body, is of great importance for the wear process. We plan to assess this subsurface damage using x-ray topographic techniques.

The lifetime and reliability of shaft seals depend on the whole spectrum of material properties. The Navy currently has little quality control on these materials and relies on the data provided by the manufacturers. Our studies have begun to throw light on of the mechanisms of wear in these materials. Further studies should

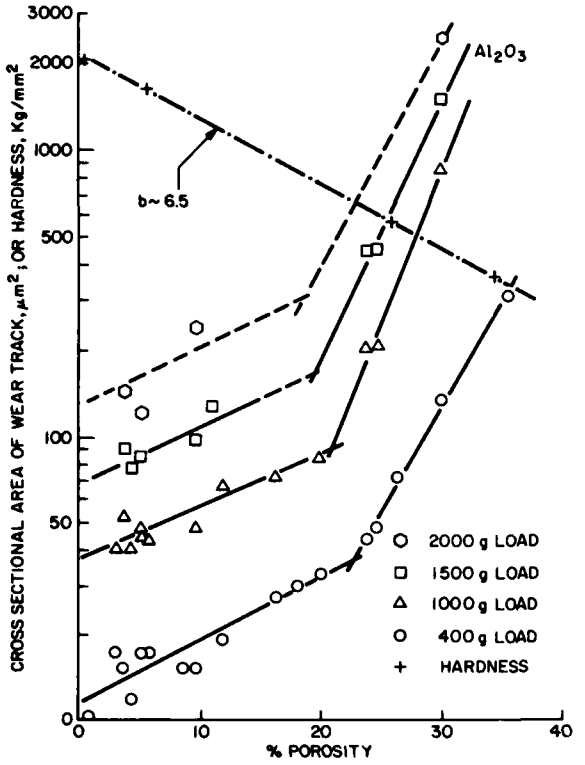

Fig. 16 — Dependence of wear on porosity in fine-grained Al_2O_3 with applied loads as the parameter.

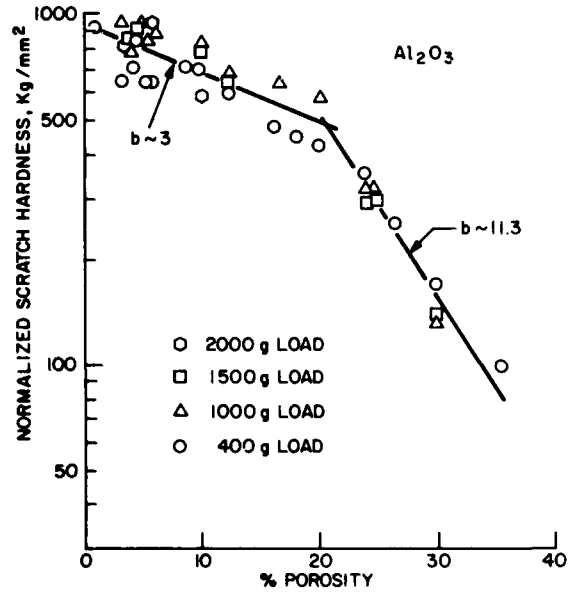

Fig. 17 — Normalized scratch hardness vs porosity

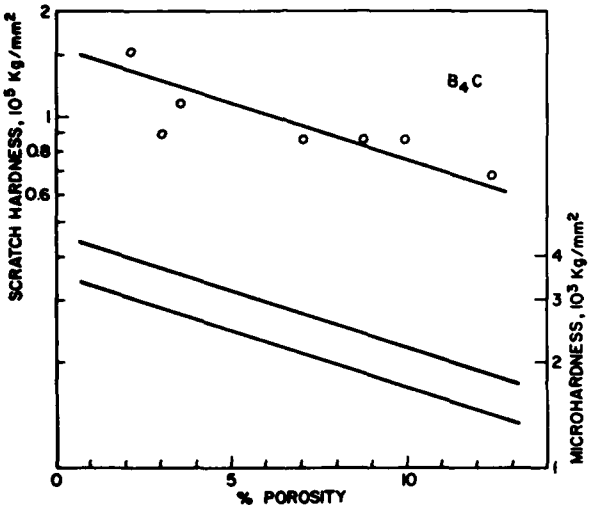

Fig. 18 — Dependence of wear on porosity in fine-grain B_4C

allow us to specify the crucial microstructural properties that are needed for reliable and long-lived shaft seals.

[Sponsored by ONR]

Porosity of Activated Carbons, by Peter D'Antonio and John Konnert, *Laboratory for the Structure of Matter*

Activated carbons are used extensively in ships and submarines as adsorbers to remove airborne pollutants and radioisotopes, and as supports for catalysts and impregnants which are used to neutralize toxic gases. Their usefulness derives from their very porous structure. The surface area of pores ranges from 1800 m^2/gm for carbon produced from coconut shell, to 3900 m^2/gm for a carbon called PX-21 prepared from petroleum coke. The pore distribution not only influences the amount of material that can be physically adsorbed at equilibrium, but also the poisoning characteristics of a surface for one reaction compared to another and the order and activation energy of a catalytic reaction. Knowledge of the porosity is therefore important when considering any particular application of activated carbon.

The distribution of pore size is usually measured by the chemical analysis techniques of gas adsorption isotherms and mercury porosimetry. However, these methods often assume a certain pore shape and are not sensitive to inaccessible occluded volume. At NRL we have developed a complementary method to determine the distribution of sizes and volumes from small-angle x-ray scattering. This type of scattering arises from the electron density differences between the voids and the carbon matrix. The voids can range in size from ten to several thousand times the x-ray wavelength. A void is characterized by its radius of gyration, R_o. By analogy to classical mechanics, R_o can be considered as the electronic radius of gyration of a particle about its electronic center of mass. The small angle scattering is expressed as a function of the parameters defining the resolution function of the experimental arrangement and $M(R_o)$, the void volume distribution. A least-squares procedure is used to refine the parameters defining $M(R_o)$, until a satisfactory fit between the calculated and observed intensities is obtained. $M(R_o)$ is represented as a sum of overlapping functions that are flexible enough to assume most smooth shapes. This technique does not assume any particular void shape, nor does it require that the intensity be inversely proportional to the fourth power of the scattering vector at large angles, as is the case with other small-angle scattering procedures. This method is especially applicable to systems such as PX-21 in which there is extensive overlap between the small- and large-angle scattering regimes.

Figure 19 shows the resulting void volume distribution for coconut shell carbon. The distribution is trimodal with peaks at radii of gyration of 6, 25, and 160 Å. Approximately 85% of the volume is in the 6-Å peak, with the remaining volume equally distributed between the 25-Å and 160-Å peaks. Similar trimodal distributions were obtained for two other commercially available activated carbons — BPL and CWS. These carbons can be impregnated with ammoniacal chromium and copper salts to form whetlerite, an effective filter of airborne pollutants which is often used in air filtration systems aboard surface ships and in gas mask cannisters.

We have demonstrated that the NRL technique can readily determine the distribution of void volume in a material from its small-angle scattering properties. Potential adsorbants can be categorized by their void volume distributions, and their suitability for certain applications can be evaluated. Further work will use this technique to study the nature of the adsorption process by impregnating coconut shell carbon with various concentrations of methyl iodine, a material having the same electron density as carbon. Changes

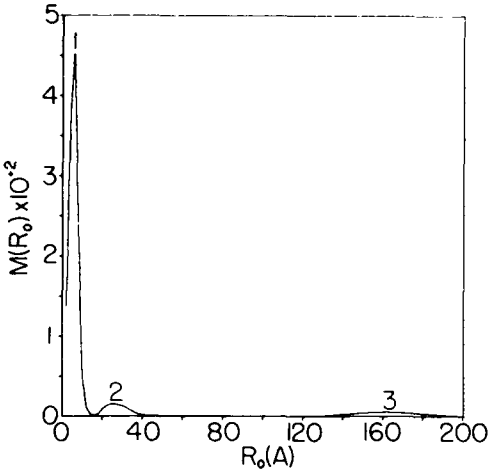

Fig. 19 — Void volume distribution, $(M)R_0$, for coconut shell carbon vs radius of gyration, $R_0(A)$. Approximately 85% of the pore volume is in the 6-Åpeak

in the void volume distribution which accompany the impregnation will be used to determine which voids are being affected and in what manner.

[Sponsored by ONR]

Quality Control Testing of Rubber Composites, by R.D. Corsaro, *Acoustics Division*

Molded rubber articles are generally manufactured by blending about ten chemical components and curing the mix in a hot press to form the final article. During large-scale manufacture, one is likely to encounter variations in the chemical ingredients used, errors on the part of factory personnel, and possibly unreported changes in the manufacturing procedure. The Navy relies heavily on quality control (QC) testing to assure that the received articles will perform acceptably. The particular QC tests are usually the standard tests of the rubber-processing industry; namely, density, durometer, elongation, and tensile strength. These standard QC tests have been found to be inadequate for some critical Navy needs.

To illustrate this, we selected a representative rubber structure—a molded rubber mat containing air cavities—and had 33 manufactured. One of these was our reference standard, while the other 32 purposely contained manufacturing defects typical of those most likely to occur in a production environment. Usually this assumed either operator forgetfulness (a chemical component completely missing or added twice) or an attempt at reducing costs (substituting a similar component which is either cheaper or speeds processing). Examining the 33 mats using the usual factory quality assurance tests we could identify less than 20% of the mats as deviating from our standard. We concluded that existing QC tests are inherently incapable of detecting most of these serious processing errors.

To develop a more suitable QC test, the 33 mats were then subjected to a wide variety of laboratory measurements. These required careful (and often destructive) sample preparation, time-consuming measurement procedures, and elaborate apparatus not suitable for use in a factory. From this detailed study, we found that a measurement of dynamic modulus was the most successful way to reveal bad rubber compositions. Fortunately, this measurement is also highly relevant to the dynamic performance of the final article, which is not measurable using the conventional static QC tests. It then became necessary to develop an apparatus capable of quickly and nondestructively measuring this property in a factory or shipyard environment.

The technique we developed is illustrated in Fig. 20. The mat to be tested is sandwiched between a shaker table and a top mass. When the shaker table is vibrated, we have a classical spring-mass problem and if the vibration frequency is just right, a spring-mass resonance is set up. By including accelerometers in the shaker table and the top mass, we can follow the motion

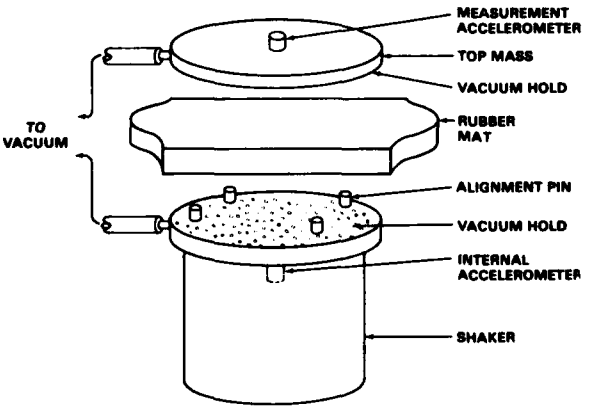

Fig. 20 — Apparatus for quality-control testing of rubber mats

of these two items while the vibration frequency is varied. This allows a very precise measurement of the resonance frequency which in turn is closely related to the dynamic modulus of the material.

The testing apparatus we have developed satisfies all our requirements. The test is quickly performed, requiring only a few minutes per test by operators with little training or technical background. It is portable, with all required components contained in one roll-around cart. Furthermore, the test is nondestructive because a novel vacuum-hold is used to fix the mat to the shaker stage and top mass instead of cement.

When used to test our 32 defective mats, this new transfer-impedance test was able to distinguish 66% of the bad mats from the reference standard (with 98% confidence in each rejection). This one test is therefore considerably more successful in detecting bad mats than all other existing quality assurance tests combined.

[Sponsored by ONR and NAVSEA]

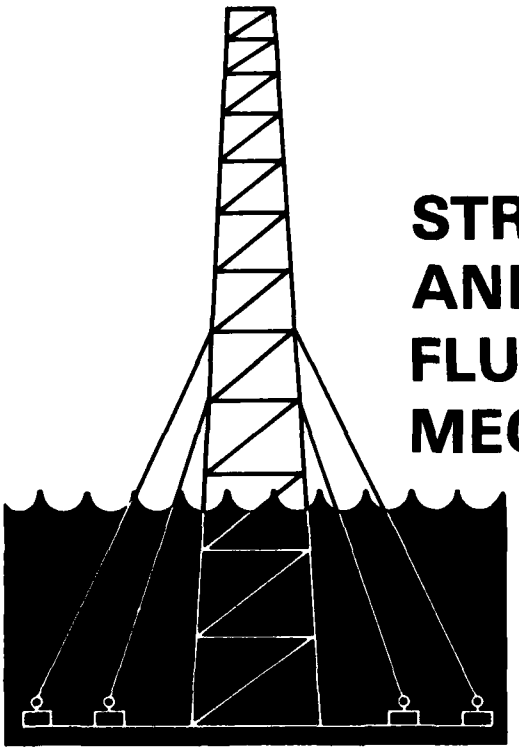

STRUCTURAL AND FLUID MECHANICS

STRUCTURAL AND FLUID MECHANICS

The application of scientific analysis to engineering problems can lead to a better understanding of behavior of structures and mechanical systems. This in turn leads to increased effectiveness of Naval operations, as the following articles show.

Actuator Placement for the Control of Large Space Structures, by R.E. Lindberg and K.T. Alfriend, *Aerospace Systems Division*

The Space Shuttle will be able to deploy satellites of unprecedented size. Since the weight of these satellites will be limited by launch costs, they will probably be very flexible and will give rise to a new generation of control problems. These problems may be analysed using practical models of flexible structures which are approximations to the actual systems and are obtained by eliminating all but a limited number of the dynamical equations. One significant problem is to develop design methods for control systems that minimize the degradation of system performance arising from unmodeled dynamics. A new aspect of the problem is that whereas the control of a rigid satellite is often independent of the location of the actuators, the placement of the actuators on a flexible structure is of primary importance in providing effective attitude and shape control.

NRL has undertaken a multiyear research effort into the dynamics and control of large flexible space structures. In 1982, work in conjunction with Columbia University has provided assessments of various methods for optimizing actuator locations [1]. This work has provided insight into the effects of various control design parameters on the optimal actuator locations. The parameters considered for our models include the control objective, the order of the model (number of modes retained) the normalization of the modes (that is, the relative emphasis placed on controlling the various modes), and the number of actuators used.

The approach taken is to choose actuator locations which maximize a quantity called the *degree of controllability.* This is a recent extension of the well-established concept of complete controllability. A system is said to be completely controllable if the controller can drive the system from any arbitrary set of initial conditions to any desired set of final conditions in finite time with finite effort. The degree of controllability is a quantitative measure of the controllability of a completely controllable system, and is related to the range of initial conditions that can be driven to a given set of final conditions using a prescribed amount of time and/or effort. (Note that for a system which is not completely controllable, the degree of controllability is zero.)

Control of the transverse oscillation of a simply supported beam—that is, a thin beam hinged at each end—is a convenient example of a structural control problem. The motion of a continuous structure can be expressed as a linear combination of an infinite number of mode shapes, each multiplied by its modal amplitude. Any practical model will be limited to a finite number of modes chosen by the designer. For a simply-supported beam, the mode shapes are sine functions, the first three of which are shown in Fig. 1 with their corresponding frequencies. Both internal and external disturbances can excite the various modes, which will not necessarily contribute equally to the overall motion of the system. The designer must then establish a normalization or weighting of the modes according to their expected contributions. In this example we can examine how the order of the model, the normalization, and the number of actuators will affect the optimal placement of actuators.

To control oscillation of the beam, force must be applied at some point or set of points along the beam. Clearly, a force at either end will not control oscillations, so for these actuator locations the beam is uncontrollable. A single actuator at any location other than the ends can control the first mode and, not surprisingly, the degree of controllability is maximized by placing the actuator at the midpoint. The second mode is uncontrollable from that location, and a single actuator must be located elsewhere if it is to control both of these modes. The normalization of the modes is then important, as seen in Fig. 2. Here, the weight N_1 assigned to the fundamental mode is varied with respect to the weight N_2. The ratio $N_1/N_2 = 4$ indicated by the horizontal dashed line is the normalization corresponding to

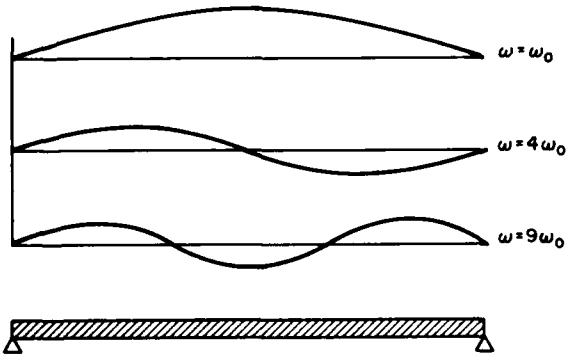

Fig. 1 — Simply-supported beam with first three mode shapes and associated frequencies. In this case, the frequencies are proportional to the squares of the mode numbers.

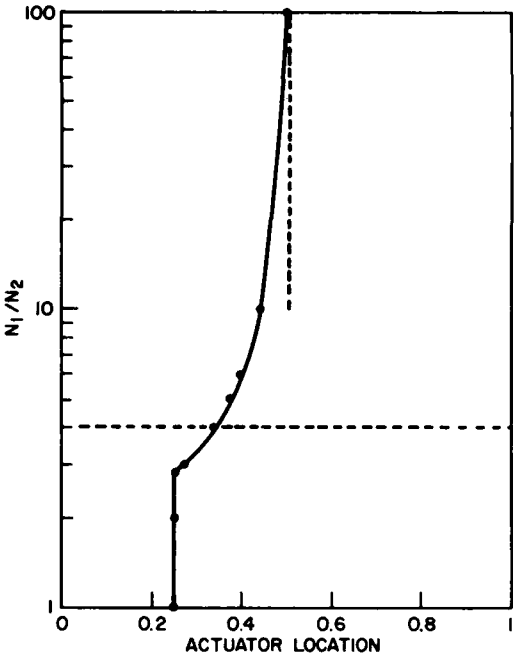

Fig. 2 — Optimal placement of one actuator for a two-mode model with variation in the weighting N_1 of the fundamental mode

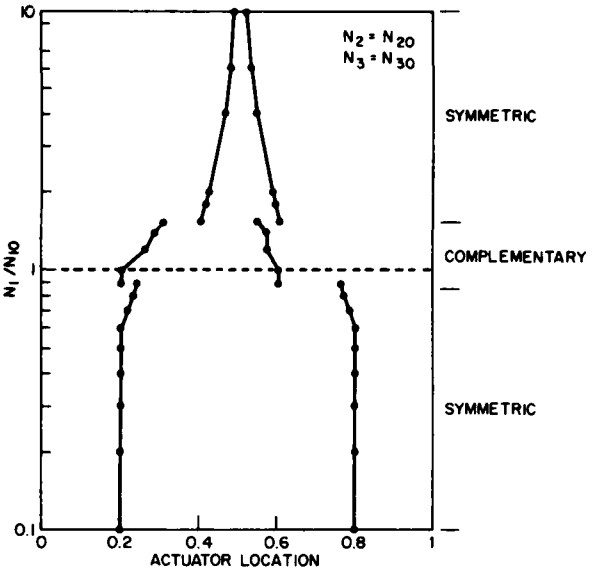

Fig. 3 — Optimal placement of two actuators for a three-mode model with variation in the weighting N_1 of the fundamental mode. N_{10} N_{20}, and N_{30} are the normalizations that would be chosen if the energy of the system is to be distributed equally among the modes.

the energy of the system being distributed equally between the modes. In the general case, this normalization is inversely proportional to the frequency of the mode.

An interesting case is when we use three modes to model the dynamics and consider the optimal placement of two actuators to control the beam (See Fig. 3). The optimal solutions then fall into two broad categories. When the optimal solution is a symmetric pair of locations, they each represent an equally optimal location at which to place a single actuator. When a non-symmetric pair of locations is optimal, each actuator provide good control authority only over some part of the model (that is some group of modes). In this case, neither location is optimal for a single actuator, and so we call the solution a complementary pair. The significance of this result is that for large systems with many actuators, the optimal placement of n actuators cannot be achieved by simply finding the n best locations for a single actuator. Continuing research on this problem will involve using these actuator placement methods, in conjunction with decentralized control techniques, to design control systems for large-order generic spacecraft models.

[Sponsored by ONR]

REFERENCE

1. R.E. Lindberg, "Actuator Placement Considerations for the Control of Large Space Structures," NRL Report 8675, May 1983.

Wave Forces on Cylinders, by Steven E. Ramberg, *Marine Technology Division*

The prediction of wave forces on marine structures or components is still largely an empirical process. The force is resolved into drag and inertial components which are proportional to simple functions of the wave-induced velocity and acceleration, respectively, with the coefficients determined from practical observations. This approach has been widely used in the absence of more detailed models of the complex flow processes that accompany unsteady wake formation in oscillatory flows such as ocean waves. Despite considerable effort by the offshore industry and others during the past 30 years, the variations in reported values of the empirical drag and inertia coefficients are still unacceptably large. Better prediction methods are needed in view of

the deeper water and harsher climates contemplated for future deployments, and the often novel requirements of naval applications.

As one part of a research program on wave-structure interactions, we have conducted a detailed study of the forces on a horizontal cylinder in laboratory waves. This configuration was chosen because it retains most features of more general wave-structure interactions while simplifying the flow to one that is uniform over the cylinder span. In addition, it has some direct practical applications. The effects of varying wave orbit shapes have been examined both on the form of the empirical equation and on the values of the empirical coefficients [1]. For example, in Fig. 4 the measured force on a cylinder in deep-water laboratory waves (circular orbits) is compared with predictions based on the customary empirical equation and on a simpler linear form developed at NRL. The efficacy of the linear approach under these conditions is clear, allowing a number of simplifications in the analysis of wave loading and in the prediction of the durability of ocean structures. Further, it was found that the more circular orbits lead to smaller drag forces; this is a welcome result since it implies that tests in purely planar oscillatory flows will produce substantial overestimates of actual wave forces.

The problem is complicated by the fact that even in a uniform wave train a body experiences forces which vary from wave to wave. We have therefore examined these wave-by-wave variations in the measured forces on a horizontal cylinder and compared them with corresponding variations in the empirical force transfer

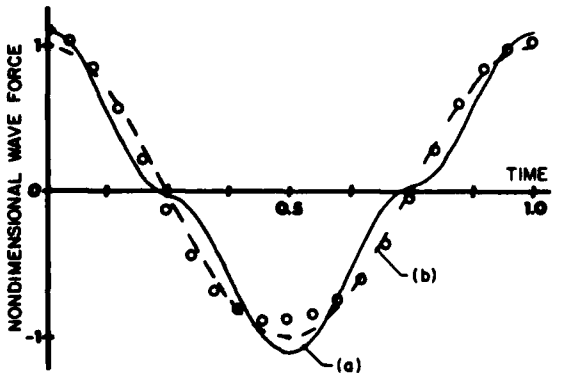

Fig. 4 — A comparison of the measured wave force on a horizontal cylinder (O) with (a) the usual empirical method —— and (b) NRL simplified deepwater method — — —

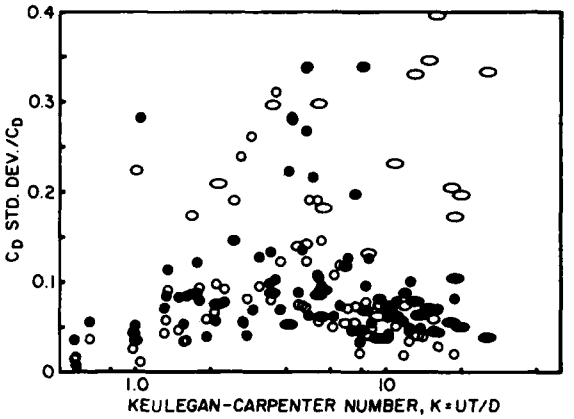

Fig. 5 — Standard deviation of consecutive wave-to-wave values of the empirical drag coefficient vs Keulegan-Carpenter number K. Ellipticity of data point indicates wave orbit shape. Open symbols: vertical force components. Closed symbols: horizontal components.

coefficients [2]. Figure 5 presents the measured cycle-to-cycle standard deviation of the drag coefficient (C_D) normalized to the average C_D over the same cycles. Results are shown for the horizontal and vertical components of the wave force under a variety of wave orbit shapes and a range of Keulegan-Carpenter numbers, K (ratio of maximum orbit size to cylinder diameter). Larger values of K, particularly for the vertical force component and the more elliptic orbits, were associated with larger cycle-to-cycle drag variations. More significantly, the indicated variations in the drag component were several times greater than the cycle-to-cycle variations in the total force and an order of magnitude greater than variations in the rms height of the waves themselves. We concluded that cycle-to-cycle phase deviations were responsible for this effect and can lead to larger apparent variations in the force coefficients than the variations in the force actually experienced by the structure. This implies a limit to the accuracy of any simple method that resolves the wave force into drag (in-phase) and inertia (out-of-phase) components.

This program has resulted in improved techniques for predicting wave forces on structures and has provided further insights into the mechanics of the wave-structure interaction.

[Sponsored by ONR]

REFERENCES

1. S.E. Ramberg and J.M. Niedzwecki, "Horizontal and Vertical Cylinders in Waves," *Ocean Engineering*, 9, 1 (1982).

2. S.E. Ramberg and J.M. Niedzwecki, *Proceedings of the 2nd International Off-Shore Mechanics and Arctic Engineering Symposium*, Jan 1983, Houston, Texas, p 165 (ASME 1983).

Vibrations of Marine Cables, by O.M. Griffin, *Marine Technology Division*

The oscillations of marine cables caused by vortex shedding, commonly termed *strumming*, result in increased hydrodynamic forces on the cables, amplified flow noise, and sometimes lead to structural damage and fatigue failures. Flow-excited oscillations are often a critical factor in the design of reliable and economical underwater cable arrays, mooring systems, drilling risers, and offshore platforms. Many components of these complex structures have unstreamlined cylindrical shapes which are conducive to vortex shedding when water flows past them. To assist the Navy with the design of submerged cable systems that limit or withstand strumming oscillations, a computer code called NATFREQ has been developed at the California Institute of Technology for the Naval Civil Engineering Laboratory (NCEL). The code calculates the natural frequencies and mode shapes of taut cables with large numbers of attached discrete masses. Until recently, this code had not been validated by field observations.

Field experiments were conducted in 1981 to study the strumming vibrations of marine cables. One of the principal objectives was to validate NATFREQ. The experiments were planned jointly by NRL and the Massachusetts Institute of Technology (MIT), and conducted at the test site by MIT. Simulations of twenty test runs using the NATFREQ code and a comparison of the simulations with selected field test data were made at NRL. The data included time histories of the measured hydrodynamic drag force on the cable, the speed of the current at various locations on the site, and the responses of accelerometers in the cable to the vortex shedding.

The site chosen for the experiment was a sandbar at the mouth of Holbrook Cove near Castine, Maine. At low tide the sandbar was exposed allowing easy access to the test equipment, while at high tide it was covered by about 3 m of water. The test section was oriented normal to the direction of the current which varied from 0 to 0.7 m/s over the tidal cycle and was essentially uniform over the length of the test section at any given moment. The test set-up is shown in Fig. 6.

A 23-m-long composite cable was developed at MIT specifically for these experiments. The outer sheath of the cable was clear flexible PVC tubing 32 mm in diameter. Three 3.2 mm stainless steel cables ran through the tubing and served as the tension-carrying members. Seven pairs of accelerometers were placed inside the PVC tubing at selected locations along the cable. The biaxial pairing of the accelerometers made it possible to determine their orientation and to measure both vertical and transverse horizontal components of acceleration.

In the experiments, cylindrical masses were clamped to the bare cable to simulate sensor housings, hydrophones, and other attached bodies. The mass elements were made of cylindrical PVC stock, 305 mm long and 89 mm in diameter, and could be loaded with lead to vary their mass. Tests were run with various numbers, locations and masses of the attached elements. The field set-up and instrumentation, and the cable design are discussed in more detail in a recent summary of the overall test program [1].

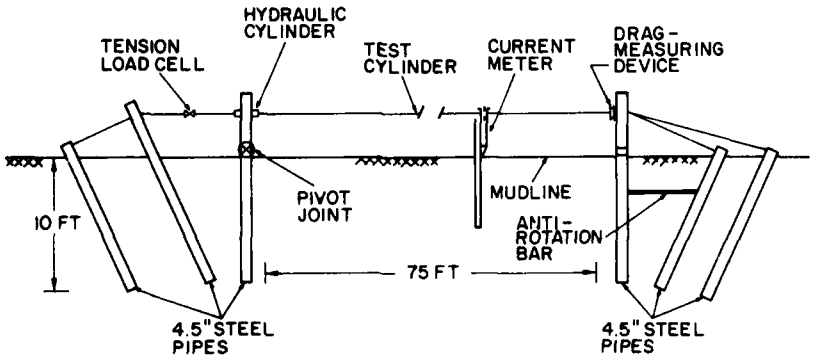

Fig. 6. — The Castine field test set-up

The natural vibration frequencies of the cable were derived at MIT from a spectral analysis of the field test data. Frequencies of the cable in air were obtained by exciting various modes in still air. The measured and computed results for the cable with seven light masses (no lead weights added) are compared in Fig. 7. The measured and computed natural frequencies in air and in water agree for cable modes up to $n = 9$. The water current speeds (up to 0.7 m/s) at the test site limited the vortex-excited strumming vibrations to the first six modes for all of the test runs.

There are discontinuous jumps in the natural frequencies when the mode number equals a multiple of the number of cable segments (number of masses plus one). This is clearly evident in Fig. 7. For the first seven modes, some or all of the masses are in motion at their various locations in the vibration pattern and the inertia of the masses reduces the natural frequencies of the cable in air to below the bare-cable values. For the $n = 8$ mode, all of the seven evenly-spaced mass elements are located at nodes of the vibration pattern, and the mode shape and frequency are identical to those of the bare cable.

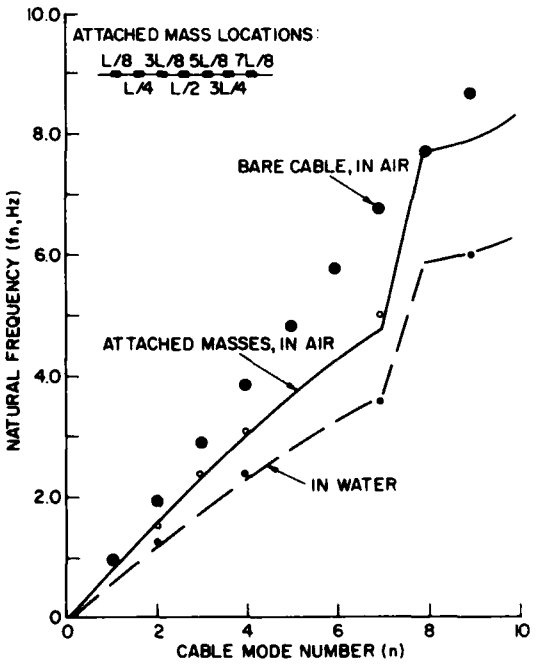

Fig. 7 — A comparison between the frequencies predicted by NATFREQ and the measured natural frequencies for a cable with seven evenly-spaced attached masses. The lines are the theoretical predictions: the points are the measured values.

The natural frequencies for the $n = 9$ and 10 modes fall below the bare cable frequencies when the masses attached to the cable are again in motion. The natural frequencies of the cable in water are lower than those in air due to the added mass effect caused by the unsteady motion of the cable and attached masses in the water. Similar agreement between the observations and the code predictions was obtained for the other test runs.

The validation of the NATFREQ computer code gives us a significant new tool for the design and analysis of underwater structures involving cables. A comparison between the hydrodynamic drag measurements made at the Castine field site and other measurements of cable drag has also been made [2].

[Sponsored by NCEL]

REFERENCES

1. J.K. Vandiver and O.M. Griffin, "Measurements of the Vortex-Excited Strumming Vibrations of Marine Cables," *Ocean Structural Dynamics Symposium '82 Proceedings,* Oregon State University, September 1982.

2. O.M. Griffin, J.K. Vandiver, R.A. Skop and D.J. Meggitt, "The Strumming Vibrations of Marine Cables," *Ocean Science and Engineering,* 7, 461 (1982).

Fire Fighting Tests, H.W. Carhart and J.T. Leonard, *Chemistry Division*

On May 26, 1981, a Marine EA-6B aircraft crashed into several parked aircraft while attempting to land on the *USS Nimitz (CVN-68).* As a result of the crash and the ensuing fire and explosions, 14 men were killed and 42 injured. Damage was estimated at $60 million of which over $53 million was attributed to destroyed and damaged aircraft.

Firefighting efforts began immediately after the crash. The *Nimitz* is equipped with a countermeasures washdown system which dispenses the NRL-developed aqueous film-forming foam (AFFF) through nozzles located in the flight deck. AFFF extinguishes a fire by smothering it. As the foam collapses, it forms a film on the surface of the fuel, which prevents vaporization and reignition. However, the AFFF system was not activated until more than two minutes after the crash. This is a critical delay, especially when ordnance is present. In addition, AFFF was not supplied to the two washdown system zones

upwind of the crash because of electrical failures. As a result, sea water was applied to the fire area instead of foam and greatly reduced the firefighting capability.

The fire was fed by the continuous flow of JP-5 fuel from an F-14 aircraft which had just been refueled. Altogether three F-14 aircraft, each holding a Sparrow missile, a Sidewinder missile, a Phoenix missile, and a quantity of 20-mm ammunition were involved in the fire. Throughout the fire, water from handlines (fire hoses) was directed at the ordnance to prevent detonation. After about 28 minutes, the fire appeared to be extinguished, and the firefighters moved in to deal with the smoldering debris. Shortly thereafter, a Sparrow missile which was concealed in the debris exploded, killing two men, injuring 29, and creating a 3-inch-deep depression in the flight deck. After this event, some experts suggested that the temperature of the warhead had exceeded its detonation or "cook-off" temperature because of the blanketing action of the foam.

The accident raised a number of questions about the effectiveness and efficiency of the Fleet's firefighting and damage control procedures. Some of these questions are:

- Does AFFF insulate ordnance from the cooling effects of sea water?
- Is there a better strategy for cooling ordnance?
- Does the simultaneous application of water and AFFF delay extinction?
- Can AFFF extinguish a running fuel fire?
- Does a coarse debris pile consisting of parts of crashed aircraft protect a fire from extinction?
- For what wartime scenarios should we design fire extinguishment strategies?

NRL was asked to provide answers to these questions by the Aircraft Carrier Flag Level Firefighting Steering Committee. A test plan was developed which included small-scale fire extinguishment tests at NRL's Chesapeake Bay Detachment and large-scale tests on a simulated aircraft carrier flight deck (Mini-deck) at the Naval Weapons Center, China Lake, California. The Mini-deck, which has an area of 7200 ft^2 is equipped with flush deck and deck edge nozzles for dispensing AFFF (Fig. 8). A steel dummy aircraft equipped with instrumented simulated ordnance was used to determine the thermal threat in various fire scenarios (Fig. 9).

Fifty-six small- and large-scale tests have been conducted to date in an effort to simulate

Fig. 8 — Fire tests on simulated aircraft carrier flight deck, Naval Weapons Center, China Lake, California

Fig. 9 — Instrumenting mock ordnance on steel dummy aircraft

problems on the *Nimitz*. For example, to simulate an aircraft wing covering a debris pile, a 9 × 11 ft shed was constructed with cinderblock walls and an oversized steel roof inclined at an angle of about 30° to the deck (Fig. 10). The debris pile was located on the side of the steel dummy aircraft and a pipe carrying JP-5 fuel at 50 gal/min was mounted under the roof to simulate a ruptured fuel tank. The debris pile shielded the running fire from attack by AFFF in the same way as did the crashed aircraft on the *Nimitz*.

Various strategies were evaluated for attacking this type of fire. For example, it was found that a fixed nozzle (monitor) playing AFFF on the debris pile from the shielded side of the fire at a rate of 12,000 gal/min could not completely extinguish the fire, even after 2 minutes of continuous application, because the AFFF could not penetrate the debris to reach the fire. However, a fireman carrying only a single 1.5-in. handline delivering AFFF at 95 gal/min was able to walk up to the debris pile and extinguish the fire within seconds because he maneuvered the stream through holes in the debris to find and extinguish the fire.

Our tests have also established that AFFF, consisting of 98% water itself, has about the same cooling capacity as sea water and does *not* form

Fig. 10 — Extinguishing a debris pile fire

an insulating blanket when sprayed on ordnance. Furthermore, the extinction time using AFFF alone is significantly less that when AFFF is used in combination with sea water.

The tests, begun in 1982, are still in progress. Already, our investigations have led to an important change in the Navy's firefighting strategy. Recognizing that it dilutes the effectiveness of AFFF, sea water will no longer be used to cool ordnance while AFFF is being used to fight a fire. The NRL program will continue; one objective is to develop the most effective combination of firefighting techniques in any given situation. The results of the tests will be incorporated into a training film to translate the lessons learned into Navy firefighting doctrine. NRL scientists will serve as technical advisors.

This program illustrates NRL's ability to respond to critical fleet needs, by combining knowledge acquired in the laboratory with full-scale field testing to provide optimum solutions to the serious Navy problem of fighting fires.

[Sponsored by NAVSEA]

Pseudospectral Solution of the Inviscid Equations of Motion, by L. Sakell, *Marine Technology Division*

Numerical solution procedures for complex flow fields are an essential tool in the design of high speed aerodynamic vehicles. Important characteristics of the vehicle such as range, payload, and controllability can be obtained from numerical solutions, thus allowing designers to identify promising vehicle concepts and configurations and greatly reducing the need for expensive wind tunnel or prototype flight testing. Numerical work itself can be quite expensive if it requires a large amount of time on large computers, and there is always a need to improve the efficiency of numerical techniques.

Work has begun at NRL on the application of a very efficient computational method to complex flow calculations. This is known as a *pseudospectral* computational technique because it uses a finite portion of an infinite series to represent a flow. Used recently to perform difficult calculations on incompressible flows, it has provided excellent spatial resolution of flow fields and has proved itself to be computationally more efficient than other methods. In extending the technique to compressible flows, the central question to be resolved is how accurately and efficiently it can treat discontinuities such as shock waves which are not present in incompressible flows.

Several classical compressible flow problems with discontinuities have been successfully treated using the pseudospectral method [1,2]. The one dimensional propagating normal shock wave was considered first; typical results are shown in Fig. 11. The computed pressure distribution is plotted and compared with the analytic solution. There is good agreement. The shock wave is maintained as a discontinuity at the proper position. This flow field has only one discontinuity, but cases with multiple discontinuities have also been treated.

Results for the classical bursting diaphragm (shock tube) problem are shown in Fig. 12. This flow results when a solid diaphragm separating a high-pressure region at rest from a low pressure region at rest is ruptured and the high pressure fluid propagates into the low pressure zone. Two types of discontinuities simultaneously result: a shock wave and a contact surface. Again, the computed solution shows excellent agreement with the analytic solution.

Having established the utility of the technique for one-dimensional flows, we then studied the two-dimensional flow over a sharp wedge travelling supersonically. This flow results in a two-dimensional shock wave originating from the vertex of the wedge. Figure 13 shows a contour plot of the density in two spatial directions from

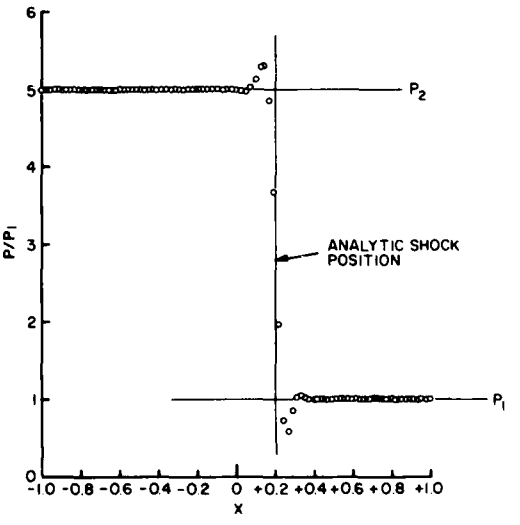

Fig. 11 — Pressure distribution in plane shock

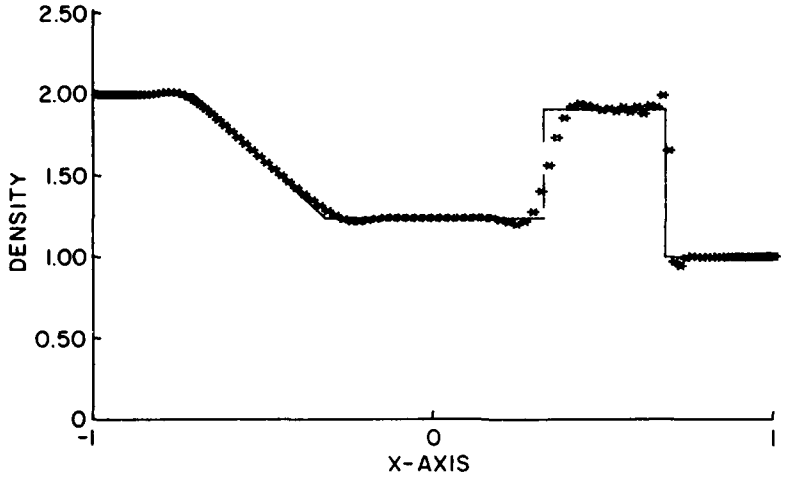

Fig. 12 — Bursting diaphragm density field

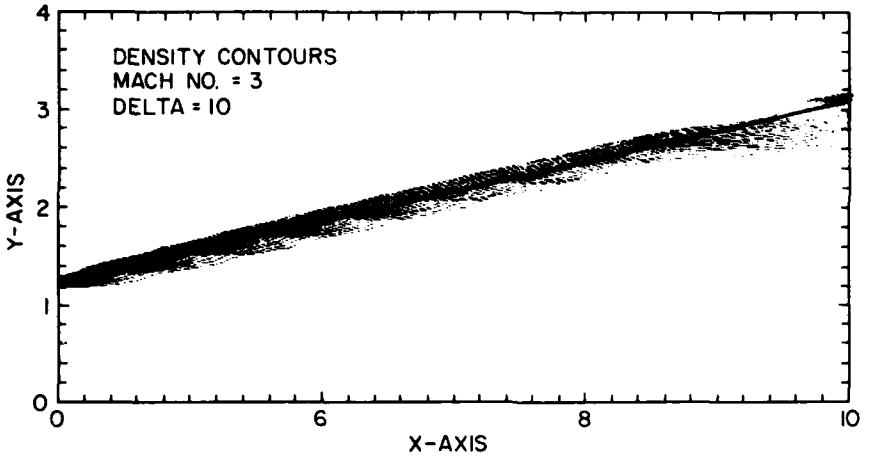

Fig. 13 — Supersonic wedge flow computed shock wave

which it can be seen that the wedge shock is well described. Both the position and orientation of the shock front are in very good agreement with the analytically-predicted position which is exactly in the middle of the computed shock zone.

Work continues at NRL on the further application of pseudospectral solution methods. Two-dimensional flow fields over airfoils are currently being computed.

[Sponsored by ONR]

REFERENCES

1. L. Sakell, "Pseudospectral Solution of One Dimensional and Two Dimensional Inviscid Flow with Shock Waves," NRL Memorandum Report 4892, Aug. 1982.

2. L. Sakell, "Solution to the Euler Equations of Motion by Pseudospectral Techniques," *Proceedings of 10th IMACS World Congress on System Simulation and Scientific Computations,* Montreal, Canada, Aug. 1982.

COMPONENT TECHNOLOGY
and SPECIALIZED DEVICES

COMPONENT TECHNOLOGY AND SPECIALIZED DEVICES

Some of the most exciting developments in applied science involve harnessing microscopic, often atomic, phenomena to perform novel operations in actual devices. This selection of articles highlights some of NRL's recent activities in this area.

An InP:Fe Laser, by P.B. Klein, J.E. Furneaux, and R.L. Henry, *Electronics Technology Division*

The use of optical fibers for communications requires ultralow-loss optical fibers, and also sources and detectors that operate in the low-loss wavelength region of the fiber. Halide glass optical fibers, which are highly transparent in the 3-5 μm region of the spectrum, are being studied at NRL. We have developed a new laser system, iron-doped indium phosphide (InP:Fe), which operates at 3.53 μm and has potential as an optical source for use with these fibers. The InP:Fe system also represents a new class of laser: the semiconductor impurity laser. Semiconductor lasers can in principle use electrical injection rather than the more cumbersome optical excitation but have hitherto been limited to emission wavelengths corresponding to the bandgap of the semiconductor. To change the laser wavelength requires the fabrication of a new semiconductor with the necessary bandgap. This sometimes requires the development of a new technology for growing materials. Impurity-doped insulator lasers (for example, Nd:YAG, ruby) may procduce new laser wavelengths simply by doping the same host materials with a different impurity or by using different transitions from the same impurity. However, these systems require optical excitation. The InP:Fe system represents a prototype impurity-doped laser in a semiconductor host, and could lead to an impurity laser excited by electrical injection.

The Fe impurity in InP resides in the group III (In) site and acts as a deep acceptor, that is, it requires a large amount of energy (approximately 0.6 eV) to free an electron trapped on the Fe center. In its neutral state, the Fe atom gives up three electrons in bonding to its P neighbors, and is therefore referred to as Fe^{3+}. In the ionized acceptor state, the Fe center has captured an additional electron and is referred to as Fe^{2+}. It is the radiative transitions between the excited state (labeled $^5T_2$) and the ground state (labeled ^5E) of the Fe^{2+} center that give rise to radiation (and laser oscillations) at 3.53 μm. The charge transfer transitions, $Fe^{3+} \rightarrow Fe^{2+}$ and $Fe^{2+} \rightarrow Fe^{3+}$, which can occur via the capture of charge carriers in the semiconductor or by photoexcitation, play a central role in producing the excited $^5T_2$ state that is responsible for the 3.53 μm emission.

Figure 1 shows the energy level scheme for *n*-type InP:Fe both before and after receiving a short (~10 ns) optical pulse from a pulsed dye

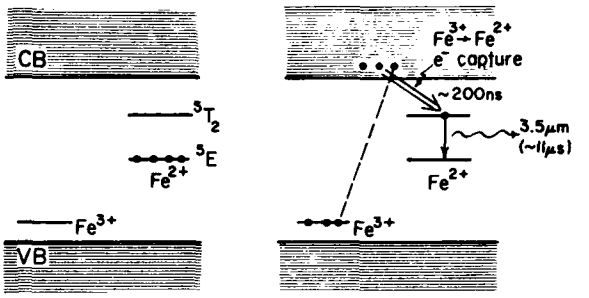

Fig. 1 — Energy level scheme for *n*-type InP:Fe before (left) and after (right) a ~10 ns dye laser pulse. The shaded regions represent the InP valence band (VB) and conduction band (CB).

laser. The shaded areas represent the valence and conduction bands of the semiconductor. Before the pulse, all the Fe centers are in the ground state of Fe^{2+}, having accepted electrons from the donor impurities that are responsible for making the InP *n*-type. There are no impurities in the Fe^{3+} state. The exciting dye laser pulse converts some of the ground state Fe^{2+} to the Fe^{3+} state (with an equal number of electrons promoted to the conduction band) and others to the excited Fe^{2+} state. Because the electron-hole pairs produced by the exciting pulse recombine in about 1 ns, the semiconductor relaxes back to the equilibrium state by two sequential processes. First, the photoexcited Fe^{3+} recombines with the equal number of electrons left in the conduction band, so that all of the Fe is back into the original Fe^{2+} state. This occurs via capture of an electron by the Fe^{3+}. Then, those Fe that are in the excited Fe^{2+} state relax to the ground state; the radiative part of this relaxation results in 3.53 μm radiation. The electron capture process, which fills the Fe^{2+} excited state, proceeds at a rate corresponding to ~200 ns per transition, but the Fe^{2+} excited state relaxes radiatively at a much slower rate (~11 μs per transition). Consequently, the population of the Fe^{2+} excited state tends to pile up, and at high enough excitation intensity (that is, above the threshold power for laser oscillations) achieves population inversion with the excited state concentration greater than the ground state concentration. Figure 2 shows that the 3.53 μm intensity increases nonlinearly with increasing excitation intensity as laser oscillations set in above the threshold power, that is, above ~100 μJ.

At present, this prototype laser system operates at low temperatures (<12°K) and with

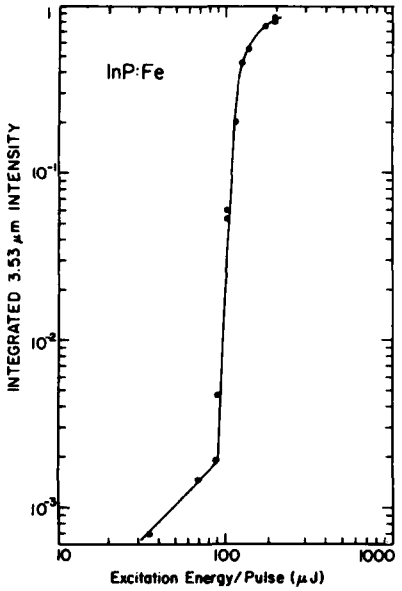

Fig. 2 — Dependence of the integrated intensity of the 3.53 μm radiation (due to Fe^{2+} in InP) upon the intensity of the exciting dye laser pulse, showing the threshold for laser oscillations at 100 μJ.

optical excitation. Future research at NRL will investigate the possibilities of electrical excitation and also new impurity/semiconductor combinations that may lead to lower thresholds and higher temperature operation.

[Sponsored by ONR]

High T_c Niobium Nitride Thin Films, by E.J. Cukauskas, *Electronics Technology Division*

There is considerable interest in the fabrication of Josephson junctions with superconducting electrodes made of refractory, high transition temperature (T_c) niobium nitride. The use of refractory material has many advantages over the conventional soft superconductors such as tin, indium and the lead alloys. Not only does niobium nitride (NbN) have a higher T_c(~ 16°K), but it is more stable mechanically, cycles well thermally, and is highly resistant to radiation damage. The Navy wants to improve the efficiency and reliability of Josephson junction devices since they have potential applications as switches in sensor, fire control, and communications systems.

Previously, niobium nitride has been prepared by reactive sputtering onto a substrate heated to 700°C. If a device structure is multilayered, the use of such elevated substrate temperatures during film growth can degrade the properties of films deposited earlier. We have developed a technique for the deposition of good quality, high-T_c niobium nitride films on a substrate at ambient temperature by incorporating controlled amounts of methane (CH_4) into the sputter gas [1].

Niobium nitride films formed at elevated substrate temperatures exhibit a T_c of 15.6°K. If the films are prepared under the same conditions after the system has been subjected to prolonged baking, the T_c is reduced several degrees and displays a broad transition temperature width, defined as the temperature interval over which the resistance of the NbN film changes from 90% to 10% of its full normal-state value. Auger analysis has revealed that NRL's high T_c niobium nitride films normally contain approximately 4% carbon. The low T_c films were found to contain less carbon (~1%), were deficient in nitrogen, and consisted of mixed ϵ and δ phases of NbN. These results suggest that niobium nitride needs another atom in its lattice to stabilize the single phase B1 structure characteristic of the high T_c material.

We have made an extensive study of the effect of carbon on the properties of niobium nitride prepared at ambient substrate temperature. All the films were prepared in an oil-free ultrahigh vacuum sputtering system, which achieved a base pressure of 7×10^{-7} Pascals after 18 hours of baking. Before film deposition, the substrates were sputter-etched in 2.5 Pa of argon at 1.4 W/cm^2 for 30 min. During film deposition, the total pressure of argon, nitrogen, and methane was maintained at 1.3 Pa. The partial pressure of nitrogen was held constant at 0.17 Pa while the methane partial pressure was varied from ambient background up to 0.26 Pa for the series of films studied. The films were deposited at 9 W/cm^2 onto quartz substrates at 20 nm/min.

All films were characterized by T_c, room temperature sheet resistance, x-ray diffraction and Auger spectroscopy properties. The sheet resistance R_s is the resistance of one square of film of thickness t and is related to the resistivity ρ by $\rho = R_s t$. Films prepared with little or no methane in the sputter gas had low T_c and a transition width of several degrees. Figure 3 shows the variation of T_c with methane partial pressure. T_c has a maximum of 15.85°K at a methane pressure of 0.08 Pa. The room temperature sheet

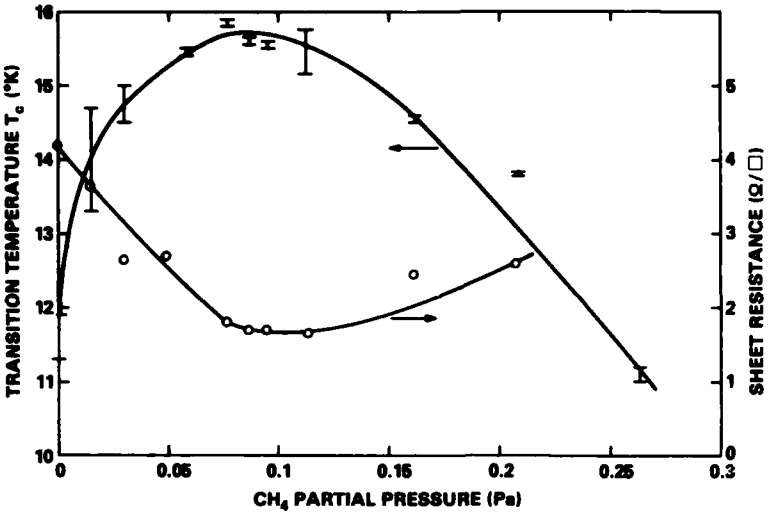

Fig. 3 — Transition temperature and room temperature sheet resistance as a function of methane partial pressure. The total pressure was 1.3 Pa with 0.17 Pa of nitrogen partial pressure. The error bars indicate the transition width.

resistance has a minimum at the same pressure, indicating that crystal defects have been reduced to a minimum at this point.

X-ray diffraction studies showed that films prepared with low methane partial pressure had a two-phase crystal structure. These films were a mixture of the hexagonal ϵ-phase and the δ-phase of NbN. The existence of two phases is the probable cause of the broad transition width observed in these films. The x-ray peaks associated with the ϵ-phase decreased with increasing methane partial pressure, and the relative magnitude of the peaks associated with the (111) and (200)-crystal planes changed. The (200)-crystal plane was at a maximum at the pressure corresponding to the maximum in T_c, indicating that here the preferred crystallite orientation was with the (200) plane parallel to the substrate.

Figure 4 illustrates the film composition as a function of methane partial pressure determined by Auger electron spectroscopy. All films studied contained approximately 3% oxygen and 50% niobium. The use of methane in the sputter gas resulted in the incorporation of carbon into the films at the expense of the nitrogen. The films were predominantly niobium nitride at low methane pressure and predominantly niobium carbon-nitride at high methane pressure.

Our research has shown that good quality high T_c niobium nitride can be prepared without the need for substrate heating during film deposition. These films can be used as electrodes in

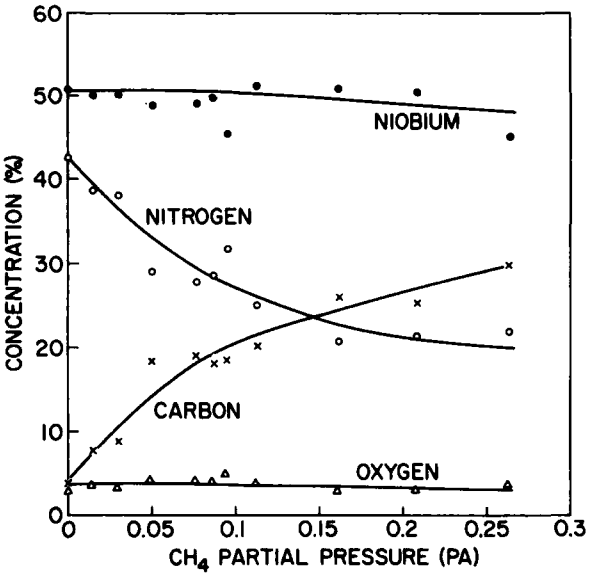

Fig. 4 — Film composition as a function of methane partial pressure, as determined by Auger spectroscopy

multilayer Josephson tunnel junctions where high substrate heating cannot be tolerated during film growth of the upper electrode. The new film preparation techniques are being used in the development of Josephson tunnel junctions having both electrodes of NbN and amorphous silicon barriers. These devices have potential use as millimeter wave detectors and mixers, as magnetometers and in high-speed digital electronics. We are continuing our investigation with a study

of the effect of oxygen on the properties of NbN thin films.

[Sponsored by NAVALEX and ONR]

REFERENCE

1. E.J. Cukauskas, "The Effects of Methane in the Deposition of Superconducting Niobium Nitride Thin Films at Ambient Substrate Temperature," *J. Appl. Phys.*, **54**, 1013, (1983).

Surface Anisotropy in Ultrathin Iron Crystals, by G.A. Prinz, *Electronics Technology Division*

NRL scientists have recently been able to grow single-crystal iron films using the technique of molecular beam epitaxy [1]. These films, grown upon single-crystal substrates of the semiconductor gallium arsenide, have potential application in solid-state planar electronic devices. Before new devices can be designed, it is necessary to know more about the magnetic properties of these films; some of these magnetic properties have proved to be surprising [2].

One of the most important properties of magnetic crystals, particularly for application to devices, is the magnetic anisotropy energy. This is the relative energy associated with the direction of the magnetic moment in the material. It may arise from the intrinsic symmetry of the crystalline structure, from strains in the material, or from the shape of the sample. In principle, an infinite sample of perfectly uniform structure and composition would have only intrinsic anisotropy energy. A thin film, on the other hand, can have a large amount of anisotropy energy because of its shape; this is surface anisotropy energy originating from the abrupt discontinuity at the surface. Any finite magnetic sample will have some surface anisotropy, but it is only when the ratio of surface area to volume becomes large that the effects of surface anisotropy become observable.

One way to study the surface anisotropy is from measurements of ferromagnetic resonance. Microwaves are directed at the film and the power absorbed is measured as a function of an applied magnetic field. The characteristic frequency at which resonance absorption occurs is displayed schematically in Fig. 5 as a function of the applied field. Two resonance curves are shown, one for the case where the applied magnetic field is in the [001] direction, that is, pointing along the edge of the crystalline cubic unit cell; and the other for when the field is in the [110] direction, along a diagonal of the unit cell face. In bulk iron the [001] direction is called the *easy* direction of magnetization because it is the direction in which the intrinsic anisotropy energies are a minimum; in the absence of an applied field the magnetic moment will point in this direction. Applying an external field along [001] adds to the effective internal anisotropy field and raises the resonance frequency. On the other hand, applying an external magnetic field along [110], perpendicular to [001], first acts to pull the magnetic moment down and at some point reduces the resonance frequency to zero. At that point the external field has overcome the effective internal anisotropy field and the magnetic moment is pointing along [110]. Further increase of the applied field then raises the resonance frequency again, as shown in Fig. 5.

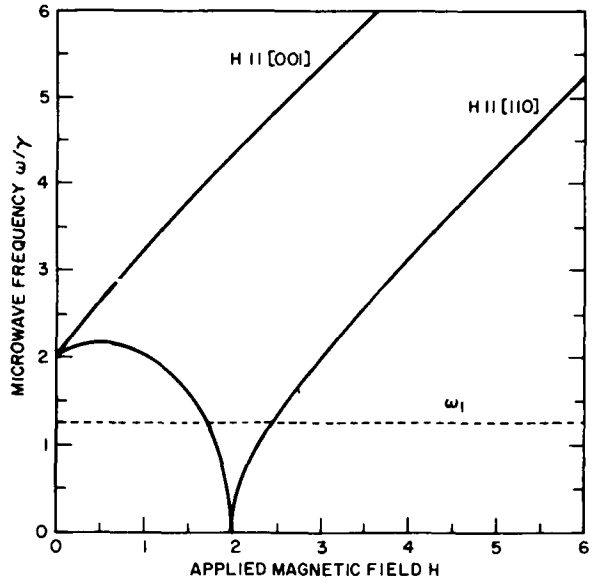

Fig. 5 — Microwave frequency (ω) vs applied magnetic field (H) for ferromagnetic resonance in bulk iron

From the figure it is clear that if microwaves of sufficiently low frequency, ω, are applied to the sample when the applied field is parallel to [110], resonances will be observed at the two points where ω crosses the resonance curve. When the applied field is parallel to [001] no resonance will be observed, because in this case ω lies below the resonance curve. This behavior is in fact observed for fairly thick films (200 Å). Figure 6 is a polar plot of the observed strength and direction of the applied magnetic field at which resonance occurs for ω = 9.2 GHz in films

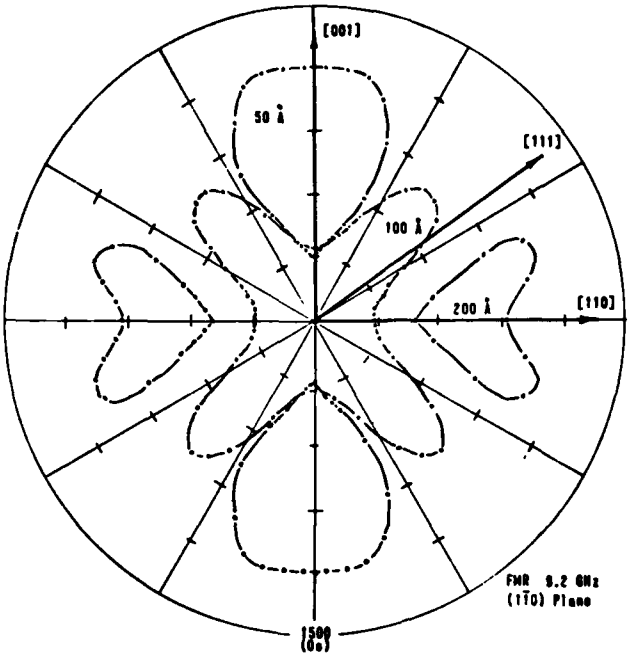

Fig. 6 — Polar plot of the ferromagnetic resonance observed at a microwave frequency of 9.2 GHz in (110) oriented epitaxial iron films of 200 Å, 100 Å and 50 Å thickness

of three different thicknesses. For a 200 Å film, the curve is heart-shaped and has two resonance points along [110] but no resonance along [001], as expected from Fig. 5.

A remarkable result is obtained as the thickness is decreased. For a 100-Å film the shape evolves into a four-lobed "flower" with only one resonance in each direction. From the four-fold symmetry it is clear that the [001] and the [110] directions are now equally easy. At this thickness the contribution from the surface anisotropy is equal to the contribution from the intrinsic anisotropies. If the thickness is further decreased this evolution continues and we see that the 50 Å film now shows two resonances for the [001] direction. This means that the anisotropic characters of the two directions have been completely interchanged. The contribution of the surface anisotropy has overwhelmed the intrinsic volume anisotropy so that [110] is now the easy axis of magnetization.

This study dramatically demonstrates the unexpectedly large alteration in material properties made possible by modern thin-film synthesis techniques and suggests new applications arising from these alterations. It also demonstrates the inadequacy of using bulk properties of materials in the design of modern microscopic electronic devices in which surface effects can dominate.

[Sponsored by ONR]

REFERENCES

1. G.A. Prinz and J.J. Krebs, "Molecular Beam Epitaxial Growth of Single-Crystal Fe Films on GaAs," *Appl. Phys. Lett.* **39**, 397 (1981).

2. G.A. Prinz, G.T. Rado, and J.J. Krebs, "Magnetic Properties of Single Crystal [110] Iron Films Grown on GaAs," *J. Appl. Phys.* **53**, 2087 (1982).

A New Technique for Growing Ternary Bulk Crystals, by E.M. Swiggard, R.L. Henry and H. Lessoff, *Electronics Technology Division*

Electronic and electro-optic applications of III-V semiconductors have expanded rapidly with the availability of bulk single crystals of the binary alloys gallium arsenide (GaAs) and indium

phosphide (InP). These semiconductors are playing an increasingly important role in microwave- and millimeter-wave technology. The direct bandgap of GaAs and InP makes these materials useful for electro-optics sources and detectors, especially in conjunction with fiber optic technology. However, there are a number of applications of the III-V semiconductors for which ternary or quaternary alloys would be better than the binary compounds. We are therefore investigating new techniques for growing single crystals of III-V ternary and quaternary alloys.

Conventional freezing processes (such as Czochralski pulling, gradient freeze or Bridgman growth) will not produce uniform crystals of ternary alloys because the composition will change continuously during solidification as the composition of the liquid changes. This can be understood from Fig. 7 which shows the freezing (liquidus) and melting (solidus) curves for the ternary gallium-indium-antimony system ($Ga_{1-x}In_xSb$). If, for example, the starting melt has a composition of 73% GaSb and 27% InSb, the first portion to freeze when the directional freezing process is initiated will consist of 96% GaSb. This will deplete the melt of GaSb and the other end of the crystal will be rich in InSb. To achieve uniform composition, zone levelling may be used (Fig. 8). In this process, a charge of GaSb and InSb that corresponds to the desired final composition is put in a boat, and a smaller charge whose composition is determined from the freezing curve in Fig. 7 is placed at the end that will first be the molten zone. By repeatedly moving the boat back and forth under the RF coil, the molten zone is moved through the ingot and a uniform composition in the solid is achieved. If one or more of the constituents has a high vapor pressure, the melt must be encapsulated: boric oxide (B_2O_3) is ideal for this purpose but must be removed prior to solidification or it will destroy the crystal. This is done with methanol, which reacts with B_2O_3 at 450°C to form gaseous trimethylborate and water. A pyrolytic boron nitride (PBN) boat must be used for this process.

Many of the III-V alloys of interest require preparation under pressure to prevent loss of volatile constituents during zone melting. To this end we constructed a high-pressure apparatus (Fig. 8) in which a 25-cm boat may be moved at speeds of 0.25 to 100 mm/hr under a pressure of up to 50 atm. A $Ga_{1-x}In_xSb$ boule produced in this apparatus is shown in Fig. 9. The B_2O_3 encapsulation was removed with methanol without fracturing the boule as it cooled to room temperature. Cross-sectional wafers were cut at

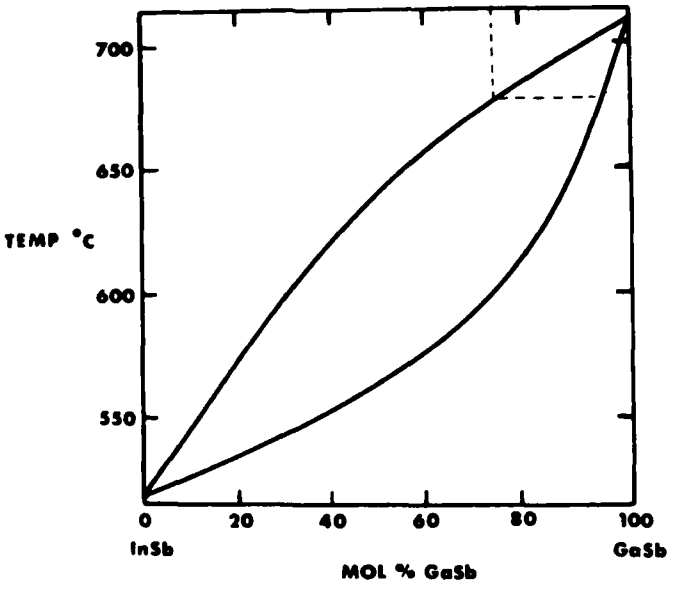

Fig. 7 — Solidus (lower) and liquidus (upper) curves for GaSb-InSb system. When the temperature is reduced, a melt having the composition corresponding to the point where the dotted line meets the liquidus curve will precipitate a solid having a composition corresponding to the point where the dotted line meets the solidus curve.

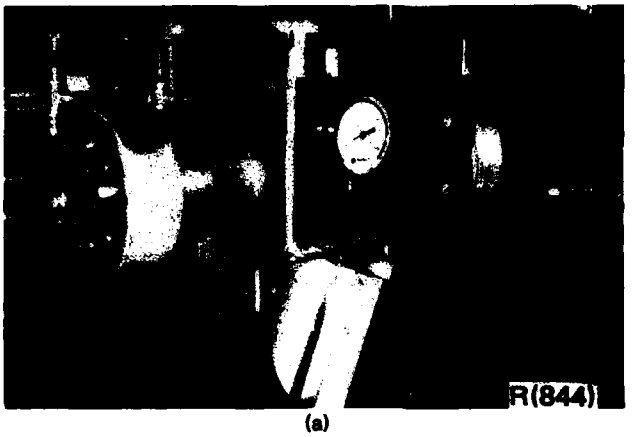

(a)

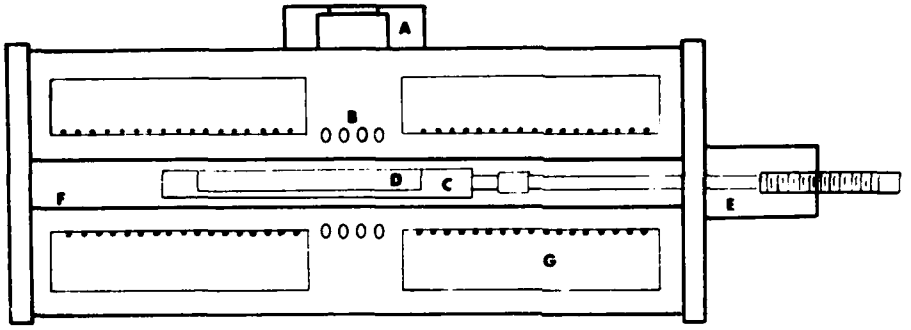

A. VIEWING PORT
B. RF COIL
C. GRAPHITE SUSCEPTOR
D. PBN BOAT
E. PULLING HEAD
F. QUARTZ TUBE
G. FURNACES

(b)

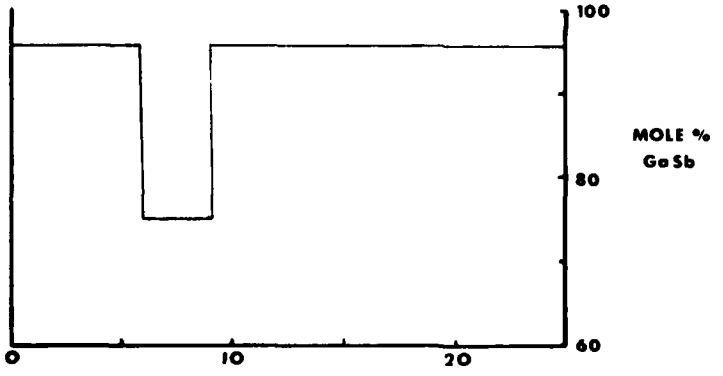

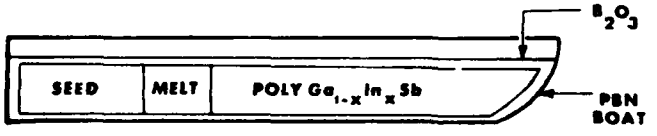

(c)

Fig. 8 — (a) High-pressure vessel used for zone levelling of alloys; (b) The zone-levelling equipment; (c) The zone-levelling technique. The melt is passed back and forth through the ingot by moving the boat through the RF heating coil.

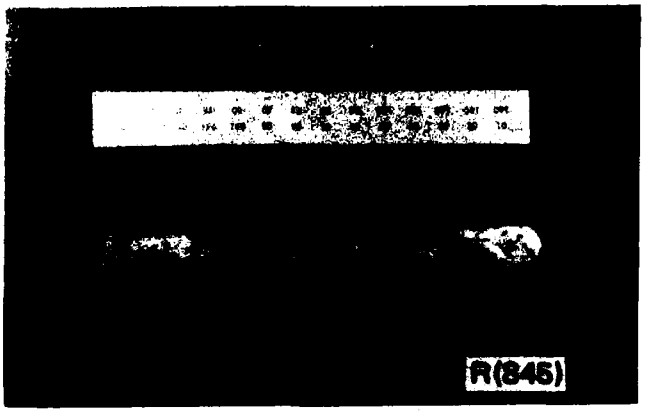

Fig. 9 — A $Ga_{1-x}In_xSb$ ingot, approximately 15 cm long

5.5 cm, 8.0 cm, and 11.5 cm from the end of the boule for analysis by x-ray powder diffraction to determine the unit cell size, from which the chemical composition of the ternary alloy could be determined (Vegard's Law). The wafers were also analyzed by an electron microprobe to determine compositional uniformity. Both the x-ray diffraction and microprobe data showed that the wafers were of satisfactorily uniform composition with respect to each other and within each wafer.

The alloy $Ga_{.47}In_{.53}As$ is of interest because its unit-cell size is identical to the unit-cell size of InP. Hence, it might be possible to use an InP single crystal to attempt seeded growth of single crystal $Ga_{.47}In_{.53}As$. However, our attempts to grow $Ga_{.47}In_{.53}As$ by zone levelling did not lead to a uniform crystal. We attribute this to the fact that around the $Ga_{.47}In_{.53}As$ composition, the slope of the melting curve is gentle, but the slope of the freezing curve is steep. Thus, small changes in the composition of the melt will cause relatively large changes in the composition of the solid being deposited. Materials grown in this composition region will require a longer boat to avoid end effects and a larger number of zone passes to achieve uniformity.

Future research will be directed toward determining those compositions that can be prepared uniformly, and developing procedures for obtaining single crystals of these alloys. The equipment and techniques will also be used to process GaAs and InP by zone refining, something that cannot be done with existing technology.

[Sponsored by ONR and NAVAIR]

Acousto-Optical Signal Processing, by J.N. Lee and R.A. Athale, *Optical Sciences Division*

Optical techniques applied to signal processing can lead to extremely high-speed operation and large data handling capability. This potential can be realized through the use of acousto-optic devices which permit the rapid input of information onto optical beams. Acousto-optical signal processors can perform specific operations and algorithms at speeds and throughputs well in excess of that of state-of-the-art digital computers. In addition, they provide good dynamic range, can be packaged in small volumes, and consume little power. Processors of this kind can provide practical near-term solutions to various computation-intensive problems in sonar, radar, and surveillance signal processing on Naval platforms, especially where size, weight, and power consumption must be limited.

We have recently developed several new acousto-optic techniques and processors for immediate Naval requirements. One such development is a compact, time-integrating Fourier transform device for application to surveillance and beam-forming schemes that have massive Fourier transform loads. Another development is an acousto-optic technique for performing matrix algebra at high speed. This technique should allow the rapid calculation in real time of noise covariance matrices to cancel noise in changing sonar and radar environments.

Although Fourier transformation by optical techniques is a familiar concept (for example, a simple lens can perform a Fourier transform of a slide), practical devices must have means for

rapid input of data and output of results if they are to use the speed of light to maximum advantage. Compact devices with very high throughput and good dynamic range can be obtained with a combination of acousto-optic cells, solid-state diode lasers and large dynamic-range photodetector arrays in new device architectures. The one-dimensional (1-D) Fourier transform integrai may be rewritten as

$$\int_0^T S(t) \exp(-i\alpha\tau t)\,dt = \int_0^T S(t) \exp\left[+i\left(\frac{\alpha}{4}\right)(t-\tau)^2\right] \exp\left[-i\left(\frac{\alpha}{4}\right)(t+\tau)^2\right] dt. \quad (1)$$

The reformulation of the right side of Eq. (1) into the form of a correlation integral enables the integral to be evaluated, using 1-D acousto-optic correlators. The multiplication required by Eq. (1) can be produced by modulation of light intensities and by diffraction of light by acoustic-wave signals; integration occurs by signal accumulation on photodetector-arrays. Here the information to be transformed, $S(t)$, is first converted from an electrical signal into information on a light beam from a diode laser; this technique takes advantage of the compactness and the linear transfer characteristics of these lasers. The light beam undergoes diffractions in two separate acoustic cells, each carrying a signal corresponding to one of the quadratic-phase terms in Eq. (1). Interference between the two resultant light beams produces the integrand on the right-hand side of the equation. The final integration is performed by signal accumulation in a photodetector array with a length equivalent to the acoustic-cell window. Figure 10 shows the output of this Fourier transform device using a 600-Hz continuous-wave tone with a 30-ms integration time. This device has a dynamic range of 30 dB.

Several significant modifications can be made to the basic concept. A more compact processor is obtained by exploiting the fact that the quadratic terms of Eq. (1) are time-reversed versions of each other. Thus only one acoustic cell is necessary if the light beam is split and the two components are propagated in opposite directions through the cell. Also, since the Fourier transform considered here is one-dimensional, the geometry of the device is planar. This makes the out-of-plane dimension available to perform many such 1-D transforms in parallel. However, this can be accomplished without increasing the number of acoustic cells because the cells carry quadratic-phase signals which are independent of

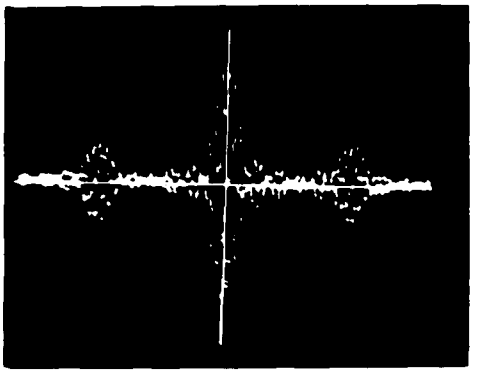

Fig. 10 — Output of Fourier transform device for 600 Hz cw signe input. The zero frequency component is at the center with positive and negative components on either side. The speckled appearance is caused by the sampling of the fringe pattern that carries the Fourier transform.

(although synchronized with) the data to be transformed. Hence, a single device may be used in applications with very large 1-D Fourier-transform loads by using a large array of individually modulated light sources.

A large number of problems encountered in processing signals from sensor arrays, such as beam-forming and adapative null steering, can be cast in terms of matrix operations. Since the computational load goes up dramatically as the size of the array increases, optical processors are attractive because their inherent parallelism allows very high throughputs. Previous optical processors for matrix algebra have required two-dimensional spatial light modulators for real-time operation since they were based on inner product decomposition, that is,

$$C_{ij} = \sum_{k=1}^{N} A_{ik} B_{kj}, \quad (2)$$

where A and B are N × N input matrices and C = AB. The performance of these inner-product processors is limited because two-dimensional (2-D) spatial light modulators of high quality are not currently available. We have addressed the problem of matrix multiplication in a different way by using 1-D acousto-optic cells, which offer high bandwidth, high resolution, and good dynamic range, and by casting the matrix multiplication operation in terms of *outer* products of the column and row vectors of the input matrices A and B, respectively. Thus,

$$C = \sum_{k=1}^{N} C^{(k)}, \quad (3)$$

where

$$C_{ij}^{k} = A_{ij} = B_{kj}.$$

An outer-product optical processor may be built with two acousto-optic cells arranged in a cross configuration (Fig. 11), since only one row/column vector is needed to calculate the outer product matrix $C^{(k)}$. The different outer product matrices are summed in a 2-D time-integrating detector array to form the product matrix C. To improve the dynamic range of the optical processor, the input matrices are encoded in an appropriate binary format so that the output matrix C is in a mixed binary format (i.e., the weight associated with the nth bit is still 2^{n-1}, but the bit itself can be > 1). This allows a trade-off of the high space-bandwidth product of the optical processor for improved accuracy (> 16 bits).

In addition to these devices and techniques, similar concepts and designs have been applied to the development of a compact acousto-optic RF spectrum analyzer of sufficient dynamic range for airborne radar warning receivers. These developments maintain laboratory performance levels while achieving the minaturization required for practical airborne systems.

[Sponsored by ONR and NAVAIR]

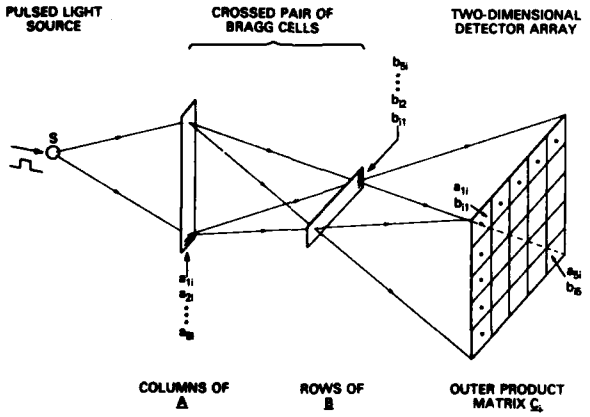

Fig. 11 — Acousto-optic matrix multiplier. The light source (S) is pulsed when the kth column of matrix A and the kth row of matrix B are inserted into the vertical and horizontal acousto-optic Braggg cells, respectively. This procedure is repeated for each pair of rows and columns until the multiplication is complete. (Beam-shaping and focussing optics have been omitted for clarity.)

Thermophotovoltaic Power Sources for Hardened Spacecraft, by J.G. Severns, *Space Systems Division*

Solar-cell arrays, the standard source of power for spacecraft, are steadily degraded by the natural radiation which is present in the environment of space and are vulnerable to the radiation produced by nuclear detonations. Degradation of the solar cells by radiation is a principal limitation on the life of a spacecraft, on its ability to operate near the center of the belts of trapped particles and on its ability to survive threats of nuclear weapons. An alternative power source, which has been used in a few cases, is a radioisotope thermal source combined with thermoelectric or thermionic power cells. This option is severely limited in its application by the costs and risks inherent in the use of large radioactive sources. Consequently, NRL has undertaken a program to develop spacecraft power systems which will convert solar energy to electrical energy with neither the radiation vulnerability of solar cells nor the costs and dangers of radioisotope systems.

Figure 12 shows the NRL concept for a hardened spacecraft power source based on thermophotovoltaic (TPV) cells. Sunlight is concentrated by mirrors and directed into a cavity with highly reflective walls. The cavity contains a thermal storage vessel with a black exterior surface which absorbs most of the solar energy. The storage vessel is filled with a substance with a high melting point (1650-2200°K) in which energy is stored as latent heat while the spacecraft is not in sunlight. Energy is reradiated from a re-entrant inner surface of the vessel onto a TPV array which is held at a much lower temperature (~300°K) by a heat pipe leading to waste heat radiators. Unlike thermoelectric and thermionic converters, whose need to operate at high temperature limits their useful lifetimes, TPV cells can operate at close to room temperature and promise high reliability over a long service life.

Work to date has concentrated on evaluating candidate radiators and TPV cells. Oxides of the rare earths, specifically erbium oxide and ytterbium oxide (Er_2O_3 and Yb_2O_3) are good candidates for selective radiators. Figure 13 compares the spectral exitance of these materials at 2000°K with that of a black body. On the same plot, the band edges of silicon and germanium semiconductors are shown, indicating the longest wavelength of radiation that can be converted to useful electric power in each of these materials. As seen, Er_2O_3 appears to match germanium and

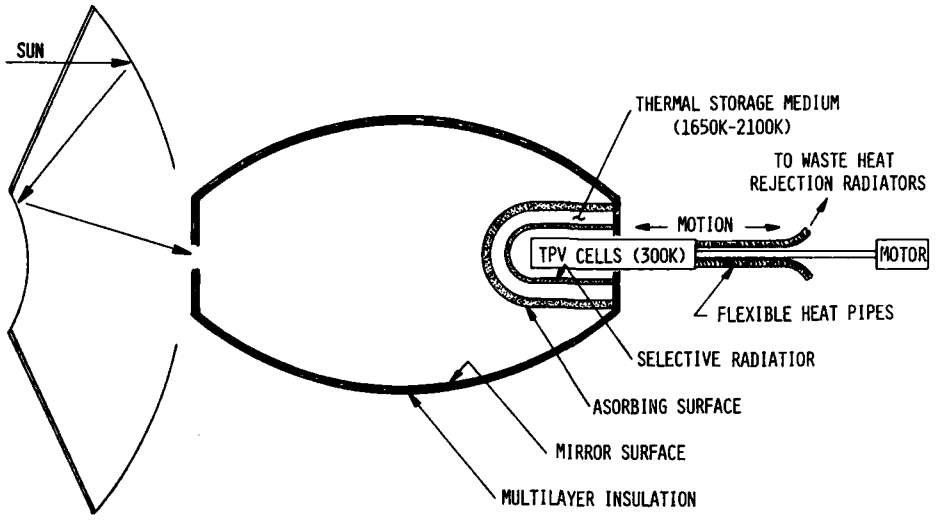

Fig. 12 — Thermophotovoltaic concept with thermal storage.

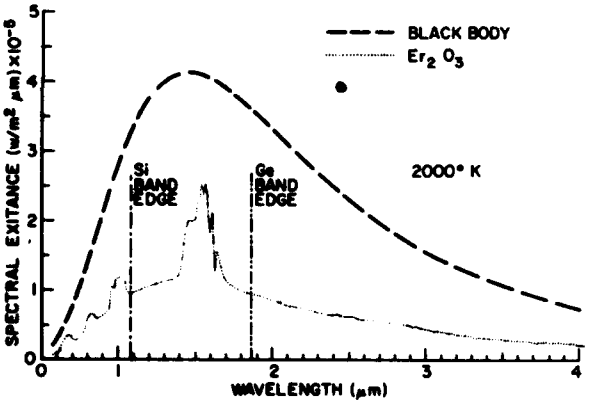

Fig. 13 — Spectral exitance of selective radiators compared with a black body

Yb_2O_3 is a fairly good match to silicon, although the higher radiator temperature required to drive a silicon TPV cell efficiently makes it a less desirable choice. Thus, we have chosen to study a germanium TPV cell illuminated either by a high-temperature black body or a hot Er_2O_3 surface. In 1982, the upper limit of conversion efficiency for a promising class of germanium TPV cell was calculated and was used to estimate the overall conversion efficiency attainable in combination with Er_2O_3. A surprising result was that in the desirable temperature region, (2000-2200°K) the calculated overall efficiency with Er_2O_3 is not much better than with a black body radiator.

The cell studied was a thin, shallow junction diode with optical mirror coating on the surfaces for light-trapping, and so-called *minority carrier mirrors* on both front and back surfaces. A minority carrier mirror is an arrangement by which minority carriers encounter a substantial potential barrier as they approach a surface or interface, causing them to be repelled from the barrier. This effectively limits recombination of the carriers at the surface, a major loss mechanism in TPV cells. This carrier mirror may be contrived in two ways: by epitaxial growth on the cell surface of a different material with a higher band gap than the bulk crystal, or by doping a region very near the surface much more strongly than the interior of the device, as in the N^+ N/P P^+ diode structure which incorporates thin layers doped N^+ and P^+ near the corresponding N and P surfaces.

Figure 14 shows cell efficiency vs thickness for a black body spectrum and for the Er_2O_3 spectrum. The peak efficiency occurs at nearly the same cell thickness for each spectrum. Surprisingly, the peak efficiency for the Er_2O_3 spectrum is not much higher than for the black body emission. This is because even though a part of the black body spectrum is wasted, it still provides more useful input than does the Er_2O_3 surface at the same temperature and distance from the cell. Since cell efficiency is dependent upon input level, the near match in peak efficiencies is explained. For the same reason the efficiency

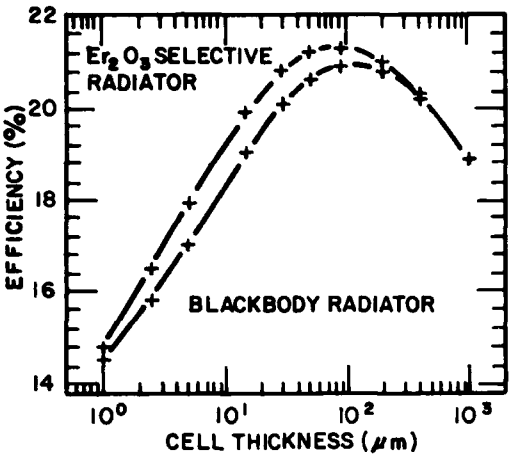

Fig. 14 — Calculated conversion efficiency as a function of cell thickness for a Ge *p-n* junction TPV system with two different radiators at 2000°K

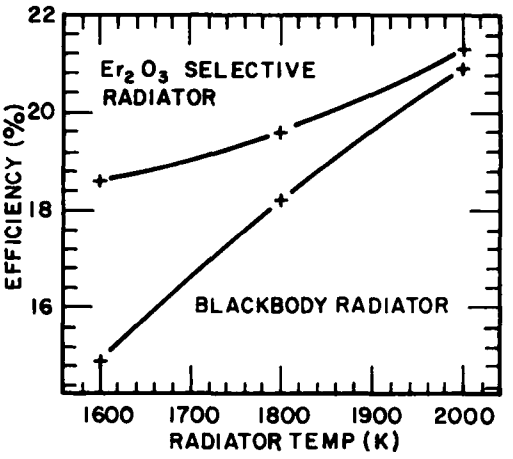

Fig. 15 — Calculated conversion efficiency as a function of radiator temperature for an optimal Ge structure 90μm thick

increases with increasing emitter temperature as shown in Fig. 15. At the higher emitter temperatures necessary to achieve good efficiency, the advantage of the Er_2O_3 selective emitter is less than had previously been supposed.

Plans for 1983 include fabrication and test of some of these cells, as well as germanium cells of a different geometry. Other candidates for the selective emitter surface will also be studied.

[Sponsored by ONR]

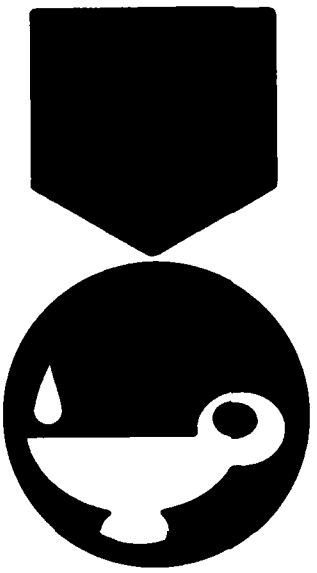

RECOGNITION: HONORS, AWARDS, and TRAINING

RECOGNITION

HONORS, AWARDS, AND TRAINING

HONORS AND INCENTIVE AWARDS

During 1982 NRL staff members earned 2336 awards under the Federal Incentive Awards program. These awards are summarized in the following table.

Distribution of
Federal Incentive Awards During 1982

Navy Distinguished Civilian Service	3
Navy Robert Dexter Conrad	1
Navy Superior Civilian Service	4
Navy Meritorious Civilian Service	3
NRL E.O. Hulburt Annual Science	1
Outstanding Performance Ratings	393
Special Achievement	243
Quality Step Increase	280
Research Publication	83
Invention and Patent	118
Employee Suggestions	77
Length of Service	735
Safety Certificates	117
Blood Donor Certificates	6
Commanding Officer's Award for Achievement in EEO	2
SES Rank of Meritorious	2
SES Bonus	4
Merit Pay Performance	264
TOTAL	2336

In addition, Laboratory employees received numerous scientific medals, military service awards, academic honors, and other forms of recognition, including election and appointment to offices in technical societies. The following is an alphabetical list of the persons receiving such recognition in 1982.

Baer, R.N., ***Biennial award of the Acoustical Society of America***

Batra, N.K., ***Secretary/Treasurer, Sonics and Ultrasonics, Chapter Washington Section, IEEE***

Bishop, S.G., ***Navy Technical Review Committee, Joint Services Electronics Program; Organizing Committe, Topical Conference on Optical Effects in Amorphous Semiconductors; Chairman, Symposium on Photoinduced Defects and Structural Modifications in Amorphous Semiconductors, American Physical Society Meeting, Philadelphia, PA; Fellowship in the American Physical Society***

Bodner, S.E., *Technical Advisor on Magnetic Fusion, Office of Management and Budget*

Brady, Jr., R.F., *President, Chemical Society of Washington; Council of the American Chemical Society from the Chemical Society of Washington; Tour Speaker, American Chemical Society; Certificate of Appreciation from the American Society of Testing and Materials, Committee D-1 on Paint and Related Coatings and Materials; Delegate to the Washington Academy of Sciences from the Washington Paint Technical Group*

Brueckner, G.E., *Research Stipend from the Japan Society for the Promotion of Science, Visiting Research Professor, University of Tokyo, Japan*

Buczek, W.A., *Meritorious Unit Commendation, Department of the Navy*

Bultman, Dr., J.D., *Associate Editor of BIOTROPICA, an international journal published by the Association for Tropical Biology*

Butkiewicz, D.F., *Vice Chairman, IEEE, Washington Chapter Computer Section*

Campbell, F.J., *Fellow of the IEEE; Chairman, Symposium on Radiation Effects, Conference on Electrical Insulation and Dielectric Phenomena*

Carruthers, G.R., *Technical Committee, Space Sciences and Astronomy American Institute of Aeronautics and Astronautics*

Carter, W.H., *General Chairman, SPIE Technical Symposium East '82, Fellow of the Optical Society of America; General Chairman for the "SPIE's Technical Symposium East," Graduate College Faculty Fellow of the University of Nebraska, Lincoln*

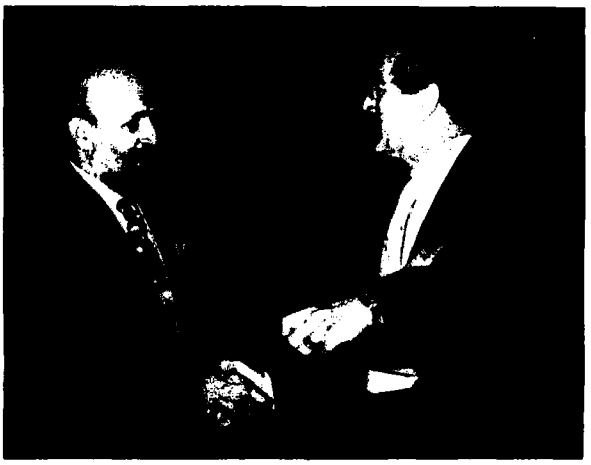

The Navy's highest honor for scientific achievement, the CAPT Robert Dexter Conrad Award, was presented to Dr. Alan Berman, (left) former NRL Director or Research, in a ceremony on June 18. The award, a medal and certificate was presented by Melvyn R. Paisley, assistant secretary of the Navy for research, engineering and systems. Paisley commended Berman for his "accomplishments as a brilliant physical scientist, as an astute administrator, as a charismatic leader, and as a respected adviser to the leaders of the nation."

Chang, C.I., *Executive committee, Army Solid Mechanics Symposium, Co-chairman, Structural Subgroup, Tri-service Laser Hardening Materials and Structural Group, Program Committee, 5th DOD Conference on Laser Vulnerability, Effects and Hardening, Editor, Journal of Fracture Mechanics Technology*

Cheng, C.-C., *Visiting Professor at the Arcetri Astrophysical Observatory, Florence, Italy*

Colton, R.J., *Certificate of Appreciation — for significant contributions to the success of the Guidance and Navigation Community's Contamination Control Seminars; Vice Chairman, Local Arrangements Committee, 29th National Symposium of the American Vacuum Society*

Cooperstein, G., *Editorial Board Laser and Particle Beams Journal, Published by Cambridge University Press*

Cosby, L.A., *Presidental Meritorious Senior Executive Award; JLCLD Electronic Warfare Panel; Tech Advisor, CNO EW Policy Panel*

Davey, J.E., *Chairman, 1982 IEEE Gallium Arsenide Integrated Circuits Symposium*

Davis, K.L., *Senior Member of IEEE; Associate Member Advisory Group on Electron Devices Working Group B; Technical Program Committee of the Ultrasonics and the Microwave and Millimeter Wave Symposia*

Doschek, G.A., *Facility scientist for the solar optical telescope*

Dubbelday, P.S., *Adjunct professor of Physics, Florida Institute of Technology, Melbourne, FL.*

Everett, W., *ALQ/149 Selection Committee Chairman*

Fairman, J.L., *Meritorious Unit Commendation, Department of the Navy*

Falabella, R., *ONR Advisory Board for Virginia Polytechnic Institute—State University Adhesion Center*

Fitzgerald, J.W., *Committee on Cloud Physics, American Meteorological Society*

Fox, R.B., *Chairman, Long-range Planning Committee; Committee on Grants and Awards of the Board of Directors, American Chemical Society*

Friebele, E.J., *George W. Morey Award from American Ceramic Society for excellence in glass research; program committee of the Glass Division of the American Ceramic Society*

Gardner, J.H., *Navy Meritorious Civilian Service Award*

Garrett, W.D., *U.S. National Coordinator of the Marine Pollution Monitoring Program operated by the Intergovernmental Oceanographic Commission (United Nations); U.S. Interagency Subgroup of Panel on International Programs and International Cooperation in Oceanography; chairman, working group on Interchange of Pollutants Between the Atmosphere and the Oceans, World Meteorological Organization;*

Drs. E. Joseph Friebele (left) and George H. Sigel, Jr., research scientists in the Optical Sciences Division receive the 1982 George W. Morey Award presented annually by the Glass Division of the American Ceramic Society for outstanding contributions to glass science and technology. Friebele and Sigel were cited for their research on the effects of ionizing radiation on fiber optic materials and waveguides, establishing NRL as the center of expertise in this field.

E. O. Hulburt (left) the Laboratory's first civilian director of research (see dedication page) receives an honorary doctorate by the Johns Hopkins University in Baltimore, Md. on July 4, 1980. In presenting Hulburt with the degree of Doctor of Humane Letters, Hopkins' Provost Richard P. Longaker said, "As a physicist, you synthesized information derived from classical optics and modern rocket aeronomy.... In scholarship and administration, you have been an inspirational leader."

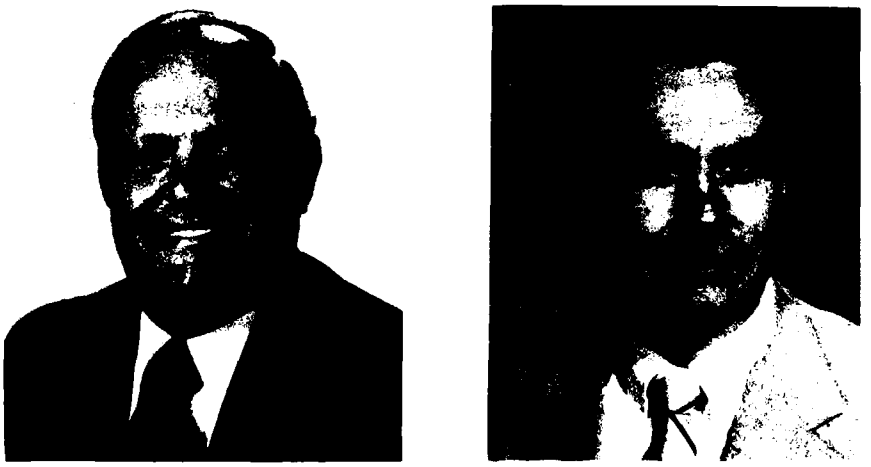

Dr. Albert I. Schindler (left) associate director of Research for Material Science and Component Technology Directorate and Lynwood A. Cosby, Superintendent of the Tactical Electronic Warfare Division were named "meritorious senior executives" at a White House ceremony November 22. President Reagan said during the presentation that government service is a partnership that depends upon a solid working relationship between those who do the talking and those who do the work. He told Schindler and Cosby, who were two of 199 recipients of the high honor, "You are among the very finest career executives in the federal government." This is the third consecutive year NRL officials have been included in the awards, and the first time two persons have been selected in one year.

Group of Experts on Methods, Standards and Intercalibration, Intergovernmental Oceanographic Commission (United Nations)

Gerber, H.E., *Editor, "Light Absorption by Aerosol Particles," Spectrum Press, Hampton, VA; member of the International Radiation Commission (IAMAP, IUGG)*

Giallorenzi, T.G., *Editor IEEE/OSA Journal of Lightwave Technology Member IEEE Ad Com, Quantum Electronics Society Member IEEE Committee on Communications and Information Policy*

Goldberg, L.S., *Organizer and Chairman for the S.P.I.E. Symposium on Picosecond Lasers and Applications and editor of the Proceedings, Los Angeles, California*

Goode, R.J., *Award of Merit, American Society for Testing and Materials*

Goodman, J.M., *Editor-in-chief: "Effect of the Ionosphere on Radiowave Systems," IESPROC., Govt. Printing Office; Delegate to Allied Naval Communications Conf.; Navy Organizer for OSD/DNA Conf. on Adaptive HF; Session Chairman for Shape Technical Centre Conference on Modern HF Radio Systems*

Goodwin, Robert L., *Superior Civilian Service Award, Department of the Navy*

Granatstein, V.L., *Associate Editor, International Journal of Electronics; Program Committee/International Conference on Lasers; Program Committee, IEEE International Conference on Plasma Science; co-editor, Proceedings of the Second U.S. Gyrotron Conference*

Griffin, O.M., *Robert T. Knapp Award of the Fluids Engineering Division of the American Society of Mechanical Engineers*

Griscom, D.L., *Regional editor for Journal of Noncrystalline Solids*

Gubser, D.U., *Vice President, Applied Superconductivity Conference: Organizing Committee—NATO Summer School on Localization, Percolation and Superconductivity, Board of Directors, Applied Superconductivity Conference*

Hahn, T.A., *ASTM Committee E-37 Thermal Analysis; Board of Directors—Thermal Expansion Symposium*

Harvey, A.B., *President of the Coblentz Society, Chairman, Finance Committee, Coblentz Society,*

Hawthorne, J.R., *First Vice Chairman, ASTM Committee E10 on Nuclear Technology and Applications, American Society for Testing and Materials; Technical Chairman, Joint ASTM IAEA Meeting on IAEA Coordinated Program on Behavior of Advanced Reactor Vessel Steels Under Neutron Irradiation, Scottsdale, AZ*

Robert J. Goode, associate superintendent and chief scientist for structural integrity technology of the Material Science and technology Division is the 1982 recipient of the Award of Merit by the American Society for Testing and Materials, the internationally recognized standards-writing organization. Goode was cited "for distinguished service in advancing the voluntary standardization of test methods for fracture and stress-corrosion cracking behavior...."

Heitmeyer, C.L., *National Academy of Science Air Force Studies Board Summer Study on Multilevel Secure Data Base Management Systems*

Hendrickson, W.A., *Co-chairman, Gordon Research Conference on Diffraction Methods in Molecular Biology; USA National Committee for Crystallography; Chairman, Fankuchen Award Committee of the American Crystallographic Association; Advisory Board of the Protein Data Bank*

Hinkley, J.A., *Chairman, Committee on Chemistry and Public Affairs, Chemical Society of Washington*

Holtzclaw, J.R., *Co-chairman of JANAF Workshop on Remote Sensing of Hazardous Materials at NBS*

Hoppel, W.A., *Associate Editor, Journal of National Research Council Geophysical Research. NRC panel to produce report on the Earth's electrical environment*

Hubler, G.K., *Bühmische Physical Society*

Imhof, P.H., *Chair Resource Sharing Advisory Group by Head Defense Technical Information Center*

Ingenito, F., *Technical Committee on Underwater Acoustics of the Acoustical Society of America; Fellow of the Acoustical Society of America*

Johnson, T.L., *Scientific Committee 68 on Microprocessors in Dosimetry, National Council on Radiation Protection and Measurements*

Kapetanakos, C.A., *Fellowship Committee, Division of Plasma Physics, American Physical Society*

Karle, I.L., *MIT Corporation Visiting Committee; National Academy of Sciences Committee for Survey of Opportunities in Chemistry (Pimentel report); listed among 1000 world scientists with most citations in the literature, Citation Index; listed in Who's Who in the World, Vol. 6; described in "Women's Book of World Records and Achievements," p. 183*

Karle, J., *President, International Union of Crystallography; Biotechnology Advisory Panel, Stanford Synchrotron Radiation Laboratory; Auditing committee, National Academy of Sciences*

Keramidas, G.A., *Board of Directors, Institute for Computational Mechanics, Southampton, England; Editorial Board, Int. Journal of Applied Mathematical Modeling*

Keskinen, M.J., *Working Group "Nature of Structure and Striations at High Latitudes" of the NASA Solar Terrestrial Physics Workshop*

Kinzig, B.J., *National Academy of Sciences Advisory Board's Subcommittee on Shock Processing*

Knudson, A.R., *Distinguished Poster Paper Award for IEEE Conference on Nuclear and Space Radiation Effects*

Krowne, C.M., *Chairman, Microwave Field Theory Session; IEEE Microwave Theory and Techniques International Symposium; Technical Program Committee*

Kurfess, J.D., *Committee on Space Astronomy and Astrophysics of the National Academy of Sciences; Secretary-Treasurer, Division of Cosmic Physics of the American Physical Society; Long Duration Balloon Study Panel sponsored by NASA, NSF and UCAR*

Landwehr, C.E., *National Academy of Science Air Force Studies Board Summer Study on Multilevel Secure Data Base Management Systems*

Leonard, J., *Editorial Advisory Board of the Journal of Fire Sciences*

Dr. Robert Hazlett (left) receives the Applied Science trophy from Sigma Xi President Dr. Jim Krebs. Hazlett, of the Chemistry Division, was cited for his work in liquid phase oxidation of hydrocarbons. His contributions "impact directly on critical Navy fleet problems related to oxidation and stability of jet fuels," the citation reads.

NRL physicist Dr. Martin Lampe of the Plasma Physics Division is pinned with the Navy Meritorious Civilian Service Award by his wife, Barbara at a ceremony held June 16. Lampe was cited for his contributions to the basic theory and technology of charged particle beams.

NRL scientist, Dr. Ming-Chang Lin who pioneered the development and use of chemical lasers for research applications, is the 1982 recipient of two prestigious awards: the Humboldt Prize from the Alexander von Humboldt Foundation and a Guggenheim Fellowship from the John Simon Guggenheim Memorial Foundation. Lin, who joined NRL in 1970, also received the 1975 Hillebrand Prize from the Washington Chapter of the American Chemical Society for his development of new chemical lasers and for his outstanding application of lasers to chemical kinetic problems.

Lewis, D., *Secretary-Treasurer, Baltimore-Washington Section, American Ceramic Society*

Lin, M.C., *Humboldt Prize, The Senior U.S. Scientist Award, granted by the Alexander von Humboldt Foundation, Guggenheim Fellowship from the John Simon Guggenheim Memorial Foundation.*

Lister, M.J., *Editorial Committee, Fourteenth Annual Precise Time and Time Interval (PTTI) Applications and Planning Meeting*

McCafferty, E., *Divisional Editor, Journal of the Electrochemical Society; Secretary-Treasurer, Corrosion Division of the Electrochemical Society; Honors and Awards Committee of the Electrochemical Society; Chairman, Olin Palludium Medal Award Committee of the Electrochemical Society; William Blum Award, National Capital Section of the Electrochemical Society; Professonal Lecturer, George Washington University*

McDonald, J.R., *Hillebrand Award, for outstanding chemist of the Chemical Society of Washington*

McLean, E.A., *Secretary, IEEE Nuclear and Plasma Sciences Society, Plasma Science and Applications Committee*

Markowitz, A.E., *Acoustical Society of America Working Group on Standards for Transducer Calibration*

Michel, D.J., *Co-chairman, Topical Conference on Ferritic Alloys for use in Nuclear Energy Technologies; American Society of Mechanical Engineers, Task Force on Crack Propagation Technology*

Moser, P.J., *Meritorious Unit Commendation, Department of the Navy*

Murday, J.S., *ONR SRO III Evaluation Committee; Chairman, American Vacuum Society Local Arrangements Committee; Chairman, Trustee Committee, American Vacuum Society*

Nisenoff, M., *Organizing and Program Committees for 3rd Conference on Refrigeration for Cryogenic Sensors and Electronic Systems; Interagency Committee on Cryogenic Refrigeration; Board of Directors of Applied Superconductivity Conference*

Oaks, O.J., *Vice Chairman, Washington Section, IEEE Instrumentation and Measurement Society*

Ossakow, S.L., *Program Committee for Invited Papers, APS Plasma Physics Division; fellow, American Physical Society; NASA/NSF Solar Terrestrial Physics Workshop; Chairman, Ionospheric Physics Subcommittee and Chairman, Working Group on Nature of Structure and Striations at High Latitudes*

Ozimina, C.D., *Vice Chairman Northern Virginia Chapter of the IEEE Control Systems Society*

Palik, E.D., *Editor, "Handbook of Optical Constants of Materials" (Academic Press, 1982-83)*

Pande, C.S., *Board of Review, Metallurgical Transactions; Mechanical Metallurgy Committee, AIME; Electrical, Magnetic and Optical Phenomena Committee, ASM*

Parnas, D.L., *Chosen by the Association of Computing Machinery as one of the "milestones of research" over the past 25 years of computer science for 1972 paper, "A Technique for Software Module Specification with Examples"*

Poche', L.B., *Audio-visual Chairman, 104th Mtg. of Acoustical Society of America (Orlando, Florida)*

Price, G.E., *Meritorious Unit Commendation, Department of the Navy*

Rath, B.B., *Fellow of the American Society for Metals; Member, Joint Commission of the Metallurgical Transactions of ASM and AIME; Chairman, Electrical, Magnetic and Optical Phenomena Committee of ASM; Symposium Organizer "Novel NDE for Materials" ASM, Dallas, TX, Feb. 1982; Co-editor, Micro- and Macromechanics of Crack Growth, ASM Publication*

Reinecke, T.L., *Fellow, American Physical Society; Sigma Xi-Research Society of America, NRL Chapter, Award for Outstanding Research in Pure Science; Steering Committee for Greater Washington Solid State Physics Colloqium*

Resing, H.A., *Editorial Board, Journal of Magnetic Resonance*

Rice, R.W., *Publication, John Jepson Award, and Long Range Planning Committee, American Ceramic Society, and the Program Committee of the Electronics Division of American Ceramic Society*

Ripin, B.H., *Associate Editor of Physical Review Letters; Executive Committee, IEEE Plasma Science Applications Committee; Co-chairman, Long-range Planning Committee of the IEEE-PSAC; CLEO Program Committee*

Rose, S.L., *Manager of Chemical Society of Washington*

Rudgers, A.J., *Facilities Chairman, Program Committee, and Session Chairman of 104th Mtg. of Acoustical Society of America (Orlando, FL)*

Sartwell, B.D., *Program Committee of the International Conference on Metallurgical Coatings*

Schindler, A.I., *Presidential Meritorious Senior Executive Award*

For his efforts toward "the understanding of interacting electronic systems and of quantum phase transitions through advances in the theory of electron-hole liquid condensation in semiconductors," Dr. Thomas L. Reinecke (left) receives Sigma Xi's Pure Science Award.

Dr. Irwin Schneider of NRL's Optical Sciences Division received the Navy Meritorious Civilian Service Award on November 30. Dr. Schneider was given the honor in recognition of his contributions in the fields of color centers and color center lasers. He was also cited for developing a method for stabilizing color centers which has transformed the color center laser from a research tool to a device with wide-ranging practical applications.

Schneider, I., *Navy Meritorious Civilian Service Award*

Schnur, J.M. *National Academy of Sciences Advisory Board's Subcommittee on Shock Processing*

Searles, S.K., *AIAA Plasma Dynamics and Laser Technical Committee*

Sheeley, Jr., N.R., *National Academy of Sciences' Committee on Solar Terrestrial Relationships*

Sheinson, Ronald, *Treasurer of Combustion Institute, Eastern Section*

Sica, L., *Treasurer, National Capital Section, Optical Society of America*

Sigel, G.H., *George W. Morey Award from American Ceramic Society; Chairman of Tri-Service Radiation Effects Working Group on Optical Fibers; Chairman of NATO RSG12, IV Task Group on Nuclear Effects on Optical Waveguides*

Singer, I.L., *Award for best poster presentation at a Poster Session of National Meeting of American Vacuum Society, Baltimore, MD*

Skelton, E.F., *National Materials Advisory Board Ad Hoc Committee on "Shock Compression Chemistry in Materials Synthesis and Processing"; Program Committee, IXth Meeting of International Association for the Advancement of High-pressure Science and Technology*

Skolnik, M.I., *Distinguished Civilian Service Award, Department of the Navy*

Slagle, J.R., *Mary P. Oenslager Career Achievement Award from Recording for the Blind, Inc.; Co-chairman, Artificial Intelligence Working Group of the Military Operations Research Society (MORS)*

Spielman, B.E., *Steering Committee 1983 IEEE Microwave & Millimeter-wave Monolithic Circuits Symposium; IEEE MTT-S Administrative Committee; Technical Program Committee IEEE International Microwave Symposium; Program Committee IEEE Microwave & mm-Wave Monolithic Symposium; Session Chairman IEEE Microwave & mm-Wave Monolithic Symposium*

Stamper, J.A., *Fellow of The American Physical Society*

Steele, L.E., *Editor and contributing author, "Structural Integrity of Light Water Reactor Components," (Applied Science Publishers LTD., U.K.); editor "Status of USA Nuclear Reactor Pressure Vessel Surveillance for Radiation Effects," Published by ASTM Phila., PA, USA (also chapter author—2 chapters); Vice Chairman, Board of Directors, American Society for Testing & Materials; Society Board of Directors & Executive Committee; Vice President, Federation of Materials Societies, ASTM Trustee of Federation*

Strobel, D.F., *Chairman, Committee on Upper Atmosphere, American Meteorological Society Member, Committee on Solar and Space Physics, Space Science Board, National Academy of Sciences*

Szuszczewicz, E.P., *NASA/NSF Steering Committee on Solar Terrestrial Physics; Co-chairman, NASA/NSF Solar-Terrestrial-Physics Working Group on High-Latitude Ionospheric Structure*

Thomas, R.E., *Special Editor for TriService Cathode Workshop, for Special Edition of "Applications of Surface Science" (North-Holland Publishing Company)*

Trzaskoma, P.P., *Vice Chairman, National Capital Section, Electrochemical Society's Member, Individual Membership Committee of the Electrochemical Society*

Turner, N.H., *Local Arrangements Committee (Short Course Coordinator) for the 29th National American Vacuum Society Symposium*

1982 Alan Berman Research Publication Awards

From the top, left to right:
J. E. Smith, D. J. Michels, M. J. Koomen
W. A. Hendrickson, H. H. Chaskelis, T. G. Giallorenzi
M. Fink, S. J. Stephanakis, W. E. Howell
A. Sharman, Jr., R. Panayappan, D. L. Venezky
S. A. Goldstein, J. R. Baker,
and Capt. J. A. McMorris II, USN

(Baltmore, MD); Job Manual Chairman, Chemical Society of Wash., (Wash. Section of the American Chemical Society); Membership Chairman, Division of Colloid and Surface Chemistry of the American Chemical Society

Valenzuela, G.R., *Outstanding Reviewer, Journal of Geophysical Research (Oceans & Atmospheres); Associate Editor (until 1985), Journal of Geophysical Research (Oceans & Atmospheres); Admissions Committee, Commission F on Remote Sensing and Wave Propagation, USNC of International Union of Radio Science; listed in 1982 Year Book of International Council of Scientific Unions*

Van Buren, A.L., *Technical Program Chairman, 104th Meeting of Acoustical Society of America (Orlando, Fl.); Chairman, International Electrotechnical Commission Working Group on Standards for Pressure Gradient Hydrophone Calibration; Chairman, Acoustical Society of America Working Group on Standards for Transducer Calibration; Technical Program Committee, 103rd Meeting of Acoustical Society of America (Chicago)*

Vegh, E., *President, NRL Chapter of Sigma Xi*

Venezky, D.L., *Secretary, American Chemical Society (ACS) Council Committee on Committees and liaison to the ASC Council Committees on Science and Chemical Safety.*

Vitkovitsky, I.M., *Invited by Van Nostrand Reinhold Company, Inc. to author a reference book on high-power switching*

Vogt, P.R., *Co-editor, Geological Society of America, Decade of North American Geology: Volume I, The Western North Atlantic*

Volin, R.H., *Technical Committee on Sound and Vibration, Design Engineering Division ASME*

Watkeys, D.E., *Meritorious Unit Commendation, Department of the Navy*

Waynant, R.W., *IEEE Research and Development Committee*

Webb, D.C., *Technical Committee on Microwave Ferrites, IEEE Magnetics Society; Technical Program Committee INTERMAG Conference; Technical Committee on Microwave Acoustics, IEEE Society on Microwave Theory and Techniques*

Welker, E., *Meritorious Unit Commendation, Department of the Navy*

Whicker, L.R., *Technical Activities Board (TAB) of IEEE; Chairman IEEE TAB Meetings Committee; Member, Technical Program Committee and Session Chairman, 1982 IEEE International Microwave Symposium*

White, C.T., Dr., *Chairman, Conducting Polymers and Polyacetylene II Session, Dallas Meeting of the American Physical Society, Dallas, Texas*

Willett, J.C., *Ad Hoc Panel on Atmospheric Electricity, Geophysics Study Committee, NRC*

Williams, Frederick, *Vice Chairman of Combustion Institute, Eastern Section*

RESEARCH PUBLICATION AWARDS

The Annual Research Publication Awards Program was established in 1968 to recognize the authors of the best NRL publications each year. These awards not only honor individuals for superior scientific accomplishments in the field of naval research, but also seek to promote continued excellence in research and in its documentation. This year the program has been changed to the Alan Berman Research Publication Awards in honor of its founder.

There were 199 separate publications in 1982 that were considered for recognition. Of those considered, 33 were selected. These selected publications comprised a total of 93 authors, who received awards. Each of the divisions was permitted $1000, which was shared by varying numbers of authors. On March 11, 1983, the awards were presented to the authors at the Alan Berman Annual Research Publication Awards Dinner held at the Bolling Air Force Base Officers' Club. Each winner received a certificate, a bronze paperweight, and a booklet of the 1982 Publications Receiving Special Recognition.

The unclassified winning papers are included in the following section under "Papers in Periodicals, Books, and Proceedings of Meetings" and are designated by daggers in the margin. NRL authors are listed below by their research units. There were 28 non-Laboratory co-authors, who are not named.

PUBLICATION AWARDS WINNERS

Office of the Director of Research (1001)

Dr. Ira B. Bernstein
Dr. David L. Book
Mr. John H. Gardner, Jr.
Dr. Wayne A. Hendrickson
Dr. Keith O. Hodgson
Dr. Gerald L. Klippenstein
Dr. Janet L. Smith
Dr. Man Sung Co

Space Science Division (4100)

Dr. Robert R. Conway
Dr. Russell A. Howard
Dr. Martin J. Koomen
Dr. Donald J. Michels
Dr. Neil R. Sheeley, Jr.

Environmental Sciences Division (4300)

Dr. John P. Dugan
Dr. Richard P. Mied
Dr. Peter C. Mignerey
Dr. William J. Plant
Mr. Arnim F. Schuetz

Plasma Physics Division (4700)

Dr. Philip G. Burkhalter
Dr. Mort Fink
Dr. Shyke A. Goldstein
Dr. Jacob Grun
Dr. Mark J. Herbst
Dr. Thomas A. Mehlhorn
Dr. David Mosher
Dr. Stavros Stephanakis
Dr. Robert R. Whitlock
Dr. Frank C. Young

Acoustics Division (5100)

Dr. Joseph A. Bucaro
Mr. James H. Cole
Dr. Thomas G. Giallorenzi
Dr. Nicholas Lagakos

Radar Division (5300)

Dr. Grealie A. Andrews
Mr. Samuel L. Sheller
Dr. Dennis B. Trizna

Tactical Electronic Warfare Division (5700)

Mr. William E. Howell
Dr. John A. LaFemina
Mr. Bryan W. McGhee
Mr. Gary T. Roan

Marine Technology Division (5800)

Dr. Henry H. Chaskelis
Dr. Alfred V. Clark, Jr.
Dr. George A. Keramidas

Underwater Sound Reference Detachment (5900)

Mr. Theodore A. Henriquez
Mr. Allan C. Tims
Mr. Allen M. Young

Chemistry Division (6100)

Dr. John C. Cooper
Dr. Allen N. Garroway
Ms. Claudia J. Hackbarth
Ms. Christine M. Hellwig
Dr. William B. Moniz
Dr. Ramanatha Panayappan
Dr. William M. Ritchey
Dr. David L. Venezky

Material Science and Technology Division (6300)

Dr. Virgil Provenzano
Dr. Kuntimaddi Sadananda
Dr. Paul Shahinian
Dr. Fred A. Smidt, Jr.
Dr. James A. Sprague

Optical Sciences Division (6500)

Dr. Michael D. Duncan
Mr. Chester F. Fisher
Dr. Thomas J. Manuccia, Jr.
Dr. John F. Reintjes
Mr. Robert J. Ginther
Dr. Kenneth H. Levin
Dr. George H. Sigel, Jr.
Dr. Danh C. Tran

Condensed Matter and Radiation Sciences Division (6600)

Mr. Robert Berger
Mr. Arthur B. Campbell
Dr. Harvey Eisen
Mr. James Ferry
Dr. Alvin R. Knudson
Mr. George Messenger
Dr. Arthur Namenson
Mr. Robert Scace
Dr. Harry Schafft
Dr. Eligius A. Wolicki

Electronics Technology Division (6800)

Dr. Alfred Forchel
Mr. Bengt Laurich
Dr. Thomas L. Reinecke
Mr. Nelson S. Saks
Dr. Wolfgang Schmid
Mr. Joachim Wagner

Information Technology Division (7500)

Mr. Ronald N. Bauman
Mr. Walter A. Buczek
Mr. Charles E. W. Hobbis
Mr. Richard K. Royce

Space Systems Division (7700)

Dr. William H. Carter
Mr. James E. Kenney
Mr. Alan P. Sharman, Jr.

Aerospace Systems Division (Code 7900)

Mr. Jay R. Baker
Dr. Shannon L. Coffey
Dr. Andreé Deprit
Mr. Danny C. Lim

CONTINUING EDUCATION AND TRAINING

NRL has established and maintains an extensive training operation to attract, develop and retain competent personnel and keep them abreast of advanced technology to support the mission of the Laboratory.

During 1982, members of the civilian staff participated in about 3300 individual training incidents. Many of these training opportunities were presented as in-house courses and video tape packages. Approximately 120 in-house courses were presented in fields such as management, technical subjects, and personal skills.

The most common study procedure was for participants to work full time at the Laboratory and take job-related scientific courses at universities and schools in the Washington area while working full time at the Laboratory. Tuition for such training is paid by NRL. There were also

the following formal programs in which 11 persons were enrolled: Advanced Graduate Research, Edison Memorial, and Select Graduate. This involves formal nomination and selections by a long-term training panel. There are two additional programs that exemplify the Laboratory's continuing associations with higher education and the academic community. They are the postdoctoral National Research Council–NRL Cooperative Research Associateship Program, which had 25 new participants in 1982, and the Navy–ASEE Summer Faculty Research Program, which had 31 participants.

The five postgraduate programs and the participation in 1982 are described in the remainder of this section.

Advanced Graduate Research Program

The Advanced Graduate Research Program, which was started in 1964, enables selected employees to devote full time to research or course work in their own or a related field for one academic year at an institution of their choice without the loss of regular salaries, leave, or fringe benefits. From the inception of the program through 1982, 137 employees have participated in this program. Criteria for eligibility include professional stature consistent with the applicant's opportunities and experience, a satisfactory program of study, and acceptance by the institution selected by the applicant. The program is open to midlevel (and above) employees who have completed six years of federal service, including four years at NRL.

The following NRL staff members began their programs in the fall of 1982.

Jack D. Ayers (Material Science and Technology), Royal Institute of Technology, Stockholm, Sweden

James E. Bulter (Chemistry), Institute for Molecular Science, Okazaki, Japan

Robert C. Eckardt (Optical Sciences), Stanford University, Stanford, California

John H. Konnert (Laboratory for the Structure of Matter), Arizona State University, Tempe, Arizona

Ming Chang Lin (Chemistry), University of Munich, Munich, W. Germany

Yung Shu Wu (Space and Communication Technology), Imperial College of Science and Technology, London, England

Edison Memorial Graduate Training Program

This program enables employees to pursue advanced studies in their fields at local universities. Eligible employees who are selected for participation in this program normally spend 24 hours per week in their work at the Laboratory and 16 hours per week in their studies. The criteria for eligibility include a minimum of one year of service at NRL, a bachelor's or master's degree in an appropriate field, and professional standing in keeping with the candidate's opportunities and experience.

From 1963 through 1982, 146 employees have studied under the Edison Program. The following began study as Edison Scholars in 1982:

Michael S. Kaplan (Aerospace Systems), George Washington University

Nicholas C. Orrick (Space Science), University of Maryland

David L. Tate (Information Technology), University of Maryland

Dorsey L. Thacker (Space Science), University of Maryland

Waylon W. Webbon (Marine Technology), University of Maryland

Select Graduate Student Program

To be eligible for this program, employees must have a college degree in an appropriate field and must have maintained at least a B average in undergraduate study. Accepted students devote a full academic year to graduate study. While actually attending school, they receive one half of their salaries, and NRL pays for tuition, books, and laboratory expenses. During the summer, they work at the Laboratory and receive normal pay and fringe benefits.

Thirty-four staff members have enrolled in the program since it began in 1967.

NRC–NRL Cooperative Research Associateship Program

Selected Research Associates, who are not NRL employees, spend up to two years here conducting research in their chosen fields in association with NRL scientists. The responsibility for evaluating and selecting the best qualified applicants rests with the National Research Council of the National Academy of Sciences and the National Academy of Engineering. The 25 new postdoctoral associates appointed in 1982 are:

80459

Frank Robbins uses a study booth in the Employment Development Branch

Barbara H. Berrie, Georgetown University, Chemistry
Richard M. Bevilacqua, Pennsylvania State University, Space Science
William M. Bone, University of Virginia, Chemistry
David J. Burinsky, Purdue University, Chemistry
James C. Culbertson, University of California, Electronics Technology
Robert P. Devaty, Cornell University, Electronics Technology
Daniel P. DiLella, University of Toronto, Chemistry
Martha C. Farmer, Duke University, Optical Science
Jacqueline Fischer, State University of NY, Space Science
Duane P. Flamig, University of Nebraska, Optical Science
Orest Glembocki, City University of NY, Electronics Technology
John M. Grossman, University of Maryland, Plasma Physics
Paul L. Hertz, Harvard University, Space Science
Mark A. Hoffbauer, University of Minnesota, Chemistry
Steve T. Kacenjar, University of Rochester, Plasma Physics
David A. Kidwell, Mass. Institute of Technology, Chemistry
Kenneth E. Kihlstrom, Stanford University, Condensed Matter and Radiation Sciences
Michael P. Kowalski, Northwestern University, Space Sciences
Daniel A. Lichtin, Columbia University, Chemistry
Patrick Nolan, University of California, Space Sciences
Timothy Renk, Cornell University, Plasma Physics
Steven Sheriff, University of Washington, Laboratory for Structure of Matter
Randy W. Simon, University of California Los Angeles, Condensed Matter and Radiation Sciences
Richard S. Simon, California Institute of Technology, Space Sciences
Daniel Stec, III, Northwestern University, Chemistry

Navy—ASEE Summer Faculty Research Program

This ONR-sponsored program affords selected university faculty members the opportunity to work for 10 summer weeks with professional peers in participating Navy laboratories on research of mutual interest. Administered by the American Society for Engineering Education, the program in 1982 (its fourth year) involved 10 Navy R&D centers and 97 faculty participants. NRL hosted 31 of these faculty participants who are listed below with their home institution and the NRL Division and Mentor with whom they worked.

M.F. Aburdene, Bucknell University, Space Systems, D.E. Wahrenberger
P.M. Bakshi, Boston College, Plasma Physics, P.J. Palmadesso
T.M. Bania, Boston University, Space Science, K.J. Johnston
T.N. Bhar, University of DC, Electronics Technology, H.L. Hughes
J.F. Chiang, State University of NY, Laboratory for Structure of Matter, I.L. Karle
D.Y. Chung, Howard University, Acoustics, J.H. Cole
M.F. Czarnecki, Florida Atlantic University, Acoustics, R.H. Feden
C.H. Douglass, Jr., Trinity College, Chemistry, J.R. McDonald
M.E. Edwards, Fayetteville State University, Optical Sciences, G.L. Trusty
A.H. Hagedoorn, University of Central Florida, Underwater Sound, R.W. Timme

E.C. Hammond, Jr., Morgan State University, Condensed Matter and Radiation Sciences, E.A. Wolicki

C.W. Hand, University of Alabama, Chemistry, D.J. Bogan

R. Heisler, Walla Walla College, Acoustics, B.B. Adams

K.M. Htun, University of Hawaii, Material Science and Technology, R.J. Goode

D.W. Hubbard, Michigan Technology University, Marine Technology, O.M. Griffin

M.J. Kaufman, Emory University, Chemistry, D.J. Bogan

R.G. Landolt, Texas Wesleyan College, Chemistry, R.G. Taylor

C.K. Manka, Sam Houston State University, Plasma Physics, B.H. Ripin

F.W. Oliver, Morgan State University, Condensed Matter and Ratiation Sciences, J.C. Ritter

L.J. Rickard, Howard University, Space Science, P.R. Schwartz

E.L. Robinson, Austin College, Optimal Sciences, J.N. Lee

C.W. Sink, Edinboro State College, Chemistry, D.R. Hardy

G.B. Taggart, Virginia Commonwealth University, Electronics Technology, T.L. Reinecke

J.L. Templeton, University of North Carolina, Chemistry, R.J. Nowak

D. Van Vechten, Howard Univeristy, Condensed Matter and Radiation Sciences, D.U. Gubser

R.L. Varley, Lehigh University, Laboratory for Computational Physics, M.H. Emery

P.J. Walsh, Fairleigh Dickinson University, Electronics Technology, H. Lessoff

M.A. Wechter, S.E. Mass. University, Chemistry, R.N. Hazlett

W. Williams, Lincoln University, Electronics Technology, R.J. Wagner

A.A. Wolf, Davidson College, Optical Sciences, E.J. Friebele

M. Yuschik, University of South Carolina, Information Technology, G.S. Kang

Summer Research Apprentice Program

The Summer Research Apprentice Program, started in 1980, enables high school juniors and sensiors to serve for eight weeks as junior research associates. Under the direction of a mentor, students gain a better understanding of research through participation and knowledge of opportunities and challenges in scientific careers. Criteria for eligibility include science and mathematics courses completed and grades achieved, scientific motivation, curiosity and capacity for sustained hard work, career plans, teacher recommendations, and ability and achievement test scores.

As part of the Department of Defense Science and Engineering Apprenticeship Program for High Schools, the NRL program has served as a prototype for other DoD programs and continues to show steady growth. In 1980, 28 students participated in the program with an increase to 75 in 1982. We anticipate 80 students for 1983's summer program.

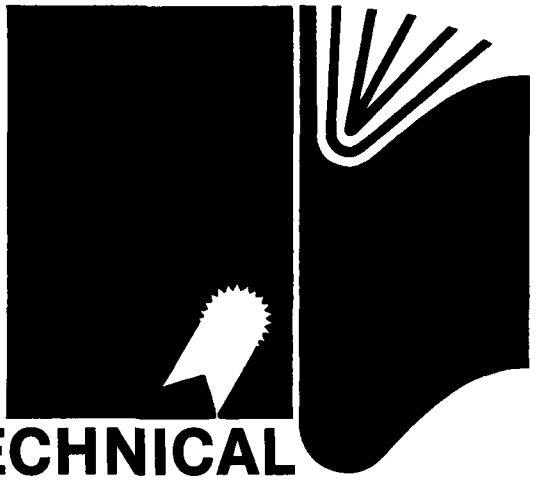

TECHNICAL OUTPUT:

PAPERS, REPORTS, and PATENTS

TECHNICAL OUTPUT

PAPERS, REPORTS, AND PATENTS

In several respects, NRL is like a factory; the input ingredients are the talents and ideas of its people and research funds; the output product is information; and this product is packaged in the form of reports, articles in science journals, books, and papers presented to scientific societies and topical conferences, and patents.

This section lists a portion of NRL's product for 1982. The omitted parts are oral presentations (about 1500), memorandum reports, all reports that carry a military security classification, and all letter reports to sponsors. In the following bibliography, an asterisk identifies a coauthor who is not a member of the NRL staff, and a dagger (†) identifies a prize-winning publication. In 59 years, NRL's pioneering research has led to 2954 patents. The table below summarizes the 1982 technical output.

Type of Contribution	Unclass.	Class.	Total
Papers in periodicals, books, and proceedings of meetings	835	0	835
NRL Reports	55	28	83
NRL Memorandum Reports	221	57	278
Books	1	0	1
Patents granted			46

PAPERS IN PERIODICALS, BOOKS, AND PROCEEDINGS OF MEETINGS

ACOUSTICS

A Digital Processing System for Acousto-Optic Visualization of Sound Fields, by H.D. Dardy and C.F. Gaumond, in *Acoustical Imaging*, Plenum Publishing Corp., New York, Vol. 11, pp. 21-37

Acoustic Classification of Submerged Targets, by S.K. Numrich, L.J. Frank, and L.R. Dragonette, in *IEEE International Conference on Acoustics, Speech, and Signal Processing (ICASSP)*, IEEE, New York, pp. 327-330

Acoustic Desensitization of Single-Mode Fibers Utilizing Nickel Coatings, N. Lagakos, I.J. Bush, J.H. Cole, J.A. Bucaro, J.D. Skogen,* and G.B. Hocker,* *Optics Letters* 7:460-462

Acoustically Induced Birefringence in Optical Fibers, by L. Flax, J.H. Cole, R.P. DePaula,* and J.A. Bucaro, *Journal of the Optical Society of America* 72:1159-1162

Advances in Fiber Optic Based Acoustic Sensors, by J.H. Cole, N. Lagakos, and J.A. Bucaro, in *Fiber Optics—Technology '82*, SPIE, Bellingham, Washington, SPIE Vol. 326, pp. 116-126

An Approximation to the Three-Dimensional Parabolic-Equation Method for Acoustic Propagation, by J.S. Perkins and R.N. Baer, *Journal of the Acoustical Society of America* 72: 515-522

Analysis and Computation of the Acoustic Scattering by an Elastic Prolate Spheroid Obtained from the T-Matrix Form lation, by L. Flax, L.R. Dragonette, V.K. Varadan,* and V.V. Varadan,* *Journal of the Acoustical Society of America* 71:1077-1082

Application of Fiber-Optic Sensors to the Detection of Air-Acoustic Signals, by G.S. Maurer, L. Schuetz, J.H. Cole, and J.A. Bucaro, *Optics Letters* 7:503-505

Boundary Reflection/Diffraction Effects and the Parabolic-Equation Split-Step Algorithm, by R.L. Dicus, *Journal of the Acoustical Society of America* 72:494-504

Calculations of the Spatial Coherence and Array Noise Gain of Wind Generated Noise, by F. Ingenito, *Oceans '82 Conference Record*, IEEE, New York, pp. 166-171

Classification of Submerged Targets by Acoustic Means, by S.K. Numrich, L. Flax, and L.R. Dragonette, in *Elastic Wave Scattering and Propagation*, Ann Arbor Science Pubs., Ann Arbor, Michigan, Chapter 9, pp. 149-175

Computation of Rigid Body Scattering by Prolate Spheroids using the T-Matrix Approach, by V.K Varadan,* V.V. Varadan,* L.R. Dragonette, and L. Flax, *Journal of the Acoustical Society of America*, 71:22-25

Erratum: "Ambient Noise Vertical Directionality in the Northeast Atlantic" [*J. Acoust. Soc. Am.* **70**, 577-58 (1981)], by S.C. Wales and O.I. Diachok, *Journal of the Acoustical Society of America* 71:1039

Erratum: "Filled Rubber Material System: Application to Echo Absorption in Water-filled Tanks" [*J. Acoust. Soc. Am.* **68** 655-664 (1980)], by R.D. Corsaro, J.D. Klunder, and J. Jarzynski, *Journal of the Acoustical Society of America* 71:224

†**Fiber Optic Acoustic Transduction**, by J.A. Bucaro, N. Lagakos, J.H. Cole, and T.G. Giallorenzi, *Physical Acoustics, Principles and Methods* 16:385-457

High-Speed Coherence Processing Using the Sectionalized Fourier Transform, by A.A. Gerlach, *IEEE Transactions on Acoustics, Speech and Signal Processing* ASSP-30:189-205

Hydrophone Nonlinearity Measurements, by M.B. Moffett* and T.A. Henriquez, *Journal of the Acoustical Society of America* 72:1-6

Measurement of Ultrasound Reflected from Liquid Layers of Submicron Thickness, by A.V. Clark and S.D. Hart, *Materials Evaluation* 40:866-873

Microbend Fiber-Optic Sensor as Extended Hydrophone, by N. Lagakos, W.J. Trott, T.R. Hickman, J.H. Cole, and J.A. Bucaro, *IEEE Journal of Quantum Electronics* QE-18:1633-1638

On the Development of Acoustically Transparent Structural Plastics, by R.E. Montgomery,* F.J. Weber,* D.F. White,* and C.M. Thompson, *Journal of the Acoustical Society of America* 71:735-741

Optimizing Fiber Coatings for Interferometric Acoustic Sensors, by N. Lagakos, E.U. Schnaus, J.H. Cole, J. Jarzynski, and J.A. Bucaro, *IEEE Journal of Quantum Electronics* QE-18:683-689

Response of a Fiber-Optic Acoustic Sensor to Low-Frequency, Broadband Excitation, by C.C. Ni and R.J. Hansen, *Journal of the Acoustical Society of America* 72:636-638

Scattering at a Rough Boundary—Extensions of the Kirchhoff Approximation, by E.G. Liszka* and J.J. McCoy, *Journal of the Acoustical Society of America* 71:1093-1100

Scattering of a CW Plane Wave by a Pulse, by D.H. Trivett and P.H. Rogers, *Journal of the Acoustical Society of America* 71: 1114-1117

Site Dependence of Wind-Dominated Ambient Noise in Shallow Water, by S.N. Wolf and F. Ingenito, in *Undersea Ambient Noise*, SACLANT Conference Proceedings No. 32, Part 2, Vol. II, pp. 22-1—22-9

Sound Propagation in a Pipe Containing a Liquid of Comparable Acoustic Impedance, by M.P. Horne and R.J. Hansen, *Journal of the Acoustical Society of America* 71:1400-1405

†**The Effect of Surface Cleanness of Thin Defects on the Reflection of Ultrasound**, by A.V. Clark, Jr., and H.H. Chaskelis, *Ultrasonics* 20:173-183

Time-Limited Sampling Theorems for Band-Limited Signals, by C.L. Byrne and R.M. Fitzgerald, *IEEE Transactions on Information Theory* IT-28:807-809

ATMOSPHERIC SCIENCES

Comments on "Comparison of Tropical Cyclone Motion and Environmental Steering," by S.W. Chang* and R.V. Madala, *Monthly Weather Review* 110:2070-2071

5500 Miles of Liquid Water and Dropsize Measurements in Supercooled Clouds Below 10,000 Feet AGL, by R.K. Jeck, in *Conference on Cloud Physics, Extended Preprint Volume*, American Meteorological Society, Boston, Massachusetts, pp. 408-411

Is the Bulk Aerodynamic Drag Coefficient Different over Coastal Waters than over the

AD-A136 193 1982 NAVAL RESEARCH LABORATORY REVIEW(U) NAVAL RESEARCH 3/3
LAB WASHINGTON DC A E ROBSON ET AL. 1983

UNCLASSIFIED F/G 14/2 NL

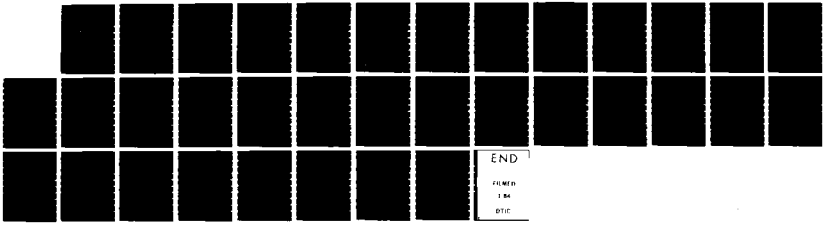

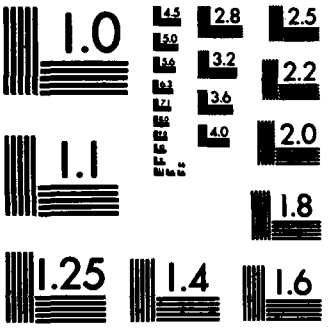

MICROCOPY RESOLUTION TEST CHART
NATIONAL BUREAU OF STANDARDS-1963-A

Open Ocean? Some Interesting Observations, by T.V. Blanc, in *First International Conference on Meteorology and Air/Sea Interaction of the Coastal Zone, Preprint Volume,* American Meterological Society, Boston, Massachusetts, pp. 31-35

Refined Monte Carlo Method for Simulating Angle Dependent Partial Frequency Redistributions, by J.S. Lee, *Astrophysical Journal* 255:303-306

The Dependence of Space Charge Spectra on Aitken Nuclear Concentrations, by R.V. Anderson, *Journal of Geophysical Research* 87:1216-1218

The Size and Scattering Coefficient of Urban Aerosol Particles at Washington, D. C., as a Function of Relative Humidity, by J.M. Fitzgerald, W.A. Hoppel, and M.A. Vietti,* *Journal of the Atmospheric Sciences* 39:1838-1852

BIOSCIENCES

Changes in Size and Shape of Liposomes Undergoing Chain Melting Transitions as Studied by Optical Microscopy, by P. Yager, J.P. Sheridan, and W.L. Peticolas,* *Biochimica et Biophysica Acta* 693:485-491

Improved Method for Determination of Respiring Individual Microorganisms in Natural Waters, by P.S. Tabor and R.A. Neihof, *Applied and Environmental Microbiolgoy* 43:1249-1255

Improved Microautoradiographic Method to Determine Individual Microorganisms Active in Substrate Uptake in Natural Waters, by P.S. Tabor and R.A. Neihof, *Applied and Environmental Microbiology* 44:945-953

Kinetics and Thermodynamic Studies of the Fusion of Small Unilamellar Phospholipid Vesicles, by B.P. Gaber and J.P. Sheridan, *Biochimica et Biophysica Acta* 685:87-93

Microbial Contamination of Ship Fuels, by R.A. Neihof, D.E. Klemme, and C.E. Patouillet, in *Distillate Fuel Stability and Cleanliness,* ASTM, Philadelphia, Pennsylvania, ASTM STP 751, pp. 126-135

Some Observations of Echolocation Clicks from Free-Swimming Dolphins in a Tank, by L.B. Poché, L.D. Luker, and P.H. Rogers, *Journal of the Acoustical Society of America* 71:1036-1038

The Fluorometric Determination of DNA in Aquatic Microorganisms Employing Hoechst 33258, by J.H. Paul and B. Myers,* *Applied and Environmental Microbiology* 43:1393-1399

The Kinetics of the Main Phase Transition of Aqueous Dispersions of Phospholipids Induced by Pressure Jump and Monitored by Raman Spectroscopy, by P. Yager and W.L. Peticolas,* *Biochimica et Biophysica Acta* 688:775-785

The Use of Hoechst Dyes 33258 and 33342 for Enumeration of Attached and Planktonic Bacteria, by J.H. Paul, *Applied and Environmental Microbiology* 43:939-944

CERAMICS, GLASSES AND PLASTICS

Advanced Ceramics for Optical and Electronic Appplications, by R.C. Pohanka* and P.L. Smith, *Naval Research Reviews* 34(4):36-45

Calculation of Thermal Expansion in Insulating and Ceramic Materials, by A.R. Ruffa, in *Thermal Expansion 7,* Plenum Press, New York, pp. 139-146

Comparison of Static, Cyclic and Thermal Shock Fatigue in Ceramic Composites, by D. Lewis and R.W. Rice, *Ceramic Engineering and Science Proceedings* 3:714-721

Damage Resistance of Fortified Surfaces of Cordierite-Based Crystallized Glass, by R.W. Rice, *Journal of the American Ceramic Society* 65:C-106—C-107

† **Fluoride Glass Preforms Prepared by a Rotational Casting Process,** by D.C. Tran, C.F. Fisher, and G.H. Sigel, Jr., *Electronics Letters* 18:657-658

Fracture Features at Internal Fracture Origins in a Commercial Crystallized Glass, by D. Lewis and J.R. Spann, *Journal of the American Ceramic Society* 65:C-173—C-174

Initial Characterization of Partially-Stabilized HfO_2 Single Crystals, by R.P. Ingel, D. Lewis, B.A. Bender, and R.W. Rice, *Ceramic Engineering and Science Proceedings* 3:577-586

Observations on the Strength of a Commercial Glass-Ceramic, by D. Lewis, *American Ceramic Society Bulletin* 61:1208-1214

Pressure-Temperature-Concentration Phase Diagram for $SbSI_xBr_{1-x}$, by Y. Porat, *Ferroelectrics Journal* 46:41-50

Raman Spectrum of Irradiated Zirconium Fluoride Glass, by K.H. Fiedler,* K.H.

Levin,* and D.C. Tran, *Physics and Chemistry of Glasses* 23:205-207

† **Rayleigh Scattering in ZrF_4-Based Glasses,** by D.C. Tran, G.H. Sigel, Jr., K.H. Levin,* and R.J. Ginther,* *Electronics Letters* 18:1046-1048

Refractory-Ceramic-Fiber Composites: Progress, Needs and Opportunities, by R.W. Rice, C.V. Matt,* W.J. McDonough, K.R. McKinney, and C.C. Wu, *Ceramic Engineering and Science Proceedings* 3:698-713

Residual Stresses and Scaling CNTD SiC to Large Sizes, by R.W. Rice and K.R. McKinney, *Journal of Materials Science Letters* 1:159-162

Room-Temperature Strength and Fracture of ZrO_2-Y_2O_3 Single Crystals, by R.P. Ingel,* R.W. Rice, and D. Lewis, *Journal of the American Ceramic Society* 65:C108-C109

Test-Microstructural Dependence of Fracture Energy Measurements in Ceramics, by R.W. Rice, in *Fracture Mechanics Methods for Ceramics, Rocks and Concrete,* ASTM, Philadelphia, Pennsylvania, ASTM STP 745, pp. 96-117

The Character of Cracks in Fracture Toughness Measurements of Ceramics, by C.C. Wu, R.W. Rice, and P.F. Becher,* in *Fracture Mechanics Methods for Ceramics, Rocks and Concrete,* ASTM, Philadelphia, Pennsylvania, ASTM STP 745, p. 127-140

Thermal Shock Testing of Optical Ceramics, by D. Lewis, in *Emerging Optical Materials,* SPIE, Bellingham, Washington, SPIE Vol. 297, pp. 120-124

CHEMISTRY

A Study of Some Epoxy Polymers for Underwater Acoustic Use, by C.M. Thompson and R.Y. Ting, in *Organic Coatings and Applied Polymer Science Proceedings,* American Chemical Society, Washington, D.C., Vol. 6, pp. 661-664

A Theoretical Study of the Ignition of Premixed Gases, by K. Kailasanath,* E.S. Oran, and J.P. Boris, *Combustion and Flame* 47:173-190

Alternative Antistatic Packaging Materials for Precision Bearings, by M.K. Bernett and H. Ravner, in *Innovation for Maintenance Technology Improvements,* National Bureau of Standards Special Publication 640, G.P.O., Washington, D.C., pp. 290-294

Amine-Cured Bisphenol-Linked Phthalonitrile Resins, by T.M. Keller and T.R. Price, *Journal of Macromolecular Science—Chemistry* A18:931-937

An Analysis of Thermal Expansion and Melting in Alkali Halides, by L.L. Boyer, in *Thermal Expansion 7,* Plenum Publishing Corp., New York, pp. 131-138

Antistatic Agents, Lubricants, and Precision Bearins, by M.K. Bernett and H. Ravner, *Lubrication Engineering* 38:481-486

AsF_5 Intercalated Graphite Conductivity and the Anisotropy of the Skin Depth via NMR Spectroscopy, by H.A. Resing, M.J. Moran, and G.R. Miller, *Journal of Chemical Physics* 76:1706-1707

Atom-Diatom Processes in Helium: The Multiple-Scattering Description of Elastic and Dissociative Collisions, by M.I. Haftel and T.K. Lim,* *Journal of Chemical Physics* 77:4515-4521

Automatic Log, Semi-Log and Linear Scaling and Plotting for Graphics 1000, by T.R. O'Neal, *Communicator 1000,* Vol. 5, No. 4

Catalytic Intermediates in the AgO_2 System. Evidence for a Nonsymmetric AgO_2 Molecule, by D.E. Tevault, R.R. Smardzewski, M.W. Urban,* and K. Nakemoto,* *Journal of Chemical Physics* 77:577-578

Catalytic Removal of NH and NH_2 Radicals by Polycrystalline Pt and Fe Surfaces, by G.S. Selwyn, G.T. Fujimoto, and M.C. Lin, *Journal of Physical Chemistry* 86:760-765

Changes in Electrode Microstructure and Charge Efficiency Produced by Pulsed Discharge of Electric Vehicle Lead Acid Batteries, by S. Caulder, A. Simon, and E. Dowgiallo,* in *1982 Intersociety Energy Conversion Engineering Conference,* IEEE, New York, pp. 616-619

Characterization of the Cure of Diether-Linked Phthalonitrile Resins, by R.Y. Ting, T.M. Keller, T.R. Price, and C.F. Poranski, in *Cyclopolymerization and Polymers with Chain-Ring Structures,* American Chemical Society, Washington, D.C., ACS Symposium Series No. 195, pp. 337-350

Charge Transfer Interaction and Electrical Conductivity of Poly(vinyl Acetals) Containing Dispersed TCNQ Radical Anion Salts, by O.K. Kim and R.B. Fox, *Journal of Polymer Science: Polymer Chemistry Edition* 20:2765-2772

Chemical Synthesis by Ion Implantation: Fluorine Intercalated Graphite, by D.C. Weber, P. Brant, M.J. Moran, C. Carosella, M.E. Preil, and J.E. Fischer, *Materials Research Bulletin* 17:749-755

Classical Approach to Third-Order Non-Linear Susceptibilities, by J.W. Fleming and A.B. Harvey, in *Non-Linear Raman Spectroscopy and its Chemical Applications,* D. Reidel Publishing Co., New York, pp.131-140

Combined XRD-XRF Improves Materials Characterization, by L.S. Birks, in *Recent Advances in Analytical Spectroscopy,* Pergamon Press, New York, pp. 27-31

^{13}C NMR of Solid Polymers and of Solids Related to Polymer Composites, by H.A. Resing, A.N. Garroway, D.C. Weber, J. Ferraris,* and D. Slottfeldt-Ellingsen, *Pure and Applied Chemistry* 54:595-610

Coupling Between the Nickel-Carbon and Carbon-Oxygen Stretch Motion in NiCO, by B.I. Dunlap, H.L. Yu,* and P.R. Antoniewicz,* *Physical Review A* 25:7-13

Crystal Chemistry of the Europium Arsenides, by F.L. Carter and L.D. Calvert,* in *Rare Earths in Modern Science and Technology,* Plenum Publishing Corp., New York, Vol. 3, pp. 351-352

Cyclopolymerization of Carbon Suboxide: Mechanism and Polymer Properties, by N.L. Yang, H. Haubenstock, and A.W. Snow, in *Cyclopolymerization and Polymers with Chain-Ring Structures,* American Chemical Society, Washington, D.C., ACS Symposium Series 195, pp. 417-442

Deterioration of Wooden Hull Planking by Cathodic Protection, by W.M. Strasburg,* M.H. Peterson, and J.E. Pinto,* *Materials Performance* 21 (9):14

Differential Scanning Calorimetry of Sodium and Potassium Nitrates and Nitrites, by C.M. Kramer, Z.A. Munir,* and J.V. Volponi,* *Thermochimica Acta* 55:11-17

Discrete and Quasicontinuum Level Fluorescence from Infrared Multiphoton Excited SF_6, by J.W. Hudgens and J.D. McDonald, *Journal of Chemical Physics* 76:173-188

Dynamics of CO Formation in the Photodissociation of HNCO and CH_2CO at 193 nm, by G.T. Fujimoto, M.E. Umstead, and M.C. Lin, *Chemical Physics* 65:197-203

Effect of Screening on the Carbon *KVV* Auger Line Shape of Alkali-Metal—Intercalated Graphite, by B.I. Dunlap, D.E. Ramaker, and J.S. Murday, *Physical Review B* 25:6439-6446

Efficient Baffles for Laser Light Scattering Experiments, by J.E. Butler, *Applied Optics* 21:3617-3618

Electrical Conductivity of Heteroaromatic Ladder Polymers, by O.K. Kim, *Journal of Polymer Science: Polymer Letters Edition* 20:663-666

Energy Transfer and Molecular Switching II. Muscle Contraction and Enzymatic Reactions, by T.W. Barrett, *Journal of Theoretical Biology* 99:293-307

Environmental Effects on Coating Materials for Use in Underwater Opto-Acoustic Detection Devices, by R.N. Capps and I.J. Bush, in *Organic Coatings and Applied Polymer Science Proceedings,* American Chemical Society, Washington, D.C., Vol. 46, pp. 619-624

Epoxy Resins Containing Fluorocarbon, by J.R. Griffith, *Chemtech* 12:290-293

EPR Spectra of NO_3 Radicals Produced by Photolysis of RDX Single Crystals, by M.D. Pace and W.B. Moniz, *Journal of Magnetic Resonance* 47:510-514

Evaluation of Environmental Effects on Candidate Polymeric Materials for Underwater Optoacoustic Sensors, by R.N. Capps, I.J. Bush, S.T. Lieberman, and S.E. Eveland, *I&EC Product Research and Development* 21:540-545

Fitting the Coulomb Potential Variationally in Linear-Combination-of-Atomic-Orbitals Density-Functional Calculations, by J.W. Mintmire* and B.I. Dunlap, *Physical Review A* 25:88-95

Formation of Vibrationally Excited C in the $(^1D_2) + C_2H_2$ Reaction, by W.M. Shaub,* T.L. Burks,* and M.C. Lin, *Journal of Physical Chemistry* 86:757-759

Fully-Converged Three-Dimensional Collision-Induced Dissociation Calculations with Faddeev-AGS Theory, by M.I. Haftel and T.K. Lim,* *Chemical Physics Letters* 89:31

Fundamentals of Ion Motion in Electric Radio-Frequency Multipole Fields, by M.H. Friedman,* A.L. Yergey,* and J.E. Campana, *Journal of Physics E:Scientific Instruments* 15:53-61

Homogeneous and Inhomogeneous Distribution of Correlation Times. Lineshapes for Chemical Exchange, by J.I. Kaplan* and

A.N. Garroway, *Journal of Magnetic Resonance* 49:464-475

Implantation into Covalent Polymeric Materials, by D.C. Weber, P. Brant,* and C.A. Carosella, in *Metastable Materials Formation by Ion Implantation,* North-Holland, New York, pp. 167-171

Infrared Reflectance Studies at Slipring Surfaces, by R.L. Mowery and R.R. Smardzewski, *Contamination Control* 4:8

Infrared Spectra of Silver Atom/Cluster Complexes with Pyridine and Their Relationship to the Surface Enhanced Raman Effect, by D.E. Tevault and R.R. Smardzewski, *Journal of Chemical Physics* 77:2221-2225

Interpretation of the Nitrogen *KVV* Auger Line Shape from Alkali Metal Nitrates, by F.L. Hutson,* D.E. Ramaker,* B.I. Dunlap,* J.D. Ganjei, and J.S. Murday, *Journal of Chemical Physics* 76:2181-2190

Kinetics of the Reactions of Methoxy and Ethoxy Radicals with Oxygen, by D. Gutman, N. Sanders,* and J.E. Butler, *Journal of Physical Chemistry* 86:66-70

Laser-Induced Emission Spectrum of CuO_2 in Argon Matrices, by D.E. Tevault, *Journal of Chemical Physics* 76:2859-2863

Light Scattering Studies of High Molecular Weight Hyaluronic Acid in Phosphate Buffer, by T.W. Barrett and J.E. Baxter, *Physiological Chemistry and Physics* 14:19-29

Magic-Angle Sample Spinning of Liquids, by A.N. Garroway, *Journal of Magnetic Resonance* 49:168-171

Marine Applications for Fluoropolymers, by J.R. Griffith, *Oceans '82 Conference Record,* IEEE, New York, pp. 541-543

Mass Spectrometry of Low-Dimensional Materials, by F.E. Saalfeld, J.J. DeCorpo, and J.R. Wyatt, in *Extended Linear Chain Compounds,* Plenum Publishing Corp., New York, Vol. 1, pp. 33-72

Measurement of the Rate Constant for Through Bridge Intra-Molecular Electron Transfer in the Intermediate of a Ru^{III} — Tl^{III} Redox Reaction Involving 3-Formylpentane-2,4-dionate as Bridging Ligand, by B.H. Berrie and J.E. Earley,* *Journal of the Chemical Society (London), Chemical Communications,* pp. 471-472

Metal Hydrides for Hydrogen Storage: A Review of Theoretical and Experimental Research, and Critically Compiled Data, by G.C. Carter* and F.L. Carter, in *Conference Proceedings of the Miami International Symposium on Metal-Hydrogen Systems,* pp. 503-529

Model Calculation of the Conformational Entropy of the High-Pressure Intermediate Phase of Polyethylene, by R.G. Priest, *Macromolecules* 15:1357-1364

Molecular Electronic Devices, ed., by F.L. Carter, Marcel Dekker, New York

Multiphoton Ionization and Fragmentation Mechanisms of CS_2, by M. Seaver,* J.W. Hudgens, and J.J. DeCorpo, *Chemical Physics* 70:63-68

Multiphoton Ionization of CH_3 Radicals in the Gas Phase, by T.G. DiGiuseppe, J.W. Hudgens, and M.C. Lin, *Journal of Physical Chemistry* 86:36-41

Multiphoton Ionization of the Trifluoromethyl Radical, by M.T. Duignan, J.W. Hudgens, and J.R. Wyatt, *Journal of Physical Chemistry* 86:4156-4161

New Electronic States in CH_3, Observed Using Multiphoton Ionization, by T.G. DiGiuseppe, J.W. Hudgens, and M.C. Lin, *Journal of Chemical Physics* 76:3337-3338

NMR Observations of Fluorine Ion-Implanted into Polyacetylene and Graphite, by L.G. Banks, H.A. Resing, D.C. Weber, C. Carosella, G.R. Miller, and P. Brant, *Journal of Physics and Chemistry of Solids* 43:351-355

NMR Study of Nylon 66 in Solution (^1H, ^{13}C, and ^{15}N NMR Using Adiabatic *J* Cross Polarization), by B.S. Holmes, W.B. Moniz, and R.C. Ferguson,* *Macromolecules* 15:129-132

On Auger Induced Decomposition/Desorption of Covalent and Ionic Systems, by D.E. Ramaker, C.T. White, and J.S. Murday, *Physics Letters* 89A:211-214

Photofragment Spectroscopy of HN_3 Cooled in a Supersonic Beam, by B.M. DeKoven and A.P. Baronavski, *Chemical Physics Letters* 86:392-396

Photofragment Spectroscopy of ICN at 266.0 nm and 299.4 nm: Vibrational and Rotational Distribution of $CN(X\ ^2\Sigma^+)$, by A.P. Baronavski, *Chemical Physics* 66:217-225

Photoreduction of Ytterbium and Samarium, by T. Donohue, in *The Rare Earths in Modern Science and Technology,* Plenum Publishing Corp., New York, Vol. 3, pp. 223-226

Polybutadiyne: Polymerization and Characterization, by A.W. Snow and J.R. Griffith, in

IUPAC, 28th Macromolecular Symposium, p. 432

Polymerization of Bisphthalonitriles. Metal-Free Phthalocyanine Formation, by N.P. Marullo and A.W. Snow, in *Cyclopolymerization and Polymers with Chain-Ring Structures*, American Chemical Society, Washington, D.C., ACS Symposium Series 195, pp. 325-336

Production of the NH Radical from the Catalytic Decomposition of NH_3 on Polycrystalline Pt and Fe Surfaces at High Temperatures, by G.S. Selwyn and M.C. Lin, *Chemical Physics* 67:213-220

Raman Spectroscopy of Avidin: Secondary Structure, Disulfide Conformation and the Environment of Tyrosine, by R.B. Honzato and R.W. Williams, *Biochemistry* 24:6201-6205

Rate of Self-Consistent-Field Convergence in the $X\alpha$ Method, by B.I. Dunlap, *Physical Review A* 25:2847-2849

Reaction of Benzyl Radical with O_2 and Cl_2, by H.H. Nelson and J.R. McDonald, *Journal of Physical Chemistry* 86:1242-1244

Reaction of $SF_5C \equiv CCF_3$ with Ni $(CO)_4$, by A.D. Berry and R.A. DeMarco, *Inorganic Chemistry* 21:457-458

Reactions of Free Radicals Produced by Laser Photolysis, by L. Pasternack, H.H. Nelson, and J.R. McDonald, *Journal of Chemical Education* 59:456-462

Reactions of Pd, Ni, and Cu Metals with Trifluoroacetic Anhydride, by D.E. Tevault, R.L. Mowery, R.A. DeMarco, and A.D. Berry, *Inorganica Chimica Acta* 60:59-66

Reactions of $SO_2(SO_3)$ with NiO-Na_2SO_4 in Nickel-Sodium Mixed Sulfate Formation and Low Temperature Hot Corrosion, by R.L. Jones and S.T. Gadomski, *Journal of the Electrochemical Society* 129:1613-1618

Relaxation Effects During Core Ionization in Metal-Metal Bonded Complexes, by P. Brant, *Journal of Electron Spectroscopy and Related Phenomena* 27:63-67

Resonance Raman Complete Polarization Studies of Ferrocytochrome C in the Long and Short Wavelength Regions: Evidence of Magnetic Resonance, by T.W. Barrett, *Journal of The Chemical Society (London), Chemical Communications* No. 789: 9-10

Secondary Ion Mass Spectrometry of Metal Halides. 2. Evidence for Structure in Alkali Iodide Clusters, by T.M. Barlak, J.R. Wyatt, R.J. Colton, J.J. DeCorpo, and J.E. Campana, *Journal of the American Chemical Society* 104:1212-1215

Solitons and SP^3 Defects in Trans-Polyacetylene, by F.L. Carter, *Polymeres Electroactifes*, Proceedings of Ecole d'Hever, Font-Romere- CNRS Montpellier, Tome II, p. 146

Solubility of Yttrium Oxide in Na_2SO_4 and NaCl Melts, by M.L. Deanhardt* and K.H. Stern, *Journal of the Electrochemical Society* 129:2228-2232

† **Some Molecular Motions in Epoxy Polymers: $A^{13}C$ Solid-State NMR Study,** by A.N. Garroway, W.M. Ritchey,* and W.B. Moniz, *Macromolecules* 15:1051-1063

Summary Abstract: On the Formation and Emission of Polyatomic Secondary Ions from Metal Salts, by R.J. Colton, T.M. Barlak, J.R. Wyatt, J.J. DeCorpo, and J.E. Campana, *Journal of Vacuum Science and Technology* 20:421-422

Summary Abstract: Evidence for Screening Effects in the Carbon *KVV* Auger Lineshape of Intercalated Graphite, by B.I. Dunlap, D.E. Ramaker, and J.S. Murday, *Journal of Vacuum Science and Technology* 20:900-901

Summary Abstract: High-Performance Molecular Secondary Ion Mass Spectroscopy (SIMS), by J.E. Campana, T.M. Barlak, J.R. Wyatt, J.J. DeCorpo, and R.J. Colton, *Journal of Vacuum Science and Technology* 20:1068-1069

Summary Abstract: Initial and Final State Screening Effects on the Auger Lineshapes of Silicon, by D.E. Ramaker,* W.N. Mei,* and N.H. Turner, *Journal of Vacuum Science and Technology* 20:563-564

Summary Abstract: Model Study of the Effects of Correlations on the *XVV*-Auger Lineshape of Chemisorbed Species, by C.T. White, J.W. Mintmire, and E.N. Economou,* *Journal of Vacuum Science and Technology* 20:565-566

Surface Analysis of Bearing Steels After Solvent Treatments. II. Lubricant-Coated Bearing Surfaces, by M.K. Bernett and H. Ravner, *American Society of Lubrication Engineers Transactions* 25:55-63

Surface Analysis: X-Ray Photoelectron Spectroscopy, Auger Electron Spectroscopy, and Secondary Ion Mass Spectrometry, by N.H. Turner and R.J. Colton, *Analytical Chemistry* 54:293R-322R

Surface Raman Scattering from Effervescent Magnetic Peroxyborates, by G.E. Walrafen,* P.N. Krishnan,* M.* Hokmabadi,* D.L. Griscom, and R.G. Munro,* *Journal of Chemical Physics* 77:3840-3846

Surface-Enhanced Raman Spectra of Benzene and Benzene-d_6 on Vapor-Deposited Sodium, by P.A. Lund, R.R. Smardzewski, and D.E. Tevault, *Chemical Physics Letters* 89:508-510

Temperature Dependence of C_3 ($X\ ^1\Sigma_g^+$) Reactions with Alkenes and Alkynes, 295-610 K, by H.H. Nelson, H. Helvajian, L. Pasternack, and J.R. McDonald, *Chemical Physics* 73:431-438

Temperature Dependence of the C_2 ($X\ ^1\Sigma_g^+$) Reaction with H_2 and CH_4 and C_2 ($X\ ^1\Sigma_g^+$ and a $^3\Pi_u$ Equilibrated States) with O_2, by W.M. Pitts and J.R. McDonald, *Chemical Physics* 68:417-422

Temperature Dependence of the Reactions of CH Radicals with Unsaturated Hydrocarbons, by M.R. Berman, J.W. Fleming, A.B. Harvey, and M.C. Lin, *Chemical Physics* 73:27-33

The Metamagnetic Properties of Hemoglobin, by T.W. Barrett, *Physics Letters* 91A:139-142

The Role of Electrodynamic Interactions on Energy Loss Intensities of Adsorbed Molecules, by P.R. Antoniewicz* and B.I. Dunlap, *Surface Science* 114:272-286

The Role of Optimum Dielectric Saturation in the Reversible Combination of Oxygen with Heme Fe^{2+} and the Tuning of Paramagnetic-Diamagnetic Switching, by T.W. Barrett, *Physics Letters* 92A:309-314

The Solubility of Manganese Oxide in Molten Sodium Chloride and Sodium Sulfate, by L.M. Deanhardt, K.H. Stern, and S.R. Wolff,* *Inorganic Chemistry* 21:2511-2512

(Trifluoroacetyl)sulphur Pentafluoride, by R.A. DeMarco and W.B. Fox, *Journal of Organic Chemistry* 47:3772-3773

Valence Bonding, Atomic Volumes, and Coordination Numbers for Y_6Mn_{23}, Th_6M_{23}, and Their Hydrides, by F.L. Carter, in *Rare Earths in Modern Science and Technology,* Plenum Publishing Corp., New York, Vol. 3, pp. 479-480

Watch your Language! by R.B. Fox and K.L. Loening,* *Chemical and Engineering News* 60:51

Weak and Strong Ignition I. Numerical Simulations of Shock Tube Experiments, by E.S. Oran, T.R. Young, J.P. Boris, and A. Cohen,* *Combustion and Flame* 48:135-148

Weak and Strong Ignition II. Sensitivity of the Hydrogen-Oxygen System, by E.S. Oran and J.P. Boris, *Combustion and Flame* 48:149-161

$Xe(^3P_2)$ + HCl ($v = 1$): Vibrational Enhancement of XeCl* Formation, by R.S.F. Chang, *Journal of Chemical Physics* 76:2943-2948

COMMUNICATIONS

A Conversational Test for Comparing Voice Systems Using Working Two-Way Communication Links, by A. Schmidt-Nielsen and S.S. Everett, in *IEEE Transactions on Acoustics, Speech, and Signal Processing* ASSPP-30:853-863

A Distributed Algorithm for Scheduling the Activation of Links in a Self-Organizing, Mobile, Radio Network, by D.J. Baker, J. Wieselthier, and A. Ephremides,* in *IEEE International Conference on Communications, ICC'82, The Digital Revolution,* IEEE, New York, pp. 2F.6.1-2F.6.5

Analysis of a Hybrid Access Scheme for Buffered Users—Probabilities Time Division, by A. Ephremides and O.A. Mowafi,* *IEEE Transactions on Software Engineering* SE-8:52-61

Discrete Utterance Speech Recognition Without Time Normalization, by J.E. Shore and D. Burton, in *IEEE International Conference on Acoustics, Speech, and Signal Processing (ICASSP82),* IEEE, New York, pp. 907-910

Discrete Utterance Speech Recognition Without Time Normalization—Recent Results, by J.E. Shore and D. Burton, in *Proceedings of the 6th International Conference on Pattern Recognition,* IEEE, New York, pp. 582-584

Distributed Network Reconfiguration in Response to Jamming at HF, by D.J. Baker, J.E. Wielselthier, A. Ephremides, and D.H. McGregor, in *1982 IEEE Military Communications Conference, Progress in Spread Spectrum Communications,* IEEE, New York, Vol. 1, pp. 23.2-1—23.2-7

Experimental Investigation of Ambient Electromagnetic Noise from 1.0 to 4.0 kHz in Italy and Norway, by R.J. Dinger, W.D. Myers, and J.R. Davis, *Radio Science* 17:285-302

Linear Wideband HF Power Amplifier Using Adaptive Feedforward Cancellation, by D.C. Andrews, E.E. Parr, T.E. Olver,* and B.S. Abrams,* in *1982 IEEE Military Communica-*

tions Conference, Progress in Spread Spectrum Communications, IEEE, New York, Vol. 1, pp. 21.6-1—21.6-8

Spread Spectrum Multiple Access Issues in the HF Intra Task Force Communication Network, by J.E. Wieselthier, in *Proceedings of the Fifth MIT/ONR Workshop on C³ Systems,* pp. 239-246

The Perception of Voice Pitch Waver over Headphones and Loudspeakers, by A. Schmidt-Nielsen and S.S. Everett, *Journal of the Acoustical Society of America* 72:1299-1302

U.S.S. Pomonkey—An HF Communication System Test Facility, by R.K. Royce, in *IEEE 1982 Antennas and Propagation International Symposium Digest,* IEEE, New York, pp. 394-397

COMPUTER SCIENCES

Computers in Oceanography—Tradeoffs and Trends, by L.J. Rosenblum and J.D. Clamons, in *Oceans '82 Conference Record,* IEEE, New York, pp. 302-306

Magnetostriction Measurements on the Mixed Valence Compound $CeSn_3$, by A.S. Edelstein and N.C. Koon, *Journal of Applied Physics* 53:7899-7901

Picture Information Measures for Similarity Retrieval, by C.C. Yang and S.K. Chang,* in *Proceedings of Computer Software and Applications Conference,* IEEE, New York, pp. 464-469

Rapid Prototyping by Means of Abstract Module Specifications Written as Trace Axioms, by J.K. Dixon, J. McLean, and D.L. Parnas, *SIGSOFT Software Engineering Notes* 7(5):45-50

The Use of Quick Prototype in the Secure Military Message Systems Project, by C.L. Heitmeyer, C.E. Landwehr, and M. Cornwell, *SIGSOFT Software Engineering Notes* 7(5):85-88

Using Formal Specifications in the Design of a Human-Computer Interface, by R.J.K. Jacob, in *Proceedings of the Human Factors in Computer Systems Conference,* pp. 315-321

ELECTRONICS AND ELECTRICITY

A High Power Gyrotron Operating in the TE_{041} Mode, by B. Arfin, K.R. Chu, D. Dialetis,* and M.E. Read, *IEEE Transactions on Electron Devices* ED-29:1911-1916

A New Failure Mechanism in Thin Gold Films at Elevated Temperatures, by D.J. LaCombe,* D.C. Dening,* and A. Christou, in *IEEE 1982 International Reliability Physics Symposium,* IEEE, New York, pp. 81-87

A Small Dual Band Satcom Antenna for X- and Q-Band, by S.J. Lin,* B.A. Munk,* S. Nichols, and R. Brown, in *IEEE 1982 Antennas and Propagation International Symposium Digest,* IEEE, New York, pp. 483-486

A Three-Cavity Gyroklystron Amplifier Experiment, by B. Arfin and A.K. Ganguly, *International Journal of Electronics* 53:709-714

Dual-Frequency Microwave Backscatter from the Ocean at Low Grazing Angles: Comparison with Theory, by D.L. Schuler, W.J. Plant, W.P. Eng, W. Alpers,* and F. Schlude,* *International Journal of Remote Sensing* 3:363-371

Experimental Examination of the Enhancement of Gyrotron Efficiencies by Use of Profiled Magnetic Fields, by M.E. Read, K.R. Chu, and A.J. Dudas,* *IEEE Transactions on Microwave Theory and Techniques* MTT-30:42-46

† **Fabrication of Surface-Channel Charge-Coupled Devices With Ultralow Density of Interface States,** by N.S. Saks, *Applied Physics Letters* 41:737-739

Fluxon Propagation in Josephson Junction Transmission Lines Coupled by Resistive Networks, by H.S. Newman and K.L. Davis, *Journal of Applied Physics* 53:7026-7032

Frequency Doublers with GaAs FET's, by C. Rauscher, in *1982 IEEE MTT-S International Microwave Symposium Digest,* IEEE, New York, pp. 280-282

Gain and Bandwidth of a Gyrotron Amplifier with Tapered Rectangular Waveguide, by S. Ahn, *International Journal of Electronics* 53:673-679

High Recovery Voltage Switch for Interruption of Large Currents, by R.D. Ford and I.M. Vitkovitsky, *Review of Scientific Instruments* 53:1098-1100

Increased Ferrimagnetic Echo Bandwidth Using Field Gradient Synthesis, by F. Bucholtz and D.C. Webb, in *1982 IEEE Ultrasonics Symposium Proceedings,* IEEE, New York, pp. 547-550

Interface State Trapping and Dark Current Generation in Buried-Channel Charge-Coupled Devices, by N.S. Saks, *Journal of Applied Physics* 53:1745-1753

Long-Term Transient Radiation-Resistant GaAs FET's, by W.T. Anderson, M. Simons,* E.E. King,* H.B. Dietrich, and R.J. Lambert, *IEEE Electron Device Letters* **EDL-3**:248-250

Modal Radiation Efficiency for Spherical-Cap Microstrip Antenna, by C.M. Krowne, in *IEEE 1982 Antennas and Propagation International Symposium Digest,* IEEE, New York, pp. 168-170

Multilayer Frequency Sensitive Surfaces of Tripoles, by L.W. Henderson,* B.A. Munk,* S. Nichols, and R. Brown, in *IEEE 1982 Antennas and Propagation International Symposium Digest,* IEEE, New York, pp. 459-462

Niobium Nitride-Niobium Josephson Tunnel Junctions with Sputtered Amorphous Silicon Barriers, by D.W. Jillie,* H. Kroger,* L.N. Smith,* E.J. Cukauskas, and M. Nisenoff, *Applied Physics Letters* **40**:747-750

Nonlinear Analysis of the Solid-State Gyrotron Oscillator with Monte Carlo Method, by A.K. Ganguly, B.J. Hui, and K.R. Chu, *IEEE Transactions on Electron Devices* **ED-29**:1197-1209

Notched InP Planar Transferred Electron Oscillators, by S.C. Binari, H.L. Grubin,* and P.E. Thompson, in *International Electron Devices Meeting,* IEEE, New York, pp. 770-773

Operating Characteristics of Thin Thermophotovoltaic Cells with Minority Carrier Mirrors and Optical Mirrors, by E.S. Vera,* J.J. Loferski,* M. Spitzer,* and J.G. Severns, in *Proceedings of the 4th E.C. Photovoltaic Solar Energy Conference,* p. 659

Prediction of Solar Cell Performance in Space, by R.L. Statler and D.H. Walker, in *Sixteenth IEEE Photovoltaic Specialists Conference,* IEEE, New York, pp. 301-306

Radiation Efficiency for Spherical-Rectangular Microstrip Antenna, by C.M. Krowne and K.Y. Wu,* in *IEEE 1982 Antennas and Propagation International Symposium Digest,* IEEE, New York, pp. 171-174

Radio Frequency Current Generation by Waves in Toroidal Geometry, by T.M. Antonen* and K.R. Chu, *Physics of Fluids* **25**:1295-1296

Self-Consistent Large Signal Theory of the Gyrotron Travelling Wave Amplifier, by A.K. Ganguly and S. Ahn, *International Journal of Electronics* **53**:641-658

Self-Consistent Non-Linear Theory of TWT Gyrotron, by A.K. Ganguly and S.Y. Ahn, in *IEEE International Electron Devices Meeting 1982, Technical Digest,* IEEE, New York, p. 379

Silicon Field Emitter Array Technology, by H.F. Gray, in *Proceedings of the 29th Full Emission Symposium,* pp. 111-118

Slow Wave Gyrotron Amplifier with a Dielectric Center Rod, by J.Y. Choe,* H.S. Uhm,* and S. Ahn, *IEEE Transactions on Microwave Theory and Techniques* **MTT-30**:700-707

GEOSCIENCES

Deformations of an Elastic Earth, by P. Lanzano, Academic Press, New York

INSTRUMENTATION

A New High Speed Photographic System for Experimental Mechanics, by J.W. Dally* and R.J. Sanford, *Mechanics Research Communications* **9**:337-341

A Precision Measuring Microscope Employing Laser Interferometry, by J.H. Adams, L.P. Beahm, and B. Stiller, in *Solid State Nuclear Track Detectors,* Pergamon Press, New York, pp. 915-918

A Scanning CARS Microscope, by M.D. Duncan, J. Reintjes, and T.J. Manuccia, *Applied Physics* **B28**:242-243

An Image Drift Compensation System for a Solar Pointed Space Telescope, by J.D.F. Bartoe, *Astrophysics and Space Science* **84**:115-132

Apparatus for Adapting a High-Pressure Light Scattering Cell to Density Measurement, by M. Abebe* and P.E. Schoen, *Journal of Applied Physics* **53**:3297-3298

Microchannel-Intensified Electrography, by H.M. Heckathorn and G.R. Carruthers, in *Instrumentation in Astronomy IV,* SPIE, Bellingham, Washington, SPIE Vol. 331, pp. 415-426

New Look at Solder-Sealed Liquid Helium Cryostats, by J.H. Claassen, *Review of Scientific Instruments* **53**:913-914

Pneumatic Driver for Diamond Anvil Cells, by A.A. Webb and S.B. Qadri, *Review of Scientific Instruments* **53**:1796-1797

†**Scanning Coherent Anti-Stokes Raman Microscope,** by M.D. Duncan, J.F. Reintjes, and T.J. Manuccia, *Optics Letters* **7**:350-352

Sensitive, High-Speed Thermometry Using Optical Fibers, by G.S. Maurer, J.H. Cole, and J.A. Bucaro, *Optics Letters* **7**:561-562

LASER SCIENCE

A Quantum Approach to Realizable Wigglers of Free-Electron Lasers, by W.W. Zachary, *Physics of Quantum Electronics* 9:1009-1012

Axial Magnetic-Field Effects in a Collective-Interaction Free-Electron Laser at Millimeter Wavelengths, R.K. Parker, R.H. Jackson,* S.H. Gold, H.P. Freund,* V.L. Granatstein, P.C. Efthimion, M. Herndon, and A.K. Kinkead, *Physical Review Letters* 48:238-242

Book Review: High-Peak-Power Nd:Glass Laser Systems, by David C. Brown, by J.M. McMahon, *IEEE Journal of Quantum Electronics* QE-18:931

Broadband CARS Probe Using the Picosecond Continuum, by L.S. Goldberg, in *Picosecond Phenomena III*, Springer-Verlag, New York, p. 94

Continuous Tuning of a Color-Center Laser Between 2 and 4 μm, by I. Schneider, *Optics Letters* 7:271-273

Correlation of Low-Frequency Intensity and Frequency Fluctuations in GaAlAs Lasers, by A. Dandridge and H.F. Taylor, *IEEE Journal of Quantum Electronics* QE-18:1738-1750

Current-Induced Frequency Modulation in Diode Lasers, by A. Dandridge and L. Goldberg, *Electronics Letters* 18:302-304

Degenerate Four-Wave Mixing in a XeCl Amplifier, by B.L. Wexler, L.J. Palumbo, J. Reintjes, and N. Djeu, *Applied Physics* B28:159-160

Design Considerations of a Compton Scattering Free-Electron Laser with an Axial Electric Field, by A. Gover,* C.M. Tang, and P. Sprangle, *Physics of Quantum Electronics* 9:795-813

Energy Carried over the Rectangular Spot Within a Hermite-Gaussian Beam, by W.H. Carter, *Applied Optics* 21:7

Experimental Study of Axial Magnetic Field Effects on the Operation of a Millimeter-Wave Free-Electron Laser, by S.H. Gold, R.H. Jackson,* R.K. Parker, H.P. Freund,* V.L. Granatstein, P.C. Efthimion,* M. Herndon, and A.K. Kinkead, *Physics of Quantum Electronics* 9:741-757

Feasibility of dc to Visible High-Power Conversion Employing a Stimulated Compton Free Electron Laser With a Waveguided CO_2 Laser Pump Wave and an Axial Electric Field, by A. Gover,* C.M Tang, and P. Sprangle, *Journal of Applied Physics* 53:124-129

FM Sideband Injection Locking of Diode Lasers, by L. Goldberg, H.F. Taylor, and J.F. Weller, *Electronics Letters* 18:1019-1020

†**Focal Shift and Concept of Effective Fresnel Number for a Gaussian Laser Beam**, by W.H. Carter, *Applied Optics* 21:1989-1994

Formulation of Normalized Nonlinear Free Electron Laser Equations, by C.M. Tang and P. Sprangle, *Journal of Applied Physics* 53:831-839

Free Electron Lasers. Millimeter and Submillimeter Lasers, by V.L. Granatstein, R.K. Parker, and P.A. Sprangle, in *CRC Handbook of Laser Science and Technology*, Vol. 1, *Lasers and Masers*, CRC Press, Inc., Boca Raton, Florida, pp. 441-453

Locking Bandwidth Asymmetry in Injection-Locked GaAlAs Lasers, by L. Goldberg, H.F. Taylor, and J.F. Weller, *Electronics Letters* 18:986-987

Measurement of Rear Surface Temperatures of Laser-Irradiated Thin Transparent Targets, by S.H. Gold and E.A. McLean, *Journal of Applied Physics* 53:784-786

Phase Conjugation in Saturable Amplifiers by Degenerate Frequency Mixing, by J. Reintjes and L.J. Palumbo, *IEEE Journal of Quantum Electronics* QE-18:1934-1940

Phase Sensitivity and Linewidth Narrowing in a Fox-Smith Configured Semiconductor Laser, by S.J. Petuchowski, R.O. Miles, A. Dandridge, and T.G. Giallorenzi, *Applied Physics Letters* 40:302-304

Picosecond Photofragmentation Experiments with a Repetitively Pulsed Mode-Locked Nd:Phosphate Glass Laser System, by L.S. Goldberg, M.J. Marrone, and P.E. Schoen, in *Picosecond Lasers and Applications*, SPIE, Bellingham, Washington, SPIE Vol. 322, pp. 199-205

Potential Characteristics and Applications of X-Ray Lasers, by D.J. Nagel, in *Advances in X-Ray Spectroscopy*, Pergamon Press, New York, Chapter 20, pp. 371-410

Progress and Trends in X-Ray Laser Research, by R.C. Elton, *Optical Engineering* 21:307-312

Repetitively Pulsed Mode-Locked Nd:Phosphate Glass Laser Oscillator-Amplifier System,

by L.S. Goldberg, P.E. Schoen, and M.J. Marrone, *Applied Optics* 21:1474-1477

Spectral Characteristics of Semiconductor Lasers with Optical Feedback, by L. Goldberg, H.F. Taylor, A. Dandridge, J.F. Weller, and R.O. Miles, *IEEE Journal of Quantum Electronics* QE-18:555-564

Stimulated Electromagnetic Shock Radiation in the Visible? by L. Cohen, N. Seeman, and K. Murray, in *Conference on Lasers and Electro-Optics, Digest of Technical Papers,* IEEE, New York, p. 74

The Effect of an Axial Guide Field on Free-Electron Lasers, by H.P. Freund,* P. Sprangle, D. Dillenburg,* E.H. da Jornada,* B. Liberman,* and R.S. Schneider,* *Physics of Quantum Electronics* 9:759-793

The Effect of Fluctuating Space-Charge Fields on Sideband Instabilities in Free-Electron Lasers, by H.P. Freund,* P. Sprangle, and C.M. Tang, *Physical Review A* 25:3121-3129

The Effect of Space Charge Fields due to Finite Length Electron Beams in the Free-Electron Laser, by C.M. Tang, H. Freund,* P. Sprangle, and W. Colson,* *Physics of Quantum Electronics* 8:503-514

The Nonlinear Aspects of Hydrodynamic Instabilities in Laser Ablation, by M.H. Emery, J.H. Gardner, and J.P. Boris, *Applied Physics Letters* 41:808-810

The Three-Dimensional Non-Linear Theory of the Free Electron Laser, by C.M. Tang and P. Sprangle, *Physics of Quantum Electronics* 9:627-650

Third Harmonic Conversion with a Focused Beam in an Infinite Medium with Positive Dispersion, by J. Reintjes, M. Diabel, and L.L. Tankersley,* in *Laser Techniques for Extreme Ultraviolet Spectroscopy,* American Institute of Physics, New York, AIP Conference No. 90, p. 491

Transient Optical Absorption in the UV, by L.F. Champagne, in *Gas Lasers,* Academic Press, New York, pp. 349-386

200-MHz Electrodeless Discharge Excitation of an XeF Laser, by C.P. Christensen,* and R.W. Waynant, *Applied Physics Letters* 41:794-796

Vacuum Ultraviolet Laser Emission from Nd^{+3}: LaF_3, by R.W. Waynant, *Applied Physics* B28:205

X-Ray Lasers, by R.C. Elton, in *CRC Handbook of Laser Science and Technology,* Vol. 1, *Lasers and Masers,* CRC Press, Inc., Boca Raton, Florida, pp. 455-460

MAGNETISM

Abstract: Theory of Ferromagnetic Resonance and Static Magnetization in Ultra-Thin Crystals, by G.T. Rado, *Journal of Applied Physics* 53:2110

Clarification of the Different Roles of Surface Anisotropy for Thermal Spin Waves and FMR Modes, by G.T. Rado and J.C. Walker,* *Journal of Applied Physics* 53:8055-8057

Composition Dependence of the Coercive Force and Microstructure of Crystallized Amorphous $(Fe_xB_{1-x})_{0.9}Tb_{0.05}La_{0.05}$ Alloys, by N.C. Koon, B.N. Das, and J.A. Geohegan, *IEEE Transactions on Magnetics* MAG-18:1448-1450

Ferromagnetic Resonance Studies of Very Thin Epitaxial Single Crystals of Iron, by J.J. Krebs, F.J. Rachford, and P. Lubitz, *Journal of Applied Physics* 53:8058-8060

Ground State Spin Excitations in $HoAl_2$, by J.J. Rhyne* and N.C. Koon, *Journal of Applied Physics* 53:8354-8356

Low Field Magnetic Properties of Amorphous $(Fe_yB_{1-y})_{1-2x}RE_xLa_x$ Alloys, by J.A. Geohegan, N.C. Koon, and B.N. Das, *Journal of Applied Physics* 53:7816-7818

Magnetic Properties of Single-Crystal (110) Iron Films Grown on GaAs by Molecular Beam Epitaxy, by G.A. Prinz, G.T. Rado, and J.J. Krebs, *Journal of Applied Physics* 53:2087-2091

Microwave Resonance and Propagation in Nonsaturated Ferromagnetic Media I. Magnetic Resonance in Single Crystal Ferrite Platelets, by F.J. Rachford, P. Lubitz, and C. Vittoria, *Journal of Applied Physics* 53:8940-8951

Microwave Resonance and Propagation in Nonsaturated Ferromagnetic Media II. Electromagnetic Wave Propagation in Uniaxially Anisotropic Insulators in Metals, by C. Vittoria and F.J. Rachford, *Journal of Applied Physics* 53:8952-8960

On Poynting's Theorem and Sources, by J.W. Butler, *Annales de la Fondation Louis de Broglie* 7:167

Theory of Ferromagnetic Resonance and Static Magnetization in Ultrathin Crystals, by G.T. Rado, *Physical Review B* 26:295-304

Verification of First-Order Magnetic Phase Transition in Single Crystal Iron Films, by F.J. Rachford, G.A. Prinz, J.J. Krebs, and K.B. Hathaway,* *Journal of Applied Physics* 53:7966-7968

MATHEMATICS

A Nonstandard Infinite Dimensional Vector Space Approach to Gaussian Functional Measures, by L.M. Pecora, *Journal of Mathematical Physics* 23:969-982

Asymptotic Properties of a State Density Approximation for Optimal Control, by W.W. Willman, in *Proceedings of the 1982 American Control Conference,* IEEE, New York, pp. 699-704

Explicit Time Integration for the Finite Element Shock Wave Equations, by E.W. Miner and R.A. Skop, in *AIAA/ASME 3rd Joint Thermophysics, Fluids, Plasm, and Heat Transfer Conference,* AIAA, New York, pp. 1-9

Factorization Theory of Meromorphic Functions and Related Topics, ed. by C.C. Yang, Marcel Dekker, Inc., New York

Further Results on the Fix-Points of Composite Transcendental Entire Functions, by C.C. Yang, *Journal of Mathematical Analysis and Applications* 90:259-269

On Common Right Factors of F and $F^{(N)}$, by N. Steinmetz* and C.C. Yang, in *Factorization Theory of Meromorphic Functions and Related Topics,* Marcel Dekker, Inc., New York, pp. 129-138

Progress in Factorization Theory of Entire and Meromorphic Functions, by C.C. Yang, in *Factorization Theory of Meromorphic Functions and Related Topics,* Marcel Dekker, Inc., New York, pp. 171-192

Reconstruction from Partial Information with Applications to Tomography, by C.L. Byrne and R.M. Fitzgerald, *SIAM Journal of Applied Mathematics* 42:933-940

Relaxation Processes and Time-Scale Transformations, by S. Teitler, A.K. Rajagopal,* and K.L. Ngai, *Physical Review A* 26:2906-2912

Repairable System Reliability: Future Research Topics, by H. Ascher and H. Feingold,* in *Reliability in Electrical and Electronic Components and Systems, EUROCON'82,* pp. 81-88

Scattering by Periodic Surfaces, by A.W. Saenz, *Journal of Mathematical Physics* 23:1115-1122

The Cavity *Q* for Ergodic Eigenmodes, by E. Ott* and W.M. Manheimer, *Physical Review A* 25:1808-1810

The Rayleigh-Taylor and Kelvin-Helmholtz Instabilities in Targets Accelerated by Laser Ablation, by M.H. Emery, J.H. Gardner, and J.P. Boris, *Physical Review Letters* 48:677-680

Time-Dependent Simulation of Flames Hydrogen-Oxygen-Nitrogen Mixtures, K. Kailasanath,* E.S. Oran, and J.P. Boris. *Numerical Methods in Laminar Flame Propagation,* Vieweg, Braunschweig, Germany, 152-166

MECHANICS

Antiplane Eigenstrain Problem of an Elliptic Inclusion in an Anisotropic Half Space, by R.A. Masumura and Y.T. Chou,* *Journal of Applied Mechanics* 104:52-54

Effect of Higher-Order Stress Terms on Model-I Caustics in Birefringent Materials, by J.W. Phillips* and R.J. Sanford, in *Fracture Mechanics: Thirteenth Conference,* ASTM, Philadelphia, Pennsylvania, ASTM STP 743, pp. 387-402

Horizontal and Vertical Cylinders in Waves, by S.E. Ramberg and J.M. Niedzwecki,* *Ocean Engineering* 9:1-15

Method for Analysis of Guyed Towers, by F. Rosenthal and R.A. Skop, *Journal of the Structural Division, Proceedings of the American Society of Civil Engineers* 108:543-558

On A Study of the Use of the (T) Integral in Fracture Analysis of Solids with Inelastic Rate-Constitutive Laws, by M. Nakagaki and S.N. Atluri,* *Journal of Pressure Vessel Technology, Transactions of the ASME* 104:331-337

On the Relativistic Definition of Spin, by I. Manning, in *Physics as Natural Philosophy. Essays in Honor of Laszlo Tisza on His Seventy-fifth Birthday,* MIT Press, Cambridge, Massachusetts, pp. 263,269

Vibrations of Inclined Slack Cables, by S.E. Ramberg and C.L. Bartholomew, *Journal of the Structural Division, Proceedings of the American Society of Civil Engineers* **108**:1662-1664

METALLURGY

A Comparison of Microstructural Effects on Fatigue-Crack Initiation and Propagation in Ti-6Al-4V, by G.R. Yoder, L.A. Cooley, and T.W. Crooker, in *23rd Structures, Structural Dynamics and Materials Conference,* AIAA, New York, pp. 132-136

A New Magnetic Amorphous Alloy System: (Fe,Co)-Bismuth, by D.W. Forester, J.V. Schelleng, P. Lubitz, P. D'Antonia, and C. George, *Journal of Applied Physics* **53**:2240-2242

Automated Data Reduction from Transmission Electron Micrographs, by J.A. Sprague, in *Advanced Techniques for Characterizing Microstructures,* Metallurgical Society of AIME, Warrendale, Pennsylania, pp. 53-69

Corrosion Rates and Electrochemical Studies of a Depleted Uranium Alloy Tungsten Fiber Metal Matrix Composite, by P.P. Trzaskoma, *Journal of the Electrochemical Society* **129**:1398-1402

Corrosion Resistance of Austenitic Fe-Cr-Ni-Mo Alloys in Marine Environments, by A.J. Sedriks, *International Metals Reviews* **27**:321-353

† **Creep Crack Growth Behavior and Theoretical Modelling,** by K. Sadananda and P. Shahinian, *Metal Science* **15**:440-455

Deformation Microstructure Developed During Fatigue Crack Propagation in Type 316 Stainless Steel at 593°F, by D.J. Michel and H.H. Smith, in *Effects of Radiation on Materials: Proceedings of the Eleventh International Symposium,* ASTM, Philadelphia, Pennsylvania, ASTM STP 782, pp. 690-700

Deformation Produced by Elevated Temperature Fatigue Crack Propagation in Type 316 Stainless Steel, by G.R. Evers, H.H. Smith, and D.J. Michel, *Metallography* **15**:409-422

Effect of Ion Implantation on Fretting Fatigue in Ti-6Al-4V Alloy, by R.G. Vardiman, D. Creighton, G. Salivar,* A. Effatian,* and B.B. Rath, in *Materials Evaluation Under Fretting Conditions,* American Society for Testing and Materials, Philadelphia, Pennsylvania, ASTM STP 780, pp. 138-149

Effect of Laser-Surface Melting On the Electrochemical Behavior of an Al-1% Mn Alloy, by E. McCafferty, P.G. Moore, and G.T. Peace, *Journal of the Electrochemical Society* **129**:9-17

Effects of Environment and Internal Hydrogen on the Sustained Load Cracking of Ti-6211, by R.W. Judy, J.E. Cox, and B.B. Rath, in *Micro and Macro Mechanics of Crack Growth,* Metallurgical Society of AIME, Warrendale, Pennsylvania, pp. 83-95

Effects of Irradiation on Fatigue and Creep-Fatigue Crack Propagation, by D.J. Michel, in *Micro and Macro Mechanics of Crack Growth,* Metallurgical Society of AIME, Warrendale, Pennsylvania, pp. 185-198

Environmental Effects on Fatigue, by P. Shahinian and K. Sadananda, in *Pressure Vessels and Piping: Design Technology—1982. A Decade of Progress,* ASME, New York, pp. 519-532

Formation of Multifilamentary V_3Ga with V-5 to -7 Atomic Percent Ga Alloys, by C.R. Spencer,* E. Adam,* E. Gregory,* F.T. Ormand,* and D.G. Howe, in *Advances in Cryogenic Engineering Materials,* Plenum Publishing Corp., New York, Vol. 28, pp. 471-481

Fractographic and Microstructural Analyses of Stress Corrosion Cracking in HY-130 Weldments, by F.W. Fraser and E.A. Metzbower, *Welding Journal* **61**:112s-116s

High Temperature Near-Threshold Fatigue Behaviour, by P. Shahinian and K. Sadananda, in *Fatigue Thresholds,* EMAS, West Midlands, UK, Vol. D, pp. 527-546

High Temperature Time-Dependent Crack Growth, by K. Sadananda and P. Shahinian, in *Micro and Macro Mechanisms of Crack Growth,* Metallurgical Society of AIME, Warrendale, Pennsylvania, pp. 119-130

High-Temperature Crack-Growth Behaviour in Nimonic PE16 and Alloy 718, by K. Sadananda and P. Shahinian, *Metals Technology* **9**:18-25

Hydrogen Effects on Inert Environment Subcritical Cracking in Ti-6Al-4V, by D.A. Meyn, in *Third International Congress on Hydrogen and Materials,* Ecole Centrale des Arts et Manufactures, Chatenax-Malabry, France, pp. 821-827

† **Initial Stages of Oxide Formation on a Co-Cr-Al-Y Coating Alloy at 700°C,** by J.A. Sprague, V. Provenzano, and F.A. Smidt,

Thin Solid Films 95:57-64

Micro and Macro Mechanisms of Crack Growth, ed. by K. Sadananda, B.B. Rath, and D.J. Michel, Metallurgical Society of AIME, Warrendale, Pennsylvania

Near-Surface Modifications for Improved Crack Tolerant Behavior of High Strength Alloys: Trends and Prospects, by L.R. Hettche and B.B. Rath, in *Surface Treatments for Improved Performance and Properties,* Plenum Publishing Corp., New York, pp. 143-171

On Microstructural Control of Near-Threshold Fatigue Crack Growth in 7000-Series Aluminum Alloys, by G.R. Yoder, L.A. Cooley, and T.W. Crooker, *Scripta Metallurgica* 16:1021-1025

Particulate Composite Surfaces by Laser Processing, by J.D. Ayers, in *Lasers in Metallurgy,* Metallurgical Society of AIME, Warrendale, Pennsylvania, pp. 117-125

Rare-Earth Transition Metal Exchange Interactions in Amorphous $(Fe_{0.82}B_{0.18})_{0.9}R_xLa_{0.1-x}$ Alloys, by N.C. Koon, B.N. Das, J.A. Geohegan, and D.W. Forester, *Journal of Applied Physics* 53:2333-2334

Relationship Between the Electronic Structure of Coherent Composition Modulated Alloys and the Supermodulus Effect, by W.E. Pickett, *Journal of Physics F: Metal Physics* 12:2195-2204

RHEED, AES and XPS Studies of the Passive Films Formed on Ion-Implanted Stainless Steel, by C.R. Clayton,* K.G.K. Doss,* Y.F. Wang,* J.B. Warren,* and G.K. Hubler, in *Ion Implantation into Metals,* Pergamon Press, New York, pp. 67-76

Significance of Nickel and Copper Content to Radiation Sensitivity and Post Irradiation Heat Treatment Recovery of Reactor Vessel Steels, by J.R. Hawthorne, in *Effects of Radiation on Materials: Eleventh Conference,* American Society for Testing and Materials, Philadelphia, Pennsylvania, ASTM STP 782, pp. 375-391

Significance of Selected Residual Elements to the Radiation Sensitivity of A302-B Steels, by J.R. Hawthorne, *Nuclear Technology* 59:440-455

The Effect of Nitrogen Implantation on Martensite in 304 Stainless Steel, by R.G. Vardiman, R.N. Bolster, and I.L. Singer, in *Metastable Materials Formation by Ion Implantation,* Elsevier-North Holland Publishing Co., New York, pp. 269-274

The Improvement of Fatigue Life in Ti-6Al-4V by Ion Implantation, by R.G. Vardiman and R.A. Kant, *Journal of Applied Physics* 53:690-694

The Surface Behavior of a Binary Alloy During Production by Ion Implantation, by G.W. Reynolds, F.R. Vozzo, R.G. Allas, A.R. Knudson, J.M. Lambert, and P.A. Treado, in *Metastable Materials Formation by Ion Implantation,* Elsevier-North Holland Publishing Co., New York, pp. 51-5

Void Formation in Neutron-Irradiated Ti-Al Alloys, by J.A. Sprague, *40th Annual Proceedings Electron Microscopy Society of America,* Washington, D.C., pp. 592-593

NUCLEAR SCIENCE

Effects of Simultaneous Exposures to Heat and Radiation on Insulation Life, by F.J. Campbell, in *Proceedings of Workshop on Nuclear Power Plant Aging,* NUREG/CP-0036, Nuclear Regulatory Commission, Washington, D.C., pp. 256-262

Hardness Assurance and Overtesting, by A.I. Namenson, *IEEE Transactions on Nuclear Science* NS-29: 1821-1826

Neutron Induced Permanent Damage in Josephson Junctions, by G.P. Mueller and M. Rosen, *IEEE Transactions on Nuclear Science* NS-29:1580-1581

$O^+(GS) \rightarrow 2^+$ (4.44 MeV) Transition Density in ^{12}C, by R.H. Bassel, B.A. Brown,* R. Lindsay,* and N. Rowley,* *Journal of Physics G: Nuclear Physics* 8:1215-1229

Review of IAEA Specialists' Meeting on Irradiation Embrittlements and Surveillance of Reactor Pressure Components, Vienna, Austria, 19-21 October 1981, by L.E. Steele, in *Radiation Metrology Techniques, Data Bases, and Standardization,* NUREG/CP-0028, Nuclear Regulatory Commission Washington, D.C., Vol. 2, pp. 809-818

Status of USA Reactor Vessel Surveillance Programs, by L.E. Steele, in *Structural Integrity of Light Water Reactor Components,* Applied Science Publishers, New York, pp. 217-247

Structural Integrity of Light Water Reactor Components, ed. by L.E. Steele, K.E. Stahlkopf,* and L.H. Larsson,* Applied Science Publishers, New York

OCEAN SCIENCE AND TECHNOLOGY

† **A Hydrodynamic Model for Open Channel Flow Problems**, by G.A. Keramidas, in *Proceedings of the 4th International Conference on Finite Elements in Water Resources*, Springer-Verlag, New York, pp. 4-37—4-50

A Note on the Generation of Capillary Waves by Steep Gravity Waves: The Effect of Wind Growth, by G.R. Valenzuela, *Journal of Geophysical Research* 87:579-581

† **A Relationship Between Wind Stress and Wave Slope**, by W.J. Plant, *Journal of Geophysical Research* 87:1961-1967

Asymmetric Geophysical Signatures in the Greenland-Norwegian and Southern Labrador Seas and the Eurasian Basin, by P.R. Vogt, L.C. Kovacs, C. Bernero,* and S.P. Srivastava,* *Tectonophysics* 89:95-160

† **Compact, Intrathermocline Eddies in the Sargasso Sea**, by J.P. Dugan, R.P. Mied, P.C. Mignerey,* and A.F. Schuetz, *Journal of Geophysical Research* 87:385-393

Computational and Experimental Studies of Problems in Marine Hydrodynamics, by O.M. Griffin, in *Computational Methods and Experimental Measurements, Proceedings of the International Conference*, Springer-Verlag, New York, pp. 474-486

Computer-Based Measurements of Incipient Wave Breaking, by S.E. Ramberg and C.L. Bartholomew, in *Computational Methods and Experimental Measurements, Proceedings of the International Conference*, Springer-Verlag, New York, pp. 102-115

Depth-to-Magnetic Source Analysis of the Arctic Ocean Region, by L.C. Kovacs and P.R. Vogt, *Tectonophysics* 89:255-294

Hydrodynamic Loads in Flexible Marine Structures Due to Vortex Shedding, by M.J. Every,* R. King,* and O.M. Griffin, *Journal of Energy Resources Technology, Transactions of the ASME* 104:330-336

Numerical Experiments with Reflecting Water Waves, by G.A. Keramidas and S.E. Ramberg, in *Computational Methods and Experimental Measurements, Proceedings of the International Conference*, Springer-Verlag, New York, pp. 392-404

On the Use of Profilometry for Ocean Wave Studies, by C.R. McClain,* D.T. Chen, and W.D. Hart,* *Journal of Geophysical Research* 87:9509-9515

Silicones in Chesapeake Bay Sediments, by R.E. Pellenbe[illegible], *Marine Pollution Bulletin* 13:427-429

Some Recent Studies of Vortex Shedding with Application to Marine Tubulars and Risers, by O.M. Griffin and S.E. Ramberg, *Journal of Energy Resources Technology, Transactions of the ASME* 104:2-13

The Birth and Evolution of Eastward-Propagating Modons, by R.P. Mied and G.J. Lindemann, *Journal of Physical Oceanography* 12:213-230

The Canada Basin: Aeromagnetic Constraints on Structure and Evolution, by P.R. Vogt, P.T. Taylor,* L.C. Kovacs, and G.L. Johnson,* *Tectonophysics* 89:295-336

The Temporal Eigenvalue Spectrum of an Ekman Boundary Layer, by G.F. Spooner, *Physics of Fluids* 25:1958-1963

Underwater Flow Visualization Experiments, by J.R. McGrath, C.M. Gordon, and D. Greenewalt, in *Oceans '82 Conference Record*, IEEE, New York, pp. 355-359

OPTICAL SCIENCES

A Grating/Crystal Monochromator for the Spectral Range 5 eV to 5 keV, by W.R. Hunter, R.T. Williams, and J.C. Rife, *Nuclear Instruments and Methods* 195:141-153

A Passive Stabilization Scheme for Fiber Interferometers Using (3 × 3) Fiber Directional Couplers, by K.P. Koo, A.B. Tveten, and A. Dandridge, *Applied Physics Letters* 41:616-618

Aberrations of Grazing Incidence Systems and Their Reduction or Toleration, by W.R. Hunter, in *Reflecting Optics for Synchrotron Radiation*, SPIE, Bellingham, Washington, SPIE Vol. 315, pp. 19-29

An Electric Field Sensor Utilizing a Piezoelectric Polyvinylidene Fluoride (PVF_2) Film in a Single Mode Fiber Interferometer, by K.P. Koo and G.H. Sigel, *IEEE Journal of Quantum Electronics* QE-18:670-675

Analysis of Fiber Interferometer Utilizing 3 × 3 Fiber Coupler, by R.G. Priest, *IEEE Journal of Quantum Electronics* QE-18:1601-1603

Applicability of SERS to the Study of Adsorption at High Pressure, by P. Podini* and J.M. Schnur, *Chemical Physics Letters* 93:86-90

Aqueous Corrosion Studies of a Fluorozirconate Glass, by C.J. Simmons,* H. Sutter,* and J.H. Simmons, *Materials Research Bulletin* 17:1203-1210

Birefringence Correction for Single-Mode Fiber Couplers, by C.A. Villarruel, M. Abebe, and W.K. Burns, *Optics Letters* 7:626-628

Changes in the Surface Composition of Si, TiO_2 and SiO_2 Induced by Pulsed Ruby-Laser Irradiation, by V.M. Bermudez, *Journal of Vacuum Science and Technology* 20:51-57

Characteristics of Fiber-Optic Magnetic-Field Sensors Employing Metallic Glasses, by K.P. Koo and G.H. Sigel, *Optics Letters* 7:334-336

Collisional Quenching of Pb $6p^2\ ^3P_1$ and $6p^2\ ^3P_2$ Metastables by Ground State Pb Atoms, by C. Reiser, N. Djeu, and R. Burnham, *Journal of Chemical Physics* 76:2332-2337

Comments on the Theory of Phase-Conjugated Waves, by E. Wolf* and W.H. Carter, *Optics Communications* 40:397-400

Compact Acoustooptical Signal Processor for Real-Time Fourier Transformation, by S.C. Lin, *Applied Optics* 21:3227-3229

Correlation Theory of Wavefields Generated by Fluctuating, Three-Dimensional, Scalar Sources II. Radiation from Isotropic Model Sources, by W.H. Carter and E. Wolf,* *Optica Acta* 28:245-259

Design Considerations for a Very-High-Speed Fiber Optic Data Bus, by H.F. Taylor, in *The National Telesystems Conference, NTC '82, Systems for the Eighties,* IEEE, New York, pp. F4.1.1-F4.1.5

Determination of Vesicle Size as a Function of Temperature by Laser Light Scattering, by E.L. Chang, J.P. Sheridan, and B.P. Gaber, in *Biomedical Applications of Laser Light Scattering,* Elsevier Biomedical Press, New York, p. 167

Digital Enhancement of the Argon Dielectronic Satellite Spectrum from a Laser-Imploded Microballoon, by J.F. Seely and J.G. Lunney,* *Optics Communications* 41:43-46

Discovery and Raman Study of an Alkane Phase Similar to the High Pressure Intermediate Phase of Polyethylene, by K.H. Fiedler, S.L. Wunder, R.G. Priest, and J.M. Schnur, *Journal of Chemical Physics* 76:5541-5550

Discrete Fourier Transformation Using a Time-Integrating, Acousto-Optical Signal Processor, by J.N. Lee, S.C. Lin, and A.B. Tveten, *Applied Physics Letters* 41:131-133

Effects of Ionizing Radiation on Amorphous Insulators, by D.L. Griscom and E.J. Friebele, *Radiation Effects* 65:63-72

Fabry-Perot Photothermal Trace Detection, by A.J. Campillo, S.J. Petuchowski, C.C. Davis, and H.-B. Lin, *Applied Physics Letters* 41:327-329

Feedback Effects in a Laser Diode Due to Rayleigh Backscattering from an Optical Fibre, by L. Goldberg, H.F. Taylor, and J.F. Weller, *Electronics Letters* 18:353-354

Fluorozirconate Glasses with Improved Viscosity Behavior for Fiber Drawing, by D.C. Tran, R.J. Ginther, and G.H. Sigel, *Materials Research Bulletin* 17:1177-1184

Graded-Layer-Thickness Bragg X-Ray Reflectors, by D.J. Nagel, T.W. Barbee,* and J.V. Gilfrich, in *Reflecting Optics for Synchrotron Radiation,* SPIE, Bellingham, Washington, SPIE Vol. 315, pp. 110-117

High-Power Low-Divergence Superradiance Diode, by C.S. Wang,* W.H. Cheng,* C.J. Hwang,* W.K. Burns, and R.P. Moeller, *Applied Physics Letters* 41:587-589

Homodyne Demodulation Scheme for Fiber Optic Sensors Using Phase Generated Carrier, by A. Dandridge, A.B. Tveten, and T.G. Giallorenzi, *IEEE Journal of Quantum Electronics* QE-18:1647-1653

Inner-Shell Excitation of Argon Dielectronic Satellite Spectral Lines in Imploded Microballoon Plasmas, by J.G. Lunney* and J.F. Seely, *Journal of Physics B: Atomic and Molecular Physics* 15:2121-2127

Instrumentation for XUV Lithography at SURF-II, by L.R. Hughey,* R.T. Williams, and J.C. Rife, *Nuclear Instruments and Methods* 195:267-272

Interference Effects in Luminescence Studies of Thin Films, by R.T. Holm, S.W. McKnight, and E.D. Palik, *Applied Optics* 21:2512-2519

Measurement of Fluctuations Affecting Domain Formation in Transferred-Electron Logic Devices Using Picosecond Optical Pulses, by T.F. Carruthers, J.F. Weller, and H.F. Taylor, *Applied Physics Letters* 40:150-152

Measurement of Optical Properties of Materials in the Vacuum Ultraviolet Spectral Region, by W.R. Hunter and D.H. Leslie, *Applied Optics* 21:2103-2114

Microwave Signal Generation Using an Optical Self-Heterodyne Technique, by L. Goldberg, J.F. Weller, and H.F. Taylor, *Electronics Letters* 18:317-318

Multiplexed Coherent Optical Processor for Calculating Generalized Moments, by J.A. Blodgett, R.A. Athale, C.L. Giles, and H.H.

Szu, *Optics Letters* 7:7-9

New Acousto-Optic Devices for Fourier Transformation, by J.N. Lee, S.C. Lin, and A.B. Tveten, in *Real Time Signal Processing V*, SPIE, Bellingham, Washington, SPIE Vol. 341, pp. 86-93

Numerical Study of Phase Conjugation in Stimulated Backscatter with Pump Depletion, by R.H. Lehmberg, *Optics Communications* 43:369-374

Observation of Low Noise in a Passive Fibre Gyroscope, by W.K. Burns, R.P. Moeller, and C.A. Villarruel, *Electronics Letters* 18:648-650

On-Blaze Scanning Monochromator for the Vacuum Ultraviolet, by W.R. Hunter, *Applied Optics* 21:1634-1642

Optical Constants in the Extreme Ultraviolet and Soft X-Ray Region, by J.C. Rife and J.F. Osantowski,* in *Reflecting Optics for Synchrotron Radiation*, SPIE, Bellingham, Washington, SPIE Vol. 315, pp. 103-109

Optical Fiber Sensor Technology, by T.G. Giallorenzi, J.A. Bucaro, A. Dandridge, G.H. Sigel, Jr., J.H. Cole, S.C. Rashleigh, and R.G. Priest, *IEEE Journal of Quantum Electronics* QE-18:626-665

Optical Guided-Wave Interactions with Magnetostatic Waves at Microwave Frequencies, by A.D. Fisher, J.N. Lee, E.S. Gaynor, and A.B. Tveten, *Applied Physics Letters* 41:779-781

Optical Techniques to Solve the Signal Fading Problem in Fiber Interferometers, by S.K. Sheem, T.G. Giallorenzi, and K. Koo, *Applied Optics* 21:689-693

Output Properties of Charge-Injection Devices: I. Read on Injection, by D.L. Weinberg and A.F. Milton, *IEEE Transactions on Electron Devices* ED-19:1483-1490

Phase Compensation in Interferometric Fiber-Optic Sensors, by A. Dandridge and A.B. Tveten, *Optics Letters* 7:279-281

Photo-Hall Measurements of High-Density Photoexcited Electrons in $Hg_{1-x}Cd_xTe$, by F.J. Bartoli, C.A. Hoffman, J.R. Meyer, and R.E. Allen, in *Physics of Narrow Gap Semiconductors*, Springer-Verlag, New York, Lecture Notes in Physics 152, pp. 126-130

Photon Correlation Spectroscopy Study on the Stability of Small Unilamellar DPPC Vesicles, by E.L. Chang, B.P. Gaber, and J.P. Sheridan, *Biophysical Journal* 39:197-201

Picosecond Coherent Anti-Stokes Raman Scattering (CARS) Microscope, by J. Reintjes, M.D. Duncan, and T.J. Manuccia, in *Picosecond Lasers and Applications*, SPIE, Bellingham, Washington, SPIE Vol. 322, pp. 87-92

Picosecond Laser Induced Fluorescence Probing of NO_2 Photofragments, by P.E. Schoen, M.J. Marrone, and L.S. Goldberg, in *Picosecond Phenomena III*, Springer-Verlag, New York, p. 269

Picosecond Time-Resolved Photoelectron Spectroscopy of ZnTe, by R.T. Williams, T.R. Royt, and J.C. Rife, *Journal of Vacuum Science and Technology* 21:509-513

Picosecond UV Photolysis and Laser-Induced Fluorescence Probing of Gas-Phase Nitromethane, by P.E. Schoen, M.J. Marrone, and J.M. Schnur, *Journal of Chemical Physics* 90:272-276

Piezoelectric PVF_2 (Polyvinylidene Fluoride) Compensator for Fiber Interferometer, by K.P. Koo and G.H. Sigel, in *Topical Meeting on Integrated and Guided-Wave Optics*, IEEE, New York, pp. WC3-1—WC3-3

Polarisation Holding in a High-Birefringence Fibre, by S.C. Rashleigh and M.J. Marrone, *Electronics Letters* 18:326-327

Polarization Characteristics of Single-Mode Fiber Couplers, by C.L. Chen* and W.K. Burns, *IEEE Journal of Quantum Electronics* QE-18:1589-1600

Polarization Coupling in Kinked Single-Mode Fibers, by R. Ulrich* and S.C. Rashleigh, *IEEE Journal of Quantum Electronics* QE-18:2032-2039

Polarization Fading in the Fiber Interferometric Sensors, by D.W. Stowe,* D.R. Moore,* and R.G. Priest, *IEEE Journal of Quantum Electronics* QE-18:1644-1647

Polarization Holding in Birefringent Single-Mode Fibers, by S.C. Rashleigh,* W.K. Burns, and R.P. Moeller, *Optics Letters* 7:40-42

Polarization Holding in Elliptical-Core Birefringement Fibers, by S.C. Rashleigh and M.J. Marrone, *IEEE Journal of Quantum Electronics* QE-18:1515-1523

Radiation Damage of Optical Fiber Waveguides at Long Wavelengths, by E.J. Friebele, K.J. Long,* and M.E. Gingerich, *Applied Optics* 21:547-553

Simplified Time-Integrating Acousto-Optical Processor for Fourier Transformation, by S.C. Lin and A.B. Tveten, *Optics Letters* 7:448-450

Simulation of Mid-Infrared Clutter Rejection: I: One-Dimensional LMS Spatial Filter and Adaptive Threshold Algorithms, by M.S. Longmire,* A.F. Milton, and E.H. Takken, *Applied Optics* 21:3819-3833

Single-Mode-Fibre Point and Extended Temperature Sensors, by S.J. Petuchowski, G.H. Sigel, and T.G. Giallorenzi, *Electronics Letters* 18:814-815

Spectra of Nb XII-XVII from a Low-Inductance Vacuum Spark, by P.G. Burkhalter, L. Cohen,* and R.D. Cowan,* *Journal of the Optical Society of America* 72:95-102

Synthetic-Heterodyne Interferometric Demodulation, by J.H. Cole, B.A. Danver,* and J.A. Bucaro, *IEEE Journal of Quantum Electronics* QE-18:694-697

UV Short-Pulse Fragmentation of Isotopically-Labeled Acetylene: Studies of Emission with Subnanosecond Resolution, by B.B. Craig, W.L. Faust, L.S. Goldberg, and R.G. Weiss, *Journal of Chemical Physics* 76:5014-5021

Visualizing Stress Fields with Photoelastic Holography, by R.J. Sanford, *Optical Engineering* 21:489-495

PLASMA PHYSICS

A High Power Complex Cavity Gyrotron for Fusion Research Devices, by Y. Carmel,* A.K. Ganguly, D. Dialetis,* R. Seeley,* M. Read, K.R. Chu, J.S. Levine, V.L. Granatstein, in *IEEE International Electron Devices Meeting 1982 Technical Digest,* IEEE, New York, pp. 372-374

A Time Dependent Three-Dimensional Simulation of the Earth's Magnetosphere: Reconnection Events, by S.H. Brecht,* J.G. Lyon,* J.A. Fedder, and K. Hain, *Journal of Geophysical Research* 87:6098-6108

A Wideband Fundamental Mode Millimeter Gyrotron TWA Experiment, by L.R. Barnett, Y.Y. Lau,* C.R. Kyler, V.L. Granatstein, and K.R. Chu, in *IEEE International Electron Devices Meeting 1982 Technical Digest,* IEEE, New York, pp. 375-378

Atomic Properties and Processes in Dense Plasmas, by J. Davis and M. Blaha,* in *Physics of Electronic and Atomic Collisions,* North-Holland Publishing Co., New York, pp. 811-822

Autoacceleration of High Power Electron Beams, by M. Friedman, *Applied Physics Letters* 41:419-421

Axial Magnetic-Field Effects in a Collective-Interaction Free-Electron Laser at Millimeter Wavelengths, by R.K. Parker, R.H. Jackson,* S.H. Gold, H.P. Freund,* V.L. Granatstein, P.C. Efthimion,* M. Herndon, and A.K. Kinkead, *Physical Review Letters* 48:238-242

Ballistic Pendula for Measuring the Momentum of a Laser-Produced Plasma, by J. Grun* and B.H. Ripin, *Review of Scientific Instruments* 53:1878-1881

Comment on 'A Transverse Kelvin-Helmholtz Instability in Magnetized Plasma' by P. Kintner and N. D'Angelo, by J.D. Huba, *Journal of Geophysical Research* 87:2574-2575

Density Effects on the Spectral Emission of a High Temperature Argon Plasma, by D. Duston and J. Davis, *Journal of Quantitative Spectroscopy and Radiative Transfer* 27:267-279

Direct Measurements of Plasma Characteristics in Space-Simulation Beam-Plasma Interactions, by E.P. Szuszczewicz, in *AIAA 20th Aerospace Sciences Meeting,* AIAA, New York, AIAA-82-0146, pp. 1-14

Electron Drift in a Linear Magnetic Wiggler With an Axial Guide Field, by J.A. Pasour, F. Mako,* and C.W. Roberson, *Journal of Applied Physics* 53:7174-7178

Electron-Beam Controlled Discharges, by R.J. Commisso,* R.F. Fernsler,* V.E. Scherrer, and I.M. Vitkovitsky, *IEEE Transactions on Plasma Science* PS-10:241-245

Erratum: Laser-Plasma Interaction and Ablative Acceleration of Thin Foils at 10^{12} 10^{15} W/cm^2, by B.H. Ripin et al., *Physics of Fluids* 24:990

Focusing Experiments with an Inverse Reflex Tetrode, by D.E. Pershing,* J. Golden, J.A. Pasour, and C.A. Kapetanakos, *Journal of Applied Physics* 53:3405-3409

Forbidden Line Emission from Highly Ionized Atoms in Tokamak Plasmas, by U. Feldman, G.A. Doschek, and A.K. Bhatia,* *Journal of Applied Physics* 53:8554-8561

Gyrotron Travelling Wave Amplifier: IV. Analysis of Launching Losses, by Y.Y. Lau,* L.R. Barnett, and V.L. Granatstein,

International Journal of Infrared and Millimeter Waves 3:45-62

Highly Resolved, Monochromatic, X-Ray Images of Laser-Produced Plasmas Through the Single-Crystal Double-Reflection Spectrometer, by B.S. Fraenkel, *Applied Physics Letters* 41:234-236

Homopolar Current Source for Mass Accelerators, by I.M. Vitkovitsky, R.D. Ford, D. Jenkins, and W.H. Lupton, *IEEE Transactions on Magnetics* MAG-18:157-159

Ignition of the Beam-Plasma-Discharge and its Dependence on Electron Density, by D.N. Walker, E.P. Szuszczewicz, and C.S. Lin,* in *Artificial Particle Beams in Space Plasma Studies,* Plenum Press, New York, pp. 371-379

Influence of Velocity Shear on the Rayleigh-Taylor Instability, by P.N. Guzdar, P. Satyanarayana, J.D. Huba, and S.L. Ossakow, *Geophysical Research Letters* 9:547-550

Injection of a High-Current Beam into a Modified Betatron Accelerator, by C.A. Kapetanakos, P. Sprangle, and S.J. Marsh,* *Physical Review Letters* 49:741-744

Integer Resonances in the Modified Betatron, by D. Chernin* and F. Sprangel, *Particle Accelerators* 12:101-106

Intense Particle Energization in the Inner Magnetosphere of Neutron Stars, by J.E. Borovsky,* C.K. Goertz,* and G. Joyce, in *Proceedings of the International Conference on Plasma Physics,* Chalmers University of Technology, Sweden, p. 57

Internal Heat Deposition in Laser Highly Accelerated Targets, by B.H. Ripin, E.A. McLean, and J.A. Stamper, *Physics of Fluids* 25:2128-2131

Level Shifts and Inelastic Electron Scattering in Dense Plasmas, by J. Davis and M. Blaha,* *Journal of Quantitative Spectroscopy and Radiative Transfer* 27:307-313

Measured Performance of Gyrotron Oscillators and Amplifiers, by V.L. Granatstein, M.E. Read, and L.R. Barnett, in *Infrared and Millimeter Waves,* Academic Press, New York, Vol. 5, pp. 267-304

† **Measurement of Enhanced Stopping of 1-MeV Deuterons in Target-Ablation Plasmas,** by F.C. Young, D. Mosher, S.J. Stephanakis, S.A. Goldstein,* and T.A. Mehlhorn,* *Physical Review Letters* 49:549-553

Measurements of Intense Ion Beams by a Novel Diagnostic Method, by A.E. Blaugrund,* S.J. Stephanakis, and S.A. Goldstein,* *Journal of Applied Physics* 53:7280-7289

Multicomponent Model of the Resistive Hose Instability, by W.M. Sharp,* M. Lampe, and H.S. Uhm,* *Physics of Fluids* 25:1456-1470

Multimode Theory and Simulation of Quasioptical Gyrotrons and Gyroklystrons, by A. Bondeson,* B. Levush,* W.M. Manheimer, and E. Ott, *International Journal of Electronics* 53:547-553

Nonlinear Evolution of Plasma Enhancements in the Auroral Ionosphere: 1. Long Wavelength Irregularities, by M.J. Keskinen and S.L. Ossakow, *Journal of Geophysical Research* 87:144-150

Physical Mechanism of Wave-Particle Resonances in a Curved Magnetic Field, by J.D. Huba and J.F. Drake,* *Physics of Fluids* 25:1207-1210

Pinched-Beam Ion-Diode Scaling on the Aurora Pulser by R.A. Meger* and F.C. Young, *Journal of Applied Physics* 53:8543-8548

Plasma Conditions Required for Attainment of Maximum Gain in Resonantly Photo-Pumped Aluminum XII and Neon IX, by J.P. Apruzese, J. Davis, and K.G. Whitney, *Journal of Applied Physics* 53:4020-4027

Repetitive Operation of an Inductively-Driven Electron-Beam Diode, by B. Fell,* R.J. Commisso,* V.E. Scherrer, and I. Vitkovitsky, *Journal of Applied Physics* 53:2818-2824

Resistive Interchange Modes in Reversed-Field Pinches, by J.M. Finn and W.M. Manheimer, *Physics of Fluids* 25:697-701

Return-Current-Driven Instabilities of Propagating Electron Beams, by H.S. Uhm* and M. Lampe, *Physics of Fluids* 25:1444-1449

Simulation of the Longitudinal Dynamics of a Cold Bunched Beam, by I. Huber, in *Proceedings of the Symposium on Accelerating Aspects of Heavy Ion Fusion,* Gesellschaft für Schwirconforsch ng, Darmstadt, West Germany, Report GSI-82-8, p. 372

Spectroscopy and Atomic Physics of Highly Ionized Krypton for Tokamak Plasmas, by A.K. Bhatia,* and U. Feldman, *Journal of Applied Physics* 53:4711-4725

Spectrum Diagnostics. The Necessity for Detailed Non-LTE Modeling of X-Ray Emission from Dense Plasmas, by K.G. Whitney and P.C. Kepple, *Journal of Quantitative Spectroscopy and Radiative Transfer* 27:281-296

†**Spot Spectroscopy: Local Spectroscopic Measurements Within Laser-Produced Plasmas,** by M.J. Herbst, P.G. Burkhalter, J. Grun,* R.R. Whitlock, and M. Fink,* *Review of Scientific Instruments* **53**:1418-1422

†**Stability of Imploding Shocks in the CCW Approximation,** by J.H. Gardner, Jr., D.L. Book, and I.B. Bernstein,* *Journal of Fluid Mechanics* **114**:41-58

Steady-State Planar Ablative Flow, by W.M. Manheimer, D.G. Colomband, and J.H. Gardner, *Physics of Fluids* **25**:1644-1652

The Linus Concept, by A.E. Robson, in *Unconventional Approaches to Fusion,* Proceedings of the Fifth Course of the International School of Fusion Reactor Technology, Plenum Press, New York, pp. 257-279

The Lower Hybrid Drift Instability in Nonantiparallel Reversed Field Plasmas, by J.D. Huba, N.T. Gladd,* and J.F. Drake,* *Journal of Geophysical Research* **87**:1697-1701

Theory of a Low Magnetic Field Gyrotron (Gyromagnetron), by Y.Y. Lau* and L.R. Barnett, *International Journal of Infrared and Millimeter Waves* **3**:619-744

Theory of a Wide-Band Distributed Gyrotron Traveling-Wave Amplifier, by K.R. Chu, Y.Y. Lau,* L.R. Barnett,* and V.L. Granatstein, *IEEE Transactions on Electron Devices* **ED-28**:866-871

Threshold Criteria for a Space Simulation Beam-Plasma Discharge, by E.P. Szuszczewicz, K. Papadopoulos,* W. Bernstein,* C.S. Lin,* and D.N. Walker, *Journal of Geophysical Research* **87**:1565-1573

Tilt and Shift Mode Stability with Line Tying, by J.M. Finn and A. Reiman,* *Physics of Fluids* **25**:116-125

Time-Dependent Plasma Behavior Triggered by a Pulsed Electron Gun Under Conditions of Beam-Plasma-Discharge, by E.P. Szuszczewicz and C.S. Lin,* in *Artificial Particle Beams in Space Plasma Studies,* Plenum Press, New York, pp. 361-370

Transverse Beam Dynamics in the Modified Betatron, by D. Chernin* and F. Sprangel, *Particle Accelerators* **12**:85-100

Wave-Mean Flow Statistics, by M.R. Schoeberl, *Journal of the Atmospheric Sciences* **39**:2363-2368

X-Rays from Laboratory and Astrophysical Plasmas, by U. Feldman, in *X-Ray and Atomic Inner Shell Physics,* American Institute of Physics, New York, AIP Conference No. 94, pp. 447-462

PHYSICS

Relaxation Processes and Time-Scale Transformations, by S. Teitler, A.K. Rajagopal,* and K.L. Ngai, *Physical Review A* **26**:2906-2912

RADAR

A Comparison Between Noncoherent and Coherent MTI's, by F.F. Kretschmer, F.L.C. Lin, and B.L. Lewis, in *Radar-82,* Institution of Electrical Engineers, London, pp. 51-55

Amplitude and Temporal Statistics of Sea Spike Clutter, by I.D. Olin, in *Radar-82,* Institution of Electrical Engineers, London, pp. 198-202

Analysis of Rain Clutter Data from a Frequency Agile Radar, by W.B. Gordon, *Radio Science* **7**:801-816

Automatic Detectors for Frequency-Agile Radar, by G.V. Trunk and P.K. Hughes, in *Radar-82,* Institution of Electrical Engineers, London, pp. 464-468

Bandpass Signal Sampling and Coherent Detection, by W.M. Waters and B.R. Jarrett, *IEEE Aerospace and Electronics Systems Journal* **AES-18**, 731-736

Bicollimated Near Field Gregorian Reflector Antenna, by J.B.L. Rao, in *IEEE 1982 Antennas and Propagation International Symposium Digest,* IEEE, New York, pp. 273-276

Bispherical Constrained Lens Antenna, by J.B.L. Rao, *IEEE Transactions on Antennas and Propagation* **AP-30**:1224-1228

Brillouin Revisited: Signal Velocity Definition for Pulse Propagation in a Medium with Resonant Anomalous Dispersion, by D.B. Trizna and T.A. Weber,* *Radio Science* **17**:1169-1180

Comparison of SCR Microwave Measurment of Directional Wave Spectra with ARSLOE In-Situ Sensor, by E.J. Walsh,* D.W. Hancock,* D.E. Hines,* and J.E. Kenney, in *Oceans '82 Conference Record,* IEEE, New York, pp. 893-900

Constraints of Low Sidelobe Phased Array, by J.K. Hsiao, in *IEEE 1982 Antennas and Propagation International Symposium Digest,* IEEE, New York, pp. 687-690

Development of the Fetch-Limited Directional Wave Spectrum, by E.J. Walsh,* D.W. Hancock,* D.E. Hines,* and J.E. Kenney, in *Oceans '82 Conference Record,* IEEE, New

York, pp. 820-825

Line Type Modulator with Pulsewidth Agility, by E.M. Piechowiak,* E.H. Hooper,* E.C. Farkas,* and M. Lipka, in *IEEE Conference Record of 1982 Fifteenth Power Modulator Symposium,* IEEE, New York, pp. 200-209

Linear Frequency Modulation Derived Polyphase Pulse Compression Codes, by B.L. Lewis and F.F. Kretschmer, *IEEE Transactions on Aerospace and Electronic Systems* **AES-18**:637-641

Multifocal Three-Dimensional Bootlace Lenses, by J.B.L. Rao, *IEEE Transactions on Antennas and Propagation* **AP-30**:1050-1056

New Polyphase Pulse Compression Waveforms and Implementation Techniques, by B.L. Lewis and F.F. Kretschmer, in *Radar-82,* Institution of Electrical Engineers, London, pp. 331-335

On the Performance Degradation of a Low Sidelobe Phased Array Due to Correlated and Uncorrelated Errors, by J.K. Hsiao, in *Radar-82,* Institution of Electrical Engineers, London, pp. 355-359

Performance Measures of an Adaptive Array in Bandlimited Noise, by K. Gerlach and R.H. Lang,* *National Telecommunications Conference, Innovative Telecommunications—Key To The Future,* IEEE, New York pp. C7.1.1-C7.1.5.

Planar Array Synthesis with Prescribed Pattern Nulls, by S.R. Laxpati, *IEEE Transactions on Antennas and Propagation* **AP-30**:1176-1183

Repeated Hypothesis Testing on a Growing Data Set, by G.V. Trunk and J.O. Coleman, *IEEE Transactions on Pattern Analysis and Machine Intelligence* **PAMI-4**:343-345

Very Strong Forces, by W.B. Gordon, in *Selected Studies,* North-Holland Publishing Co., New York, pp. 79-91

RADIATION TECHNOLOGY

Average Silicon Neutron Displacement Kerma Factor at 1 MeV, by A.I. Namenson, E.A. Wolicki, and G.C. Messenger,* *IEEE Transactions on Nuclear Science* **NS-29**:1018-1020

Bragg Diffractors with Graded-Thickness Multilayers, by D.J. Nagel, J.V. Gilfrich, and T.W. Barbee,* *Nuclear Instruments and Methods* **195**:63-65

Channeling Radiation and Coherent Bremsstrahlung, by H. Überall and A. W. Sáenz, *Physics Letters* **90A**:370-374

†**Charge Collection Measurements for Energetic Ions in Silicon,** by A.B. Campbell and A.R. Knudson, *IEEE Transactions on Nuclear Science* **NS-29**:2067-2071

Coherent Bremsstrahlung at Low Energies, by A.W. Sánz and H. Überall, *Physical Review B* **25**:4418-4430

Curing High Performance Structural Adhesives by Electron-Beam Radiation, by F.J. Campbell and W. Brenner,* *Naval Engineers Journal* **94**(3):160-166

DOD Application of Implantation-Modified Materials, by G.K. Hubler, in *Metastable Materials Formation by Ion Implantation,* North-Holland, New York, pp.341-354

Electrical and Structural Characterization of Implantation Doped Silicon by Infrared Reflection, by G.K. Hubler, P.R. Malmberg, C.N. Waddell,* W.G. Spitzer,* and J.E. Fredrickson,* *Radiation Effects* **60**:35-47

Energy Dispersive Measurements of Diffracted Synchrotron Radiation as a Function of Pressure: Applications to Phase Transitions in KCl and KI, by E.F. Skelton, J. Kirkland,* and S.B. Qadri,* *Journal of Applied Crystallography* **15**:82-88

Flash X Radiography of Laser-Accelerated Targets, by R.R. Whitlock, S.P. Obenschain, and J. Grun,* *Applied Physics Letters* **41**:429-431

Layered Synthetic Microstructures as Dispersing Devices in X-Ray Spectrometers, by J.V. Gilfrich, D.J. Nagel, and T.W. Barbee,* *Applied Spectroscopy* **36**:58-61

Mechanical Property Improvements on Ion Implanted Diamond, by N.E.W. Hartley, in *Metastable Materials Formation by Ion Implantation,* Elsevier Science Publishing Co., New York, pp.295-302

Near Surface Analysis with Energetic Ion Beams, by C.R. Gossett, in *Industrial Applications of Surface Analysis,* American Chemical Society, Washington, D.C., ACS Symposium Series No. 199, pp. 49-68

Reducing Errors in Dosimetry Caused by Low Energy Components of Co-60 and Flash X-Ray Sources, by D.B. Brown and C.M. Dozier, *IEEE Transactions on Nuclear Science* **NS-29**:1996-1999

Self-Ion Sputtering Yields for Copper, Nickel and Aluminum, by R.G. Allas, A.R. Knudson, J.M. Lambert, P.A. Treado, and G.W. Reynolds, *Nuclear Instruments and Methods* **194**:615-619

2D-ACAR: The Reconstruction of Momentum Densities of αCuZn and αCuGe, by L.M. Pecora and A.C. Ehrlich, in *Proceedings of the International Conference on Position Annihilation*, North-Holland Publishing Co., New York, p. 340

Understanding and Improving Crystals for X-Ray Fluorescence, by L.S. Birks and D.B. Brown, in *Advances in X-Ray Spectroscopy*, Pergamon Press, New York, Chapter 3, pp. 58-75

X-Ray Characteristics and Applications of Layered Synthetic Microstructures, by J.V. Gilfrich, D.J. Nagel, and N.G. Loter,* *Advances in X-Ray Analysis* **25**:355-364

SOLID STATE

A New Standardless Quantitative Electron Probe Microanalysis Technique Applied to III-V Compound Semiconductors, by K.P. Zangalis* and A. Christou, *Thin Solid Films* **97**:287-294

Alpha Induced Upsets in Josephson Tunnel Junctions, by R. Magno, M. Nisenoff, R. Shelby,* J. Kidd, and A.B. Campbell, *IEEE Transactions on Nuclear Science* **NS-29**:2090-2094

An Analysis of Normal-State Phonon Properties of 2H-$TaSe_2$ and -$NbSe_2$, by J.L. Feldman, *Physical Review B* **25**:7132-7140

Anomalous Superconducting Properties of $Sn_xEu_{1.2-x}Mo_6S_8$ at High Pressure and High Magnetic Field, by W.W. Fuller, S.A. Wolf, C.Y. Huang,* D.W. Harrison,* H. Luo,* and S. Maekaw, *Physical Review B* **26**:1442-1445

Assessment of High-Temperature Metallization for I^2 L and CMOS Technologies, by A. Christou and B.R. Wilkins, *IEEE Transactions on Industrial Electronics* **IE-29**:145-148

Atom and Carrier Depth Distribution of Beryllium Implanted into Silicon, by R.G. Wilson* and J. Comac, *Journal of Applied Physics* **53**:3003-3009

Band Structure and Superconductivity in Bi_3Sr and Bi_3Eu, by D.A. Papaconstantopoulos, B.M. Klein, L.L. Boyer, and J.W.D. Connolly,* *Physical Review B* **26**:4951-4956

BRSG Conference on Optical Techniques in Magnetic Resonance, by T.A. Kennedy, *European Scientific Notes* **ESN 36-6**:136-137

Confirmation of the EPR Identification of $Cr^{4+}3d^2$ in p-Type Cr-Doped GaAs by Means of Applied Uniaxial Stress, by J.J. Krebs and G.H. Stauss, *Physical Review B* **26**:2296-2297

Criterion for Multi-Ion Scattering in Free Carrier Transport, by J.R. Meyer and F.J. Bartoli, *Journal of Physics C: Solid State Physics* **15**:1987-1999

Density Dependence of Electron-Hole-Liquid Correlation Factor in Ge: Experiment, by J.C. Culbertson* and J.E. Furneaux, *Physical Review Letters* **49**:1528-1531

Dielectric Constant of Semi-Insulating Indium Phosphide, by R.E. Neidert, S.C. Binari, and T. Weng, *Electronics Letters* **18**:987-988

Effects of Disorder on Properties of A15 Materials, by C.M. Soukoulis* and D.A. Papaconstantopoulos, *Physical Review B* **26**:3673-3681

Electron Energy Distributions During Pulsed Laser Annealing and Damage of Silicon, by R.T. Williams, M.N. Kabler, J.P. Long, J.C. Rife, and T.R. Royt, in *Laser and Electron-Beam Interactions with Solids*, Elsevier Science Publishing Co., New York, p. 97

Electronic Structure of Substoichiometric Ti-Fe Hydride, by D.A. Papaconstantopoulos and A.C. Switendick,* *Journal of the Less-Common Metals* **88**:273-288

Electronic Structure of the Intermetallic Compound TiNi, by D.A. Papaconstantopoulos, G.N. Kamm, and P.N. Poulopoulos,* *Solid State Communications* **41**:93-96

Epitaxial Growth of Fe on GaAs by Metalorganic Chemical Vapor Deposition in Ultrahigh Vacuum, by R. Kaplan and N. Bottka, *Applied Physics Letters* **41**:972-974

Erratum: Cluster Formation in Two-Dimensional Random Walks: Application to Photolysis of Silver Halides, by H.B. Rosenstock and C.L. Marquardt, *Physical Review B* **25**:1396

Fully Ion Implanted InP Junction FET's, by J.B. Boos, H.B. Dietrich, T.H. Weng, K.J. Sleger, S.C. Binari, and R.L. Henry, *IEEE Electron Device Letters* **EDL-3**:256-258

Generalization of the Theory of the Electron-Phonon Interaction: Thermodynamic Formulation of Superconducting- and Normal-State Properties, by W.E. Pickett, *Physical Review B* **26**:1186-1207

Giant Resistivity and X-Ray Diffraction Anomalies in Low-Dimensional $ZrTe_5$ and $HfTe_5$, by E.F. Skelton, T.J. Wieting, S.A. Wolf, W.W. Fuller, D.U. Gubser, T.L. Fran-

cavilla, and F. Levy,* *Solid State Communications* **42**:1-3

High Resolution Magneto-Optical Studies of Free and Bound Hole Excitations in InSb, by R. Kaplan, R.J. Wagner, D.G. Seiler,* C.L. Littler,* M.H. Weiler,* and W. Zawadzki,* in *Physics of Narrow Gap Semiconductors,* Springer-Verlag, New York, Lecture Notes in Physics 152, pp.188-191

Hole Localization and Charge Transfer Excitation of Fe^{2+} in GaP:Fe by Time-Dependent Photoluminescence Measurements, by P.B. Klein and K. Weiser,* *Solid State Communications* **41**:365-368

^1H NMR in a-Si, by W.E. Carlos and P.C. Taylor, *Physical Review B* **26**:3605-3616

I-V Characteristics of MESFETs with Nonuniform Carrier Distribution, by T.H. Weng, *IEEE Transactions on Electron Devices* **ED-29**:1641-1643

Infrared Studies of Isothermal Annealing of Ion-Implanted Silicon: Refractive Indices, Regrowth Rates, and Carrier Profiles, by C.N. Waddell,* W.G. Spitzer,* G.K. Hubler, and J.E. Fredrickson,* *Journal of Applied Physics* **53**:5851-5861

Intermediate Range Order in Amorphous Phosphorus, by J.S. Lannin,* B.V. Shanabrook, and F. Gompf,* *Journal of Non-Crystalline Solids* **49**:209

International Symposium on GaAs and Related Compounds and Related Laboratory Visits, by H. Lessoff and D.E. Davis,* *ONR Tokyo Scientific Bulletin* **7**:17-40

Laser Annealed and Thermal Annealed Refractory Ohmic Contacts to GaAs, by W.T. Anderson, A. Christou, J.F. Giuliani, and H.B. Dietrich, *IEEE Transactions on Industrial Electronics* **IE-29**:149-153

LEED Investigation of the Si (112) Surface Structure, by R. Kaplan, *Surface Science* **116**:104-116

Low-Temperature Microwave Spectroscopy of Naβ-Alumina, by U. Strom, M. von Schickfus,* and S. Hunklinger,* *Physical Review B* **25**:2405-2417

Magnetic Field Dependence of the Photoresponse of the Electron Inversion Layer on (100)Si, by C.F. Lavine,* R.J. Wagner, and D.C. Tsui,* *Surface Science* **113**:112-117

Magnetic Field Induced Superconductivity, by W.W. Fuller, S.A. Wolf, C.Y Huang,* D.W. Harrison,* and H. Luo,* *Journal of Applied Physics* **53**:2622-2624

Magnetic-Field-Induced Superconductivity, by W.W. Fuller, S.A. Wolf, C.Y Huang,* D.W. Harrison,* H. Luo,* and S. Mackaw,* *Physical Review B* **25**:1990-1992

Magneto-Optical Detection of Deep Acceptor Impurities in p-InSb, by C.L. Littler,* D.G. Seiler,* R. Kaplan, and R.J. Wagner, *Applied Physics Letters* **41**:880-882

Measurements of the Quantized Hall Steps in Si at the ppm Level, by R.J. Wagner, C.F. Lavine,* M.E. Cage,* R.F. Dzinba,* and B.F. Field,* *Surface Science* **113**:10-15

Molecular Beam Epitaxial Growth of Single Crystal Al Films on GaAs (110), by G.A. Prinz, J.M. Ferrari, and M. Goldenberg,* *Applied Physics Letters* **40**:155-157

Molecular Hydrogen in a-Si:H, by W.E. Carlos and P.C. Taylor, *Physical Review B* **25**:1435-1438

Multiplet Structures in the Reflection Spectra of Perovskite Fluorides in the Soft X-Ray Region, by H. Onuki* and J.D. Rife, *Physical Review B* **26**:654-657

New Developments in the Defect Structure of Implanted Furnace-Annealed Silicon on Sapphire, by E.D. Richmond and A.R. Knudson, *Thin Solid Films* **93**:347-357

NMR Study of Low-Energy Excitations in *n*Naβ-Alumina, by S.G. Greenbaum, U. Strom, and M. Rubinstein, *Physical Review B* **26**:5226-5229

Nonlinear Interaction of an rf Field with a Bulk Superconductor, by G.C. Bailey and A.C. Ehrlich, *Physics Letters* **92A**:457-460

ODMR Investigation of the PGa Antisite Defect in GaP, by N. Killoran,* B.C. Cavenett,* M. Godlewski,* T.A. Kennedy, and N.D. Wilsey *Journal of Physics C* **15**:L723-L728

Oxygen Adsorption on the Indium Antimonide (110) Surface, by V.M. Bermudez and V.H. Ritz, *Physical Review B* **26**:3297-3308

Partial Gapping of the Fermi Surface and Superconductivity in $Eu_xMo_6S_8$, by R.C. Lacoe, S.A. Wolf, P.M. Chaikin,* C.Y. Huang,* and H.L. Luo,* *Physical Review Letters* **48**:1212-1215

Photo-Hall Measurements on Laser-Generated Electron-Hole Plasmas in $Hg_{1-x}Cd_xTe$, by F.J. Bartoli, J.R. Meyer, R.E. Allan, and C.A. Hoffman, *Journal of Vacuum Science and Technology* **21**:241-243

Photoluminescence and Transport Studies of Impurity Redistribution in Fe- and Cr-Doped InP, by B.V. Shanabrook, P.B. Klein,

P.G. Siebenmann, H.B. Dietrich, R.L. Henry, and S.G. Bishop, in *Semi-Insulating III-V Materials*, Shiva Publ., Ltd., England, pp. 310-313

Photoluminescence Excitation Spectroscopy of the 0.645 eV Emission Band in Semi-Insulating GaAs, by B.V. Shanabrook, P.B. Klein, and S.G. Bishop, in *Semi-Insulating III-V Materials*, Shiva Publ., Ltd., England, pp. 160-165

Preparation and Properties of 2H SiC Crystals, by A. Addamiano, *Journal of Crystal Growth* **58**:617-622

Radiation-Induced Paramagnetism in a-Si:H, by W.M. Pontuschka, W.E. Carlos, P.C. Taylor, and R.W. Griffith,* *Physical Review B* **25**:4362-4376

Rapid High Pressure Structural Information from Energy Dispersive Analyses of Diffracted Synchrotron Radiation, by E.F. Skelton, *Advances in Earth and Planetary Science* **12**:61-72

Reliability of Amorphous Metallizations for GaAs FETs, by A. Christou, W.T. Anderson, M.L. Bark, and J.E. Davey, in *IEEE 1982 International Reliability Physics Symposium*, IEEE, New York, pp. 188-193

Renormalized Thermal Distribution Function in an Interacting Electron-Phonon System, by W.E. Pickett, *Physical Review Letters* **48**:1548-1551

Report on the 1982 GaAs Device Reliability Workshop, by A. Christou, in *IEEE 1982 International Reliability Physics Symposium*, IEEE, New York, pp. 276-277

Resistive and Magnetic Susceptibility Transitions in Superconducting $(TMTSF)_2ClO_4$, by D.U. Gubser, W.W. Fuller, T.O. Poehlers,* J. Stokes,* D.O. Cowan,* M. Lee,* and A.N. Bloch,* *Molecular Crystals and Liquid Crystals* **79**:225-234

Secondary Electron Emission and Conductivity Mechanisms of Epitaxial MgO Films, by J.W. Gibson and R.E. Thomas, *Applications of Surface Science* **14**:56-72

Stable High Temperature Tantalum Silicide Schottky Barrier on Gallium Arsenide, by W.F. Tseng and A. Christou, in *International Electron Device Meeting (IEDM)*, IEEE, New York, pp. 174-176

Stark Effect on SiOH and SiH Molecules in SiO_2, by E.D. Palik, R.T. Holm, A. Stella,* and H.L. Hughes, *Journal of Applied Physics* **53**:8454-8461

Study of $Sn_xEu_{1.2-x}Mo_6S_8$ Under High Pressure and High Magnetic Field, by C.Y. Huang,* D.W. Harrison,* S.A. Wolf, W.W. Fuller, and H.L. Luo,* *Physica B+C* **109&110**:1649-1656

Study of the Etch-Stop Mechanism in Silicon, by E.D. Palik, J.W. Faust, Jr., H.F. Gray, and R.F. Greene, *Journal of the Electrochemical Society* **129**:2051-2059

Summary Abstract: Changes in the Surface Composition of Si, TiO_2, and SiO_2 Induced by Pulsed Ruby-Laser Irradiation, by V.M. Bermudez, *Journal of Vacuum Science and Technology* **20**:741-742

Superconductivity Properties of Amorphous Transition Metal Alloys, by J. Flasck,* J. Wood,* A.S. Edelstein, J.E. Keem,* and F.P. Missell,* *Solid State Communications* **44**:649-652

Symmetric Relaxation of the Hydrogen-Saturated Silicon Vacancy, by W.E. Pickett, *Physical Review B* **26**:5650-5657

Synthesis and Study of Electrochemically Grown Salts of Organic π-Donors, by M.M. Lee,* J.P. Stokes,* F.M. Wiygul,* T.J. Kistenmacher,* D.O. Cowan,* T.O. Poehler,* A.N. Bloch,* W.W. Fuller, and D.U. Gubser, *Molecular Crystals and Liquid Crystals* **79**:145-154

†**Systematics of Electron-Hole Liquid Condensation from Studies of Silicon with Varying Uniaxial Stress,** by A. Forchel,* B. Laurich,* J. Wagner,* W. Schmid,* and T.L. Reinecke, *Physical Review B* **25**:2730-2747

Temperature Dependence of Strength and Fracture Toughness of ZrO_2 Single Crystals, by R.P. Ingel, D. Lewis, R.W. Rice, and B.A. Bender, *Journal of the American Ceramic Society* **65**:C-150—C-152

Temperature Dependence of the Spin-Waves in $ErFe_{29}$, by K. Clausen,* J.J. Rhyne,* B. Lebeck,* and N.C. Koon, *Journal of Physics C: Solid State Physics* **15**:3587-3596

The Coordination of Boron in a-Si:(B,H), by S.G. Greenbaum, W.E. Carlos, and P.C. Taylor, *Solid State Communications* **43**:663-666

The IVth International Conference on the Electronic Properties of Two-Dimensional Systems (EP22D-IV), by J.J. Quinn and B.D. McCombe, *Comments on Solid State Physics* **10**:139-154

The Structure of Displacement Cascades in Silicon, by G.P. Mueller, N.D. Wilsey, and M.

Rosen, *IEEE Transactions on Nuclear Science* NS-29:1493-1497

Theoretical Determination of Electronic Charge Densities in Covalently Bonded Semiconductors, by C.S. Wang and B.M. Klein, in *Electron Distributions and the Chemical Bond*, Plenum Press, New York, pp. 133-151

Theoretical Studies of Hydrogen Interstitials in AB_2 Structure Laves Phase Compounds, by B.M. Klein and W.E. Pickett, *Journal of the Less-Common Metals* 88:231-237

Theory for Electron Mobilities in *n*-Type $Hg_{1-x}Cd_xTe$ and CdTe at Low Temperatures, by J.R. Meyer and F.J. Bartoli, *Journal of Vacuum Science and Technology* 21:237-240

Thermal Potential, Mechanical Instability, and Melting Entropy, by A.R. Ruffa, *Physical Review B* 25:5895-5900

Thermoelectric Power of $HfTe_5$ and $ZrTe_5$, by T.E. Jones,* W.W. Fuller, T.J. Wieting, and F. Levy,* *Solid State Communications* 42:793-798

Transferability and the Electron-Phonon Interaction: A Reinterpretation of the Rigid-Muffin-Tin Approximation, by W.E. Pickett, *Physical Review B* 25:745-754

Transient Infrared Reflection and Transmission of Silicon During Pulsed Laser Annealing, by S.C. Moss and C.L. Marquardt, *Laser and Electron-Beam Interactions with Solids*, Elsevier Science Publishing Co., Inc., New York, pp. 79-84

SPACE SCIENCE AND TECHNOLOGY

A Magnetic Cloud and a Coronal Mass Ejection, by L.F. Burlaga,* L. Klein,* N.R. Sheeley, D.J. Michels, R.A. Howard, M.J. Koomen,* R. Schwenn,* and H. Rosenbauer, *Geophysical Research Letters* 9:1317-1320

A Numerical Simulation of Cooling Coronal Flare Plasma, by G.A. Doschek, J.P. Boris, C.C. Cheng, J.T. Mariska, and E.S. Oran, *Astrophysical Journal* 258:373-383

A Phase-Coherent Link Via Synchronous Satellite Developed for Very Long Baseline Radio Interferometry, by S.H. Knowles, W.B. Waltman, J.L. Yen,* J. Galt,* D.N. Fort, W.H. Cannon,* D. Davidson,* W. Petrachenko,* and J. Popelar,* *Radio Science* 17:1661-1670

A Transient 77-keV Emission Feature from the Crab Pulsar, by M.S. Strickman, J.D. Kurfess, and W.N. Johnson, *Astrophysical Journal* 253:L23-L27

Active Galactic Nuclei and Particle Acceleration in Accretion Disks Around Massive Black Holes, by M. Kafatos,* M.M. Shapiro, and R. Silberberg, in *Compendium in Astronomy*, D. Reidel Publishing Company, New York pp. 323-345

Airborne Observations of the Orion Molecular Hydrogen Emission, by D.S. Davis,* H.P. Larson,* and H.A. Smith, *Astrophysical Journal* 259:166-179

An 80 Day X-Ray Light Curve of 3C371, by W.A. Snyder,* K.S. Woods, D.J. Wentis, J.F. Meekins, H.W. Smathers, E.J. Byram, T.A. Chubb, and H. Friedman, *Astrophysical Journal* 259:38-47

An Accurate Position for the 6-cm OH Maser in W3, by L.J. Rickard,* D.A. Crocker,* P.F. Bowers, and S.R. Spangler,* *Astronomical Journal* 87:1806-1809

An Analysis of the OI 1304 ÅDayglow Using a Monte Carlo Resonant Scattering Model with Partial Frequency Redistribution, by R.R. Meier and J-S. Lee, *Planetary and Space Science* 30:439-450

An Explanation for the Systematic Flow of Plasma in the Solar Transition Region, by J.P. Boris and J.T. Mariska, *Astrophysical Journal Letters* 258:L49-L52

Analysis of Nitrogen and Oxygen Far Ultraviolet Auroral Emissions, by R.R. Meier, R.R. Conway, P.D. Feldman,* D.J. Strickland,* and E.P. Gentieu,* *Journal of Geophysical Research* 87:2444-2452

Anomalous Auroral Electron Distribution Due to an Artificial Ion Beam in the Ionosphere, by T.E. Moore,* R.L. Arnoldy,* R.L. Kaufman,* L.J. Cahill,* P.M. Kintner,* and D.N. Walker, *Journal of Geophysical Research* 89:7569-7579

Balloon Observations of Galactic High-Energy X-Ray Sources, by G.S. Maurer, W.N. Johnson, J.D. Kurfess, and M.S. Strickman, *Astrophysical Journal* 254:271-278

Candidate Radio Sources for a Radio/Optical Reference Catalog, by A. Witzel* and K.J. Johnston, *Abhandlungen aus der Hamburger Sternwarte* 10(3):151-164

Charge Exchange in the Io Torus and Exosphere, by R.E. Johnson* and D.F. Strobel,

Journal of Geophysical Research **87**:10385-10393

Chemistry and Evolution of Titan's Atmosphere, by D.F. Strobel, *Planetary and Space Science* **30**:839-848

Comparison of VLBI, TV and Traveling Clock Techniques for Time Transfer, by J.H. Spencer, E.B. Waltman, K.J. Johnston, N.J. Santini, W.J. Klepczynski,* D.N. Matsakis,* P.E. Angerhofer,* and G.H. Kapla,* in *Proceedings of the Thirteenth Annual Precise Time and Time Interval(PTTI) Conference, Applications and Planning Meeting*, NASA Conference Publication 2220, pp. 231-241

Coronographic Observations of Two New Sungrazing Comets, by N.R. Sheeley, R.A. Howard, M.J. Koomen,* and D.J. Michels, *Nature* **300**:239-242

Direct Measurements of Impulsive Extreme Ultraviolet and Hard X-Ray Solar Flare Emission by J.M. Horan, R.W. Kreplin, and G.G. Fritz, *Astrophysical Journal* **255**:797-805

Doppler Wavelength Shifts of Ultraviolet Spectral Lines in Solar Active Regions, by U. Feldman, L. Cohen,* and G.A. Doschek, *Astrophysical Journal* **255**:325-328

Electron Density Diagnostic Line Ratios from the n=3 Lines of OV, by K.G. Widing, J.G. Doyle,* P.L. Dufton,* and A.E. Kingston,* *Astrophysical Journal* **257**:913-917

EUV Emission for Titan's Upper Atmosphere: Voyager I Encounter, by D.F. Strobel and D.W. Shemansky,* *Journal of Geophysical Research* **87**:1361-1368

Evidence for Coherent Emission with a 12 Millisecond Period During a Burst from MXB1728-34, by D. Sadeh,* E.J. Byram, J. A. Chubb, H. Friedman, R.L. Hedler, J.F. Meekins, K.S. Wood, and D.J. Yentis, *Astrophysical Journal* **257**:214

Extreme Ultraviolet Spectra of Solar Active Regions and Their Analysis, by K.P. Dere, *Solar Physics* **77**:77-93

Far Ultraviolet Wide Field Imaging with a Spartan (Experiment of Opportunity) Payload, by G.R. Carruthers, H.M. Heckathorn, and C.B. Opal, in *AIAA Sounding Rocket Conference*, AIAA, New York, pp. 24-31

Far-Infrared Observations of FU Orionis, by H.A. Smith, H.A. Thronson,* C.J. Lada,* D.J. Strickland,* and R.R. Meier, *Astrophysical Journal* **258**:170-176

Geopositioning Accuracy of an Autonomous Navigation System Using Landmarks, by F.L. Markley, in *Proceedings of the 1982 American Control Conference*, IEEE, New York, pp. 628-633

High Resolution X-Ray Spectra of Solar Flares VI. Impulsive Soft X-Ray Flares, by U. Feldman, G.A. Doschek, and R.W. Kreplin, *Astrophysical Journal* **260**:885-893

High Spectral and Spatial Resolution Observations of the 12.28 Micron Emission from H_2 in the Orion Molecular Cloud, by S.C. Beck,* E.E. Bloemhof,* E. Serakyn,* C.H. Townes,* A.T. Tokunaga,* J.H. Lacey, and T.H.A. Smith, *Astrophysical Journal* **253**:683-687.

Infrared Atomic Hydrogen Line Formation in Luminous Stars, by J.H. Krolik* and H.A. Smith, in *Regions of Recent Star Formation*, Reidel, Boston, pp. 161-166

Infrared Spectra of Galactic Center Sources, by E.R. Wollman,* H.A. Smith, and H.P. Larson,* *Astrophysical Journal* **258**:506-514

Ionospheric Irregularity Physics Modelling, by S.L. Ossakow, M.J. Keskinen, and S.T. Zalesak, in *AIAA 20th Aerospace Sciences Meeting*, AIAA, New York, AIAA-82-0147, pp. 1-16

Is the SiO Maser in Orion Associated with a Late Type Star? by P.R. Schwartz, *Annals of the New York Academy of Sciences* **395**:216-220

Kalman Filtering for Spacecraft Attitude Estimation, by F.L. Markley and E.J. Lifferts, in *AIAA 20th Aerospace Sciences Meeting*, AIAA, New York, Paper 82-0070, pp. 417-429

Laboratory Simulation of Injection Particle Beams in the Ionosphere, by S.H. Knowles, W.B. Waltman, and R.H. Smith,* in *Artificial Particle Beams in Space Plasma Studies*, Plenum Press, New York, pp. 289-329

Large Scale X-Ray and Radio Structures Associated with Compact Extragalactic Sources, by P. Biermann,* K. Fricks,* K.J. Johnston, H. Kuhr,* I.I.K. Pauling-Toth,* P.A. Strittmatter,* M. Urbanik,* and A. Witzel,* *Astrophysical Journal* **282**:21-25

Magnetic Measurements of Coronal Holes During 1975-1980, by K.L. Harvey,* N.R. Sheeley, and J.W. Harvey,* *Solar Physics* **79**:149-160

Nearly Simultaneous Observations of Vibrationally Excited J=1 → 0, J=2 → 1, J=3 → 2, and J=4 → 3 SiO Masers, by P.R. Schwartz, B. Zuckerman,* and J.M. Bologna,

Astrophysical Journal **256**:L55-L59

Observational Constraints for a Theoretical Model Describing the Soft X-Ray Flare, by U. Feldman, C.C. Cheng, and G.A. Doschek, *Astrophysical Journal* **255**:320-324

Observations of 1 Ceres and 2 Pallas at Centimeter Wavelengths, by K.J. Johnston, P.K. Seidelmann,* and C.M. Wade,* *Astronomical Journal* **87**:1593-1599

†**Observations of a Comet on Collision Course with the Sun**, by D.J. Michels, N.R. Sheeley, Jr., R.A. Howard, and M.J. Koomen,* *Science* **215**:1097-1102

Observations of Coronal Structure During Sunspot Maximum, by N.R. Sheeley Jr., R.A. Howard, M.J. Koomen, D.J. Michels, K.L. Harvey,* and J.W. Harvey,* *Space Science Reviews* **33**:219-231

Observations of SiO Maser Emission from R LEO During Its Summer 1981 Maximum, by F.O. Clark,* J.A. Waak, and J.M. Bologna, *Astronomical Journal* **87**:1803-1805

Precise Radio Source Positions from Interferometric Observations, by G.H. Kaplan,* F.J. Josties,* P.E. Angerhofer,* K.J. Johnston, and J.H. Spencer, *Astronomical Journal* **87**:570-576

Quiet Sun Observations of the Al I Autoionization Lines λ1932 and λ1936, by J.W. Cook and O. Kjeldseth Moe,* *Solar Physics* **76**:109-116

Radiation Field in the Troposphere and Stratosphere from 240-1000 nm I. General Analysis, by R.R. Meier, D.E. Anderson, and M. Nicolet,* *Planetary and Space Science* **30**:923-933

Radiation Field in the Troposphere and Stratosphere II. Numerical Analysis, by M. Nicolet,* R.R. Meier, and D.E. Anderson, *Planetary and Space Science* **30**:935-983

Radio Jets in NGC 4151, by K.J. Johnston, M. Elvis,* D. Kjer,* and B.S.P. Shen,* *Astrophysical Journal* **262**:61-65

Radio Source Reference Frames, by K.J. Johnston and J.S. Ulvestad,* in NOAA Technical Report NOS95-NGS24, pp. 7-18

Recommended Satellite Imagery Capabilities for Disaster Management, by P.B. Richards, C.J. Robinove,* and D.R. Wiesnet,* in *Proceedings of the 33rd IAF Congress*, AIAA, New York

S IV Emission-Line Ratios in the Sun, by P.L. Dufton,* A. Hibbert,* A.E. Kingston,* and G.A. Doschek, *Astrophysical Journal* **257**:338-344

Search for Red-Shifted CH_2O, H_2O, O_2 and NH_3 in Seyfert Galaxies and Quasars, by D.M. Matsakis,* J.M. Bologna, P.R. Schwartz, and D.L. Thacker, *Publications of the Astronomical Society of the Pacific* **94**:26-30

†**Self-Absorption of the N_2 Lyman-Birge-Hopfield Bands in the Far Ultraviolet Dayglow**, by R.R. Conway, *Journal of Geophysical Research* **87**:859-866

Simultaneous Radio and X-Ray Activity in SS 433, by E.R. Seaquist,* W.S. Gilmore,* K.J. Johnston, and J.E. Grindlay,* *Astrophysical Journal* **260**:220-232

Simultaneous Radio Scattering and White Light Observation of a Coronal Transient, by R. Woo,* J.W. Armstrong,* N.R. Sheeley, R.A. Howard, D.J. Michels, and M.J. Koomen, *Nature* **300**:157-159.

Solar Physics Branch, E.O. Hulburt Center for Space Research, Naval Research Laboratory, by G.E. Brueckner, *Bulletin of the American Astronomical Society* **14**:411-415

Solar Transition Regions Response to Variations in the Heating Rate, by J.T. Mariska, J.P. Boris, E.S. Oran, T.R. Young, and G.A. Doschek, *Astrophysical Journal* **255**:783-796

Solar Transition Zone Pressures from EUV Observations of O IV and N IV, by K.P. Dere, J-DF. Bartoe, and G.E. Brueckner, *Astrophysical Journal* **259**:366-371

Space Schmidt Telescope, by J.D. Wray,* H.J. Smith,* K.G. Henize,* and G.R. Carruthers, in *Advanced Technology Optical Telescope*, SPIE, Bellingham, Washington, SPIE Vol. 332, pp. 141-150

Space Technology Contributions to Emergency and Disaster Management, by P.B. Richards, *Advances in Earth Oriented Applications of Space Technology* **1**:215-221

Spectroscopy of the OI 989- and 7990-Å Multiplets in the Dayglow and Aurora, by R.R. Meier, *Journal of Geophysical Research* **87**:6307-6316

SS 433 — Observing Evolution in a Precessing, Relativistic Jet, by R.M. Hjellming* and K.J. Johnston, in *Extragalactic Radio Astronomy, I.A.U. Symposium 97*, D. Reidel Publishing Co., Boston, Massachusetts, pp. 197-204

The Condensational Instability in the Solar Transition Region and Corona, by E.S. Oran, J.T. Mariska, and J.P. Boris, *Astrophysical Journal* **254**:349-360

The Coronal Field Lines of an Evolving Bipolar Magnetic Region, by N.R. Sheeley, *Astrophysical Journal* **255**:316-319

The Distribution of the $^2\pi_{3/2}$ OH Maser Emission Associated With W49N, by K.J. Johnston and S.S. Hansen,* *Astronomical Journal* **87**:803-807

The Dynamics of Accelerating Coronal Bullets, by J.T. Karpen, E.S. Oran, J.T. Mariska, J.P. Boris, and G.E. Brueckner, *Astrophysical Journal* **261**:375-386

The Extended Radio Structure of Compact Extragalactic Sources, by R.A. Perley,* E.B. Fomalont*, and K.J. Johnston, *Astrophysical Journal* **255**:L93-L97

The Extreme-Ultraviolet Spectrum of a Solar Impulsive Burst, by K.G. Widing, *Astrophysical Journal* **258**:835-845

The Impulsive and Gradual Phases of a Solar Limb Flare as Observed from the Solar Maximum Mission Satellite, by A.I. Poland,* M.E. Machado,* C.J. Wolfson,* K.J. Frost,* B.E. Woodgate,* R.A. Shine,* P.J. Kenny,* C.C. Cheng, E.A. Tandberg-Hanssen, E.C. Bruner,* and W. Henze,* *Solar Physics* **78**:201-213

The Observation of a Coronal Transient Directed at Earth, by R.A. Howard, D.J. Michels, N.R. Sheeley, and M.J. Koomen,* *Astrophysical Journal* **213**:L101-L104

The S3-4 Ionospheric Irregularities Satellite Experiment: Probe Detection of Multi-Ion Component Plasmas and Associated Effects on Instability Processes, by E.P. Szuszczewicz, J.C. Holmes, and M. Singh,* *Astrophysics and Space Science* **86**:235-248

The Space Ultraviolet Radiation Environment (SURE) Experiment for Shuttle Space Flight, by C.S. Weller, in *AIAA Sounding Rocket Conference*, AIAA, New York, pp. 32-34

The Spectral Dependence of Dust Emissivity at Millimeter Wavelengths, by P.R. Schwartz, *Astrophysical Journal* **252**:589-593

The Utility of Landsat-D and Other Satellite Imaging Systems in Disaster Management, by P.B. Richards, NASA Report DPR S-79677, National Aeronautics and Space Administration, Washington, D.C.

The Variability of Mesospheric Water Vapor, by C.J. Gibbins,* P.R. Schwartz, D.L. Thacker, and R.M. Bevilacqua,* *Geophysical Research Letters* **9**:131-134

†Third-Order Solution to the Main Problem in Satellite Theory, by S.L. Coffey and A. Deprit,* *Journal of Guidance, Control, and Dynamics* **5**:366-371

Three Rich Clusters of Galaxies with Bimodal or Clumpy X-Ray Morphologies, by M.P. Ulmer* and R.G. Cruddace, *Astrophysical Journal* **258**:434-438

Two Micron Observations of ^{12}CO and ^{13}CO in the Red Giant Sources IRS 7, IRS 12, and IRS 19, by G.C. Augason,* H.A. Smith, E.R. Wollman,* H.P. Larson,* and H.R. Johnson,* in *The Galactic Center*, American Institute of Physics, New York, pp. 82-84

Ultraviolet Continuum Absorption ($\geq$ 1000 Å) Above the Quiet Sun Transition Region, by G.A. Doschek and U. Feldman, *Astrophysical Journal* **254**:371-375

Very High Resolution Observations of the Radio Source in the Supernova Remnant G127.1+0.5, by B.J. Geldzahler and D.B. Shaffer,* *Astrophysical Journal* **260**:L69-L74

VLA Observations of a Highly Symmetric OH Maser in a Bipolar Nebula, by M. Morris,* P.F. Bowers, and B.E. Turner,* *Astrophysical Journal* 259:625-633

VLA Observations of Mass Loss from T Tauri Stars, by M. Cohen,* J.H. Bieging,* and P.R. Schwartz, *Astrophysical Journal* **253**:707-715

VLBI Observation of 21 Compact Radio Sources North of Declination 70°, by A. Eckart,* P. Hill,* K.J. Johnston, I.I.K. Pauling-Toth,* J.H. Spencer, and A. Witzel,* *Astronomy and Astrophysics* **108**:157-160

VLBI Observations of the Nucleus and Jet of M87, by M.J. Reid,* J.H.M.M. Schmitt,* F.N. Owen,* R.S. Booth,* P.N. Wilkinson,* D.B. Shaffer,* K.J. Johnston, and P.E. Harder,* *Astrophysical Journal* **263**:615-623

STRUCTURE RESEARCH

A Procedure for Joint Refinement of Macromolecular Structures with X-Ray and Neutron Diffraction Data from Single Crystals, by A. Wlodawer* and W.A. Hendrickson, *Acta Crystallographica* **A38**:239-247

Conformational Flexibility and Characteristics of Cyclic Tetra- and Pentopeptides, by I.L. Karle, in *Molecular Structure and Biological Activity*, Elsevier Science Publishing Co., New York, pp. 215-227

Crystal Structure of the 1:1 Mixture of Cyclic (L-Ala-L-Pro-L-Phe-L-Pro) and Cyclic

(L-Ala-L-Pro-L-Phe-L-Pro) and Cyclic (L-Ala-L-Pro-D-Phe-L-Pro), by C.C. Chiang and I.L. Karle, *International Journal of Peptide and Protein Research* **20**:133-138

Experimental Investigation of Large Amplitude Motions: Illustrations from Current Research, by A.H. Lowrey, in *Diffraction Studies on Non-Crystalline Substances*, Akademiai Kiado, Budapest, pp. 199-241

Formulas for *n*-tet Phase Invariants and Embedded Seminvariants for all Space Groups, by J. Karle, *Acta Crystallographica* **A38**:327-333

General Phase-Invariant Formulas of Higher Order: Expected Values, by J. Karle, *Proceedings of the National Academy of Sciences* **79**:2125-2127

Heavy Atoms in Structure Determination, by J. Karle, in *Computational Crystallography*, Oxford University Press, New York, pp. 174-200

Peptide Conformation: Variability and Uniqueness by I.L. Karle and J. Karle, in *Conformation in Biology*, Festschrift Celebrating the Sixtieth Birthday of G.N. Ramachandran, F.R.R.S., Adenine Press, New York, pp. 119-131

Raman Spectroscopic Determination of the Secondary Structure of Crystalline Nerve Growth Factor, by R. Williams, B. Gaber, and J. Gunning,* *Journal of Biological Chemistry* **257**:13321-13323

Resolved-Anomalous Phase Determination in Macromolecular Crystallography, by J.L. Smith and W.A. Hendrickson, in *Computational Crystallography*, Oxford University Press, New York, pp. 209-222

Special Phase-Invariant Formulas of Higher Order: Expected Values, by J. Karle, *Proceedings of the National Academy of Sciences* **79**:1337-1339

Stereochemistry of a Complex Diindenopyradione, by J.L. Flippen-Anderson and F.D. Mills,* *Acta Crystallographica* **B38**:495-498

Structural Ordering in Amorphous $TbFe_2$ and **YFe_2**, by P. D'Antonio, J.H. Konnert, and J.J. Rhyne,* *Journal of Applied Crystallography* **15**:452-460

The Tricyclic Photorearrangement Product from the Addition of 3-Methyl-5,6-diaza-2,4-cyclohexadien-1-one to 2-Propenol, 7-Hydroxymethyl-8-methyl-2,3-diazatricyclo-[3.3.0.$0^{2,8}$]octan-4-one, $C_8H_{12}N_2O_2$, by I.L. Karle, *Acta Crystallographica* **B38**:1022-1024

***trans-syn* Cyclobutane-Type Photodimers of 1,3,3 - Trimethyl - 2,4(1H,3H) - pyridinedione and 1,3,3,6 - Tetramethyl - 2,4(1H,3H) - pyridinedione**, by I.L. Karle, *Acta Crystallographica* **B38**:1016-1018

Unusual Intramolecular Hydrogen Bonding in Cycloamanide A, Cyclic (LPro-LVal-LPhe-LPhe-LAla-Gly). A Crystal Structure Analysis, by C.C. Chiang, I.L. Karle, and T. Wieland,* *International Journal of Peptides and Protein Research* **20**:414-420

†**X-ray Absorption Spectroscopy of the Dimeric Iron Site in Azidomethemerythrin from *Phascolopsis Gouldii***, by W.A. Hendrickson, M.S. Co,* J.L. Smith, K.O. Hodgson,* and G.L. Klippenstein,* *Proceedings of the National Academy of Sciences* **79**:6255-6259

FORMAL REPORTS

ACOUSTICS

8575 **Predicted Beam Patterns of Bottom-Deployed, Horizontal Dipoles in the Straits of Florida**, by W.C. Dixon

8600 **Frequency Dispersion of Sound in Undersea Propagation**, by A.A. Gerlach, K.D. Flowers, R.B. Johnson, W.L. Anderson, and E.L. Kunz

8607 **Solving the Parabolic Equation for Underwater Acoustic Propagation by the Split-Step Algorithm**, by J.S. Perkins, R.N. Baer, E.B. Wright, and L.F. Roche*

8623 **Stern-Aspect Noise Radiated by the Cycloidally Propelled Vessel *Seacon* and its Comparison with that Radiated by Conventionally Propelled Vessels**, by S.C. Wales and B.B. Adams

†8633 **The Development of a High-Power, Low-Frequency Underwater Acoustic Source for Use in a Deep-Towed Geophysical Array System**, by A.M. Young, A.C. Tims, and T.A. Henriquez

ATMOSPHERIC SCIENCES

8536 **A Time-Dependent Oceanic Aerosol Profile Model,** by S.G. Gathman

8647 **Profile-Bulk Method Formulas for Calculating Flux and Stability in the Marine Atmospheric Surface Layer and a Survey of Field Experiments,** by T.B. Blanc

8652 **Atmospheric Methane Concentrations in the Arctic and Subarctic Regions: 1971-1979,** by R.A. Lamontagne

CHEMISTRY

8523 **NRL 324-m^3 Chamber Pressurization Experiment: Pressurant Concentration Histories With and Without Obstacles to Flow**, by J.P. Stone, J.I. Alexander, T.T. Street, H.J. St. Aubin, and F.W. Williams

8550 **Combustion Scaling and Modeling Gas Mixing Data in NRL 5000-Liter Facility with Flow Obstacle**, by S.R. Lustig, D. Indritz, J.P. Stone, and F.W. Williams

8588 **An Improved Light Hydrocarbon Analysis System**, by R.A. Lamontagne

8609 **Scale-Modeling of Inert Pressurant Distribution as Applied to Fire Extinguishment by Nitrogen Pressurization**, by J.P. Stone, F.W. Williams, H.W. Carhart, and R.C. Corlett

8630 **Pyrolysis of Organic Compounds Containing Long Unbranched Alkyl Groups**, by G.W. Mushrush and R.N. Hazlett

8643 **Large-Scale Pressurizable Fire Test Facility — FIRE I**, by J.I. Alexander, J.P. Stone, T.T. Street, F.W. Williams, and H.J. St.Aubin

COMMUNICATIONS

8570 **On Pitch-Synchronous Abridgment of the Linear Prediction Residual**, by N.D. Smith

8583 **A Conversational Test for Comparing Voice Systems Using Working Two-Way Communication Links**, by A. Schmidt-Nielsen and S.S. Everett

8589 **The Perception of Pitch Waver in Synthetic Vowels Heard over Headphones and Loudspeakers**, by A. Schmidt-Nielsen and S.S. Everett

8604 **An Approach to Describing the Functional Requirements of an Embedded Communication System**, by C.L. Heitmeyer and J.D. McLean

†8610 **Pointing Performance of the 8300 Series Datron Antennas**, by J.E. Kenney and A.P. Sharman

8614 **Second Report of the Multirate Processor (MRP) for Digital Voice Communications**, by G.S. Kang and L.J. Fransen

8638 **An Architecture for the High-Frequency Intratask Force (ITF) Communication Network**, by D.J. Baker, A. Ephremides, and J.E. Wieselthier

8645 **Improvement of the Narrowband Linear Predictive Coder, Part 1 — Analysis Improvements**, by G.S. Kang and S.S. Everett

8651 **On the Solution of a Fokker-Planck Equation in the Presence of Correlated Noise**, by H.N. Ho and R.H. Lang*

COMPUTER SCIENCES

8561 **Computer Program for Microwave GaAs MESFET Modeling**, by R.E. Neidert and C.J. Scott

8598 **A Comparison of Errors in Different Software-Development Environments**, by D.M. Weiss

8611 **A FORTRAN-Based Program for Computerized Algebraic Manipulation**, by R.R. Dasenbrock

MATHEMATICS

8573 **Fourier Transform Reconstruction from Inexact Data**, by C.L. Byrne and R.M. Fitzgerald

8619 **The Application of Fuzzy-Set Theory to the Burnthrough Range Equation**, by F. Gross, D.J. Hanrahan, and S.T. Hood

8624 **Load Numbers, Solid Earth Tides, and Liquid Core Dynamics**, by P. Lanzano

MECHANICS

8631 **Procedures for Conducting Shock Tests on Navy Class HI (High Impact) Shock Machines for Lightweight and Medium-weight Equipments**, by E.W. Clements

SPACE SCIENCE AND TECHNOLOGY

8487 **Revised S201 Catalog of Far-Ultraviolet Objects**, by T. Page,* G.R. Carruthers, and H.M. Keckathorn

8599 **Long Term Frequency Stability Analysis of the GPS NAVSTAR 6 Cesium Clock**, by T.B. McCaskill, S.B. Stebbins, and C. Carson,

8608 **Prototype Design and Initial Test Evaluation of a Global-Positioning System Time-Transfer Receiver (GPS/TTR)**, by O.J. Oaks, A.H. Frank, S.R. Falvey, M.J. Lister, J.A. Buisson, S.C. Wardrip,* and H.F. Warren,*

RADAR

8540 **Polyphase Pulse Compression Waveforms**, by F.F. Kretschmer and B.L. Lewis

8557 **High-Resolution Radar Sea Scatter, Experimental Observations and Discriminants**, by J.P. Hansen and V.F. Cavaleri

8558 **The Design of a Real-Time Signal Sorter**, by T.R. Husson and R.H. Evans

8571 **Automatic Detectors for Frequency-Agile Radars**, by G.V. Trunk

8572 **Detection Strategies for High-Resolution Radar**, by P.K. Hughes

8574 **Broad-Band Mirror-Scanned Surveillance Radar Antenna**, by B.L. Lewis, J.P. Shelton, E.E. Maine, N.V. O'Neal, and C.L. Moody

†8579 **Estimation of the Sea Surface Radar Cross Section at HF from Second-Order Doppler Spectrum Characteristics**, by D.B. Trizna

8584 **Suppression of Second Time Around Radar Returns Using PRI Modulation**, by K. Gerlach and G.A. Andrews

8586 **Properties of Even-Length Barker Codes and Specific Polyphase Codes with Barker Type Autocorrelation Functions**, by S. Gabbay*

8591 **A Comparison of Noncoherent and Coherent MTI**, by F.F. Kretschmer, F.C. Lin, and B.L. Lewis

8596 **End-Fire Hybrid Array Antennas**, by W.K. Kahn

8603 **Tracking Closely Spaced Multiple Sources via Spectral-Estimation Techniques**, by W.F. Gabriel

8625 **Effects of Bandwidth Limitation on Polyphase Coded Pulse Compression Systems**, by B.L. Lewis, F.F. Kretschmer, and F.C. Lin

8627 **Computing the Grazing Angle of Specular Reflection**, by A. Miller and E. Vegh

8628 **On the Accuracy of a Numerical Integration Procedure for Computing Diffraction Fields Using Table-Look-Up**, by J.K. Hsiao

8632 **On the Number of Degrees of Freedom Used by an Adaptive Antenna Array in a Non-Narrowband Noise Environment**, by K. Gerlach

8635 **Doppler Properties of Polyphase Coded Pulse Compression Waveforms**, by F.F. Kretschmer and B.L. Lewis

8636 **Adaptive Antenna Subarraying Using a Weighted Butler Matrix**, by K. Gerlach and G.A. Andrews

8639 **Rain Clutter Statistics**, by W.B. Gordon and J.D. Wilson

AWARD-WINNING NRL MEMORANDUM REPORT

†4845 **Mercury Contamination of a Community Water Supply: Diagnosis and Restoration**, by J.C. Cooper, C.J. Hackbarth, C.M. Hellwig, R. Panayappan, and D.L. Venezky

AWARD-WINNING SPECIAL LABORATORY PUBLICATION

†**Piece Part Neutron Hardness Assurance Guidelines for Semiconductor Devices**, by A. Namenson, E.A. Wolicki, R. Berger,* H. Eisen,* J. Ferry,* G. Messenger,* R. Scace,* and H. Schafft*

PATENTS GRANTED IN 1982

4,300,768—Dispersion Compensated Acoustic Surface Waveguides Using Diffused Substrates, May 18 to Peter H. C. Huang, Joseph F. Weller, and Thomas G. Giallorenzi

4,309,109—**Pulsed Interferometric Remote Gauge,** January 5 to Jerry A. Blodgett and Raymond A. Patten

4,310,843—**Electron Beam Controlled Array Antenna,** January 12 to Max N. Yoder

4,313,170—**Autocorrelation Side Lobe Reduction Device for Phase-Coded Signals,** January 26 to Bernard L. Lewis and Frank F. Kretschmer

4,315,093—**Fluorinated Polyphthalocyanines,** February 9 to Teddy M. Keller and James R. Griffith

4,316,201—**Low-Barrier-Height Epitaxial Ge-GaAs Mixer Diode,** February 16 to Aristos Christou and John E. Davey

4,318,099—**Clutter Filter Using a Minimum Number of Radar Pulses,** March 2 to James K. Hsiao

4,319,242—**Integrated Weapon Control Radar System,** March 9 to Bernard L. Lewis

4,321,549—**Switching Quadrature Detector,** March 23 to James P. Hansen

4,321,559—**Multiwavelength Self-Pumped Solid State Laser,** March 23 to Leon Esterowitz and Robert C. Echardt

4,323,641—**Photographic Image Enhancement by a Gold-Toning Neutron-Activation Process,** April 6 to Clarence D. Bond

4,323,867—**Frament-Tolerant Transmission Line,** April 6 to Clifford L. Temes

4,325,744—**Method and Composition for Cleaning Metal Surfaces,** April 20 to Ramanathan Panayappan and David L. Venezky

4,327,377—**Phase-Slipped Time Delay and Integration Scanning System,** April 27 to Edward H. Takken

4,327,493—**Method and Apparatus for Measurement of Distance Between Holes with Parallel Axes,** May 4 to Lee R. Dickerson

4,328,496—**Delay Control for a Pulse Repeat-Back Jamming System,** May 4 to Charles F. White

4,328,498—**Phased Array Antenna for Satellite,** May 4 to Max N. Yoder

4,328,569—**Array Shading for a Broadband Constant Directivity Transducer,** May 4 to James W. Trott and Jacek Jarzynski

4,330,343—**Refractory Passivated Ion-Implanted GaAs Ohmic Contacts,** May 18 to Aristos Christou and John E. Davey

4,330,570—**Elective Photoinduced Condensation Technique for Producing Semiconducting Compounds,** May 18 to John F. Giuliani and Abe Auerbach

4,330,689—**Multirate Digital Voice Communication Processor,** May 18 to George S. Kang, Lawrence J. Fransen, and Evans L. Kline

4,330,763—**Resonantly Pumped Mid-IR Laser,** May 18 to Leon Esterowitz and Melvin R. Kruer

4,336,362—**Acetylene-Terminated Dianil Monomer and the Polymer Therefrom,** June 22 to Theodore R. Walton

4,338,560—Albedo Radiation Power Converter, July 6 to Leo W. Lemley

4,345,207—**Method and Apparatus for Obtaining Enhanced NMR Signals.** August 17 to Richard D. Bertrand, Gerard C. Chingas, Allen N. Garroway, and William B. Moniz

4,346,348—**Laser Technique for Accurately Determining the Compensation Density in N-Type Narrow Gap Semiconductor,** August 24 to Filbert J. Bartoli and Jerry R. Meyer

4,346,420—**Magnetoplasmadynamic Switch,** August 24 to Peter J. Turchi

4,347,485—**Excimer-Pumped Blue-Green Laser,** August 31 to Leon Esterowitz, Roger E. Allen, Melvin R. Kruer, and Filbert J. Bartoli

4,347,593—**Piezoceramic Tubular Element with Zero End Displacement,** August 31 to James W. Trott

4,347,891—**Thermochemical Energy Transport Process,** September 7 to Talbot A. Chubb

4,348,074—**Application of Ion Implantation to LiNbO Integrated, Optical Spectrum Analyzers,** September 7 to William K. Burns and Thomas G. Giallorenzi

4,351,776—**Preparation of Iodophthalonitrile,** September 9 to Teddy M. Keller and James R. Griffith

4,356,296—**Fluorinated Diacrylic Esters and Polymers Therefrom,** October 26 to James R. Griffith and Jacques G. O'Rear

4,357,180—**Annealing of Ion-Implanted GaAs and InP Semiconductors,** November 2 to Bela Molnar

4,357,608—**Scanning Radar System,** November 2 to Bernard L. Lewis

4,359,411—**Flexible Semiconductive Polymers,** November 16 to Oh-Kil Kim and Robert B. Fox

4,359,735—**Multimpling-Channel Pulse Compressor** November 16 to Bernard L. Lewis and Frank F. Kretschmer, Jr.

4,359,736—**Frequency-Phase Coding Device,** November 16 to Bernard L. Lewis

4,359,738—**Clutter and Multipath Suppressing Sidelobe Canceller Antenna System,** November 16 to Bernard L. Lewis

4,360,182—**High-Agility Reflector Support and Drive System,** November 23 to James W. Titus

4,360,924—**Laser Bottlenecking Technique,** November 23 to J. Gary Eden

4,361,879—**Ferrofluid Transducer,** November 30 to Pieter S. Dubbelday and Robert W. Timme

4,362,932—**Wide Band Data Processing Technique,** December 7 to Bernard L. Lewis

4,362,968—**Slow-Wave Wideband Cyclotron Amplifier,** December 7 to Kwo R. Chu, Phillip A. Sprangle, and Victor L. Granatstein

4,363,114—***Low Noise* Remote Optical Fiber Sound Detector,** December 7 to Joseph A. Bucaro, James H. Cole, and Henry D. Dardy

4,364,048—**Interleaved Sweep Radar Display for Improved Target Detection,** December 14 to William M. Waters and George J. Linde

NRL Review Staff

Research Area Editors

Anthony E. Robson, *Senior Science Editor*

John T. Mariska, *General Science and Technology*

Felix Rosenthal, *Systems Research and Technology*

Richard Nekritz, *Material Science and Component Technology*

Jay W. Schwartz, *Space and Communications Technology*

Technical Information Staff

Earle E. Kirkbride, *Division Head*

Richard H. Baturin, *Staff Editor* and *Publication Coordinator*

Stanley Weintraub, *Associate Editor*

Dora B. Wilbanks and Staff, *Computerized Technical Composition (CTC)*

Jean Moon, *CTC Publication Coordinator*

Augustine Cook, *Assistant CTC Publication Coordinator*

Dolores J. Zimmer and Staff, *Graphic Services*

John C. Moon, *Cover*

DIRECTORY OF KEY OFFICES AND PERSONNEL

Code	Office	Incumbent	Ext.
	EXECUTIVE DIRECTORATE		
1000	Commanding Officer	CAPT J. A. McMorris II, USN	73403
1001	Director of Research	Dr. T. Coffey	73301
1003	DEEO Officer	Mrs. S. Eaton	72486
2610	Public Affairs Officer	Mr. J. W. Gately, Jr.	72541
1200	Chief Staff Officer	CAPT J. B. Morris, USN	73621
1220	Head, Security Branch	Mr. M. B. Ferguson	73048
1300	Comptroller	Mr. R. W. Steinbeck	73405
1400	Head, Management Information Division	Dr. A. H. Aitken	73666
1800	Civilian Personnel Officer	Mr. D. J. Blome	73421
1810	Personnel Operations	Mr. D. J. Blome†	73030
	TECHNICAL SERVICES DIRECTORATE		
2000	Associate Director of Research for Technical Services	Mr. J. D. Brown	72879
2004	Patent Counsel	Dr. W. T. Ellis	73428
2010	Safety Officer	Mr. H. C. Kennedy, Jr.	72249
2020	Head, Administrative Office	Mrs. L. V. Dabney	73858
2300	Engineering Services Officer	Mr. J. D. Brown*†	72879
2400	Supply Officer	CMDR J. R. McGraa, USN	73446
2500	Public Works Officer	CDR J. W. MacLaughlin, USN	73371
2600	Head, Technical Information Division	Mr. E. E. Kirkbride	73388
2700	Chesapeake Bay Division Officer	Vacancy	(301) 257-2111
2800	Head, Research Computation Division	Mr. A. B. Bligh	72751
	RESEARCH DIRECTORATES		
4000	Associate Director of Research for General Science and Technology	Dr. T. Coffey*	73324
4040	Laboratory for Computational Physics	Dr. J. P. Boris	73055
4100	Space Sciences Division Superintendent	Dr. H. Gursky	73363
4300	Environmental Sciences Division Superintendent	Dr. C. H. Cheek*	72974
4700	Plasma Physics Division Superintendent	Dr. S. L. Ossakow	72723
5000	Associate Director of Research for Systems Research and Technology	Mr. R. R. Rojas	73294
5100	Acoustics Division Superintendent	Dr. J. C. Munson	73482
5300	Radar Division Superintendent	Dr. M. I. Skolnik	72936
5700	Tactical Electronic Warfare Division Superintendent	Mr. L. A. Cosby	72191
5800	Marine Technology Division Superintendent	Dr. R. T. Swim	73314
5900	Underwater Sound Reference Detachment Superintendent	Dr. J. E. Blue	(305) 859-5720 AUTOVON 791-4111
6000	Associate Director of Research for Material Science and Component Technology	Dr. A. I. Schindler	73566
6030	Laboratory for Structure of Matter	Dr. J. Karle	72665
6070	Head, Health Physics Staff	Mr. J. N. Stone	72232
6100	Chemistry Division Superintendent	Dr. H. W. Carhart*	73026
6300	Material Science and Technology Division Superintendent	Dr. B. B. Rath*	73566
6500	Optical Sciences Division Superintendent	Dr. T. G. Giallorenzi	73171
6600	Condensed Matter and Radiation Sciences Division Superintendent	Dr. J. T. Schriempf	72931
6800	Electronics Technical Division Superintendent	Vacancy	73525
7000	Associate Director of Research for Space and Communication Technology	Dr. B. Wald	72964
7500	Communications Sciences Division Superintendent	Dr. J. R. Davis	72903
7700	Space Systems Division Superintendent	Mr. P. G. Wilhelm	72073
7900	Aerospace Systems Division Superintendent	Dr. R. A. LaFande	73468

† Additional Duty
* Acting

END

FILMED

1-84

DTIC